NORTHWESTERN UNIVERSITY

Exciton and Spin Dynamics of Singlet Fission in Polycrystalline Chromophore Films

A DISSERTATION

SUBMITTED TO THE GRADUATE SCHOOL
IN PARTIAL FULLFILLMENT OF THE REQUIREMENTS

for the degree

DOCTOR OF PHILOSOPHY

Field of Chemistry

By

Youn Jue Bae

EVANSTON, ILLINOIS

December 2020

Abstract

Exciton and Spin Dynamics of Singlet Fission in Polycrystalline Chromophore Films

Youn Jue Bae

Singlet Fission (SF) is a down-conversion process in organic chromophores where one high-energy singlet exciton is converted into two low-energy triplet excitons. Such carrier multiplication aspects of SF are promising in increasing the solar cell efficiency. The generation of two bound spin triplet states from the same singlet exciton also provides an interesting platform to study spin entanglement, which is an important concept for quantum information science and spintronics. As such, SF process necessitates fundamental understanding of exciton and electron spin dynamics.

The first half of this thesis investigates important design principles for anthracene-based SF chromophores. Although SF was first discovered in single crystals of anthracene, it has ~3% efficiency because the SF process needs to occur from the second excited singlet state, where internal conversion to the first excited singlet state is a dominant process. We increase π conjugation of anthracene by adding phenylethynyl groups at the 9,10 positions to form 9,10-bis(phenylethynyl)anthracene (BPEA). This lowers both the singlet and the triplet excited state energies. Unlike anthracene, BPEA has the correct energetics for SF to occur from the first singlet excited state, allowing fast and efficient SF. Since SF requires two or more coupled chromophores, we first synthesized the BPEA covalent dimer and further explored SF dynamics in solid state films. These results are summarized in chapters 2 and 3.

The second half of the thesis focuses on electron spin dynamics of SF by directly probing the spin sublevels using time-resolved electron paramagnetic resonance spectroscopy. Understanding

how the triplet spin sublevel is populated provides information on how triplets in organic chromophores are generated. In chapter 4, we investigate the triplet polarization pattern in various anthanthrone and anthanthrene compounds to identify triplets produced via intersystem crossing versus SF. In chapter 5, we directly probe the quintet sublevel population and verify the recent theoretical work that discusses how the orientation of the magnetic field with respect to the crystal axis alters quintet sublevel state mixing.

Acknowledgements

For none of this work would have been possible without your help, I sincerely want to thank all of you who helped me finish my study.

First of all, I want to thank my PhD adviser, Prof. Mike Wasielewski for his support and mentorship since the beginning to the very end. There are so many lessons I have learned from you starting from small things as doing experiments correctly, making right figures to writing manuscripts and proposals. I really appreciate your constructive feedback and opportunities you gave me to improve. Your enthusiasm and dedication to science always inspired me to pursue science and to become a better scientist. Also, thank you for opening the door for me to move on to the next step. I will always remember the valuable skills and lessons you taught me, and I will put them into good use.

I would like to thank my committee members, Prof. Lin Chen, Prof. Emily Weiss and Prof. Franz Gaiger, for making time to give me constructive feedback and guidance on my project and proposed research.

I want to thank the numerous people I worked with in the Wasielewski group. Thank you, Prof. Yi-Lin Wu, for the numerous scientific discussion we had. Your creativity always inspires me. Thanks to Jonathan Schultz for always bringing positive vibes and joy to our office. Thank you, Dr. Joseph Christensen, who helped to better shape me as a scientist and for making me numerous molecules. Thanks to Dr. Jiawang Zhou for helping me with running multiple samples and for an enjoyable collaboration we had. I also really appreciate, Prof. Katie Mauck, Dr. Brian

Phelan, Dr. Ryan Young, Dr. Matt Krzyaniak, Dr. Eileen Foszcz for training me on multiple instruments in house and all the scientific discussions we had. I learned a lot from you all! Special thanks to Prof. Katie Mauck, who really helped me to adjust to the group when I started. Thank you, Amanda Mahoney, for helping me with anything you can help me with. Thank you Dr. Xingang Zhao for making me a molecule and for your help with synthesis and Prof. Marek Majewski, for connecting me with an interesting series of molecules, that resulted as a chapter in my thesis and helping me with miscellaneous stuff in B-lab. Thank you to Prof. Jae Yoon for helping me with occasional optics problems and for connecting me with Dr. Jooyoung Sung at SPIE conference. I really appreciate your friendship and I hope we can meet again with Jon in Korea.

I would like to thank all of my external collaborators. Thank you Gyeongwon Kang for being patient with me and running many calculations for me. I learned a lot while having lots of fun! Thank you, Prof. Schatz for providing constructive feedback on the manuscripts and helpful discussions. Thank you to Dr. Christos Malliakas who taught me so much about crystallography concepts and numerous experimental help at IMSERC. Thank you, Prof. Daiki Shimizu, for making me an awesome series of molecules and for helpful scientific discussions. I learned a lot and had lots of fun working with you. Thank you Prof. Hiroki Nagashima, who taught me everything about EPR spectral fitting and for providing directions for my project. Thank you to Prof. Marcin Stepien, for sharing your porphyrin samples and Prof. Jeff Morin for your anthanthrone and anthanthrene samples, which gave me a great opportunity to study new systems. Thank you Dr. Joe Strzalka and Dr. Qingteng Zhang for helping me with GIWAXS analysis.

I also want to thank my undergraduate advisers, Prof. Wendy Queen and Prof. Stephen Leone and mentors, Prof. Eunseon Cho and Dr. Natalie Gibson from UC Berkeley. Thank you, Prof. Wendy Queen, for your mentorship and support. I still remember how much I enjoyed working on my first project at the Molecular Foundry. Thank you for showing me that science is truly fun and for always guiding me in the right direction. Your sincerity always motivates me to go further. I truly aspire to be like you one day! Thank you, Prof. Steve Leone, for all of your support and mentorship. I first found that physical chemistry is my favorite subject from taking your class and it was even more fun to work with cool lasers in the basement of Hildebrand hall. Thank you for giving me an opportunity to work in your fantastic group and for all of your sincere advice that always helps me to go in the right direction. Thank you, Prof. Eunseon Cho for helping me with my very first project and for your continued support since then. I learned so much from you and had so much fun working with you. You are truly my role model! Thank you Dr.Natalie Gibson, for teaching me a lot of concepts and skills, even when you were extremely busy with many projects!

I also want to thank my friends who showed me endless support. Thank you, Dr. Jose Martinez, who always help me to enjoy my time in the lab. It was always fun working with you in the B lab and thank you for helping me with synthesis and anything you could help me with. Thank you to Dr. Jieun Lee, Dr. Jiyun Hong, Dr. Youngpyo Hong, Dr. Soyoung Seo, and Yijing Chen for your companionship and for sharing all those fun moments with me. A special thanks to Dr. Jooyoung Sung, who gave me a lot of opportunities to visit fantastic labs around the world and for your encouragement and mentorship. I never felt alone going through my PhD because of you fine people.

Lastly, I would like to deeply thank my family who always give me unconditional support and love. Thank you so much my grandmother, Jung Rye Lee, my dad, Dam Bae, my mom, Ockhee Kim, my sister, Kyung Won Bae, my brother, Hyun Joon Bae, and my husband, Richard Hong. You all are the meaning of my life and with you, I always feel like I can do anything. Thank you so much for being there for me. Thanks, dad, for always bringing me to best places around the world and providing me with anything I need and grandmother for taking care of me and bringing me to all the playgrounds around the neighborhood when I was a kid. Thank you, Kyung Won who is the funniest person I know in the world and my best friend/sister/travel mate for spending quality time with me and always feeding me with great foods. Thank you, Hyun Joon, who is the coolest brother in the world with so much swag and sending me care packages with lots of snacks that solve my sugar cravings. Special thanks to my husband/soulmate, Richard, who read these chapters, listened to my talks numerous times even when you are falling asleep, and probably knows SF as much as I do. Lastly, a special thanks to my mom, Ockhee, who comes to the U.S. every year to cook for me and to spend time with me. Without your sacrifice and dedication, I would not have been where I am at. For this reason, I would like to dedicate my thesis for you, mom! 엄마 사랑해.

Dedication

For my mom, Ockhee Kim

Table of Contents

List of Schemes

List of Figures

List of Tables

Chapter 1. Introduction:

Importance of Using Both Optical and Magnetic Spectroscopy for Studying Singlet Fission

1.1 Singlet Fission

Singlet fission (SF), the process by which a singlet exciton created in an assembly of two or more interacting chromophores energetically down-converts into two triplet excitons, was first discovered in 1965 in crystalline anthracene.[1] SF occurs when there are at least two or more interacting chromophores and there are two major involved.[2] The first step is the formation of a correlated triplet pair, $^1(T_1T_1)$. Upon absorption of a photon by their ground state $^1(S_0S_0)$, a singlet exciton $^1(S_1S_0)$ is produced and is rapidly converted to a correlated triplet pair state, $^1(T_1T_1)$. This process occurs in the fs- ps time scale because there is no spin flip during this process and the singlet spin configuration is maintained from $^1(S_0S_0)$ to $^1(T_1T_1)$. The second step is the dissociation of the correlated triplets, $^1(T_1T_1)$ into two separate triplets, T_1. When both the first and the second steps occur, one can truly say that SF is occurring. In fact, once the $^1(T_1T_1)$ state is formed, it could decay to ground state instead of dissociating into two independent triplet (T_1) states.[3-5] Because of this down-conversion nature, SF process requires $E(S_1) \geq 2E(T_1)$, although SF has also been observed when the process is slightly uphill in energy.

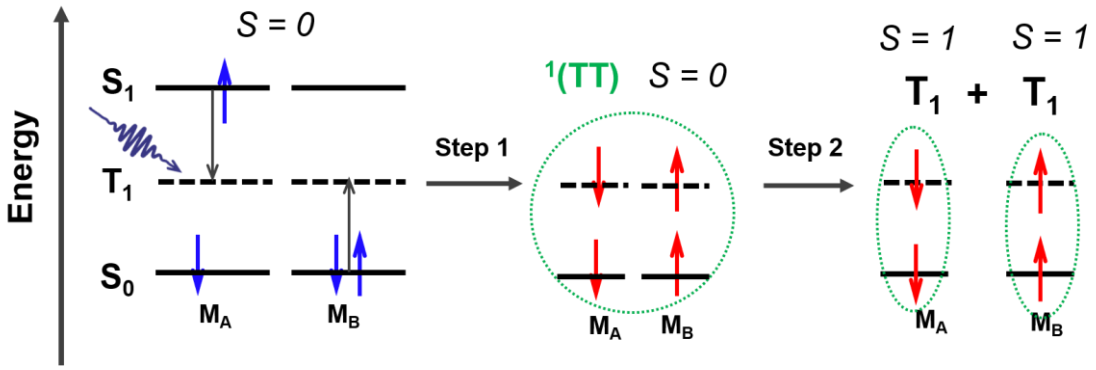

Figure 1.1. Two major steps in SF. Step 1 is the formation of a correlated triplet pair

Following the first observation of delayed fluorescence resulting from SF in anthracene crystals in 1965,[6] the magnetic field effect studies in tetracene crystals further validated that SF is

in fact occurring in these polyarene crystals.[7-9] After these experimental observations, numerous theoretical studies further described the SF dynamics.[10-12] Since then, in 2004, there was a renewed attention in SF, because of its ability to overcome the Shockley-Queisser limit on the theoretical efficiency of single-junction solar cells.[2, 13] Specifically, SF chromophores can mitigate thermalization losses, where the absorbed photon energy in excess of the band gap is lost to heat.[14] The triplet excitons can be harvested by either energy transfer or charge transfer to ultimately create charge carriers.[15, 16]

Stemming from this exciting opportunity to increase solar cell efficiency, burst of studies related to SF photovoltaics were published. Initial SF studies have focused on polyacene based systems including anthracene, tetracene, and pentacene.[17] Due to lack of chemical and photo-instability in polyacenes,[18] collective effort was put together to find more robust SF chromophores, such as rylene,[19-21] and diketopyrrolopyrrole (DPP) [22, 23] derivatives. Following the discovery of new SF chromophores, numerous PV devices were fabricated, still mostly using tetracene and pentacene. The first device was fabricated using pentacene and C_{60}, where pentacene is used as electron donor and C_{60} as electronic acceptor.[24] Following this device fabrication, a milestone was reached by demonstrating the ability to exceed the 100% external quantum efficiency;[25] however, the power conversion efficiency of this system is as low as (1.8 ± 0.1)%. Thus, different design architectures for devices were developed. For instance, instead of using solely organic molecules where SF chromophores take role is charge separation, incorporation of inorganic components such as semiconducting quantum dots was used to generate charges[26] and to mediate energy transfer to silicon solar cells.[27] In addition, direct energy transfer from tetracene triplet to silicon solar cell was also demonstrated.[28]

1.2 Motivation for New SF Chromophores

Although numerous SF devices were successfully fabricated, demonstrating the proof of concept, their power conversion efficiency are still low ranging from 1-5%. In order to improve device efficiency, multiple approaches have been taken including studying mechanisms of triplet dissociation,[29-31] changing device structure,[26, 27, 32] and expanding the library of SF chromophores that can be coupled to semiconducting layer.[33-38] Among these approaches we will focus on developing new SF chromophores in this thesis.

In order to expand the library of SF chromophores, the following requirements need to be satisfied:[39] 1. SF chromophores need to be robust and strongly absorb blue lights 2. SF needs to occur fast enough to outcompete any unwanted photophysical processes. 3. SF process needs to be efficient, creating the maximum number of the triplets. 4. the triplet energy of SF chromophores needs to be greater than the bandgap of the semiconducting acceptor layer. Considering the thermodynamic limit, the ideal bandgap of the semiconducting layer should be between 1.1-1.3 eV. This means the triplet energy of SF chromophores must be greater than 1.1 eV. Although there are many SF chromophores that satisfy the first three requirements, there are only a few that satisfy the last one. Thus, the most recent studies focus in finding SF chromophores with high triplet energies. A few studies include adjusting the aromaticity of the excited state using Baird's rule to manipulate singlet and triplet energy gap,[36] twisting the core of perylenediimide to increase both the singlet and triplet excited state energy[37] and computing a series of blue absorption chromophores and their triplet energy to find optimal SF chromophores.[38] In this thesis, we will focus on anthracene-based SF chromophores, 9,10-bis(phenylethynyl)anthracene (BPEA).

1.3 Optical Spectroscopy for Studying SF Chromophores

When studying SF systems, optical spectroscopy techniques including time-resolved absorption, vibrational, fluorescence, and 2D electronic spectroscopy, are widely used. Optical spectroscopy is particularly appealing because it can probe fast dynamics and thus, is suitable for monitoring the first step of SF, which is the conversion of the singlet exciton to the spin single correlated triplet pair, (T_1T_1). Previous studies have shown sub 100fs SF dynamics in pentacene[40] and the importance of vibronic coupling for this ultrafast SF to occur.[41-43] In addition, using ultrashort pump pulse, one can identify whether the SF process is a coherent or an incoherent process in a particular system.[44, 45] Using vibrational spectroscopy, the nature of the intermediate correlated triplet state, (T_1T_1) can also elucidated.[3, 46-48] Furthermore, optical spectroscopy also allows spatial mapping of exciton transport. Use of transient absorption microscopy (TAM) with spatial resolution of ~50 nm and temporal resolution of 200fs allows visualization of exciton transport in single crystal of tetracene.[49] Using the polarization resolved TAM, the lifetime of the bound triplet of TIPS-pentacene can be revealed.[50]

In addition to the short-time scale, optical spectroscopy allows studies in long-time scales to investigate the second step of the SF, which is the dissociation of the (T_1T_1) state into two triplets. In tetracene systems, quantum beating indicating superposition of zero-field triplet states (T_1T_1) states, with the overall singlet spin state, is observed using time-resolved fluorescence spectroscopy.[51] Optical spectroscopy accompanied with the external magnetic field provides an indirect way to probe spin evolution that occurs in the second step of SF. When the spin exchange coupling is weak, at relatively low magnetic field, the magnetic field dependent triplet dissociation has been observed in covalent terrylenediimide (TDI) dimers and 1,6-diphenyl-1,3,5-hexatriene crystals.[52, 53] At high magnetic fields, strongly coupled triplets can be also probed.[54] Such field-

dependent signal is observable during the second step but not in the first step and when the energy matching between the correlated triplet and the dissociated triplet is satisfied.[55] Using optically detected magnetic resonance (ODMR) geminate and non-geminate triplet recombination process has been also distinguished in SF systems.[56, 57]

In this thesis, we used transient absorption and emission spectroscopy to obtain the rate of the excited state dynamics and the triplet yield. These characteristics determine the efficiency of SF in various BPEA and its derivatives in solid-state films. They will be discussed extensively in Chapter 2 and 3. We also use the external magnetic field for transient absorption measurement to probe the magnitude of spin exchange coupling as shown in Chapter 5.

1.4 Magnetic Spectroscopy for Studying SF Chromophores

Although there were numerous interesting studies reported using optical spectroscopy, there are few caveats in using optical spectroscopy. First, there exists the distortion of the ground state absorption spectra due to thermal heating of the sample upon photoexcitation. The resulting thermal spectrum, which is the difference in the ground state absorption spectrum at high and low temperature, looks extremely similar to the triplet excited state absorption spectrum in numerous SF systems.[35, 58-60] This spectral similarity makes identifying the originating state challenging. Second, the energy difference among the three different spin states of the correlated triplet, singlet, triplet and quintet as well as the separated triplet is too small to resolve using optical spectroscopy. Since this energy difference is in microwave region, the use of magnetic spectroscopy such as time-resolved electron paramagnetic resonance (TREPR) is an excellent tool for studying spin dynamics occurring in the second step of SF.

TREPR is particularly useful because it can directly probe the spin sublevel population using microwave sources. Understanding how the triplet sublevels are populated provides information about how the triplet is generated. For instance, since the triplet generated from SF needs to come from the singlet state, the triplet of ms = 0 Zeeman state is selectively populated, resulting in a different triplet polarization pattern from that generated via intersystem crossing.[57, 61, 62] In chapter 4, we elucidate triplet formation mechanism in various anthanthrene and anthanthrone compounds using TREPR.

In addition to the mechanism of triplet formation, probing spin sublevel population provides a global picture of how triplets are decaying because TREPR is sensitive to each of the spin states generated. Upon generation of $(T_1T_1)^1$ state, nine possible spin states can be constructed only considering coupling of the angular momentum of two triplets.[10] Among the nine, one is the spin singlet, three are triplets and five are the quintets. However, fine-structure interactions couple the different spin states, such that the solutions to the full spin Hamiltonian do not have pure spin multiplicity but they rather have mixed character.[5] For instance, the symmetric singlet and the quintet states are mixed while the singlet cannot mix with the asymmetric triplet, which is asymmetric. The quintet state, $(T_1T_1)^5$ was first observed in a covalent pentacene dimer using TREPR and the identity of each spin state was confirmed by measuring the relative nutation frequency of the quintet and triplet.[5] Shortly after this study, the quintet state in crystalline tetracene film was observed only when exciton diffusion was sufficiently slowed at liquid Helium temperature.[63] In this study, the coherence time of the quintet and triplet state was measured for the first time and its near the μs range timescale. This opens up the organic triplet state as a viable

source of coherent state for quantum information science and spintronics application.[63] Following this study, different TREPR spectra were obtained when triplets were entangled.[64]

More in-depth mechanistic studies were also followed and identified each spin state's decay pathway using TRERP. In covalent TDI dimers, in which the two TDI molecules are linked by a single bond between their imide nitrogen atoms. Since there is a node between the two TDIs, the exchange coupling is small. Here, TREPR study reveals the mixing of $(T_1T_1)^5$ and $(T_1T_1)^3$ results in annihilation of the triplets to produce a single uncorrelated T_1 state, instead of two separate triplets. In the aggregated frozen solution of TIPS-pentacene and tetracene, selective sublevel populations with the ms = 0, -1, -2 Zeeman states as a result of modulation of exchange coupling via triplet exciton diffusion.[65]

TRPER is also a particularly useful technique because the orientation information of the molecule with respect to the magnetic field can be revealed. For instance, two different sets of pentacene molecular dimers crystals were fabricated using molecular beam deposition.[66] Using TREPR, Kay and co-workers found that parallel dimers are better at dissociating triplets than herringbone geometry. By rotating the sample around the magnetic field, they were also able to map out the triplet dissociation dynamics at a specific orientation with respect to the magnetic field. In addition, the temperature dependent triplet dissociation path was elucidated in a single crystal of tetracene without the line broadening present in polycrystalline or amorphous samples.[67] Recent theory work showed that depending on the orientation of the SF molecule with respect to the magnetic field, the quintet sublevel state mixing changes, resulting in different triplet decay pathways.[4] In chapter 5, we experimentally observe this orientation effect using highly textured TDI and quaterrylenediimide films and TREPR.

Both the optical and magnetic spectroscopy provide rich information related to exciton and spin dynamics embedded in SF chromophores. Although each optical and magnetic spectroscopy provides important information, when both are used in complimentary to each other, in-depth and wholistic understanding can be achieved about the SF systems.

Chapter 2. Balancing Charge Transfer and Frenkel Exciton Coupling Leads to Excimer Formation in Molecular Dimers: Implications for Singlet Fission

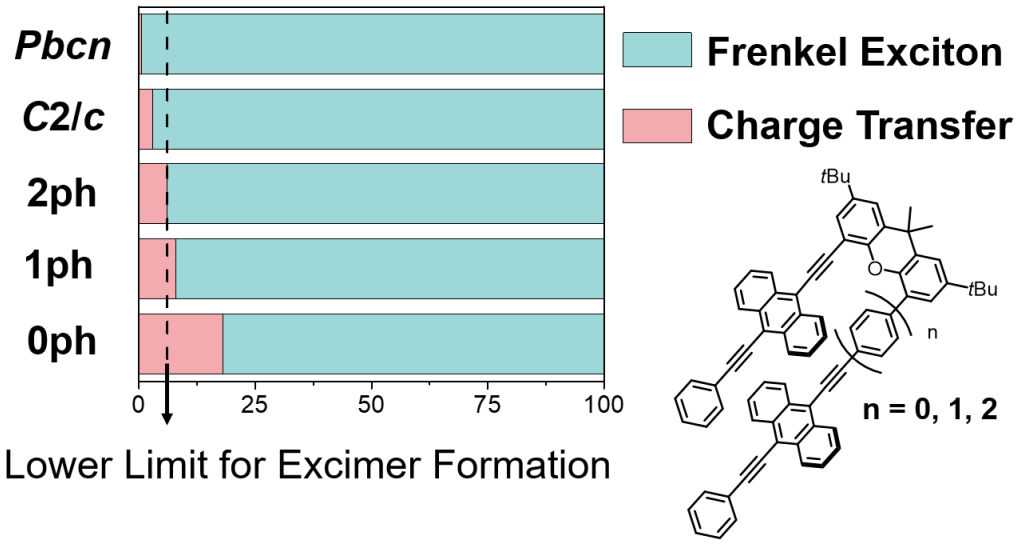

2.1 Introduction

Photoexcitation of molecular chromophore aggregates often results in the formation of excimer states in which an exciton on one chromophore electronically interacts with one or more neighboring chromophores resulting in overall stabilization of the system. Excimer formation is observed in various types of chromophore assemblies including covalent dimers,[68-71] aggregates in solution,[72-74] and in the solid-state,[20] which is of particular interest to organic electronics[75, 76] and photovoltaics.[77, 78] Often times, excimer states can act as an exciton traps[79] and decrease the quantum yield of desired products or device performance.[80] This occurs when the excimer formation rate is faster than the targeted processes such as exciton diffusion, charge transfer and transport, and singlet fission (SF).[81, 82] However, in some cases, excimers have been proposed to act as intermediates in desirable photophysical process; for example, to mediate SF in polycrystalline 3,6-bis(aryl)diketopyrrolopyrrole (DPP) films[22] and perylene-3,4:9,10 bis(dicarboximide) (PDI) covalent dimers.[83] Traditionally, the excimer state has been defined as a linear combination of Frenkel exciton (FE) and charge transfer (CT) states. Defining $|S_1S_0>$ and $|S_0S_1>$ as states where the excitation resides on one of the two molecules, and $|AC>$ and $|CA>$ where the cation and anion reside on either molecule, the excimer state, |Ex>, can be expressed as:[84]

$$|Ex> = a(|S_1S_0> + |S_0S_1>) + b(|CA> + |AC>) \qquad (2.1)$$

where a and b are coefficients and the squares of these coefficients indicate the relative contributions of the FE and CT states. The relative degree to which the FE and CT states contribute to |Ex> depends on the electronic interactions in molecular aggregates as dictated by the interchromophore distance, orientation, and solvation environment.[85, 86]

The contribution from the FE state can be understood as the Coulombic interactions among the molecules comprising the aggregates as described by the Kasha model.[87] These Coulombic interactions are dictated by the relative orientations of transition dipole moments and result in Davydov splitting, which can be easily observed in the steady state absorption spectra of the aggregates.[88] Contributions of the CT state to the excimer state have been widely recognized from the observed solvent polarity dependence of excimer formation.[71, 72, 85, 86] In many systems, having large CT character stabilizes the excimer state resulting in faster excimer formation in higher yield. For instance, in the case of extended viologens, a shorter distance between the two chromophores leads to increased CT character and thus faster excimer formation,[86] while for PDI dimers and aggregates, excimers with increased CT character have been observed in highly polar solvents.[72, 85] Recently, folded geometries of PDI dimers were shown to have similar CT and FE contributions based on their calculated exciton couplings.[71, 89] It has also been reported that a CT contribution comparable to that of the FE state allows for singlet fission leading to $^1(T_1T_1)$ multiexciton state formation.[85] Although it is widely assumed that most excimer states have a large FE contribution with a small degree of CT character that stabilizes the excimer state, it remains unclear what degree of CT state contribution relative to the FE states is necessary to facilitate or avoid excimer formation, leading to important implications for the role of excimers in other photophysical processes, such as SF.

Here, we synthesized covalent dimers of 9,10-bis(phenylethynyl)anthracene (BPEA) using a xanthene bridge and a phenylene spacer (**Scheme 2.1**) to systematically tune the electronic coupling between two BPEA molecules and to study their excited state dynamics. BPEA is an extensively studied industrial dye that has a near unity fluorescence quantum yield in solution.

Recently, it has been shown than BPEA in the solid state undergoes efficient SF.[33, 34, 90] However, we found that excimer formation is the dominant photophysical process in covalent BPEA dimers based on solvent-dependent transient absorption and time-resolved fluorescence studies. In addition to the experimental studies, we calculated the exciton couplings to quantify the contribution of FE and CT states in BPEA and other systems including PDI covalent dimers and polycrystalline DPP systems. Such calculations show a correlation between excimer formation dynamics and the relative ratio of FE to CT state contribution to the overall electronic description of the excimer.

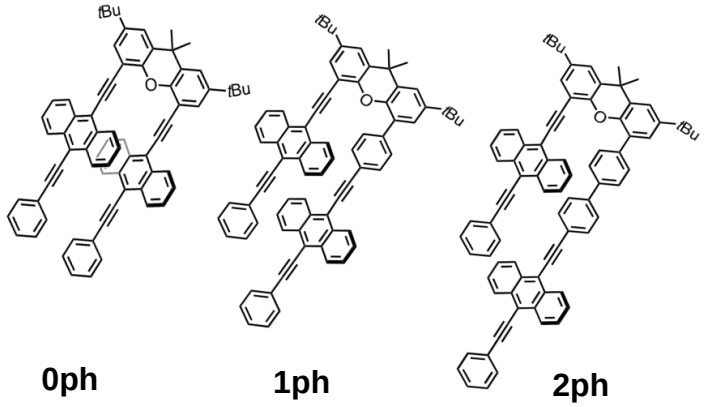

Scheme 2.1. BPEA covalent dimers: 0ph, 1ph, and 2ph.

2.2 Experimental Details

2.2.1 Synthesis of BPEA dimers. BPEA covalent dimer **0ph** was synthesized by Sonogashira coupling of 4,5-dibromo-2,7-di-*tert*-butyl-9,9-dimethylxanthene and 9-ethynyl-10-phenylehynylanthracene in 27% yield. The reaction also gave mono-substituted xanthene **S2.1** in 67% yield, which was further used for preparing slipped dimers **1ph** and **2ph**. Namely, **1ph** and **2ph** were synthesized by Suzuki–Miyaura coupling of **S2.1** and the corresponding boronic esters **S2.4** and **S2.5**, respectively (**Scheme 2.2**, see Supporting Information for detailed procedure).

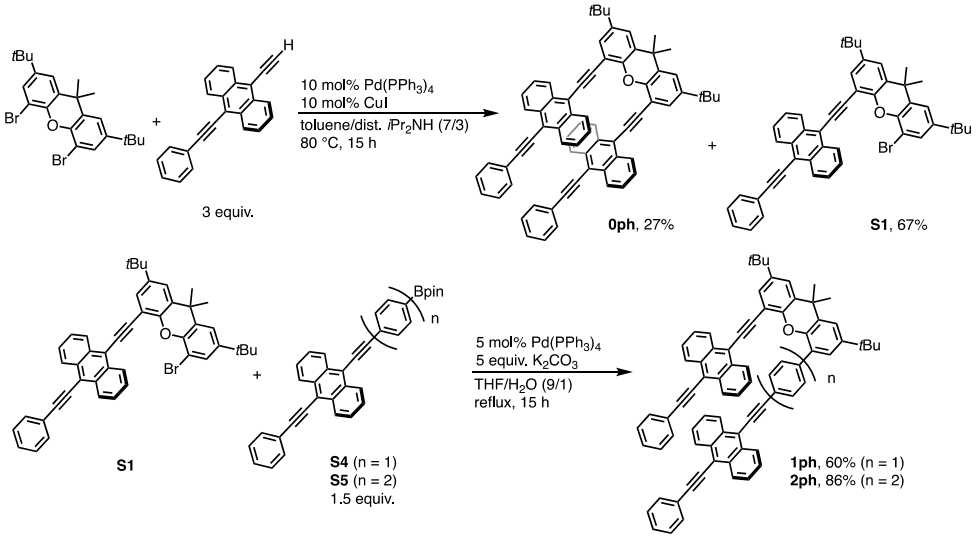

Scheme 2.2. Synthesis of covalent BPEA dimers 0ph, 1ph, and 2ph.

2.2.2 Spectroscopy. UV-Vis absorption spectra were acquired in toluene (Tol), dichloromethane (DCM) and *N*,*N*-dimethylformamide (DMF) on a Shimadzu UV1800 absorption spectrometer. Emission spectra were collected using a Horiba Nanolog spectrofluorometer. Fluorescence quantum yields, Φ_F, were determined by using the front face mode with a HORIBA Nanolog spectrofluorometer equipped with an integrating sphere (Horiba Quanta - φ).

The femtosecond transient absorption (fsTA) experiments were conducted using instruments described previously.[91] The 414 nm pump pulses were generated using a laboratory-built collinear optical parametric amplifier and attenuated to 1 μJ/pulse.[92] The pump pulses were depolarized to suppress the effects of orientational dynamics. Transient absorption spectra were detected using a customized Helios/EOS spectrometer (Ultrafast Systems, LLC), where the Helios spectrometer is used for pump-probe delays up to 7.4 ns and the EOS spectrometer is used for pump-probe delays of 0.6 ns to 340 μs. The optical density of the samples was ~0.3 at the excitation wavelength (λ_{ex} = 414nm) in 2 mm cuvettes.

Picosecond time-resolved fluorescence (psTRF) data were collected using a Hamamatsu C4780 streak camera. The 414 nm,15 nJ laser pulses from a Spirit-NOPA-3H were utilized as the excitation source. Data were collected using 2 ns, 10 ns and 100 ns time windows; the instrument response function (IRF) was ~2% of the acquisition window, with the highest time resolution being 40 ps. The IRF was determined from the pump scatter using Gaussian deconvolution as described in Supporting information. The optical density of the samples was kept below 0.1 at the excitation wavelength in 2 mm cuvettes. All data were acquired in the single-photon counting mode using the Hamamatsu HPD-TA software.

2.2.3 Exciton Coupling (*J*) Calculation. The effective exciton coupling (*J*) is the sum of contributions from Coulombic (J_{Coul}) and CT (J_{CT}) coupling. Here, *J* is calculated by simulating the steady-state absorption spectra of the BPEA compounds through time-propagation of the Frenkel-Holstein Hamiltonian.[42] To capture the spectral linewidths, we applied a Gaussian windowing function to the calculated linear response prior to Fourier transformation to the frequency domain. We first simulated the BPEA monomer spectrum to extract a Huang-Rhys

factor of ~0.9 for the primary ~1300 cm^{-1} vibration apparent in the vibronic structure of the experimental spectra. Keeping the Huang-Rhys factor constant across the molecular series, we simulated the linear response of the dimers to determine the effective exciton coupling values. Further details regarding these simulations can be found in the SI.

In order to calculate J_{CT} of BPEA dimers, the HOMO-HOMO and LUMO-LUMO couplings, which are the 1-electron transfer integral of the LUMO and HOMO orbitals of the two molecules, respectively, were calculated from the integral matrix elements using the Amsterdam Density Functional (ADF) package[93] at the density functional level of theory (DFT). Here, the BPEA dimers are geometry optimized in DCM using B3LYP basis and Grimme3 dispersion correction functional to account for π-π interactions. Optimized structures are shown in **Figure 2.29**. Following the optimization, the xanthene bridge is removed similar to the method used for previous systems[94] to calculate transfer integrals. For calculating the one-electron coupling, the triple ζ with two polarization functions (TZ2P) basis set and the B3LYP exchange-correlation functional were chosen. Fock and overlap integral matrix elements were calculated using the TRANSFERINTEGRALS key with the fragment orbital approach as implemented in ADF. The effective coupling between orbitals *i* and *f*, V_{if}, was calculated using the following equation:[95]

$$V_{if} = \frac{J_{if} - \frac{1}{2}S_{if}(e_i + e_f)}{1 - S_{if}^2} \qquad (2.2)$$

where J_{if} is the Fock matrix element between a pair of monomers, S_{if} is the overlap integral, e_i and e_f are the Fock matrix elements within a monomer. The calculated matrix elements for the corresponding systems are shown in **Table 2.6**.

The CT state energy, *E*(CT), was calculated by performing single-point energy calculation using Density functional theory (DFT) calculations. Geometries of BPEA and PDI monomers (**Figure 2.5**) were optimized in QChem (v. 5.0) with the B3LYP functional and 6-31G* basis set in gas phase followed by further optimization using a polarizable continuum model (C-PCM) and the specified optical and static dielectric constants for each solvent medium. A single point energy calculation on the optimized geometry was performed and convergence was reached to obtain the energy of neutral, anion and cation species. The energy of anion and cation is scaled by subtracting the energy of neutral species and the *E*(CT) was calculated as the sum of cation and anion energy.[35, 96] Example input files and the values are reported in **Table 2.7**.

Given that the V_{HH} and V_{LL} coupling values are smaller than the energy difference between CT and S_1 state, we calculated J_{CT}[88, 97] in the perturbative limit:

$$J_{CT} = -2 \cdot \frac{(V_{HH}V_{LL})}{E(CT) - E(S_1)} \qquad (2.3)$$

where the S_1 energy is calculated using TDDFT and *E*(CT) is calculated as described above. The Coulomb coupling, J_{Coul}, is then calculated by subtracting J_{CT} from the effective coupling *J* for BPEA dimers. A detailed description of computational method is described in the Supporting Information.

2.3. Results

2.3.1 Steady state optical properties. Ground state absorption spectra of the covalent BPEA dimers in DCM were obtained to qualitatively compare exciton coupling among BPEA dimers (**Figure 2.1**).The absorption maxima of 0-0 and 0-1 transitions in BPEA monomer in DCM are 464 nm and 438 nm, respectively, and the 0-0 transition has a greater intensity than the 0-1 transition. Due to multiple conformers in the solution phase, the BPEA monomer in solution has

a broad absorption.[98] Unlike the BPEA monomer, the 0-1 transitions in the BPEA covalent dimers

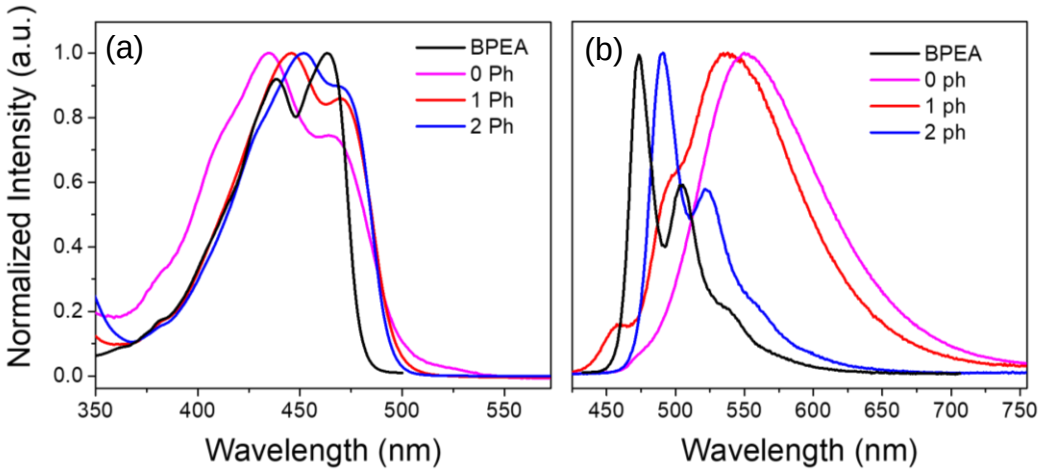

Figure 2. 1. (a) Steady state absorbance and (b) emission spectra of BPEA monomer and dimers in DCM.

have greater intensities than the 0-0 transitions, indicating *H*-type intramolecular interactions.[88] Presumably, strong π-π interactions drive the BPEA molecules to stack even with phenyl spacers. The absorption maxima of the 0-0 and 0-1 bands of **0ph** are 466 nm and 435 nm, respectively, which are comparable to the BPEA monomer. In contrast, the 0-0 and 0-1 transitions of both **1ph** and **2ph** are red shifted (**Table 2.1**). Steady state absorbance spectra of the BPEA dimers in Tol are shown in Figure S1 with the corresponding peak positions and Φ_F (**Table 2.5**).

Table 2.1. The absorption and emission maxima, singlet state energies ($E(S_1)$), and fluorescence quantum yields of BPEA monomer and dimers in DCM.

	0-0 (nm)	0-1 (nm)	$E(S_1)$ (eV)	Φ_F (%)
BPEA	464	438	2.60	95 ± 5
0ph	466	435	2.52	59 ± 3
1ph	471	446	2.55	92 ± 7
2ph	473	452	2.57	82 ± 9

The steady state fluorescence spectrum of the BPEA monomer in DCM has a clear vibronic progression of 0-0, 0-1 and 0-2 transitions. In contrast, **0ph** in DCM has a significantly broadened

emission spectrum without a strong vibronic progression, which is characteristic of excimer formation in BPEA.[99] The emission spectrum of **1ph** is also broadened, but shows a somewhat more well-defined 0-0 and 0-1 vibronic progression with maxima at 457 nm and 494 nm, similar to that reported for a BPEA cyclophane.[100] Dimer **2ph** has a vibronic progression similar to BPEA monomer that is red shifted. Although there are minor differences in the absorption spectra of the dimers between DCM and Tol, their steady-state emission spectra change significantly depending on the solvent polarity (**Figure 2.7**). For example, the emission maxima of **0ph** and **1ph** are shifted more in DCM than in Tol, whereas the intensity ratio between 0-0 and 1-0 in Tol is greater than in DCM. Assigning the onset of the steady state absorbance and emission spectra as the first singlet excited state energy, $E(S_1)$, the BPEA monomer has the largest $E(S_1)$ = 2.60 eV followed by **2ph** (2.57 eV), **1ph** (2.55 eV), and **0ph** (2.52 eV) (Table 1). Unlike BPEA monomers, $\Phi_F < 1$ in the BPEA dimers, indicating changes to their excited state dynamics relative to the monomer.

2.3.2 Excited state dynamics. We performed time-resolved fluorescence (TRF) spectroscopy to investigate the excited state dynamics of the BPEA dimers. The BPEA monomer in DCM has near-unity Φ_F with a singlet excited state lifetime of 3.2 ± 0.2 ns. On the other hand, upon photoexcitation of **0ph**, excimer formation is observed within the 40 ps instrument response function (IRF) (**Figure 2.8**). By globally fitting the different time windows of the TRF spectra (**Figure 2.2**) using excimer decay time constants of 50 ± 40 ps, 3 ± 2 ns and 30 ± 2 ns are obtained (**Table 2.2**).

Table 2.2. Excimer formation and decay times-constants from TRF measurements for BPEA dimers in DCM and Tol.

	0ph DCM	**0ph** Tol	**1ph** DCM	**1ph** Tol	**2ph** DCM	**2ph** Tol
τ_1	50 ± 40 ps	1.7 ± 0.2 ns	27 ± 40 ps	220 ± 40 ps	200 ± 40 ps	510 ± 40 ps

τ_2	3 ± 2 ns	3.0 ± 2 ns	700 ± 40 ps	830 ± 40 ps	2.8 ± 0.2 ns	2.4 ± 0.2 ns
τ_3	30 ± 2ns	23 ± 2 ns	4 ± 2 ns	4.0 ± 2 ns		
τ_4			15 ± 2 ns	8 ± 2 ns		

We also measured the TRF spectra in Tol to gauge the solvent polarity dependence of the excimer formation dynamics. There are changes in both the time constants and the emission

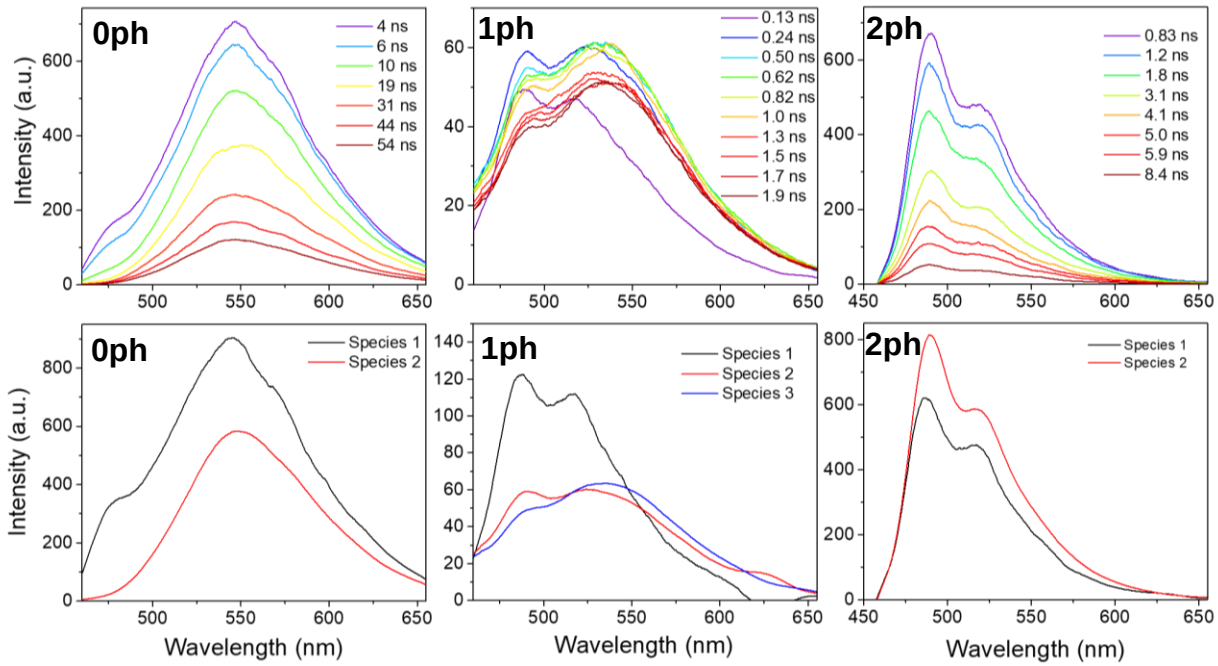

Figure 2.2. TRF spectra of BPEA dimers in DCM upon photoexcitation at λ_{ex}=414nm (15nJ/pulse). The TRF spectra are globally fitted using evolution-associated decay and the resulting spectral fits are shown in the bottom panel. Additional time windows, wavelength fits and population vs. time fits are shown in **Figure 2.8-20.**

maxima. All the excimer formation and decay time-constants are slower in Tol than those in DCM for **0ph** and **1ph** (**Table 2.2**). In addition, the emission peaks are more red-shifted in DCM than in Tol, which is in good agreement with the steady-state emission spectra (**Figures 2.8-2.20**). Unlike **0ph** and **1ph**, **2ph** exhibits biexponential emission decays without significant spectral changes (Figure 2). By fitting the spectra using an A → B → GS model, the first decay time constant is faster in DCM than in Tol, whereas the second component remains the same.

Since the temporal resolution in our TRF experiments is limited, femtosecond transient absorption (fsTA) spectroscopy was used to investigate the excimer formation rate. Upon photoexcitation of the **0ph** dimer in DCM at 414 nm (1 uJ/pulse), a ground state bleach (GSB) and stimulated emission (SE) feature occur between 420 nm and 550 nm, while the singlet excited state absorption (ESA) has maxima at 588 nm and 955 nm (**Figure 2.3**). Following the rapid disappearance of the singlet ESA, an excimer state is formed as evident in the rise of a new ESA feature between 483 nm and 600 nm. By globally fitting the spectra using an A $\rightarrow$ B $\rightarrow$ C $\rightarrow$ GS model, species A shows ESA spectral features similar to S_1 of the BPEA monomer. The stronger GSB of the 0-0 band at 468 nm relative to that of the 0-1 band at 436 nm further supports the assignment of species A to the singlet excited state, i.e. the FE state (**Figure 2.3**). Following rapid decay of this state, the ratio between the 0-0 and 0-1 bands also changes to that typical of an *H*-type aggregate in species B. Both species B and C are the ESA of the excimer state. The spectral features of species B and C are similar, but a major difference exists in the ratio of the peak at 588 nm to the shoulder at 503 nm. From the global fitting, the excimer formation time constant is 0.4 ± 0.3 ps, with two different excimer decay time constants of 80 ± 5 ps and 31 ± 2 ns (**Table 2.3**). These values are in good agreement with those obtained from the TRF measurements. The same analysis was performed on **0ph** in Tol and the resulting spectral fits are shown in Figure S15. Both

the excimer formation and the decay time constants are slower than those of **0ph** in DCM as reported in **Table 2.3**.

Table 2.3. Excimer formation and decay times-constants from TA measurements for BPEA dimers in DCM and Tol.

	0ph DCM	**0ph** Tol	**1ph** DCM	**1ph** Tol	**2ph** DCM	**2ph** Tol
τ_1	0.4 ± 0.3 ps	0.8 ± 0.3 ps	13 ± 4 ps	42 ± 3 ps	3.0 ± 0.3 ps	2.0 ± 0.3 ps
τ_2	80 ± 5 ps	180 ± 10 ps	210 ±40 ps	1.5 ± 0.2 ns	100 ± 10 ps	22 ± 5 ps
τ_3	31 ± 2 ns	3.4 ± 0.5 ns	3.5 ± 0.8 ns	3.6 ± 0.1 ns	3.1 ± 0.3 ns	2.3 ± 0.2 ns
τ_4		24 ± 3 ns	16 ± 4 ns	8 ± 1 ns		

Similarly, in **1ph**, the early time features result from the singlet excited or FE state. There is a pronounced S_1 GSB and SE at 400-500 nm, where the 0-0 peak is more intense than 0-1 peak along

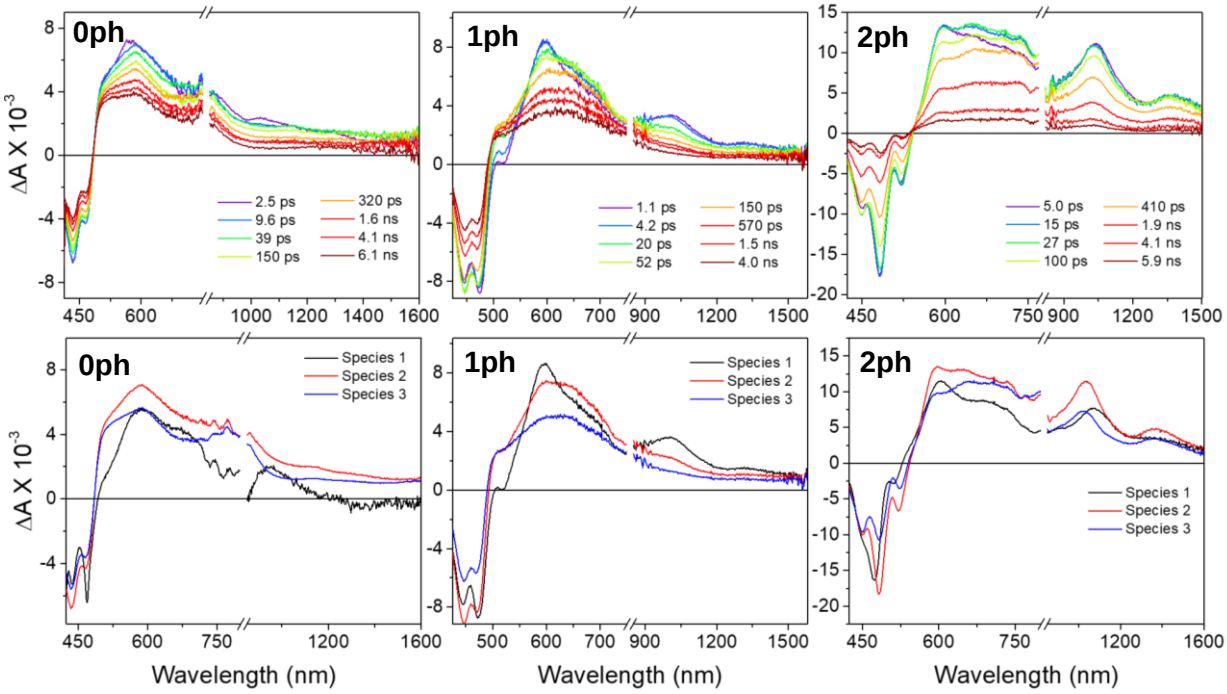

Figure 2.3. FsTA spectra of BPEA dimers in DCM upon photoexcitation at λ_{ex}=414nm (1 μJ/pulse). The fsTA spectra are globally fitted using A → B→ C →GS kinetic model and the resulting spectral fits are shown in the bottom panel. Wavelength fits and population vs. time fits are shown in **Figure 2.18-28**.

with ESA maxima at 597 nm and 1024 nm. Globally fitting the spectra using an A → B → C → D → GS model, the excimer formation time constant is 13 ± 4 ps, followed by the three different excimer decay time constants (**Table 2.3**). These decay time-constants are in good agreement with those obtained from TRF measurements. The overall slow formation and decay time constants of the excimer in Tol indicate that the excited state dynamics of these dimers are solvent polarity dependent. In addition, compared to **0ph**, the excimer formation rate is significantly slower in **1ph** and thus, a clear ESA of the singlet or FE state is observed in species A.

In the case of **2ph**, the overall ESA spectra have a more pronounced vibronic progressions. Globally fitting the spectra using an A → B → GS model, species A results from the singlet excited state and has an ESA with local maxima at 603 nm, 1076 nm, and 1391 nm. Species B has a new spectral feature at 650 nm, which is assigned to the BPEA anion based on its spectral similarity to the chemically reduced BPEA monomer.[101] In addition, this anion spectral feature is more pronounced in **2ph** in DMF, which is a higher polarity solvent than DCM (**Figure 2.28**). We attribute this anion feature to a small degree of symmetry-breaking charge separation (SB-CS). Species C has spectral features similar to species B but with a decreased amplitude. For **2ph** in Tol, the overall spectral features do not change over time, indicating that SB-CS is absent and the multiple decay time constants are attributed to solvation and multiple conformers. Regardless, SB-CS is a minor decay pathway given the high Φ_F of **2ph** in all three solvents. The Φ_F of **2ph** in DMF is 77 ± 3 % and 90 ± 5% in Tol. In addition to the decrease in Φ_F, there is also a red shift in the emission spectrum in DMF and a stronger 0-1 vibronic peak compared to Tol and DCM (**Figure 2.7**).

2.3.3 Quantification of Excimer state. Based on the results from fsTA and TRF spectroscopies, there is a significant solvent dependence in the excited state dynamics of the BPEA dimers. Faster excimer formation and slower decay dynamics are observed in higher dielectric environments for **0ph** and **1ph**. In addition, SB-CS is only observable in high polarity solvents for **2ph**. In order to further understand these changes in excited state dynamics, we calculated the contribution of FE and CT character in the excimer state by diagonalizing the following electronic Hamiltonian matrix:

$$H_{el} = \begin{bmatrix} E_{S1} & J_{Coul} & V_{HH} & V_{LL} \\ J_{Coul} & E_{S1} & V_{LL} & V_{HH} \\ V_{HH} & V_{LL} & E_{CT} & 0 \\ V_{LL} & V_{HH} & 0 & E_{CT} \end{bmatrix} \quad (1)$$

where J is the exciton coupling, V_{HH} and V_{LL} are the HOMO-HOMO and LUMO-LUMO one-electron couplings, respectively, for the two BPEA molecules in the dimer. Here, the four basis states are S_0S_1, S_1S_0, CA and AC and diagonalizing this Hamiltonian matrix results in four excimer eigenstates. The detailed description is given in the Supporting Information. Diagonalizing this electronic Hamiltonian provides four excimer eigenstates with the corresponding energies shown in the Supporting Information. Since the lowest energy state presumably has the highest population, we compare the FE and CT contribution in the lowest excimer eigenstate in **Table 2.4**.

Table 2.4. The square coefficients |a| and |b| and the energy of excimer state in DCM and Tol.

	0ph DCM	**0ph** Tol	**1ph** DCM	**1ph** Tol	**2ph** DCM	**2ph** Tol
$\|a\|^2$	0.41	0.49	0.46	0.50	0.47	0.50
$\|b\|^2$	0.088	0.0040	0.039	0.0012	0.028	0.00092
$\|a\|^2/\|b\|^2$	4.7	125	12	414	17	540
Energy	2.28 eV	2.28 eV	2.31 eV	2.32 eV	2.30 eV	2.32 eV

Comparing the $|a|^2$ / $|b|^2$ (i.e. the FE/CT) ratio among the BPEA dimers in DCM, **0ph** has the smallest ratio (4.7) followed by **1ph** (12) and **2ph** (17). This indicates that **0ph** has the greatest CT contribution in DCM. Although this trend is similar across the dimers in Tol, the magnitude of the ratio is significantly greater than those in DCM. Such a result is reasonable because in low polarity solvent like toluene, the CT state energy is higher, thus there is poorer mixing of the CT state with the FE state in Tol. In addition, the energy of the excimer state (**Table 2.4**) decreases with an increasing CT contribution. Thus, **0ph** has both the greatest CT contribution and the lowest excimer state energy.

2.4 Discussion

2.4.1 Comparison between experimental rates and calculated coupling. There is good qualitative agreement for all BPEA dimers between the experimentally observed excimer formation rates and the exciton coupling values. Based on the fsTA and TRF spectroscopy results, **0ph** has the fastest excimer formation rate (**Table 2.1**) and also has the greatest excitonic coupling value J = 420 cm^{-1}. Although both **1ph** and **2ph** have similar excitonic coupling values of 240 cm^{-1} and 200 cm^{-1}, respectively, only **1ph** forms the excimer. In order to understand this trend, we have to compare the contribution from the FE and CT states. All dimers have greater contributions from the FE state than the CT state; however, **2ph** has the lowest contribution from the CT state based on the smallest J_{CT} and FE/CT ratio. In fact, the J_{CT} value of **1ph** is almost twice that of J_{Coul} compared to these values for **2ph** (**Table 2.8**). The greater CT contribution in **1ph** allows facile excimer formation, whereas **2ph** behaves like the BPEA monomer with a small degree of CT. However, it is unclear how the FE/CT ratio affects SB-CS.

Based on the calculated coefficients, the greater degree of CT contribution, i.e. larger |b| values, lead to lowering of the CT state energies. Experimentally, lower energy excimer state emission is observed from **0ph** (2.25 eV) compared to **1ph** (2.29 eV). From the calculations, **0ph** has the lower excimer state energy (2.28 eV) compared to **1ph** (2.31 eV) in DCM. Thus, the calculations show that increasing the CT contribution lowers the excimer state energy, and moreover, there is a near quantitative agreement between the experimentally observed excimer state energy and the calculated energy. A similar trend is also seen in Tol. It should be noted that the excimer state energy is similar across different dimers, but their dynamics are significantly different due to changes in electronic coupling.

2.4.2 Coefficients calculated in PDI and DPP systems. Since the FE/CT ratio provides rich information about BPEA dimer systems, we have also calculated these values for different systems

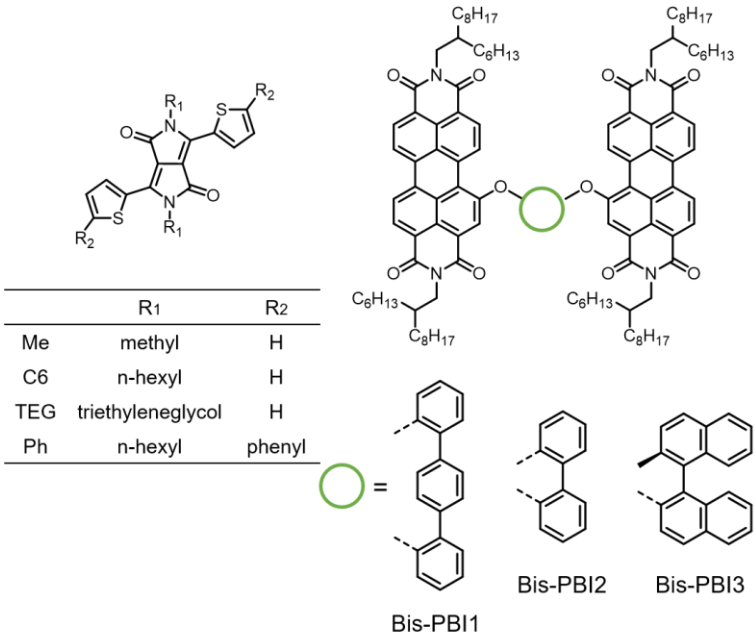

Figure 2.4. Previously reported polycrystalline DPP and PDI covalent dimers. These systems are used to calculate FE and CT contributions in this work.

that form excimers such as the crystalline DPP system and PDI covalent dimers in solution (Figure

4). Previous studies have shown that a selection of DPP systems undergo SF via an excimer intermediate state.[22, 23, 102] Different crystal packing structures lead to changes in electronic coupling and result in excimer-mediated SF or direct SF from the singlet excited state. Among different DPP derivatives, the *n*-hexyl (**C6**) derivative forms excimers with the fastest rate followed by methyl (**Me**), and triethyleneglycol (**TEG**) derivatives.[103] In contrast, the phenyl-DPP (**Ph**) derivative undergoes SF without an excimer intermediate state. Comparing the FE/CT ratio for DPP systems, **C6** has the smallest value of 6.4 followed by **Me** (23), **TEG** (110), and **Ph** (1900) (see Supporting Information). This trend is also seen in the excimer formation rate where the fastest rate occurs in **C6** $(\sim 0.9\ ps)^{-1}$ followed by **Me** $(\sim 2.7\ ps)^{-1}$, and **TEG** $(\sim 10.1\ ps)^{-1}$. Similar to BPEA dimers, a greater CT state contribution lowers the excimer state energy as evidenced by **C6** having the lowest excimer state energy of 2.00 eV followed by **Me** (2.15 eV), **TEG** (2.16 eV), and **Ph** (2.42 eV). All these trends in the DPP system further support the idea that excimer formation is facilitated by a greater CT contribution, and when there is a lack of CT contribution as shown in **Ph** derivative, excimer formation is inhibited.

In the case of PDI covalent dimers (**Figure 2.4**), **Bis-PDI1** has a FE/CT ratio of 6.2, whereas **Bis-PDI2** and **Bis-PDI3** have the ratios of 0.68 and 0.70, respectively. **Bis-PDI1** forms excimers within <200 fs whereas **PDI2** and **PDI3** form a mixed state in ~50 ps, which is composed of $^1(S_0S_1)$, $^1(T_1T_1)$, and CT states, similar to the mixed state observed in terrylenediimide (TDI) dimers.[3] The **PDI2** and **PDI3** dimers are unique cases because the lowest excimer eigenstate has a greater contribution from the CT state than the FE state, leading to a FE/CT ratio less than 1. Kim and co- workers suggested that a comparable contribution of FE and CT states prevents excimer formation, but rather facilitates multiexciton generation.[71] On the other hand, **PDI1** dimer,

which forms excimers rapidly, still has a greater contribution from FE similar to the BPEA covalent dimers and some of the DPP systems.

Based on the FE/CT ratio calculated in variety of dimer systems including BPEA, PDI, and DPP, there seems to be a threshold for a CT contribution to facilitate excimer formation (Figure 5). For instance, in the BPEA covalent dimers, when the ratio is greater than 12, the excimer state does not form as seen in **2ph**, setting the upper limit of FE/CT for excimer formation. In crystalline DPP systems, the ratio is much greater, beyond 110, for prohibiting excimer formation. In contrast, for the covalent PDI dimers, when the ratio is below 0.7, e.g. for **PDI3**, there is also no formation of excimer state, setting the lower limit of FE/CT for excimer formation. Although the exact value of these thresholds varies among different systems, there appears to be a specific range of FE/CT values to facilitate excimer formation within the same series of molecular compounds

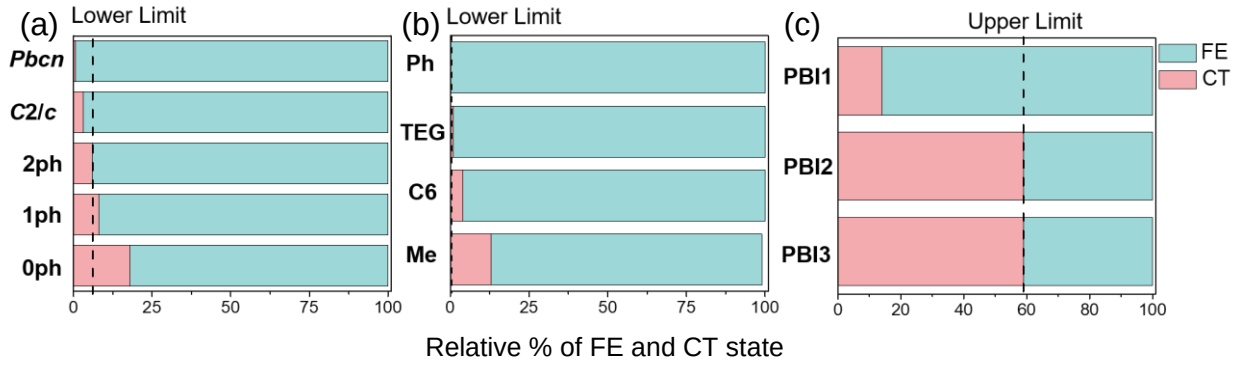

Figure 2.5. Calculated contribution of FE ($\frac{a^2}{(a^2+b^2)} \cdot 100\%$) and CT states ($\frac{b^2}{(a^2+b^2)} \cdot 100\%$). The lower limit of CT contribution for excimer formation is shown as a dashed line for (a) BPEA and (b) DPP system and the upper limit is shown for (c) PDI systems.

2.4.3 Absence of singlet fission. Based on the singlet ($E(S_1)$ = 2.52-2.60 eV) and triplet excited state energies ($E(T_1)$ = 1.24-1.30 eV), the latter of which were obtained using multiple triplet

sensitizers[104] (see Supporting Information), BPEA covalent dimers have favorable energetics for SF; however, unlike in solid state BPEA, where efficient SF occurs, either excimer formation or fluorescence is a major decay pathway in covalent BPEA dimers. There are two reasons.

First, the excimer formation rate is much faster than the SF rate observed in the solid-state film due to a larger degree of CT contribution in BPEA dimers compared to solid-state BPEA. We calculated the FE/CT ratio for both the *C*2/*c* and *Pbcn* polymorphs of BPEA in solid-state films and the ratios are 38 for *C*2/*c* and 180 for *Pbcn* polymorphs (Figure 5). These values are far greater than the ratio observed in **2ph**, which is 17, and thus it is reasonable that there is no excimer formation in *C*2/*c* and *Pbcn* BPEA films.

Second, presumably for SF to occur in covalent dimers, there needs to be a significant contribution from the CT state as seen in the **PDI2** and **PDI3** dimers. Both **PDI2** and **PDI3** have CT contributions that are larger than those of FE, and only these two dimers undergo SF. In addition, upon photoexcitation of TDI dimers, a spectroscopically observable mixed state, composed of $^1(S_0S_1)$, $^1(T_1T_1)$ and CT states is formed.[3] Due to a large CT state contribution, both cation and anion species are spectroscopically observable in TDI dimers.[3] Similarly, in pentacene systems, where ultrafast SF occurs, the CT character is calculated to range from 50-94%.[105] Thus, in BPEA covalent dimers, the CT contribution is insufficient to drive SF, but it also exceeds the threshold necessary for the CT contribution to promote excimer formation. Presumably, the CT contribution can be balanced in specific molecular designs to avoid excimer formation and to promote SF.

2.5 Conclusions

We have synthesized covalent BPEA dimers using a xanthene bridge and changed the longitudinal distance between the two BPEA units by changing the number of phenyl spacers. Based on fsTA and TRF measurements, excimer formation is a major decay pathway for **0ph** and **1ph**, whereas fluorescence emission from the S_1 state with a small degree of SB-CS is observed for **2ph**. Solvent-polarity dependent excited state dynamics confirms the importance of the CT state in excimer formation. We quantified the contribution of the FE and CT states and found that there are different lower and upper thresholds in the FE state character relative to that of the CT state among different systems including BPEA, DPP, and PDI molecular aggregates that facilitate excimer state formation. Such quantitative analysis using exciton coupling could aid in designing molecular aggregates to avoid excimer state formation and to favor singlet fission.

2.6 Acknowledgements

This work was supported by the U.S. Department of Energy, Office of Science, Office of Basic Energy Sciences under Award DE-FG02-99ER14999 (M.R.W.). G.K. and G. C. S. were supported by U.S. Department of Energy, Office of Science, Office of Basic Energy Sciences under Award DE-SC000475. Y.B. gratefully acknowledges support from the Ryan Fellowship and the International Institute for Nanotechnology at Northwestern University. D.S. acknowledges a JSPS fellowship for young scientists and Grant-in-Aid for Scientific Research on Innovative Areas MEXT, “Science of Atomic Layers (SATL)”. J.D.S. acknowledges support from the National Science Foundation Graduate Research Fellowship Program under Grant No. DGE-1842165. This work made use of the IMSERC at Northwestern University, which has received support from the Soft and Hybrid Nanotechnology Experimental (SHyNE) Resource (NSF ECCS-1542205), the State of Illinois, and the International Institute for Nanotechnology (IIN).

2.7 Supplementary Information

2.7.1 Synthesis

Instrumentation and Materials. All reagents and solvents were of commercial reagent grade and were used without further purification unless where noted. Diisopropylamine was distilled from CaH_2 before use. All reactions were carried out under N_2 atmosphere. Preparative separations were performed by silica gel column chromatography. ^{1}H and ^{13}C NMR spectra were recorded on a Bruker Avance III 500 MHz system equipped with DCH CryoProbe, and chemical shifts were reported as the δ scale relative to internal standards $CHCl_3$ (δ = 7.26 ppm for ^{1}H, 77.16 ppm for ^{13}C) or 1,1,2,2-tetrachloroethane-*d* (δ = 6.00 ppm for ^{1}H, 73.78 ppm for ^{13}C). 9-Ethynyl-10-phenylehynylanthracene was prepared according to a literature.[106] High Resolution Mass Spectra (HRMS) were obtained with an Agilent LCTOF 6200 series mass spectrometer using electrospray ionization (ESI) and APPI.

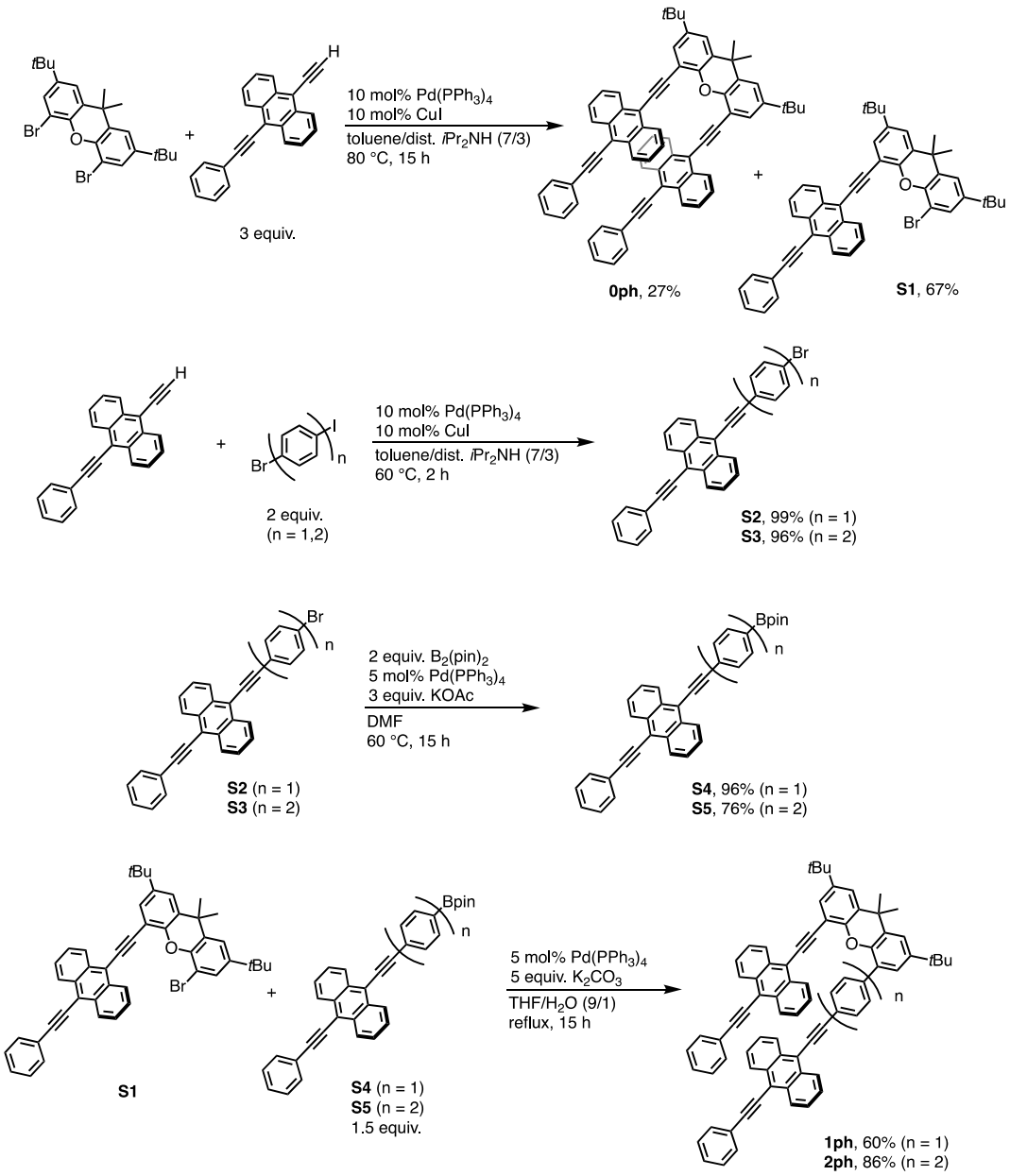

Scheme 2.3. Overview of the synthesis of **0ph**, **1ph**, and **2ph**.

Synthetic procedures.

4,5-bis-(10-phenylethynylanthracen-9-ylethynyl)-2,7-di-*tert*-butyl-9,9-dimethylxanthene (**0ph**) and 4-bromo-5-(10-phenylethynylanthracen-9-ylethynyl)-2,7-di-tert-butyl-9,9-dimethylxanthene (**S2.1**)

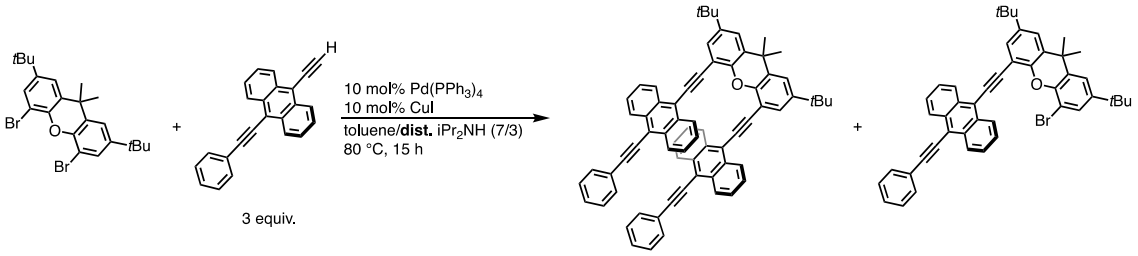

A mixture of 4,5-dibromo-2,7-di-*tert*-butyl-9,9-dimethylxanthene (120 mg, 0.25 mmol), 9-ethynyl-10-phenylehynylanthracene (227 mg, 0.75 mmol, 3 equiv.), $Pd(PPh_3)_4$ (29 mg, 10 mol%), and CuI (4.8 mg, 10 mol%) in toluene/*i*Pr_2NH (7/3 mL) was stirred at 80 °C for 15 h. The reaction mixture was extracted with CH_2Cl_2 and washed with water and brine. Organic mixture was separated and dried over anhydrous Na_2SO_4. The crude mixture was purified by silica gel column chromatography (eluent: CH_2Cl_2/hexanes = 1/9). Collected fractions were concentrated, and recrystallization from MeOH gave 4-bromo-5-(10-phenylethynylanthracen-9-ylethynyl)-2,7-di-*tert*-butyl-9,9-dimethylxanthene (118 mg, 0.17 mmol, 67 %) and 4,5-bis-(10-phenylethynylanthracen-9-ylethynyl)-2,7-di-*tert*-butyl-9,9-dimethylxanthene (62 mg, 68 µmol, 27%), respectively.

0ph: ^{1}H NMR (1,1,2,2-tetrachloroethane-d_2, 298 K) δ/ppm = 8.39 (t, J = 7.4 Hz, 4H), 8.14 (d, J = 8.5 Hz, 4H), 7.64 – 7.58 (m, 6H), 7.55 (d, J = 2.3 Hz, 2H), 7.33 (t, J = 7.4 Hz, 2H), 7.27 (t, J = 7.4 Hz, 5H), 7.18 (t, J = 7.4 Hz, 5H), 7.04 (t, J = 7.4 Hz, 4H), 1.82 (s, 6H), 1.43 (s, 18H); ^{13}C NMR (1,1,2,2-tetrachloroethane-d_2, 298 K) δ/ppm = 148.80, 145.64, 131.50, 130.88, 130.78, 129.67, 128.25, 128.13, 128.06, 127.01, 125.90, 125.90, 125.78, 125.70, 123.69, 123.68, 123.42, 117.92, 117.40, 111.30, 101.81, 97.91, 90.35, 86.58, 74.00, 73.78, 73.56, 34.66, 34.40, 32.41, 31.38. ESI-HRMS (*m/z*): calculated for $C_{71}H_{55}O^+$ ([M+H]$^+$): 999.4247, found: 923.4243.

S2.1: ^{1}H NMR ($CDCl_3$, 298 K) δ/ppm = 8.97 (dd, J = 3.5, 3.0 Hz, 2H), 8.70 (dd, J = 3.5, 3.0 Hz, 2H), 7.82 – 7.77 (m, 2H), 7.71 – 7.62 (m, 5H), 7.52 – 7.41 (m, 5H), 7.38 (d, J = 2.2 Hz, 1H), 1.71 (s, 6H), 1.42 (s, 9H), 1.34 (s, 9H); ^{13}C NMR ($CDCl_3$, 298 K) δ/ppm = 148.82, 147.21, 146.07, 145.27, 132.32, 131.86, 131.14, 129.95, 128.94, 128.78, 128.74, 128.72, 128.43, 127.20, 127.01, 126.76, 123.83, 123.70, 121.97, 119.38, 118.33, 111.58, 110.57, 102.35, 98.90, 90.67, 86.82, 77.41, 77.16, 76.91, 35.42, 34.74, 32.53, 31.74, 31.63, 31.56.

9-(4-bromophenylethynyl)-10-(phenylethynyl)anthracene **S2.2**

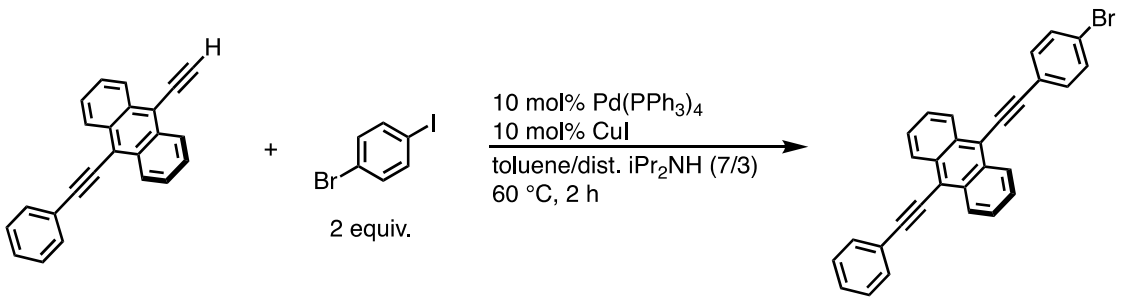

To a mixture of 1-bromo-4-iodobenzene (283 mg, 1.0 mmol), $Pd(PPh_3)_4$ (58 mg, 0.05 mmol, 10 mol%), and CuI (4.8 mg, 0.05 mmol, 10 mol%) in toluene/iPr$_2$NH (7/3 mL), was added 9-ethynyl-10-phenylehynylanthracene (151 mg, 0.50 mmol). After stirring at 60 °C for 3 h, the reaction mixture was poured onto water and extracted with CH_2Cl_2. Organic phase was washed with brine and dried over anhydrous Na_2SO_4. The crude mixture was purified with silica gel column chromatography (eluent: CH_2Cl_2/hexanes = 1/9). Recrystallization from MeOH gave **S2** (226 mg, 0.50 mmol, 99%).

^{1}H NMR ($CDCl_3$, 298 K) δ/ppm = 8.73 – 8.68 (m, 2H), 8.68 – 8.64 (m, 2H), 7.79 (dd, J = 8.3, 1.6 Hz, 2H), 7.69 – 7.62 (m, 6H), 7.60 (d, J = 8.3 Hz, 2H), 7.50 – 7.41 (m, 3H); ^{13}C NMR ($CDCl_3$, 298 K) δ/ppm = 133.21, 132.27, 132.24, 132.02, 131.87, 128.93, 128.75, 127.48, 127.25, 127.12, 127.02, 123.51, 123.11, 122.52, 119.02, 118.11, 102.77, 101.34, 87.82, 86.56, 77.41, 77.16, 76.91.

9-[4-(4,4,5,5-tetramethyl-1,3,2-dioxaborolan-2-yl)phenylethynyl]-10-phenylethynylanthracene (**S4**)

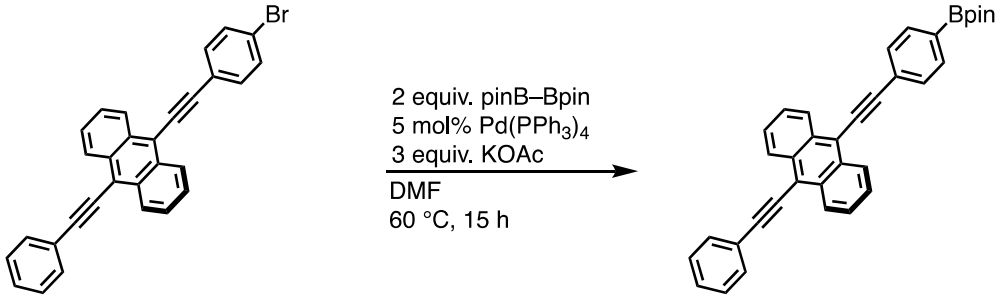

A mixture of **S2.2** (137 mg, 0.30 mmol), $B_2(pin)_2$ (152 mg, 0.60 mmol, 2 equiv.), $Pd(PPh_3)_4$ (17 mg, 15 µmol, 5 mol%), and KOAc (88 mg, 0.90 mmol, 3 equiv.) in DMF (30 mL) was stirred at 80 °C for 15 h. The reaction mixture was extracted with CH_2Cl_2 and washed with water and brine. Organic mixture was separated and dried over anhydrous Na_2SO_4. Recrystallization from MeOH gave **S2.4** (145 mg, 0.29 mmol, 96%).

^{1}H NMR ($CDCl_3$, 298 K) δ/ppm = 8.68 – 8.54 (m, 4H), 7.80 (d, J = 8.0 Hz, 2H), 7.68 (t, J = 7.6, 6.6 Hz, 4H), 7.59 – 7.51 (m, 4H), 7.42 – 7.31 (m, 4H), 1.29 (s, 12H); ^{13}C NMR ($CDCl_3$, 298 K) δ/ppm = 134.96,

132.31, 132.25, 131.86, 130.97, 128.88, 128.74, 127.42, 127.06, 127.01, 126.20, 123.57, 118.83, 118.48, 102.73, 102.66, 87.97, 86.63, 84.21, 77.41, 77.16, 76.91, 25.07.

4-(10-phenylethynylanthracen-9-ylethynylphenyl)-5-(10-phenylethynylanthracen-9-ylethynyl)-2,7-di-*tert*-butyl-9,9-dimethylxanthene (**1ph**)

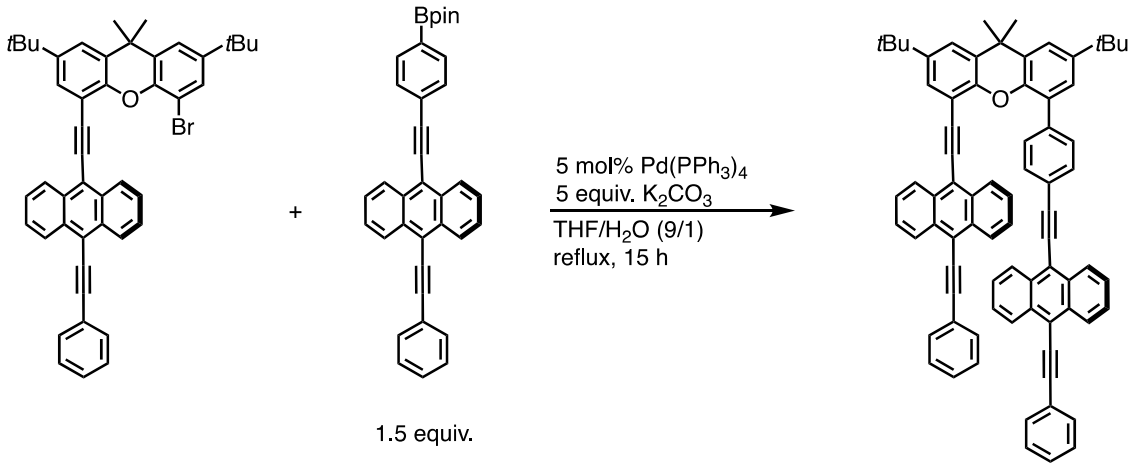

A mixture of **S2.1** (50 mg, 71 µmol), **S2.4** (54 mg, 107 µmol, 1.5 equiv.), $Pd(PPh_3)_4$ (4.1 mg, 3.6 µmol, 5 mol%), and K_2CO_3 (49 mg, 0.36 mmol, 5 equiv.) in THF/water (9/1 mL) was heated to reflux for 15 h. The reaction mixture was extracted with CH_2Cl_2 and washed with water and brine. Organic mixture was separated and dried over anhydrous Na_2SO_4. The crude mixture was purified by silica gel column chromatography (eluent: CH_2Cl_2/hexanes). Recrystallization from MeOH gave **1ph** (43 mg, 43 µmol, 60%).

^{1}H NMR ($CDCl_3$, 298 K) δ/ppm = 8.44 (d, J = 7.7 Hz, 2H), 8.40 (d, J = 8.0 Hz, 2H), 8.19 – 8.14 (m, 2H), 8.14 – 8.10 (m, 2H), 7.74 (dd, J = 7.9, 1.3 Hz, 2H), 7.62 (d, J = 8.3 Hz, 2H), 7.58 (d, J = 2.4 Hz, 1H), 7.55 – 7.37 (m, 13H), 7.26 (d, J = 2.3 Hz, 1H), 7.18 – 7.14 (m, 3H), 6.88 – 6.80 (m, 4H), 1.78 (s, 6H), 1.40 (s, 9H), 1.38 (s, 9H); ^{13}C NMR ($CDCl_3$, 298 K) δ/ppm = 149.52, 146.08, 145.69, 145.50, 138.17, 132.28, 132.20, 132.07, 132.02, 131.76, 131.24, 131.00, 130.34, 130.11, 129.62, 128.94, 128.72, 128.61, 128.10, 128.06, 127.61, 127.56, 127.29, 127.14, 126.67, 126.63, 126.49, 126.30, 126.22, 124.01, 123.66, 122.86, 122.41, 121.49, 119.43, 119.02, 118.66, 117.96, 111.42, 102.72, 101.97, 101.95, 98.45, 90.64, 87.21, 86.59, 86.21, 77.41, 77.16, 76.91, 35.17, 34.79, 34.76, 32.49, 31.73, 31.67. ESI-HRMS (*m/z*): calculated for $C_{77}H_{59}O^+$ ([*M*+H]$^+$): 999.4560, found: 999.4536.

9-(4-bromobiphenylenylethynyl)-10-phenylethynylanthracene (**S2.3**)

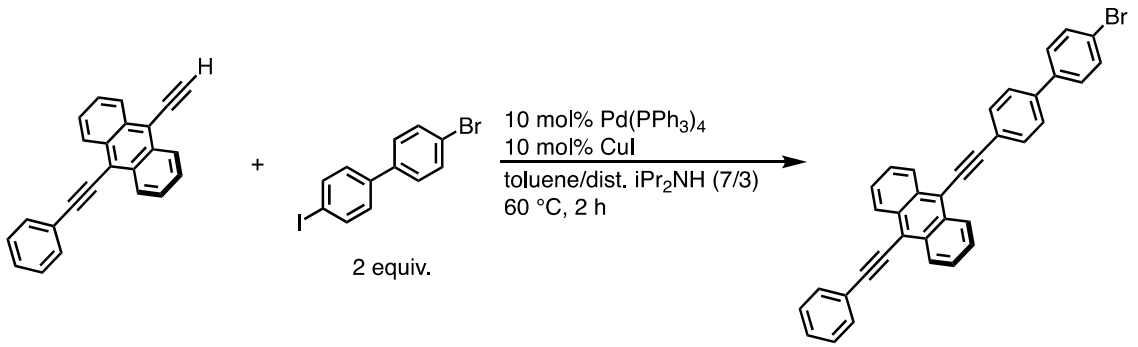

To a mixture of 4-bromo-4'-iodobiphenyl (359 mg, 1.0 mmol), $Pd(PPh_3)_4$ (58 mg, 0.05 mmol, 10 mol%), and CuI (4.8 mg, 0.05 mmol, 10 mol%) in toluene/*i*Pr_2NH (7/3 mL), was added 9-ethynyl-10-phenylehynylanthracene (151 mg, 0.50 mmol). After stirring at 60 °C for 3 h, the reaction mixture was poured onto water and extracted with CH_2Cl_2. Organic phase was washed with brine and dried over anhydrous Na_2SO_4. The crude mixture was purified with silica gel column chromatography (eluent: CH_2Cl_2/*n*-hexane = 1/9). Recrystallization from MeOH gave **S2.3** (258 mg, 0.48 mmol, 96%).

^{1}H NMR ($CDCl_3$, 298 K) δ/ppm = 8.72 – 8.67 (m, 4H), 7.83 (d, J = 8.4 Hz, 2H), 7.77 (dd, J = 8.1, 1.5 Hz, 2H), 7.67 – 7.61 (m, 6H), 7.59 (d, J = 8.5 Hz, 2H), 7.51 (d, J = 8.5 Hz, 2H), 7.48 – 7.39 (m, 3H); ^{13}C NMR ($CDCl_3$, 298 K) δ/ppm = 140.31, 139.39, 132.39, 132.28, 132.22, 131.87, 128.91, 128.80, 128.75, 127.48, 127.38, 127.20, 127.06, 127.02, 123.56, 122.90, 122.26, 118.80, 118.49, 102.68, 102.30, 87.70, 86.62, 77.41, 77.16, 76.91.

9-[4-(4,4,5,5-tetramethyl-1,3,2-dioxaborolan-2-yl)biphenylenylethynyl]-10-phenylethynylanthracene (**S2.5**)

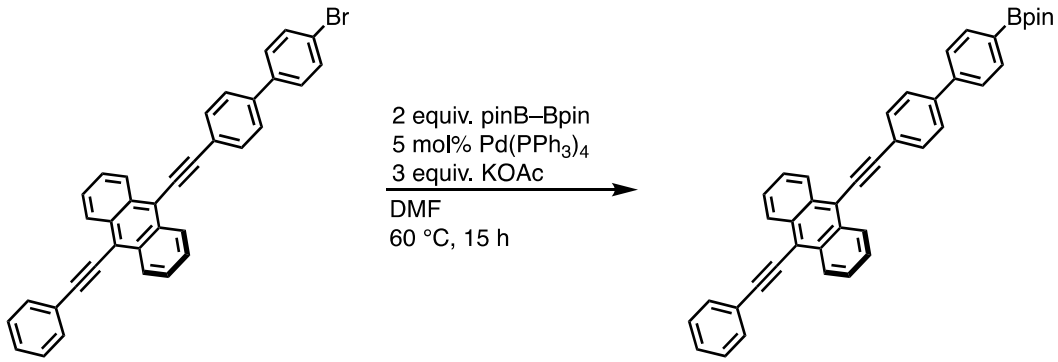

A mixture of **S3** (160 mg, 0.30 mmol), $B_2(pin)_2$ (152 mg, 0.60 mmol, 2 equiv.), $Pd(PPh_3)_4$ (17 mg, 15 µmol, 5 mol%), and KOAc (88 mg, 0.90 mmol, 3 equiv.) in 30 mL of DMF was stirred at 80 °C for 15 h. The reaction mixture was extracted with CH_2Cl_2 and washed with water and brine. Organic mixture was separated and dried over anhydrous Na_2SO_4. Recrystallization from MeOH gave **S5** (136 mg, 0.23 mmol, 76%).

^{1}H NMR ($CDCl_3$, 298 K) δ/ppm = 8.75 – 8.68 (m, 4H), 7.93 (d, J = 8.2 Hz, 2H), 7.86 (d, J = 8.2 Hz, 2H), 7.79 (dd, J = 7.1, 1.5 Hz, 2H), 7.73 (d, J = 8.2 Hz, 2H), 7.70 – 7.64 (m, 6H), 7.49 – 7.42 (m, 3H); ^{13}C NMR ($CDCl_3$, 298 K) δ/ppm = 143.06, 141.37, 135.55, 132.28, 131.86, 128.87, 128.74, 127.49, 127.44, 127.03, 127.00, 126.51, 123.58, 122.76, 118.69, 118.62, 102.62, 102.53, 87.56, 86.66, 84.06, 77.41, 77.16, 76.91, 25.05.

4-[4-(10-phenylethynylanthracen-9-ylethynylphenyl)-phenyl]-5-(10-phenylethynylanthracen-9-ylethynyl)-2,7-di-*tert*-butyl-9,9-dimethylxanthene (**2ph**)

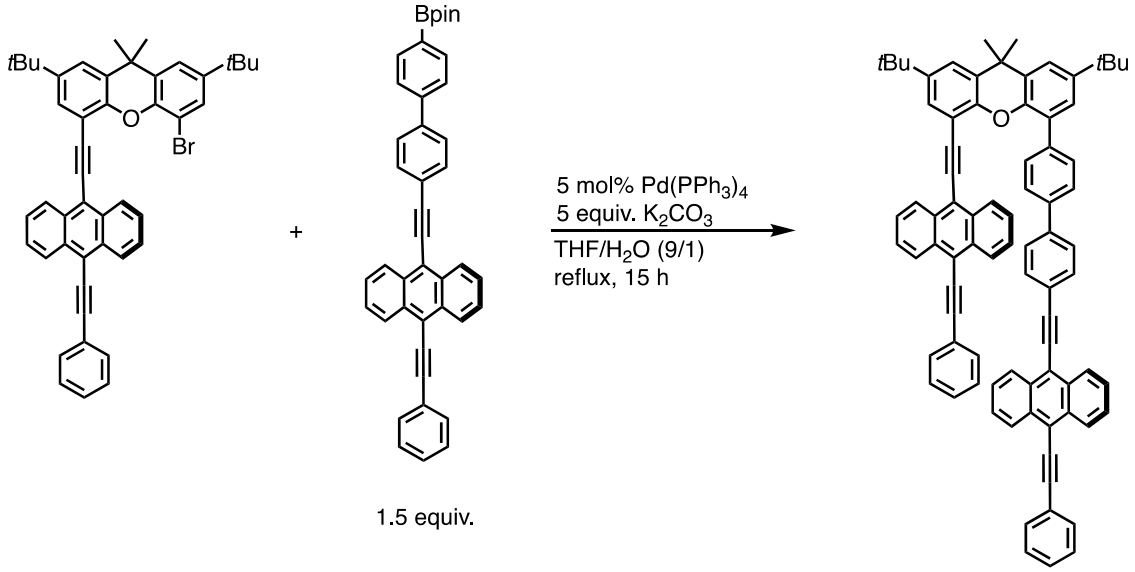

A mixture of **S2.1** (30 mg, 43 µmol), **S2.5** (49 mg, 64 µmol, 1.5 equiv.), $Pd(PPh_3)_4$ (2.5 mg, 22 µmol, 5 mol%), and K_2CO_3 (29 mg, 0.22 mmol, 5 equiv.) in THF/water (9/1 mL) was heated to reflux for 15 h. The reaction mixture was extracted with CH_2Cl_2 and washed with water and brine. Organic mixture was separated and dried over anhydrous Na_2SO_4. The crude mixture was purified with silica gel column chromatography (eluent: CH_2Cl_2/hexanes). Recrystallization from MeOH gave **2ph** (40 mg, 37 µmol, 86%).

^{1}H NMR ($CDCl_3$, 298 K) δ/ppm = 8.70 (d, J = 8.6 Hz, 2H), 8.59 (d, J = 8.7 Hz, 2H), 8.56 (d, J = 8.7 Hz, 2H), 8.48 (d, J = 8.6 Hz, 2H), 7.81 (d, J = 6.7 Hz, 2H), 7.70 (d, J = 8.2 Hz, 2H), 7.63 (t, J = 7.6 Hz, 2H), 7.60 – 7.41 (m, 16H), 7.30 (d, J = 2.3 Hz, 1H), 6.83 (d, J = 8.1 Hz, 2H), 6.68 (t, J = 7.3 Hz, 1H), 6.63 (t, J = 7.3 Hz, 2H), 6.47 (d, J = 8.2 Hz, 2H), 1.78 (s, 6H), 1.40 (s, 9H), 1.38 (s, 9H); ^{13}C NMR ($CDCl_3$, 298 K, 171027-01C) δ/ppm = 149.58, 146.02, 145.63, 145.58, 139.78, 137.64, 137.36, 132.27, 132.20, 132.17, 131.87, 131.70, 131.50, 130.28, 130.26, 130.17, 128.88, 128.85, 128.77, 128.33, 128.13, 128.09, 127.58, 127.53, 127.26, 127.21, 126.94, 126.81, 126.74, 126.72, 126.36, 126.09, 125.92, 123.75, 123.68, 123.18, 122.11, 121.64, 119.18, 119.11, 118.64, 118.13, 111.21, 103.40, 102.81, 102.43, 98.83, 90.06, 87.04, 86.83, 86.44, 77.41, 77.16, 76.91, 35.19, 34.77, 34.75, 32.43, 31.73, 31.67. ESI-HRMS (*m/z*): calculated for $C_{83}H_{63}O^+$ ([*M*+H]$^+$): 1075.4873, found: 1075.4867.

2.7.2 Kinetic fitting for TA and TRF

Prior to kinetic analysis, the fsTA and data were background/scatter-subtracted and chirp-corrected, and the similar data sets were spectrally merged (Surface Xplorer 4, Ultrafast Systems, LLC). The kinetic analysis was performed using home written programs in MATLAB and was based on a global fit to selected wavelength/frequency kinetics. The time-resolution is given as w = 300 fs (full width at half maximum, FWHM); the assumption of a uniform instrument response across the frequency domain and a fixed time-zero (t0) are implicit in global analysis. Kinetic data from multiple different wavelengths/frequencies were fit using the global analysis described below. Each wavelength/frequency was given an initial amplitude that is representative of the spectral intensity at time t0 and varied independently to fit the data. The time/rate constants and t0 are shared between the various kinetic data and are varied globally across the kinetic data in order to fit the models described in the text. We globally fit the dataset to a specified kinetic model and use the resultant populations to deconvolute the dataset and reconstruct species-associated spectra. The MATLAB program numerically the solves the differential equations through matrix methods, then convolutes the solutions with a Gaussian instrument response function with width w before employing a least-squares fitting using a Levenberg-Marquardt or Simplex method to find the parameters which result in matches to the kinetic data. Once the fit parameters are established, they are fed directly into the differential equations, which were solved for the populations of the states in model—i.e., A(t), B(t), and C(t), etc. Finally, the raw data matrix (with all the raw data) is deconvoluted with the populations as functions of time to produce the spectra associated with each species.

2.7.3 Steady state absorbance and emission

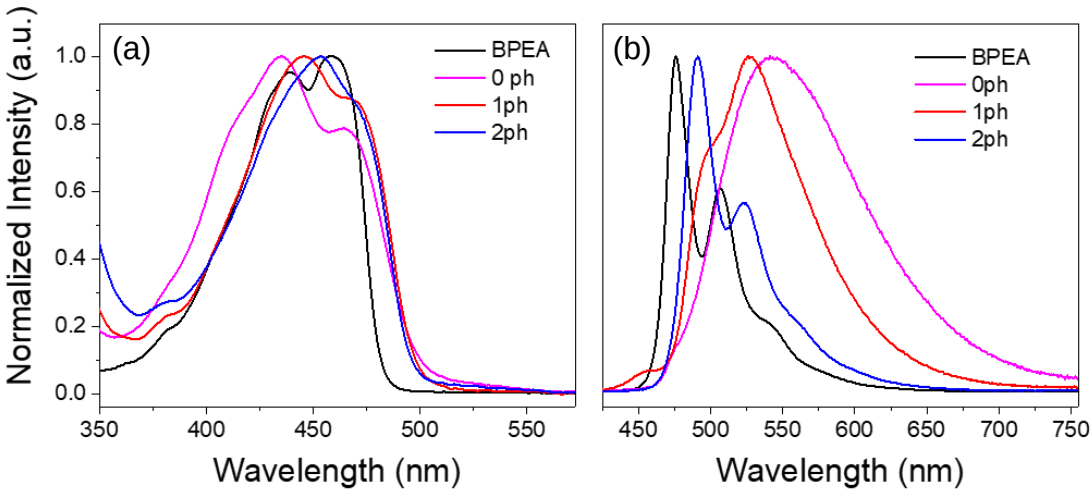

Figure 2.6. (a) steady state absorbance and (b) emission spectra of BPEA monomer

Table 2.5. The peak positions, $S_1(E)$, and FLQY of BPEA monomer and dimers in toluene.

	0-0 (nm)	0-1 (nm)	$S_1(E)$ (eV)	Φ_{fl} (%)
BPEA	458	439	2.64	100 ± 2
0ph	465	435	2.53	44 ± 3
1ph	471	447	2.55	87 ± 3
2ph	471	454	2.57	90 5

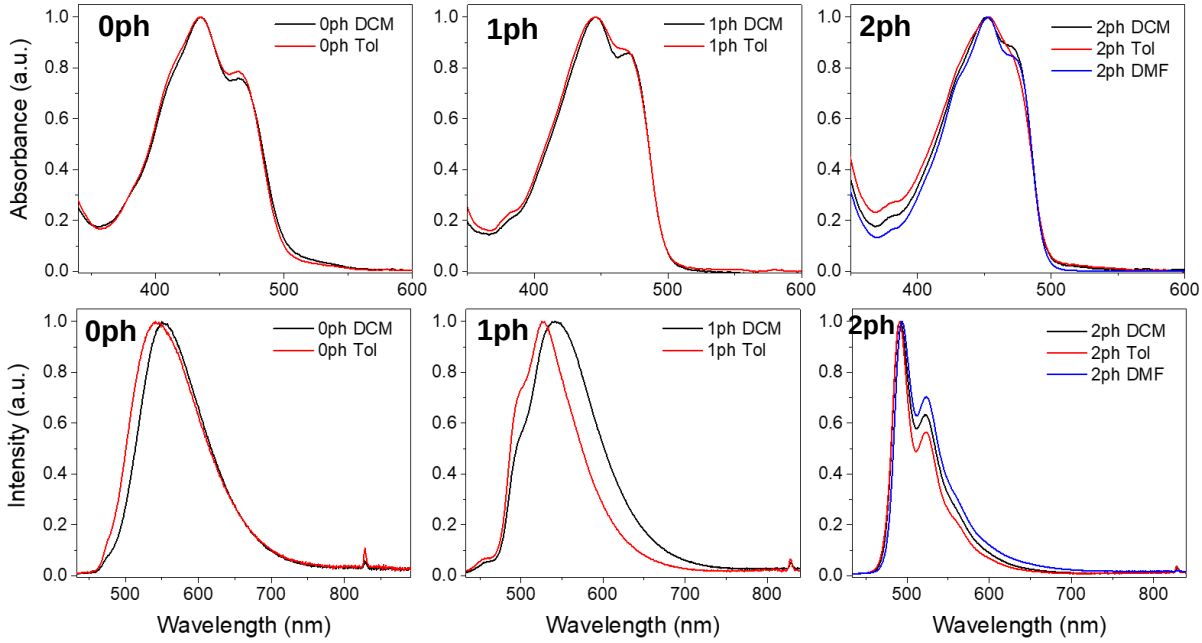

Figure 2.7. (Top) steady state absorbance and (Bottom) emission spectra of BPEA

2.7.4 Additional TRF data

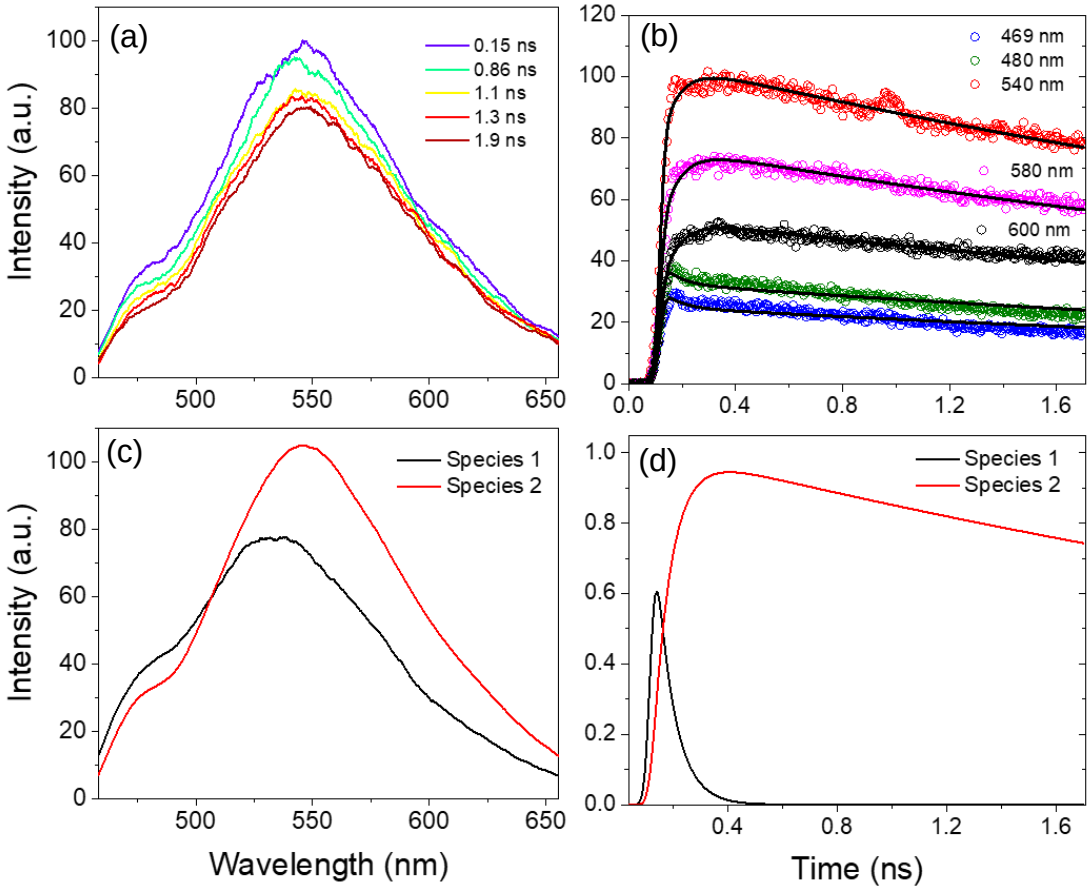

Figure 2.8. Global analysis of the (a) TRF data for **0ph** in DCM for the 2 ns time window. (b) Wavelength kinetic fits, (c) evolution-associated spectra and (d) population *vs.* time fits to a sequential A → B → GS model.

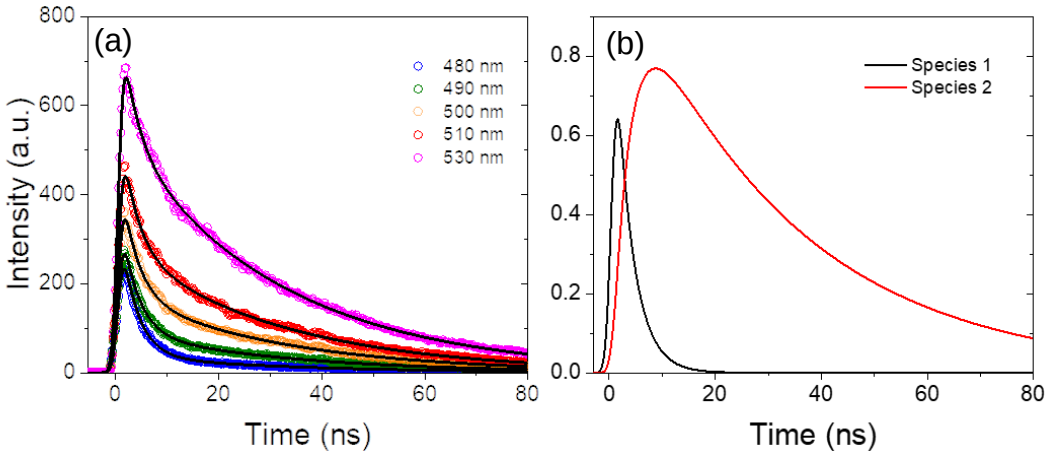

Figure 2.9. Global analysis of the TRF data for **0ph** in DCM for the 100 ns time window. (a) Kinetic fits to a sequential A → B → GS model and (b) population *vs.* time fit.

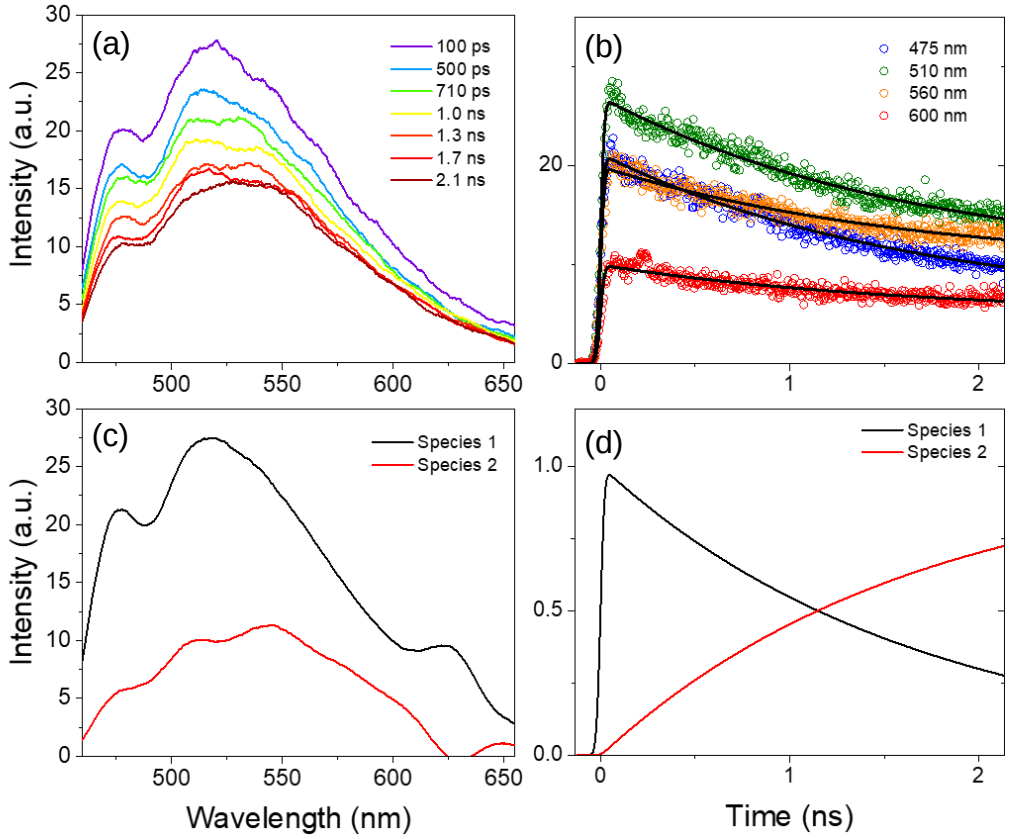

Figure 2.10. Global analysis of the (a) TRF data for **0ph** in Tol for the 2 ns time window. (b) Wavelength kinetic fits, (c) evolution-associated spectra and (d) population *vs.* time fits to a sequential A → B → GS model.

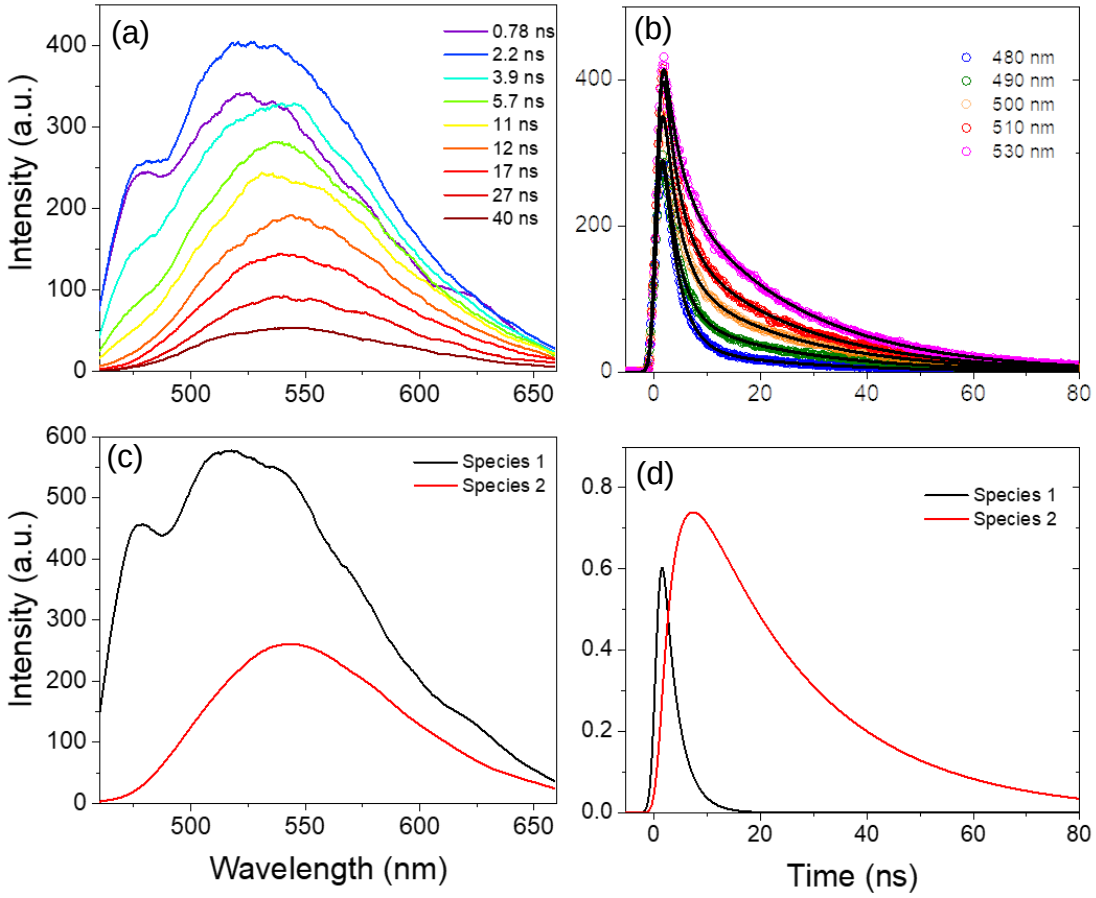

Figure 2.11. Global analysis of the (a) TRF data for **0ph** in Tol for the 100 ns time window. (b) Wavelength kinetic fits, (c) evolution-associated spectra and (d) population *vs.* time fits to a sequential A → B → GS model.

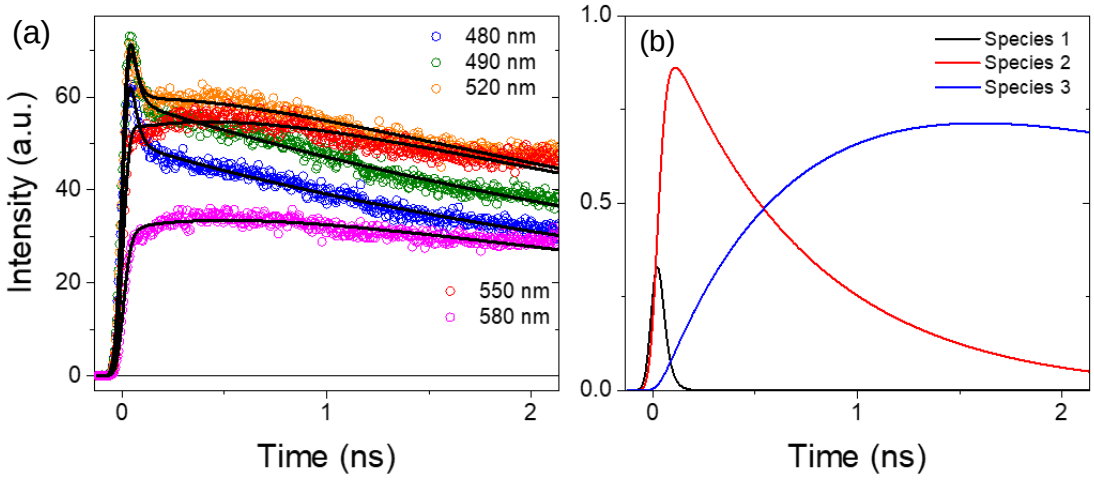

Figure 2.12. Global analysis of the TRF data for **1ph** in DCM for the 2 ns time window. (a) Kinetic fits to a sequential A → B → C → GS model and (b) population *vs.* time fit.

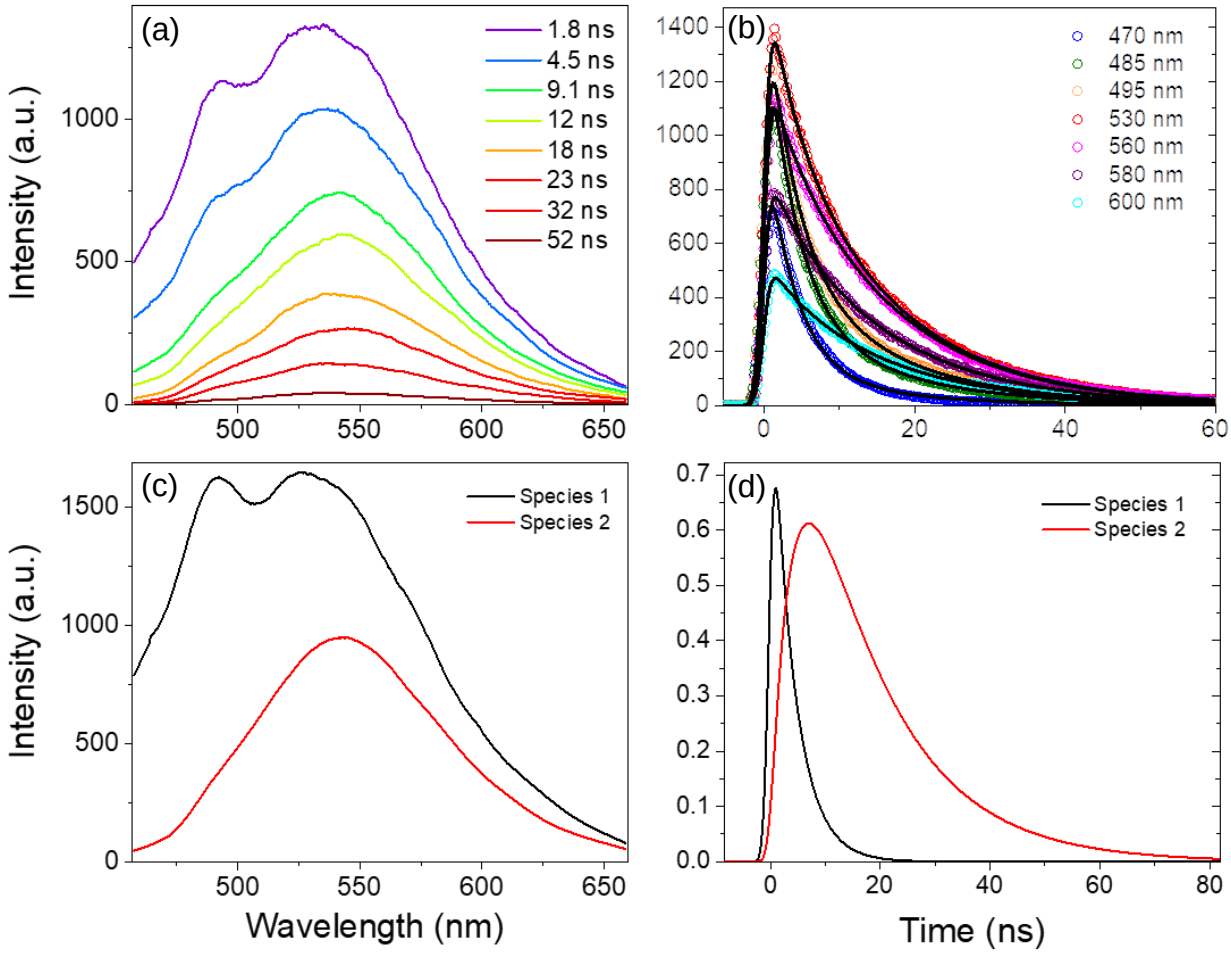

Figure 2.13. Global analysis of the (a) TRF data for **1ph** in DCM for the 100 ns time window. (b) Wavelength kinetic fits, (c) evolution-associated spectra and (d) population *vs.* time fits to a sequential A → B → GS model.

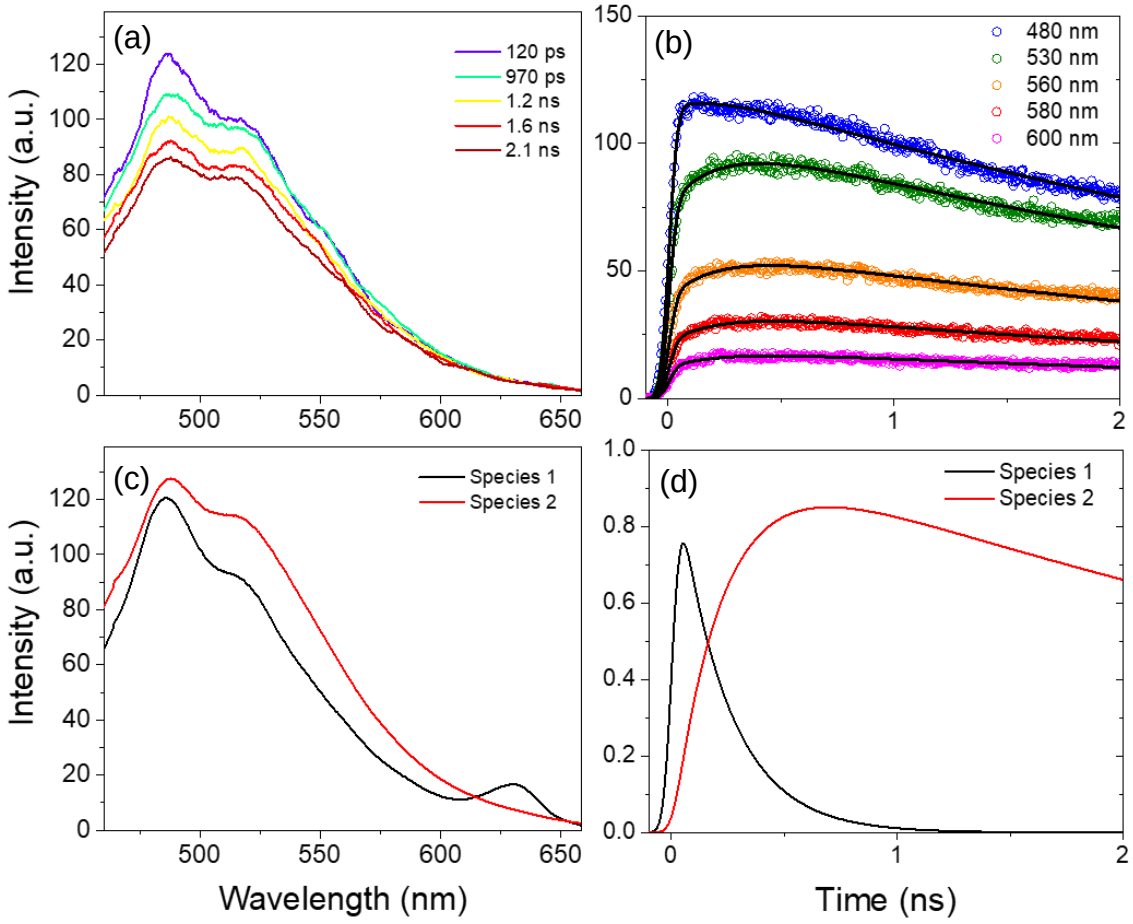

Figure 2.14. Global analysis of the (a) TRF data for **1ph** in Tol for the 2 ns time window. (b) Wavelength kinetic fits, (c) evolution-associated spectra and (d) population *vs.* time fits to a sequential A → B → GS model.

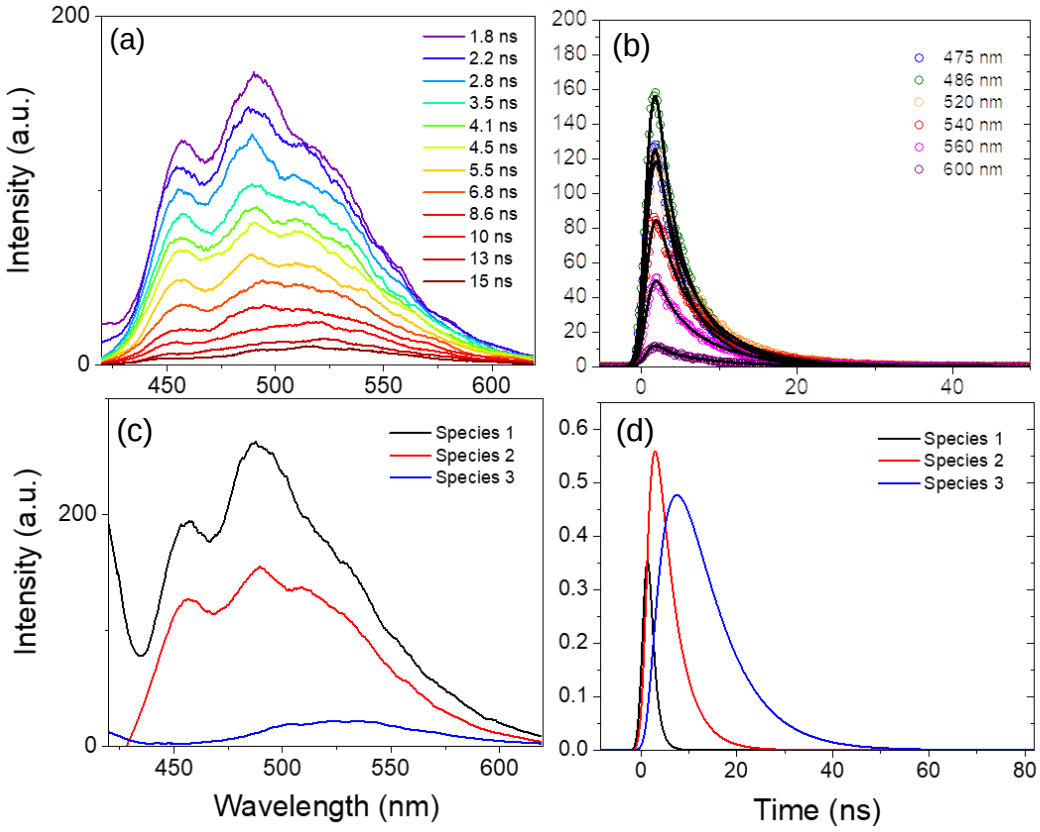

Figure 2.15. Global analysis of the (a) TRF data for **1ph** in Tol for the 100 ns time window. (b) Wavelength kinetic fits, (c) evolution-associated spectra and (d) population *vs.* time fits to a sequential A → B → C→ GS model.

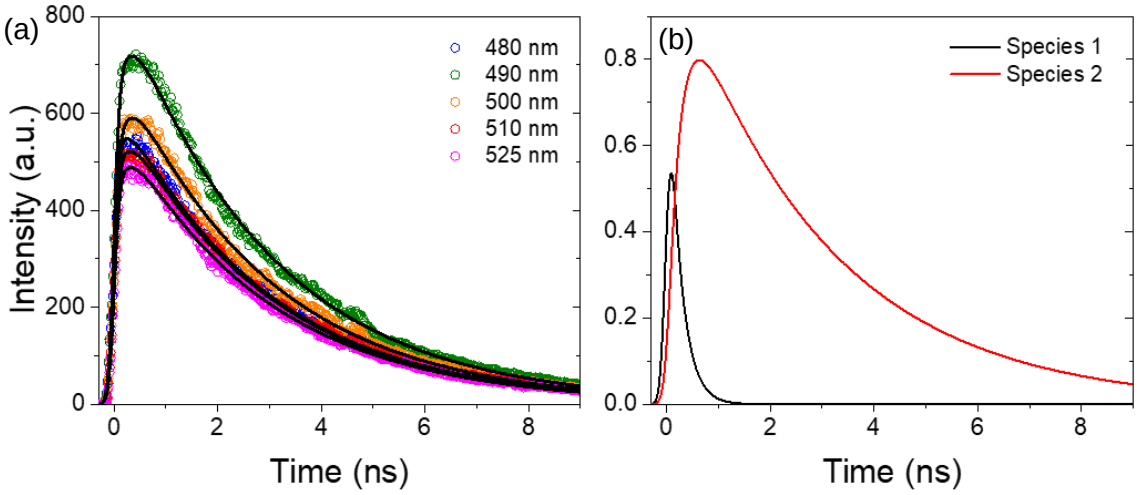

Figure 2.16. Global analysis of the TRF data for **2ph** in DCM for the 10 ns time window. (a) Kinetic fits to a sequential A → B → C → GS model and (b) population

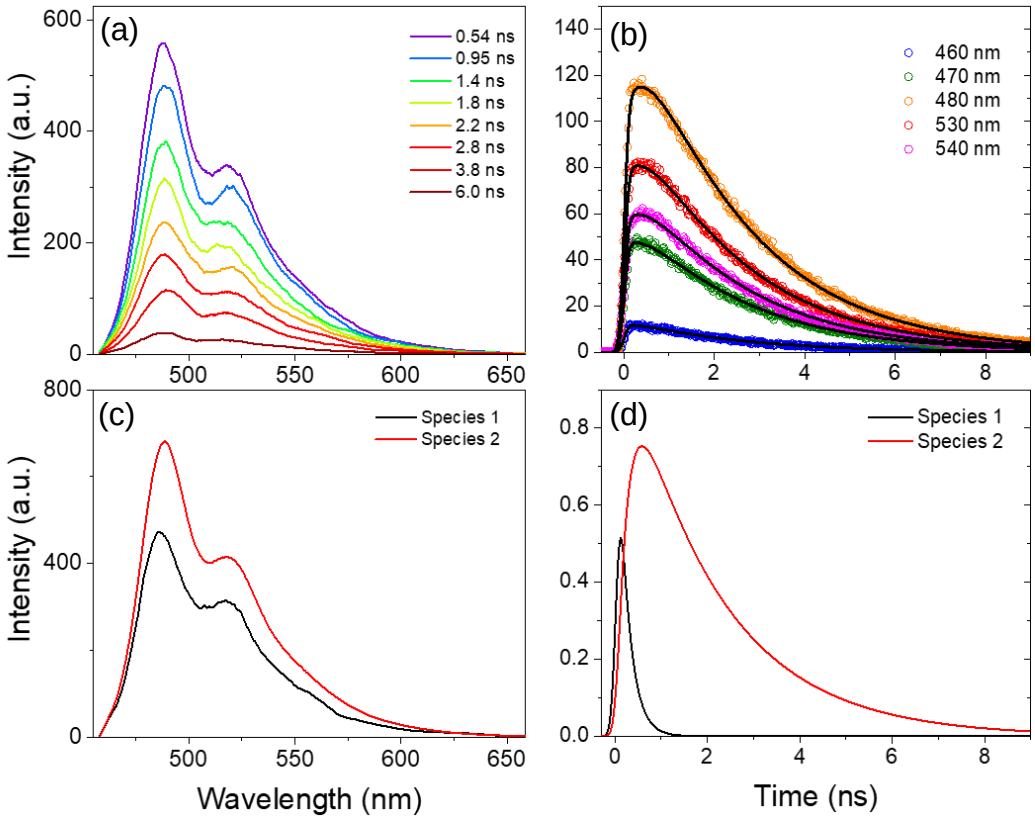

Figure 2.17. Global analysis of the (a) TRF data for **2ph** in Tol for the 10 ns time window. (b) Wavelength kinetic fits, (c) evolution-associated spectra and (d) population vs. time fits to a sequential A → B → GS model.

2.7.5 Additional TA data

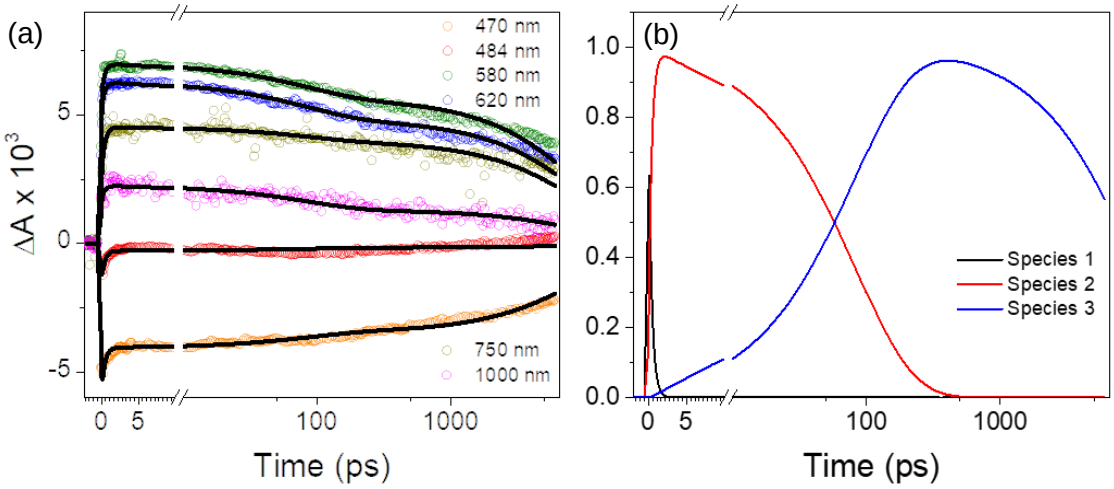

Figure 2.18. Global analysis of the fsTA data for **0ph** in DCM. (a) Kinetic fits to a sequential A → B → C → GS model and (b) population *vs.* time fit.

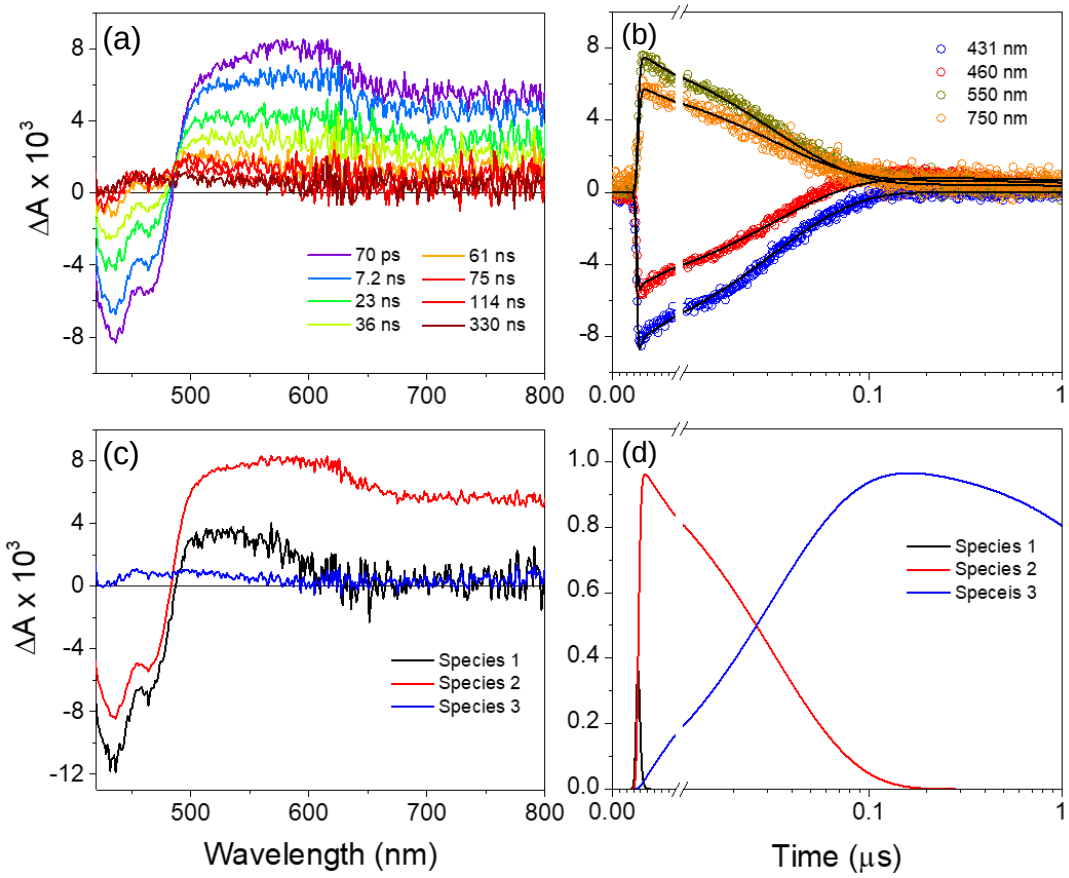

Figure 2.19. Global analysis of the (a) fsTA data for **0ph** in DCM for the time window of 1us. (b) Wavelength kinetic fits, (c) evolution-associated spectra and (d) population vs. time fits to a sequential A → B → GS model. Here, species 3 is assigned to the triplet excited state formed vis intersystem crossing.

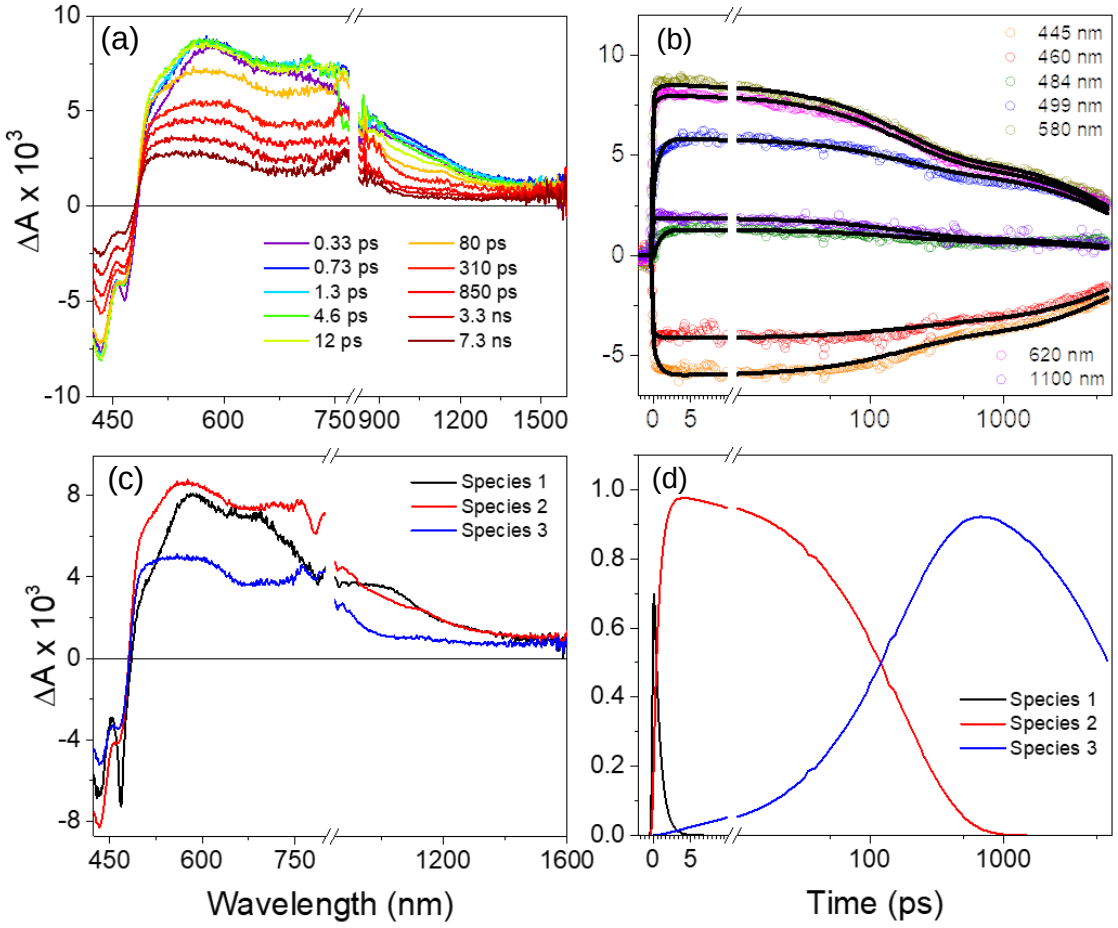

Figure 2.20. Global analysis of the (a) fsTA data for **0ph** in Tol for the time window of 7.4 ns. (b) Wavelength kinetic fits, (c) evolution-associated spectra and (d) population vs. time fits to a sequential A → B → GS model.

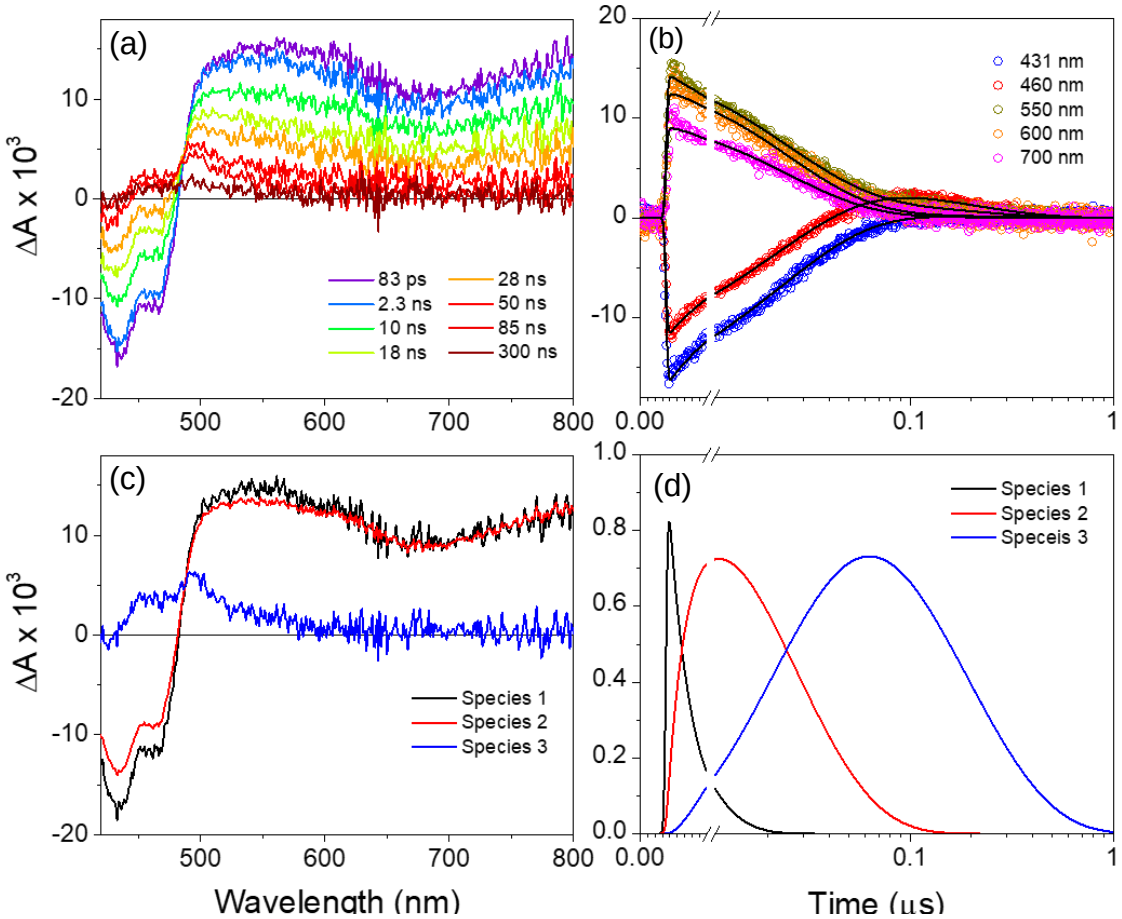

Figure 2.21. Global analysis of the (a) fsTA data for **0ph** in Tol for the time window of 1us. (b) Wavelength kinetic fits, (c) evolution-associated spectra and (d) population vs. time fits to a sequential A → B → GS model. Here, species 3 is assigned to the triplet excited state formed vis intersystem crossing.

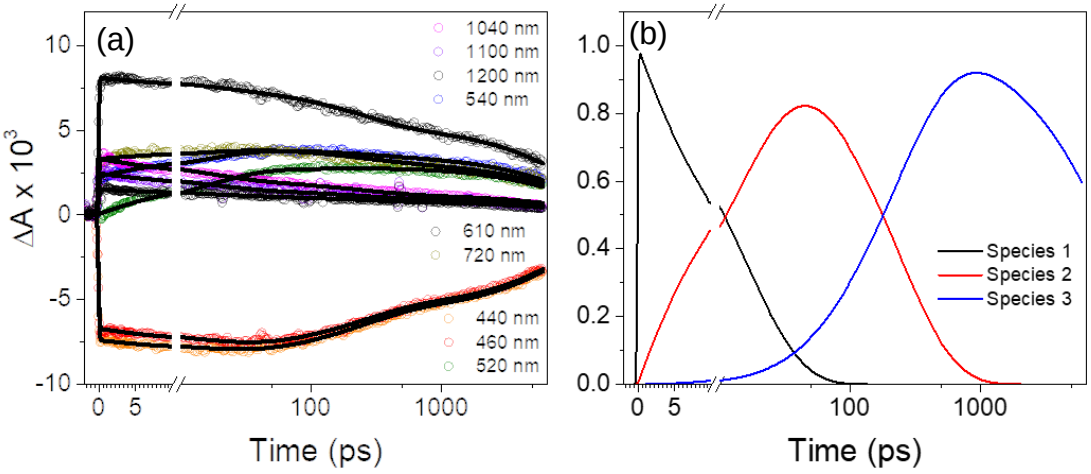

Figure 2.22. Global analysis of the fsTA data for **1ph** in DCM. (a) Kinetic fits to a sequential A → B → C → GS model and (b) population *vs.* time fit.

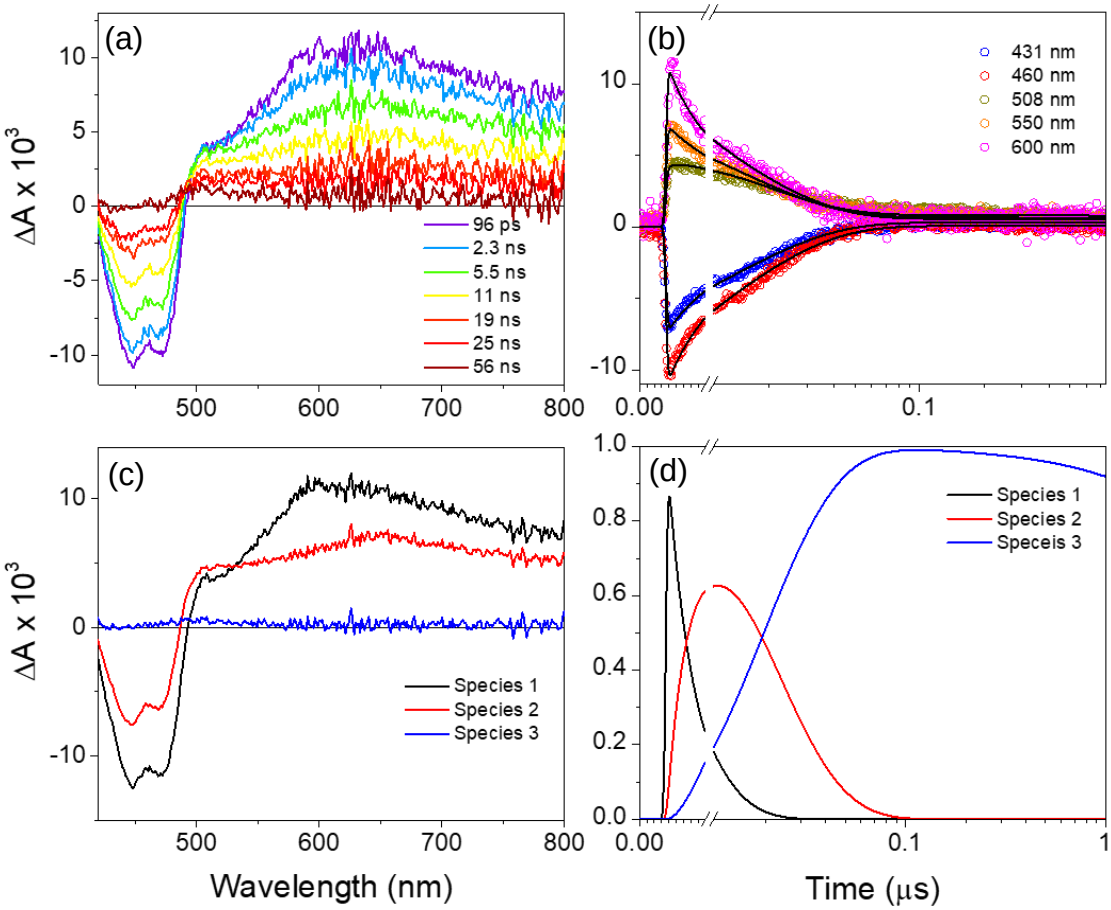

Figure 2.23. Global analysis of the (a) fsTA data for **1ph** in DCM for the time window of 1us. (b) Wavelength kinetic fits, (c) evolution-associated spectra and (d) population vs. time fits to a sequential A → B → GS model. Here, species 3 is assigned to the triplet excited state formed vis intersystem crossing.

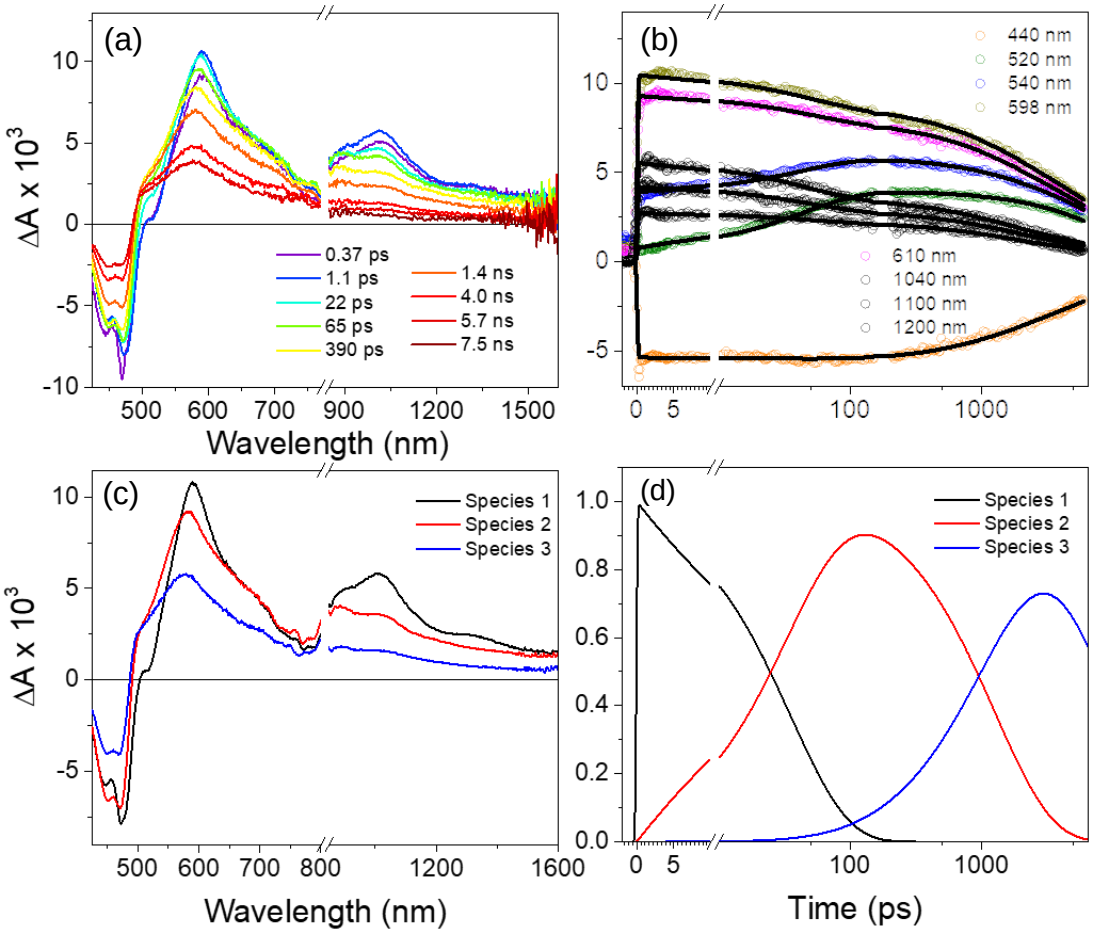

Figure 2.24. Global analysis of the (a) fsTA data for **1ph** in Tol for the time window of 7.4 ns. (b) Wavelength kinetic fits, (c) evolution-associated spectra and (d) population vs. time fits to a sequential A → B → C → GS model.

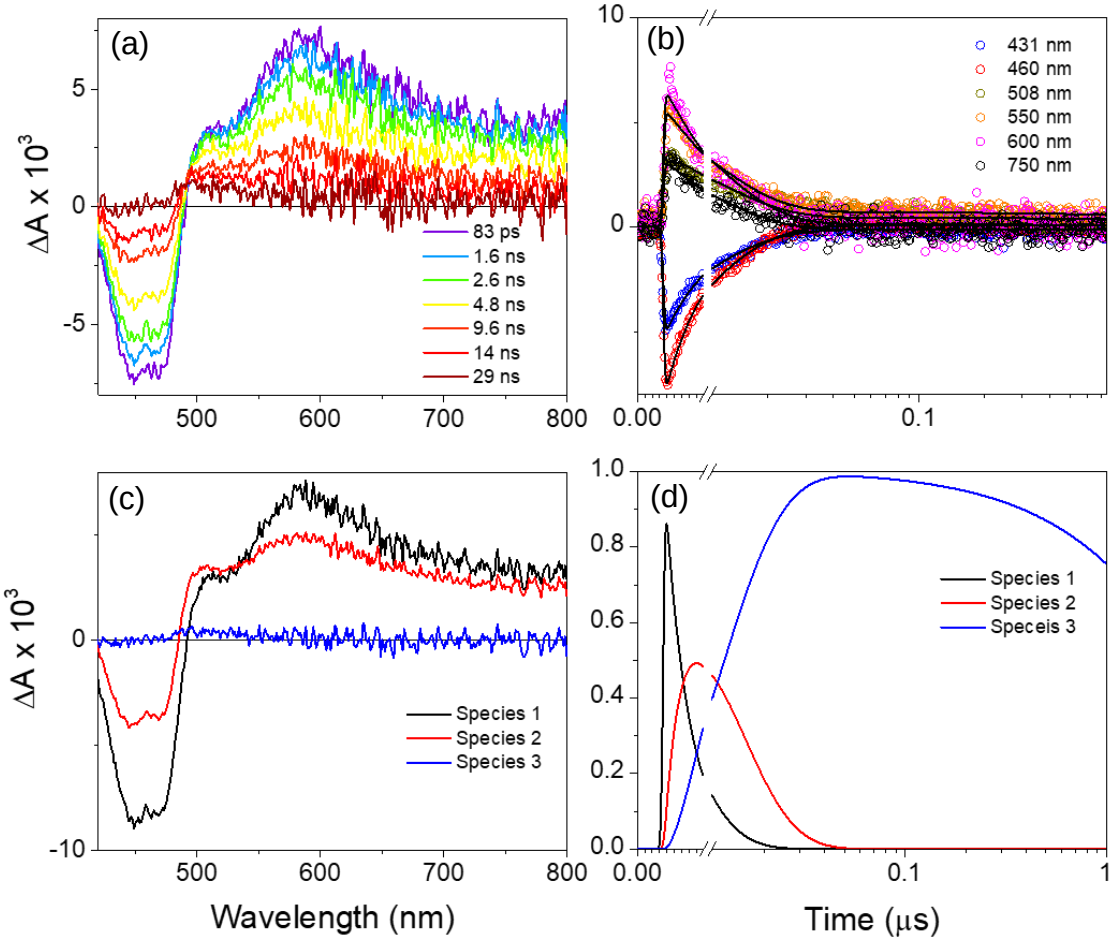

Figure 2.25. Global analysis of the (a) fsTA data for **1ph** in Tol for the time window of 1us. (b) Wavelength kinetic fits, (c) evolution-associated spectra and (d) population vs. time fits to a sequential A → B → GS model. Here, species 3 is assigned to the triplet excited state formed vis intersystem crossing.

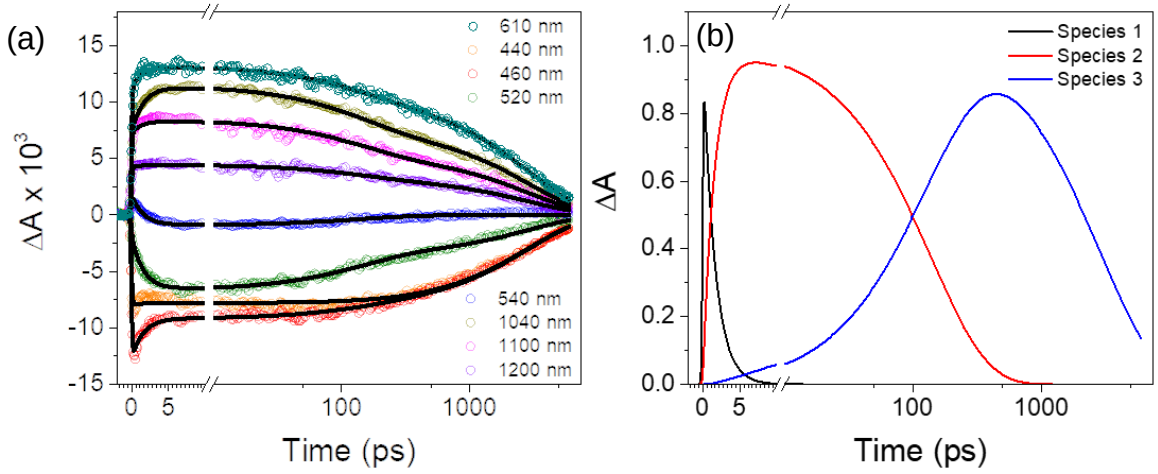

Figure 2.26. Global analysis of the fsTA data for **2ph** in DCM. (a) Kinetic fits to a sequential A → B → C → GS model and (b) population *vs.* time fit.

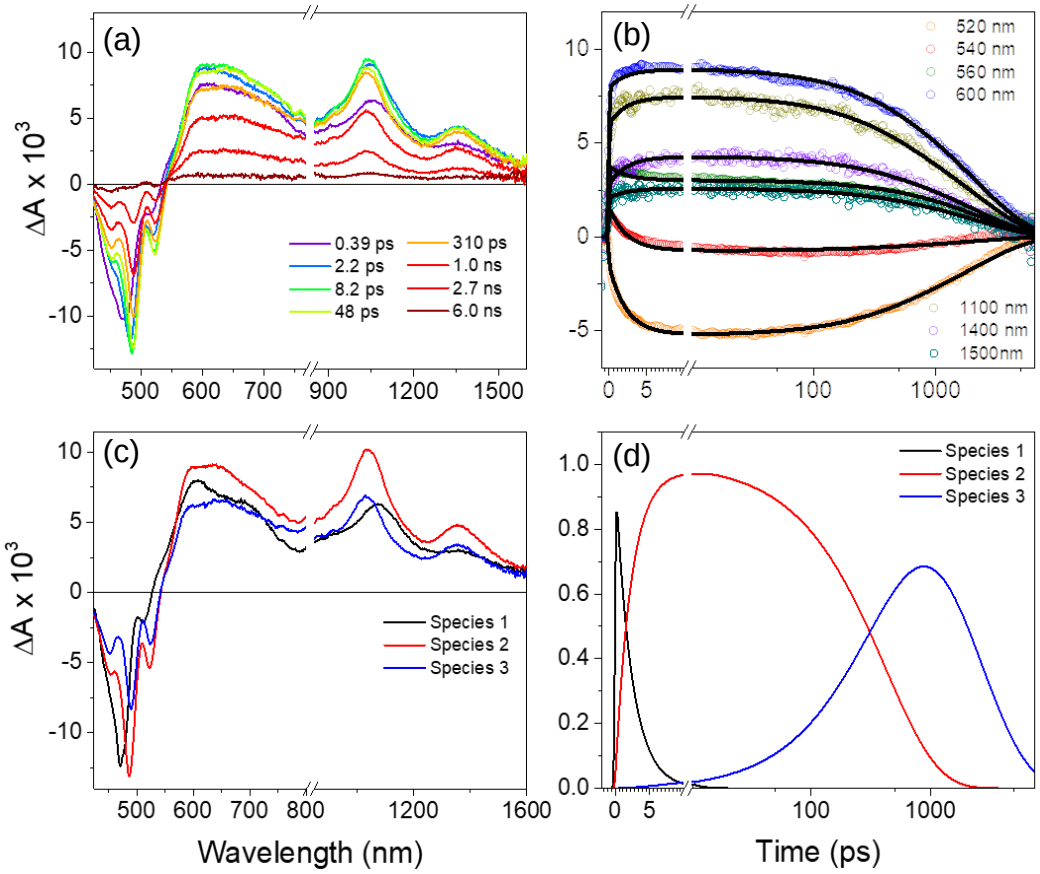

Figure 2.27. Global analysis of the (a) fsTA data for **2ph** in Tol for the time window of 7.4 ns. (b) Wavelength kinetic fits, (c) evolution-associated spectra and (d) population vs. time fits to a sequential A → B → C → GS model.

2.7.6 2ph DMF

In order to confirm the presence of symmetry breaking charge (SBCT) occurring in higher polarity solvent, we collected fsTA spectra of **2ph** in DMF. The early time features are similar to those observed in DCM and Tol; however, in the later time, there is a distinct new feature around 650nm which is assigned to anion feature due to spectral similarity to chemically reduced BPEA monomer.[101] By globally fitting the spectra using A→ B→ C→ GS, three times constants (τ_1 = 2.3 ± 0.3 ps), (τ_2 = 110 ± 3 ps), and (τ_3 = 7.7 ± 0.2 ns), are obtained. Species 1 is attributed to singlet

ESA whereas species 2 and 3 have both singlet ESA shown in the near infrared region and anion feature in the visible region. Thus, τ_1 and τ_2 are time constants for formation of SBCT species and τ_3 is decay time constant. Note that in both species 2 and 3 there is still a significant amount singlet excited state. This and high fluorescence quantum yield indicate that SBCT is a minor decay pathway in 2ph and most of the decay is via fluorescence. Presumably, there is a pseudoequilibrium between singlet excited state and CT state where the amount increases with polarity of the solvent.[35]

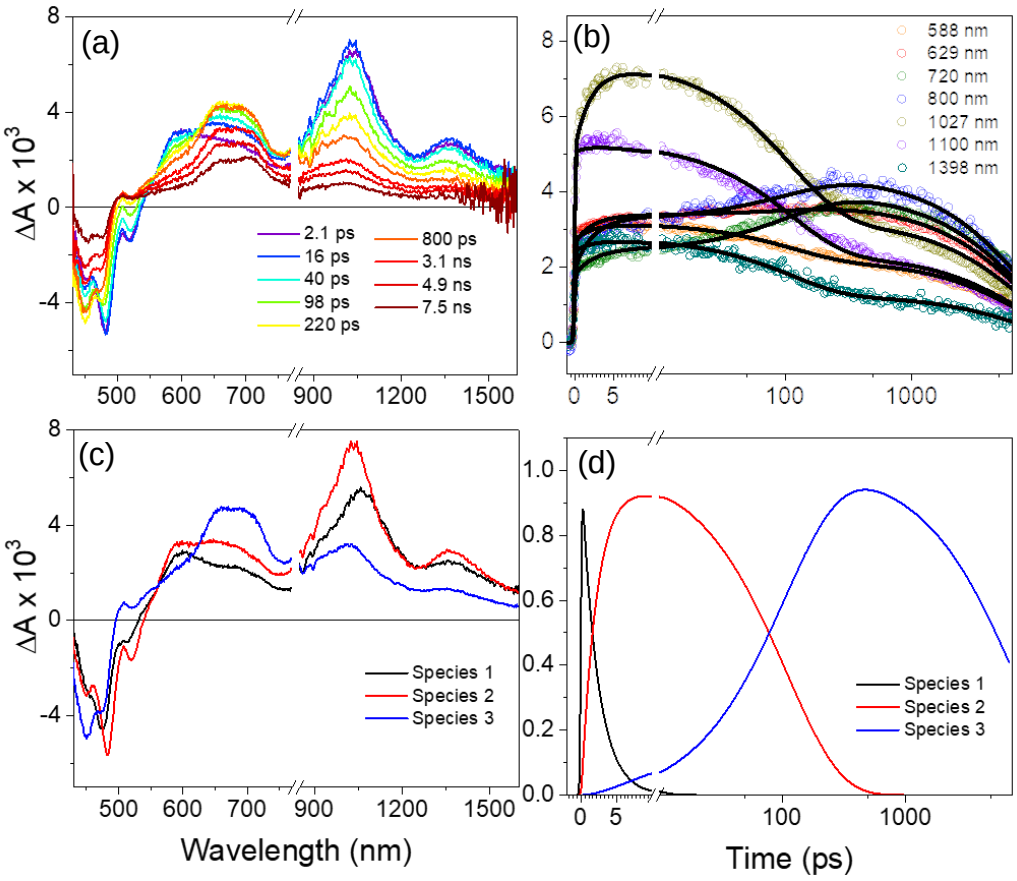

Figure 2.28. Global analysis of the (a) fsTA data for **2ph** in DMF for the time window of 7.4 ns. (b) Wavelength kinetic fits, (c) evolution-associated spectra and (d) population vs. time fits to a sequential A → B → C → GS kinetic model.

2.7.7 Details for calculation

Transfer integrals calculation

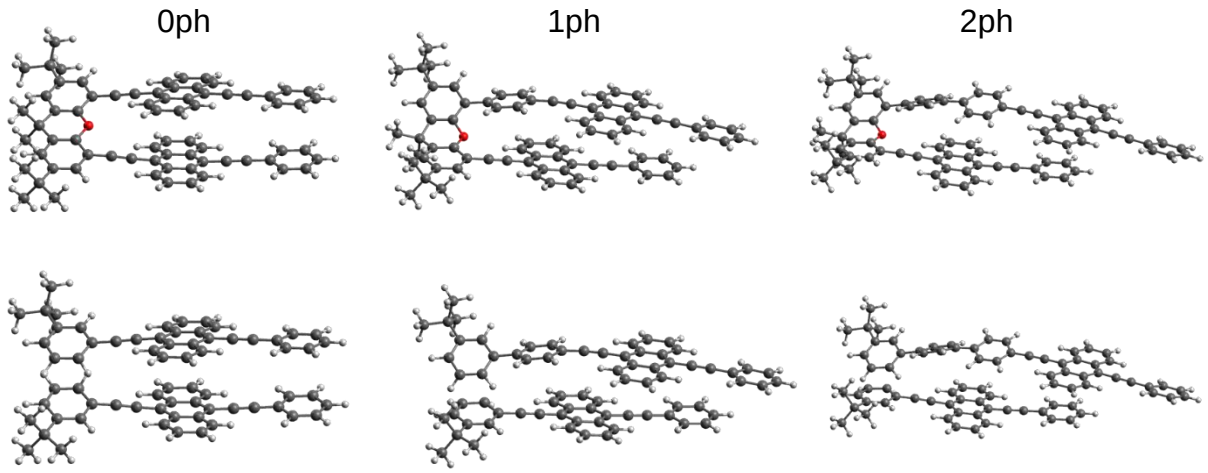

Figure 2.29. (Top) Geometry optimized BPEA dimers using B3LYP basis and Grimme3 dispersion correction functional. (Bottom) Fragmented BPEA dimers.

Table 2.6. The calculated matrix elements *S*, *J*, and *V*. All units are in meV.

(meV)	S_{HH}	S_{LL}	J_{HH}	J_{LL}	V_{HH}	V_{LL}
0ph	2.65	-9.85	-45.5	85.6	-31.5	59.6
1ph	5.36	-2.94	-59.7	25.3	-31.4	17.5
2ph	-8.35	-2.05	95.2	13.9	51	8.31

S_1 energy calculation using TDDFT

We calculated the S_1 energy of BPEA and PDI monomer (Figure S25) using QChem (version 5.0).[107] The optimized ground state geometry was performed using DFT and the excited state energies are calculated using TDDFT at the B3LYP/6-31G* level by specifying dielectric constant of DCM and Tol. The calculated S_1 energy for BPEA is 2.3448 eV in DCM and 2.3445 eV in Tol. For PDI monomer, the S_1 energy is 2.2324 eV in DCM and 2.2418 eV in Tol.

Charge transfer state energy calculation

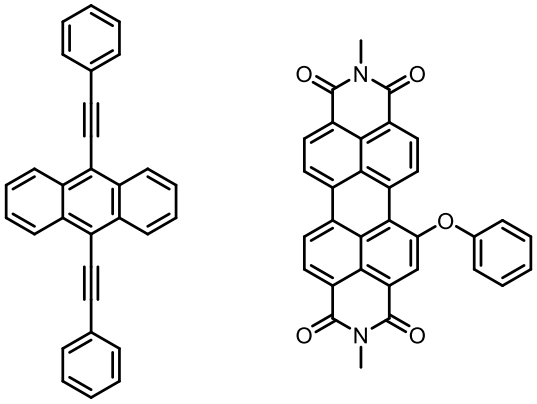

Figure 2.30. BPEA monomer and PDI-ref molecule used to calculate singlet point

Example input file for single-point energy of BPEA cation

Table 2.7. Single point energy of BPEA and PDI-ref in DCM and Tol. Energy units are in Hartree.

(Hartree)	BPEA DCM	BPEA Tol	PDI-ref DCM	PDI-ref Tol
Neutral	-1152.61	-1152.60	-1714.12	-1714.11
Cation	-1152.42	-1152.40	-1713.90	-1713.88
Anion	-1152.70	-1152.68	-1714.24	-1714.22
CT state	0.09105	0.1215	0.08239	0.1128
CT state (eV)	2.48	2.24	3.31	3.07

Example calculation of *E*(CT) of BPEA in DCM

E(Cation*) = *E*(cation)- *E*(Neutral)

E(Anion*) = *E*(Anion)-*E*(Neutral)

E(CT) = *E*(Cation*) + *E*(Anion*)

$molecule

1 2

C	-0.7102010571	-3.6721717266	-0.0011156782
C	-1.4000931783	-2.4874046998	-0.0009078810
C	-0.7189151155	-1.2337141551	-0.0006988810
C	0.7189070918	-1.2337142907	-0.0006927968
C	1.4000856003	-2.4874044755	-0.0008913759
C	0.7101938080	-3.6721717051	-0.0011066030
C	-1.4292323305	-0.0000668646	-0.0004931462
C	1.4292249804	-0.0000678482	-0.0004865439
C	0.7189075270	1.2335792018	-0.0003386371
C	-0.7189143391	1.2335792950	-0.0003394250
C	-1.4000932819	2.4872685748	-0.0001847549
H	-2.4847471201	2.4811024227	-0.0001932338
C	-0.7102016415	3.6720359680	-0.0000405404
C	0.7101932530	3.6720361382	-0.0000388752
C	1.4000856563	2.4872691048	-0.0001800650
H	-1.2495884931	-4.6154197212	-0.0012831363
H	-2.4847467051	-2.4812396676	-0.0009050427
H	2.4847392477	-2.4812388215	-0.0008756119
H	1.2495820878	-4.6154192201	-0.0012789395
H	-1.2495899147	4.6152834785	0.0000619672
H	1.2495811018	4.6152839089	0.0000746907
H	2.4847393513	2.4811038610	-0.0001933603
C	2.8475567490	-0.0000667211	-0.0003809090
C	4.0667623539	-0.0000571074	-0.0002826660
C	-2.8475638998	-0.0000642373	-0.0004004191
C	-4.0667694841	-0.0000630065	-0.0002963357
C	5.4898049063	-0.0000585874	-0.0001772065
C	6.2085187795	1.2135964477	0.0003300305

```
C       6.2085038649  -1.2137319488  -0.0005855611
C       7.6001042715   1.2084872825   0.0004218286
H       5.6623798485   2.1519392779   0.0006625223
C       7.6000832680  -1.2086427873  -0.0004833249
H       5.6623418891  -2.1520610245  -0.0009930356
C       8.3014621740  -0.0000802226   0.0000189638
H       8.1402604871   2.1513723724   0.0008126266
H       8.1402340778  -2.1515311555  -0.0007968788
H       9.3879193773  -0.0000933910   0.0000934407
C      -5.4898119595  -0.0000536139  -0.0001721793
C      -6.2085327970  -1.2137045344  -0.0005607286
C      -6.2085039714   1.2136238125   0.0003331451
C      -7.6001182784  -1.2085875206  -0.0004407802
H      -5.6623993219  -2.1520505266  -0.0009610819
C      -7.6000833636   1.2085425278   0.0004449397
H      -5.6623365908   2.1519497803   0.0006422539
C      -8.3014692551  -0.0000160705   0.0000614301
H      -8.1402798375  -2.1514695854  -0.0007429519
H      -8.1402287439   2.1514339767   0.0008383929
H      -9.3879264522   0.0000032687   0.0001506384
$end


$rem
jobtype        opt
method             PBE0
basis          6-31G*
THRESH                          14
SCF_CONVERGENCE 8
MAX_SCF_CYCLES    200
```

MEM_STATIC 10000

MEM_TOTAL 20000

GUI 2

solvent_method pcm

$end

$pcm

Theory CPCM

Method SWIG

Solver Inversion

Radii BONDI

$end

$solvent

Dielectric 38.25

OpticalDielectric 2.32288081

$end

Effective *J* calculation

We simulated the steady-state absorption spectra of the BPEA compounds using a previously described Frenkel-Holstein Hamiltonian formalism.[42] Briefly, the time-independent Hamiltonian for a dimer is written as follows:

$$H = \varepsilon_1 c_1^\dagger c_1 + \varepsilon_2 c_2^\dagger c_2 + J(c_1^\dagger c_2 + c_2^\dagger c_1) + \omega_0 b_1^\dagger b_1 \qquad \text{(eq. 2.4)}$$

$$+\omega_0 b_2^\dagger b_2 + \omega_0 \sum_{n=1,2} c_n^\dagger c_n [\lambda(b_n^\dagger + b_n) + \lambda^2]$$

where ε_n represents the electronic transition energy of chromophore *n* in the dimer, $c_n^{(\dagger)}$ and $b_n^{(\dagger)}$ are the fermionic and vibrational annihilation (creation) operators, respectively, of chromophore *n*, J is the effective excitonic coupling value, ω_0 is the frequency of the vibration, and λ^2 is the Huang-Rhys factor. $\hbar$ is taken to equal unity in Equation S1. We restricted the number of vibrational quanta within the system to a maximum of 10 to ease computational effort while still capturing transitions to higher-lying vibronic states.

The transition dipole operator is described as:

$$\mu(\tau_i) = \sum_{n=1,2} \mu_n^E (c_n^\dagger + c_n) \qquad \text{(eq. 2.5)}$$

where τ_i reflects the time after optical interaction *i*, and μ_n^E reflects the magnitude of the interaction with the electric field with chromophore *n*. We do not extract meaning from the latter parameter due to normalization of the computed and experimental spectra. Assuming the system begins in the ground vibrational state, the linear response involving two optical field interactions (at times τ_1 and τ_2) is expressed as:

$$R(\tau) = \left\langle 0 \middle| \mu(\tau_2) U(\tau_2, \tau_1) \mu(\tau_1) \middle| 0 \right\rangle \qquad \text{(eq. 2.6)}$$

where free propagation under the system Hamiltonian is captured by the operator *U*.

$$U(\tau) = \exp(-iH\tau) \qquad \text{(eq. 2.7)}$$

Spectral linewidths were imposed by multiplying the time-domain linear response by a Gaussian windowing function. The absorption spectrum was obtained via fast Fourier transformation of equation S3 after windowing.

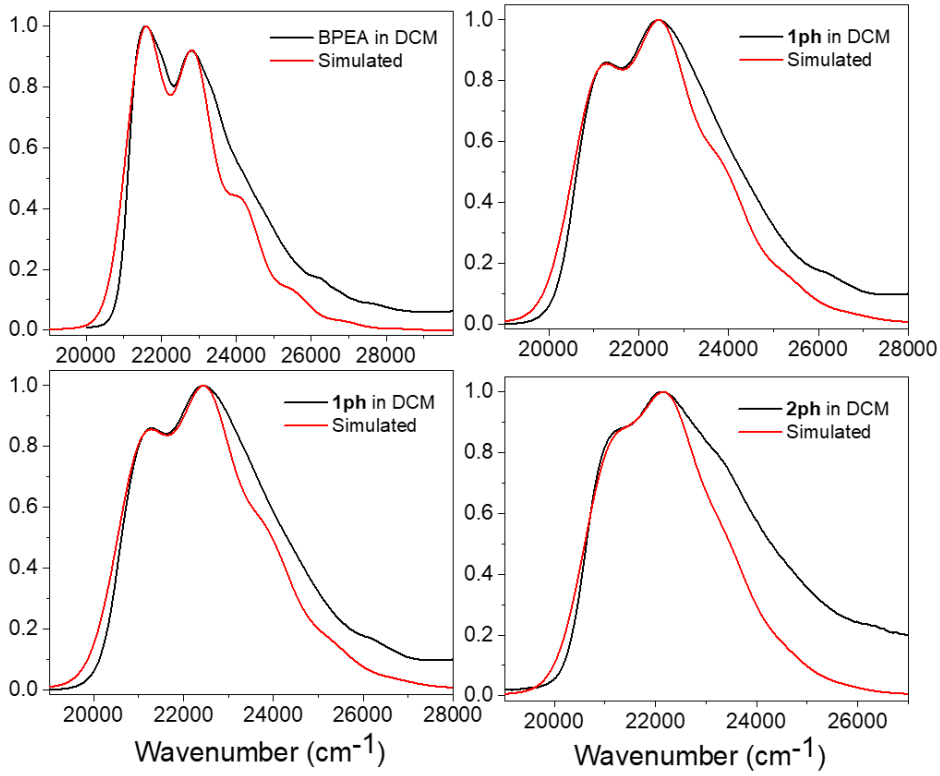

Figure 2.31. Simulated absorbance spectra of BPEA monomer and dimers in DCM

Table 2. 8. J_{Coulb} and J_{CT} of BPEA dimers in DCM

	J (cm^{-1})	J_{Coulb} (cm^{-1})	J_{CT} (cm^{-1})
0ph	420	190	230
1ph	230	173	67
2ph	200	251	-51

Coulomb coupling in BPEA and DPP crystals

The Coulomb coupling J_{coulb} is calculated by using the following equation under the point-dipole approximation:[87, 108]

$$J_{Coulb} = \frac{\mu^2(1 - 3\cos^2\theta)}{4\pi\varepsilon R^3} \qquad (eq.\ 2.8)$$

Here, the parameters defining the relative orientation between the two molecules, R and θ are obtained from the reported crystal structures of DPP[22] and BPEA[35] and the values are shown in Table S5. The same dimer is used to calculate the HOMO-HOMO and LUMO-LUMO coupling. The previously reported transition dipole moments, μ of BPEA (4.05 D)[109] and DPP (5.6 D)[110] are used to calculate J_{coulb},

Table 2.9. The relative orientation between the two molecules, R and θ in BPEA and DPP crystals

	BPEA C2/*c*	BPEA P*bcn*	C6 DPP	Me DPP	TEG DPP	Ph DPP
R (nm)	0.5357	0.4866	0.5391	0.4906	0.7285	0.6257
θ (°)	85.7	81.6	41.4	48.9	30.1	34.0
J_{coulb} (cm^{-1})	401	510	-692	-400	-510	-685

Excimer eigenstates calculation

The coefficients a and b are calculated by diagonalizing the 4x4 matrix, as shown in the top 5 rows in the below table, using the eig function in MATLAB. The 4 eigenstates are shown in the bottom rows followed by the corresponding eigenvalues, which are excimer state energy shown in the last row.

For BPEA covalent dimers, each component is calculated in this work and is thoroughly described above. For PDI covalent dimers only the S_1 and CT energies are calculated in this work and other components are from the previous work.[89] For BPEA and DPP solid-state systems, only J_{Coulb} is calculated in this work and the rest of values are calculated in previous work.[35, 102]

Sample (cm^{-1})	S0S1	S1S0	CA	AC
S0S1	$E(S_1)$	J_{Coulb}	V_{HH}	V_{LL}
S1S0	J_{Coulb}	$E(S_1)$	V_{LL}	V_{HH}
CA	V_{HH}	V_{LL}	E(CT)	0
AC	V_{LL}	V_{HH}	0	E(CT)
eigenstates				
	Excimer 1	Excimer 2	Excimer 3	Excimer 4
Sample	S0S1	S1S0	CA	AC
S0S1	a(Ex1)	a(Ex2)	a(Ex3)	a(Ex4)
S1S0	a(Ex1)	a(Ex2)	a(Ex3)	a(Ex4)
CA	b(Ex1)	b(Ex2)	b(Ex3)	b(Ex4)
AC	b(Ex1)	b(Ex2)	b(Ex3)	b(Ex4)
eigenvalues				
Sample (eV)	E(Ex1)	E(Ex2)	E(Ex3)	E(Ex4)

0ph DCM

0ph (cm^{-1})	S0S1	S1S0	CA	AC
S0S1	18911	191	-254	481
S1S0	191	18911	481	-254
CA	-254	481	19977	0
AC	481	-254	0	19977
eigenstates				
	Excimer 1	Excimer 2	Excimer 3	Excimer 4
0ph	S0S1	S1S0	CA	AC
S0S1	0.6422	0.687	0.1676	0.2958
S1S0	-0.6422	0.687	0.1676	-0.2958
CA	0.2958	-0.1676	0.687	-0.6422
AC	-0.2958	-0.1676	0.687	0.6422
eigenvalues				
0ph (eV)	2.2792	2.3616	2.4839	2.519

0ph Tol

0ph (cm^{-1})	S0S1	S1S0	CA	AC
S0S1	18909	456	-254	481
S1S0	456	18909	481	-254
CA	-254	481	26676	0
AC	481	-254	0	26676
eigenstates				
	Excimer 1	Excimer 2	Excimer 3	Excimer 4
0ph	S0S1	S1S0	CA	AC
S0S1	-0.7043	-0.7068	0.0219	0.0625
S1S0	0.7043	-0.7068	0.0219	-0.0625
CA	-0.0625	0.0219	0.7068	-0.7043
AC	0.0625	0.0219	0.7068	0.7043
eigenvalues				
0ph (eV)	2.2802	2.4005	3.3085	3.3157

1ph DCM

1ph (cm^{-1})	S0S1	S1S0	CA	AC
S0S1	18911	173	-253	141
S1S0	173	18911	141	-253
CA	-253	141	19977	0
AC	141	-253	0	19977
eigenstates				
	Excimer 1	Excimer 2	Excimer 3	Excimer 4
1ph	S0S1	S1S0	CA	AC
S0S1	0.6789	0.7018	-0.0867	0.1976
S1S0	-0.6789	0.7018	-0.0867	-0.1976
CA	0.1976	0.0867	0.7018	-0.6789
AC	-0.1976	0.0867	0.7018	0.6789
eigenvalues				
1ph (eV)	2.3092	2.3646	2.4787	2.4912

1ph Tol

1ph (cm^{-1})	S0S1	S1S0	CA	AC
S0S1	18909	250	-253	141
S1S0	250	18909	141	-253
CA	-253	141	26676	0
AC	141	-253	0	26676
eigenstates				
	Excimer 1	Excimer 2	Excimer 3	Excimer 4
1ph	S0S1	S1S0	CA	AC
S0S1	0.7063	0.707	-0.0105	0.0346
S1S0	-0.7063	0.707	-0.0105	-0.0346
CA	0.0346	0.0105	0.707	-0.7063
AC	-0.0346	0.0105	0.707	0.7063
eigenvalues				
1ph (eV)	2.3114	2.3756	3.3078	3.31

2ph DCM

2ph (cm^{-1})	S0S1	S1S0	CA	AC
S0S1	18911	252	411	67
S1S0	252	18911	67	411
CA	411	67	19977	0
AC	67	411	0	19977
eigenstates				
	Excimer 1	Excimer 2	Excimer 3	Excimer 4
2ph	S0S1	S1S0	CA	AC
S0S1	-0.6867	-0.6419	-0.1685	0.2965
S1S0	0.6867	-0.6419	0.1685	0.2965
CA	0.1685	0.2965	-0.6867	0.6419
AC	-0.1685	0.2965	0.6867	0.6419
eigenvalues				
2ph (eV)	2.3031	2.3487	2.4875	2.5044

2ph Tol

2ph (cm^{-1})	S0S1	S1S0	CA	AC
S0S1	18909	192	411	67
S1S0	192	18909	67	411
CA	411	67	26676	0
AC	67	411	0	26676
eigenstates				
	Excimer 1	Excimer 2	Excimer 3	Excimer 4
2ph	S0S1	S1S0	CA	AC
S0S1	-0.7065	0.7057	0.0305	0.0444
S1S0	0.7065	0.7057	-0.0305	0.0444
CA	0.0305	-0.0444	0.7065	0.7057
AC	-0.0305	-0.0444	-0.7065	0.7057
eigenvalues				
2ph (eV)	2.3192	2.3649	3.3095	3.3114

C2/c BPEA solid-state sample

C2/c (cm^{-1})	S0S1	S1S0	CA	AC
S0S1	20485	401	-404	968
S1S0	401	20485	968	-404
CA	-404	968	28308	0
AC	968	-404	0	28308
eigenstates				
	Excimer 1	Excimer 2	Excimer 3	Excimer 4
C2/c	S0S1	S1S0	CA	AC
S0S1	0.698	0.7051	0.0533	0.1134
S1S0	-0.698	0.7051	0.0533	-0.1134
CA	0.1134	-0.0533	0.7051	-0.698
AC	-0.1134	-0.0533	0.7051	0.698
eigenvalues				
C2/c (eV)	1.9861	2.0843	2.8351	2.8531

Pbcn BPEA solid-state

Pbcn (cm^{-1})	S0S1	S1S0	CA	AC
S0S1	20888	510	494	-94
S1S0	510	20888	-94	494
CA	494	-94	28227	0
AC	-94	494	0	28227
eigenstates				
	Excimer 1	Excimer 2	Excimer 3	Excimer 4
Pbcn	S0S1	S1S0	CA	AC
S0S1	0.7052	-0.7059	0.0412	-0.0525
S1S0	-0.7052	-0.7059	0.0412	0.0525
CA	-0.0525	0.0412	0.7059	-0.7052
AC	0.0525	0.0412	0.7059	0.7052
eigenvalues				
Pbcn (eV)	2.0334	2.1375	2.825	2.8271

Me - DPP

Me (cm^{-1})	S0S1	S1S0	CA	AC
S0S1	17984	-400	126	975
S1S0	-400	17984	975	126
CA	126	975	22662	0
AC	975	126	0	22662
eigenstates				
	Excimer 1	Excimer 2	Excimer 3	Excimer 4
Me	S0S1	S1S0	CA	AC
S0S1	-0.6924	-0.6945	0.1328	-0.1437
S1S0	-0.6924	0.6945	-0.1328	-0.1437
CA	0.1437	-0.1328	-0.6945	-0.6924
AC	0.1437	0.1328	0.6945	-0.6924
eigenvalues				
Me (eV)	2.152015	2.259392	2.830006	2.83819

C6 - DPP

C6 (cm^{-1})	S0S1	S1S0	CA	AC
S0S1	17984	-692	1282	1596
S1S0	-692	17984	1596	1282
CA	1282	1596	23469	0
AC	1596	1282	0	23469
eigenstates				
	Excimer 1	Excimer 2	Excimer 3	Excimer 4
C6	S0S1	S1S0	CA	AC
S0S1	0.658	0.7056	0.046	0.259
S1S0	0.658	-0.7056	-0.046	0.259
CA	-0.259	0.046	-0.7056	0.658
AC	-0.259	-0.046	0.7056	0.658
eigenvalues				
C6 (eV)	2.003596	2.313205	2.912461	3.050465

TEG -DPP

TEG (cm^{-1})	S0S1	S1S0	CA	AC
S0S1	17984	-509	-197	-666
S1S0	-509	17984	-666	-197
CA	-197	-666	26453	0
AC	-666	-197	0	26453
eigenstates				
	Excimer 1	Excimer 2	Excimer 3	Excimer 4
TEG	S0S1	S1S0	CA	AC
S0S1	0.7039	0.7059	0.0414	-0.067
S1S0	0.7039	-0.7059	-0.0414	-0.067
CA	0.067	-0.0414	0.7059	0.7039
AC	0.067	0.0414	-0.7059	0.7039
eigenvalues				
TEG (eV)	2.156603	2.289523	3.283447	3.290143

Ph - DPP

Ph (cm^{-1})	S0S1	S1S0	CA	AC
S0S1	16452	-686	435	-330
S1S0	-686	16452	-330	435
CA	435	-330	20404	0
AC	-330	435	0	20404
eigenstates				
	Excimer 1	Excimer 2	Excimer 3	Excimer 4
Ph	S0S1	S1S0	CA	AC
S0S1	0.7069	-0.6902	-0.016	-0.1537
S1S0	0.7069	0.6902	-0.016	0.1537
CA	-0.016	0.1537	-0.7069	-0.6902
AC	-0.016	-0.1537	-0.7069	0.6902
eigenvalues				
Ph (eV)	2.423559	2.608679	3.13726	3.163174

Bis-PBI1

PBI1 (cm^{-1})	S0S1	S1S0	CA	AC
S0S1	18004	678	428	66
S1S0	678	18004	66	428
CA	428	66	18082	0
AC	66	428	0	18082
eigenstates				
	Excimer 1	Excimer 2	Excimer 3	Excimer 4
PBI1	S0S1	S1S0	CA	AC
S0S1	-0.6562	0.3467	0.2635	0.6163
S1S0	0.6562	0.3467	-0.2635	0.6163
CA	0.2635	-0.6163	0.6562	0.3467
AC	-0.2635	-0.6163	-0.6562	0.3467
eigenvalues				
PBI1 (eV)	2.1303	2.2076	2.2601	2.3509

Bis-PBI2

PBI2 (cm^{-1})	S0S1	S1S0	CA	AC
S0S1	18004	554	547	697
S1S0	554	18004	697	547
CA	547	697	18082	0
AC	697	547	0	18082
eigenstates				
	Excimer 1	Excimer 2	Excimer 3	Excimer 4
PBI2	S0S1	S1S0	CA	AC
S0S1	0.4506	0.6898	0.1554	0.545
S1S0	0.4506	-0.6898	-0.1554	0.545
CA	-0.545	0.1554	-0.6898	0.4506
AC	-0.545	-0.1554	0.6898	0.4506
eigenvalues				
PBI2 (eV)	2.1145	2.1595	2.2462	2.4286

Bis-PBI3

PBI3 (cm^{-1})	S0S1	S1S0	CA	AC
S0S1	18004	545	675	658
S1S0	545	18004	658	675
CA	675	658	18082	0
AC	658	675	0	18082
eigenstates				
	Excimer 1	Excimer 2	Excimer 3	Excimer 4
PBI3	S0S1	S1S0	CA	AC
S0S1	0.4548	0.7068	-0.0193	0.5414
S1S0	0.4548	-0.7068	0.0193	0.5414
CA	-0.5414	-0.0193	-0.7068	0.4548
AC	-0.5414	0.0193	0.7068	0.4548
eigenvalues				
PBI3 (eV)	2.1032	2.1647	2.2421	2.4388

2.7.8 Triplet sensitization

In order to obtain the range of the triplet excited state energy E(T_1), two triplet sensitizers, $PdPc(Obu)_8$ and Pd- **NDP** were used. There was no sign of triplet energy transfer from $PdPc(Obu)_8$ which has triplet energy of 1.12 eV;[111] however, there is a triplet energy transfer from Pd-**NDP** which has a triplet energy of 1.30 eV (**Figure 2.32**).[104]

Solutions of BPEA dimers and Pd-**NDP** were selectively excited using 560 nm (Figure S26). Upon the excitation of the porphyrin, singlet excited-state absorption (ESA) is observed at early times which then changes as the population undergoes intersystem crossing with the rate of $(2.5 \pm 0.2\ ps)^{-1}$ to create ^{3*}Pd-**NDP**. Triplet energy transfer then occurs via diffusion and the triplet ESA of BPEA dimers is observed after few μs in the spectral region of 350 nm to 530 nm.

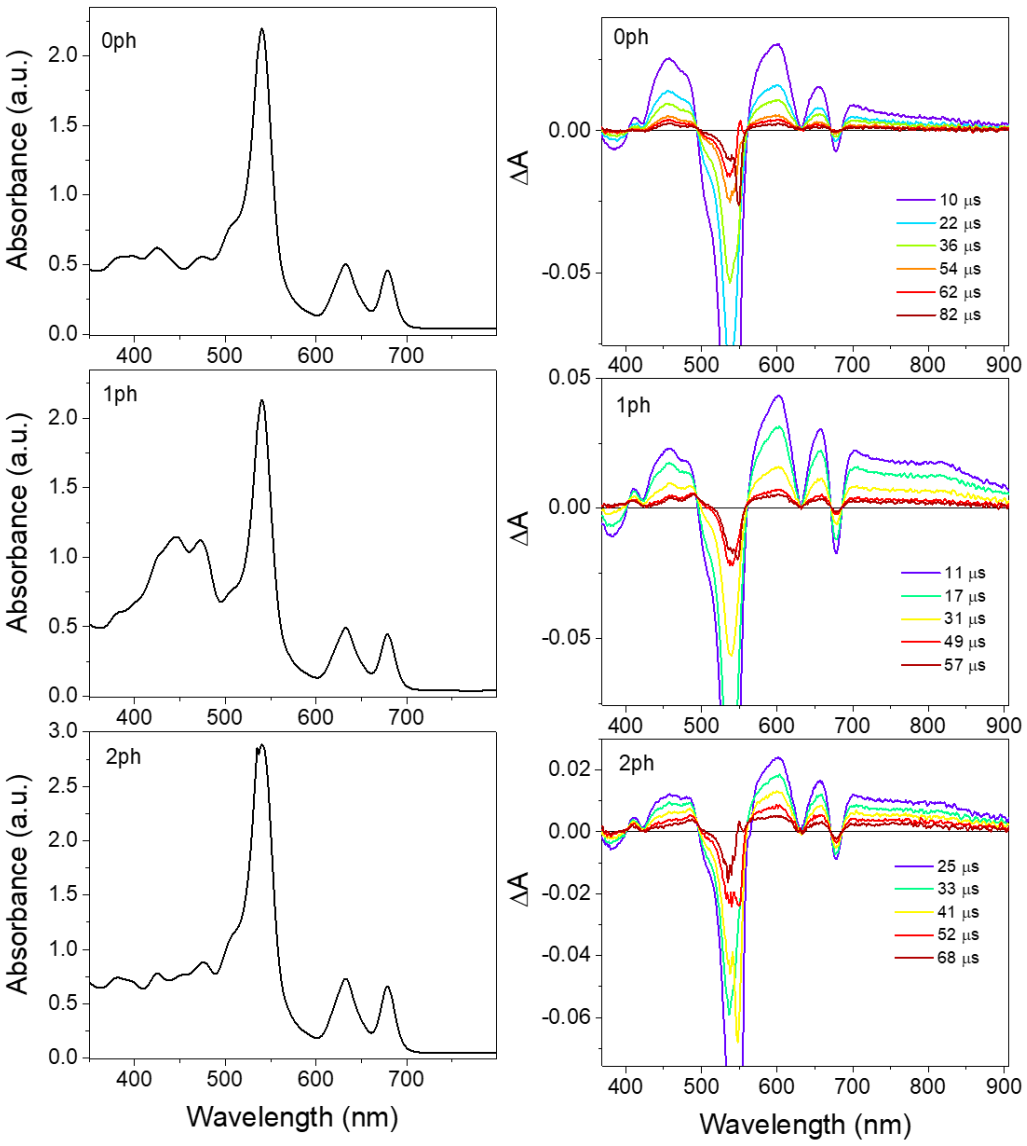

Figure 2.32. Steady-state absorbance and fsTA spectra of BPEA dimers mixed with triplet sensitizer, Pd-**NDP** in deoxygenated DCM excited at 560 nm (1μJ/pulse).

Chapter 3. Design Principles for Efficient Singlet Fission in Solid State 9,10-Bis (phenylethynyl)anthracene

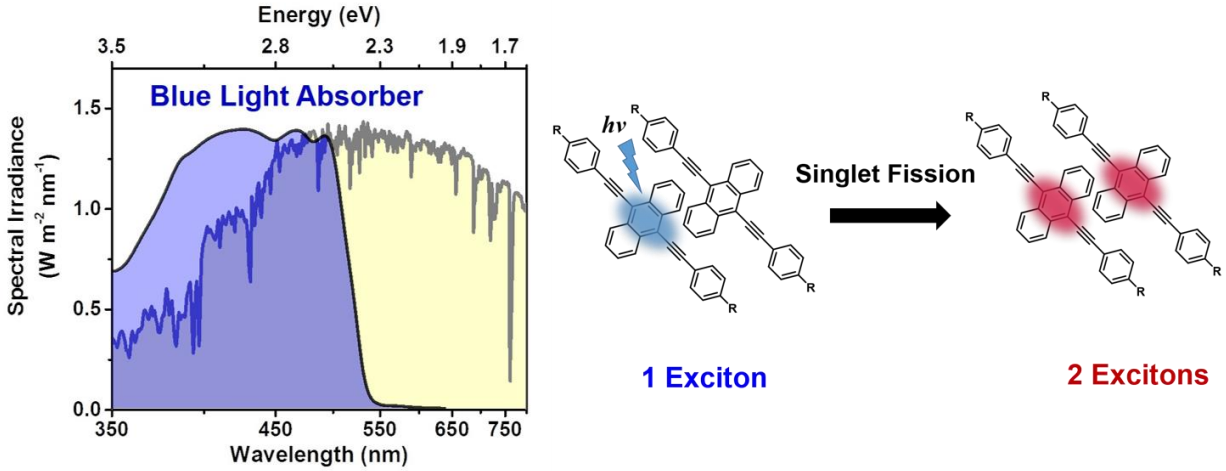

The result of this chapter is published in and adapted with permission from *J. Am. Chem. Soc.* **2018**, 140, 45, 15140–15144. Copyright 2018 American Chemical Society. Partly reproduced from *J. Chem. Phys*. **2019**, 151, 044501, with the permission of AIP Publishing and from Proc. SPIE. 11084, Physical Chemistry of Semiconductor Materials and Interfaces XVIII, 110840Q 2019. Copyright 2019 Society of Photo-Optical Instrumentation Engineers (SPIE).

Conference presentation is stored here: https://www.spiedigitallibrary.org/conference-proceedings-of-spie/11084/110840Q/Design-principles-for-efficient-singlet-fission-in-anthracene-based-organic/10.1117/12.2527346.short?webSyncID=ce46e9e6-ec7a-49da-b6a0-cbad059329ad&sessionGUID=883c9d90-2bc9-993c-ed26-8bead49a2853&SSO=1

3.1 Introduction

Singlet fission (SF) is a multiple exciton generation process in organic semiconductors where a singlet exciton, generated via photon absorption, energetically down-converts into two triplet excitons.[112] Over the past decade, SF chromophores have attracted renewed attention because of their ability to overcome the Shockley–Quiesser limit on the theoretical efficiency of single-junction solar cells by mitigating thermalization losses.[13] Specifically, down-converted low energy triplet excitons can be harvested by either energy transfer or charge transfer to single junction solar cells, which then increases the closed-circuit current.[39] Previous studies have demonstrated Dexter type energy transfer from two triplet excitons in tetracene and pentacene to lead-based quantum dots and silicon solar cell.[28, 113, 114] Charge transfer from the triplet exciton is also possible if the SF chromophores are paired with a suitable electron acceptor or donor; for example, a solar cell using pentacene coupled with C_{60} achieved an external quantum efficiency of 133 %.[25] Recently, triplet exciton transfer from tetracene to a silicon single junction cell has been demonstrated, where of the 133% exciton transfer from the tetracene layer to Si, 56 % comes from singlet excitons and 76 % from triplet excitons.[28] Such competition between singlet and triplet exciton transfer exists as a result of the slow SF rate in tetracene. Thus, it is crucial to discover SF materials that have high triplet energies, ideally greater than a band gap of 1.1- 1.3 eV, with fast SF rates.

Although anthracene has been demonstrated to undergo SF,[6] SF is only viable from higher lying singlet excited state because of its high triplet energy (1.8 eV). In anthracene crystals, SF is competitive with internal conversion and thus SF efficiency is extremely low (3%). However, functionalization of anthracene with phenylethynyl groups at 9,10 positions to form BPEA

achieves better energetics for SF. This modification lowers the triplet energy to ~1.20 eV while maintaining the singlet energy at ~ 2.40 eV in solid-state thin film.[35] In addition, BPEA is a robust, industrial dye with excellent thermal and photo-stability,[115-117] and and versatile synthetic modularity.[117, 118] Here, we summarize the packing structure dependent SF dynamics of BPEA and its derivatives in the solid-state using time-resolved optical spectroscopies, and electronic structure calculations. The SF rate and efficiency for organic chromophores in the solid state depend on interchomophore electronic coupling, which in turn, depends on the crystal morphology. The role of coupling becomes more critical in cases where SF is either isoergic or somewhat endoergic. For example, perylenediimide (PDI) structures that undergo facile SF have about a 3 Å slippage along the N-N long-axis direction of the PDIs resulting in high SF yields even though the process is endoergic by about 0.2 eV.[59, 119] In tetracene systems, which are also endoergic by about 0.2 eV, efficient SF is observed when slippage occurs either in the long- or short-axis directions with weaker π-π interactions.[120] Similar behavior is observed for diketopyrrolopyrroles, where SF is isoergic and may be mediated by an excimer state having significant CT character.[22, 121] In contrast, for systems wherein SF is exoergic, such as pentacenes[122-128] and terrylenediimides,[20, 52, 129-131] a wider variety of interchromophore geometries leads to highly efficient SF. We systematically control molecular packing of BPEA by changing the composition of polymorphs and adding functional groups at the *para* position of the phenyls (**Scheme 3.1**). Such changes in molecular structure result in different packing, ultimately modulating both the electronic coupling and thermodynamic driving force.

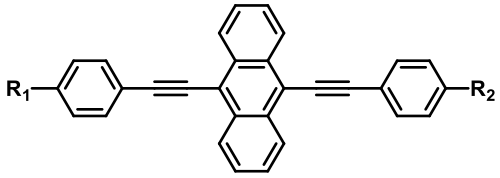

	R_1	R_2
BPEA	H	H
F_2	F	F
FOMe	F	OMe
$(OMe)_2$	OMe	OMe

Scheme 3.1. The BPEA derivatives used in this study.

3.2 Experimental Details

3.2.1 Synthesis

All chemicals were obtained from commercial suppliers and used as received unless otherwise noted. BPEA polycrystalline solid was purchased from Sigma Aldrich and was used without further purification Column chromatography was performed using silica gel from Sorbent Technologies. ^{1}H NMR spectra were recorded at ambient temperature at 500 MHz. Chemical shifts are reported in ppm relative to TMS. NMR resonance multiplicities are reported with the following abbreviations: s = singlet, d = doublet, and m = multiplet, and coupling constants are reported in Hz. High Resolution Mass Spectra (HRMS) were obtained with an Agilent LCTOF 6200 series mass spectrometer using electrospray ionization (ESI) and APPI.

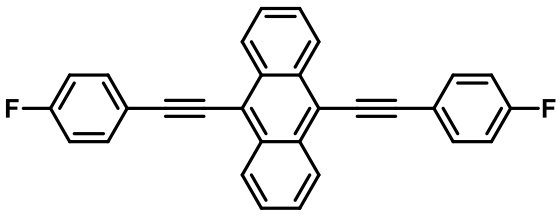

F_2-BPEA. 9,10-Dibromoanthracene (0.50 g, 1.5 mmol), 1-ethynyl-4-fluorobenzene (0.48 g, 0.46 mL, 4 mmol), CuI (0.14 g, 0.75 mmol), and diisopropylamine (15 mL) were added to THF (15 mL) in a dry round bottomed flask. The solution was degassed with $N_{2(g)}$ for 10 minutes. $Pd(PPh_3)_2Cl_2$ (0.09 g, 0.13 mmol) was added, and the solution was degassed for an additional 10 minutes. The solution was then stirred over night at 80 °C under a $N_{2(g)}$ atmosphere. The solvent was removed by rotary evaporation, and the crude material was purified by chromatography on silica gel (25% DCM in hexanes). Compound **F_2-BPEA** was obtained in 19% yield (0.163 g). ^{1}H NMR (500 MHz, $CDCl_3$, δ): 8.65 (dd, *J* = 6.6, 3.3 Hz, 4H), 7.74 (dd, *J* = 8.7, 5.4 Hz, 3H), 7.63 (dd, *J* = 6.7, 3.2 Hz, 4H), 7.14 (dd, *J* = 8.6, 8.6 Hz, 4H). ESI-HRMS (*m/z*): calculated for $C_{30}H_{16}F_2$ M^+: 414.1220, found: 415.1293 $(M+H)^+$.

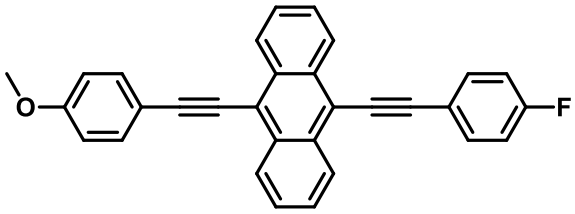

FOMe-BPEA. 9,10-Dibromoanthracene (0.67 g, 2.0 mmol), 4-ethynylanisole (0.28 g, 0.27 mL, 2.1 mmol), 1-ethynyl-4-fluorobenzene (0.25 g, 0.24 mL, 2.1 mmol), CuI (0.198 g, 1.04 mmol), and diisopropylamine (20 mL) were added to THF (20 mL) in a dry round bottomed flask. The solution was degassed with $N_{2(g)}$ for 10 minutes. $Pd(PPh_3)_2Cl_2$ (0.112 g, 0.16 mmol) was added, and the solution was degassed for an additional 10 minutes. The solution was then stirred over night at 80 °C under a $N_{2(g)}$ atmosphere. The solvent was removed by rotary evaporation, and the crude material was purified by chromatography on silica gel (15% DCM in hexanes). **FOMe-BPEA** was obtained in 19% yield (0.163 g). ^{1}H NMR (500 MHz, $CDCl_3$, δ): 8.72 – 8.59 (m, 4H), 7.74 (dd, *J* = 8.8, 5.3 Hz, 2H), 7.70 (d, *J* = 8.8 Hz, 2H), 7.64 – 7.59 (m, 4H), 7.14 (dd, *J* = 8.7, 8.7

Hz, 2H), 6.97 (d, *J* = 8.7 Hz, 2H), 3.87 (s, 3H). ESI-HRMS (*m/z*): calculated for $C_{31}H_{19}FO$ M^+: 426.4904, found: 427.1493 $(M+H)^+$.

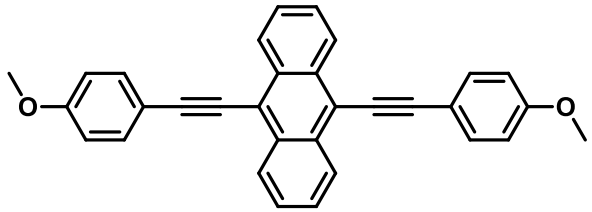

(OMe)$_2$-BPEA was prepared as described in *Chem. Sci.*, **2016**, *7*, 370.

3.2.2 Single crystal structure and x-ray spectroscopy

The crystal structure of **BPEA** has been reported previously. Crystals of **F$_2$-** and **FOMe-BPEA** were grown by slow solvent evaporation of each compound from chloroform solutions. The crystals were mounted on a polymer loop with Paratone oil, and the data were collected at 100 K on a Bruker Kappa APEX II CCD diffractometer equipped with a Cu Kα 1 μS microfocus source with MX optics. The data were absorption-corrected using SADABS. The structure was solved using SHELXT and refined using SHELXL using Olex 2 software.[132] The structures have been deposited in the Cambridge Crystallographic Data Centre database. CCDC number for **F$_2$** is 1909837 and for **FOMe** is 1907242.

3.2.3 Film preparation details

Thin film samples were deposited on sapphire substrates at room temperature at a rate of 0.2 Å/s in a vacuum thermal evaporator (Denton Vacuum DV502-A), followed by solvent-vapor annealing using CH_2Cl_2 overnight. Film thicknesses were measured at 10 different spots with a Veeco Dektak 150 surface profilometer with a 5.0 μm diameter stylus.

3.2.4 Steady-state spectroscopy

Steady-state absorption spectra of the solution samples were measured using a Shimadzu UV-1800 spectrometer and scatter-corrected spectra of the film samples were measured using a Shimadzu UV-3600 UV/Vis/NIR spectrometer equipped with an integrating sphere. Steady-state fluorescence spectra of solution and film samples were measured in the front-face mode with a HORIBA Nanolog spectrofluorimeter equipped with an integrating sphere (Horiba Quanta - φ) for absolute fluorescence quantum yield determination.

3.2.5 Triplet energies

Two different triplet sensitizers, palladium octabutoxyphthalocyanine, $PdPc(OBu)_8$[111] and Pd-NDP (Fig. S2),[133] $E(T_1)$ = 1.12 eV and 1.30 eV, respectively, were used to determine the triplet energy of the BPEA derivatives in solution. The synthesis and photophysical properties of $PdPc(OBu)_8$ were reported in previous studies. To determine the triplet spectra in thin films, CH_2Cl_2 solutions containing **BPEA** and its deriatives and $PdPc(OBu)_8$ (9:1 weight ratio) at a concentration of 15 mg/mL were spin-coated at 1000 rpm. **Figure 3.6** shows the steady-state absorption spectra and excited-state dynamics of the sensitized films. In order to confirm triplet formation in the thin films and estimate their triplet energies, oxygen ($E(S_1)$ = 0.98 eV) was also used as a triplet energy acceptor.

3.2.6 Transient absorption spectroscopy

FsTA experiments on the thin films were performed using 14 nJ, 414 nm, 100 fs excitation pulses generated by a 100 kHz repetition rate laser system described in detail previously,[22] but with a few modifications needed to probe 390-490 nm. The 414 nm pump pulse was generated by a non-collinear parametric amplifier (Spirit NOPA 2H, Spectra Physics), which was seeded by 1.25 W from a Spirit amplifier (4 W, 300 fs, Spirit 1040-4, Spectra Physics). Before reaching the sample, the pump was chopped at 50 kHz and was focused to a 1 mm spot size at the sample using

a pinhole. The visible–NIR continuum was generated as previously described;[134] however, this study also required a UV-visible continuum probe. This UV-visible continuum was generated using the remaining ~2.75 W of Spirit 1040 nm output focused into a β-barium borate crystal (Type I at 1040 nm, 1.5 mm thick, Eksma Optics) to generate 520 nm pulses, which were then used to drive white light generation. The residual 1040 nm fundamental was removed using a 1000 nm short-pass filter (SPF) before the 520 nm beam was focused into a 5 mm yttrium aluminum garnet (YAG) crystal to generate a continuum from 390 – 580 nm. This continuum was truncated by a 500 nm SPF to remove the residual 520 nm pump light before being focused onto the sample. Detection was carried out with a lab-built spectrometer and 100 kHz CMOS line camera as described previously.[22] The 420-490 nm continuum from this set-up combined with the 490-800 nm continuum generated using 1040 nm allowed probing over a broad spectral range. Nanosecond transient absorption (nsTA) spectroscopy was performed with a 7 ns, 416 nm laser pulse at 10 Hz repetition rate. Details of the apparatus are given elsewhere.[19]

3.2.7 Data processing and global analysis

The TA data were subjected to global kinetic analysis to obtain the evolution- and decay-associated spectra respectively, and kinetic parameters as described in detail previously.[130]

3.2.8 Computational details

The electronic couplings were calculated from the integral matrix elements using the Amsterdam Density Functional (ADF) package[93] at the density functional level of theory (DFT). The triple ζ with two polarization functions (TZ2P) basis set and the B3LYP exchange-correlation functional were chosen. Fock and overlap integral matrix elements were calculated using the TRANSFERINTEGRALS key with the fragment orbital approach as implemented in ADF.

The effective coupling between orbitals *i* and *f*, V_{if}, was calculated using the following equation:[95]

$$V_{\mathrm{if}} = \frac{\mathrm{J_{if}} - \frac{1}{2}\mathrm{S_{if}}(\mathrm{e_i}+\mathrm{e_f})}{1-\mathrm{S_{if}^2}} \qquad \text{(eq. 3.1)}$$

where J_{if} is the Fock matrix element between a pair of monomers, S_{if} is the overlap integral, e_i and e_f are the Fock matrix elements within a monomer. The calculated matrix elements are shown in Table S3.

Singlet and triplet excitation energies, $E(S_1)$ and $E(T_1)$, were calculated using the time-dependent density functional theory (TDDFT) with the ADF package. $E(T_1T_1)$ was obtained by doubling $E(T_1)$. The CT state energy, E(CT), was calculated using a Weller-like equation:

$$E(\mathrm{CT}) = IP + EA + E_{\mathrm{elec}} + E_{\mathrm{ind}} \qquad \text{(eq. 3.2)}$$

Here, ionization energy (*IP*) and electron affinity (*EA*) of monomer were obtained from DFT, whereas the induction (E_{ind}) and electrostatic (E_{elec}) energies were determined using the classical the Direct Reaction Field (DRF) method[135] suggested by Mirjani *et al.*[136] Atomic charges of both neutral and charged dimers for DRF calculations were obtained from Mulliken population analysis using DFT. The calculated values energies are shown in **Table 3.5**.

Considering the first-order coupling of CT states to the initially excited singlet state, S_1, and the final triplet state, (T_1T_1), the effective electronic coupling for the superexchange mechanism,[137] $J_{SE,eff}$, was calculated using the Eq. 3.3:

$$\mathrm{J_{SF,eff}} = < \mathrm{S_1S_0^1}|\hat{\mathrm{V}}|\mathrm{T_1T_1^1} > = < \mathrm{S_1S_0^0}|\hat{\mathrm{H}}_{\mathrm{el}}|\mathrm{T_1T_1^0}$$

$$> -\frac{2(\mathrm{V_{LL}V_{LH}} - \mathrm{V_{HH}V_{HL}})}{[\mathrm{E(CT)} - \mathrm{E(TT)}] + [\mathrm{E(CT)} - \mathrm{E(S_1)}]} \qquad (eq.\,3.3)$$

The first term on the right-hand side of the equation will be ignored since the direct two-electron coupling is small compared to the four 1-electron coupling. V_{LL} and V_{HH} are the 1-electron coupling of the LUMO and HOMO of the two molecules, respectively, whereas V_{LH} and V_{HL} are the

electronic couplings between the LUMO of the first molecule and the HOMO of the second molecule, and vice versa. Using the values specified in **Table 3.4** and **3.5**, $J_{SE,eff}$ values were determined.

3.3 Results and Discussion

3.3.1 Structural characterization

BPEA films, **1** and **2** are prepared by thermal vapor deposition of BPEA, followed by solvent vapor (CH_2Cl_2) annealing for film **1** and thermal annealing at 120 ˚C for film **2**. Films **3**, **4** and **5** are prepared by thermal vapor deposition of 4,4′-difluoro-BPEA (**F_2**), 4-fluoro-4′-methoxy-BPEA

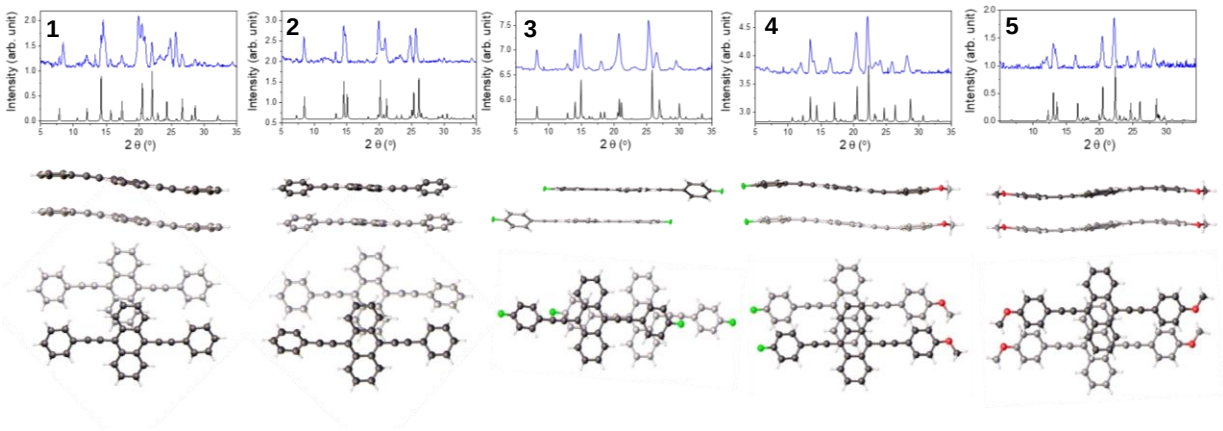

Figure 3.1. Comparison of the simulated PXRD pattern from a single crystal (black) and PXRD of the polycrystalline powder scraped off a vapor-deposited/annealed films (blue) of **1-5** with the respective nearest dimer unit within the crystal structure. In the crystal structure, green atoms are fluorine, red are oxygen, white are hydrogen and grey are carbon.

(**FOMe**) and 4,4′-dimethoxy-BPEA (**$(OMe)_2$**), respectively, followed by solvent vapor (CH_2Cl_2) annealing. The powder X-ray pattern (PXRD) of the molecules scraped off films deposited on the sapphire substrate is compared to the simulated PXRD from the single crystal structure (**Figure 3.1**).

All but film **1**, which is composed of two different polymorphs (*C*2/*c* and *Pbcn* space groups) of BPEA crystals, have only a single polymorph. The composition of *C*2/*c* and *Pbcn* polymorph in film **1** is determined to be 61.2 ± 0.5 % and 38.8 ± 0.5 %, respectively, using Rietveld fitting (**Figure 3.5**).[35] Since *C*2/*c* polymorph is the major composition in film **1**, the dimer unit in **Figure 3.1** shows *C*2/*c* packing structure. All films are highly crystalline based on the peak sharpness compared to other SF thin films of rylene[19, 20] and acene derivatives.[138]

The difference in packing structure of each film is highlighted in the dimer from the crystal structure (**Figure 3.1**). The chromophore packing within the crystal structures of **1-5** is analyzed by extracting the nearest dimer unit within the crystal structure. The π–π, lateral slip and longitudinal slip distances are shown in Table 1. All of the dimer units have π–π distance close to 3.40 Å. Films **1** and **2** have the same longitudinal slip distance (0.8 Å) but different lateral slip distances. Film **3** has a large longitudinal slip distance (7.28 Å) but almost no lateral slip, while **4** and **5** have significant lateral slip distances of 3.93 Å and 3.87 Å, respectively, and almost no longitudinal slip. Films **4** and **5** have shorter longitudinal slip distances compared to films **1** and **2**.

Table 3.1. π–π, lateral and longitudinal slip distances of the nearest dimer unit within the crystal structures BPEA (1-2) and its derivatives (3-5).

Films	π – π (Å)	Lateral slip distance (Å)	Longitudinal slip distance (Å)
1	3.40	4.06	0.800
2	3.45	3.34	0.800
3	3.35	0.367	7.280
4	3.41	3.93	0.345
5	3.42	3.87	0.336

3.3.2 Photophysical Characterization

Steady state absorbance and emission spectra of the films were measured (**Figure 3.2**) to obtain the first excited singlet energy, *E*(S1). Among the five films, film **3** has the highest *E*(S1) of 2.48 eV followed by **1** (2.43 eV), **2** (2.43 eV), **4** (2.34 eV), and **5** (2.34 eV).

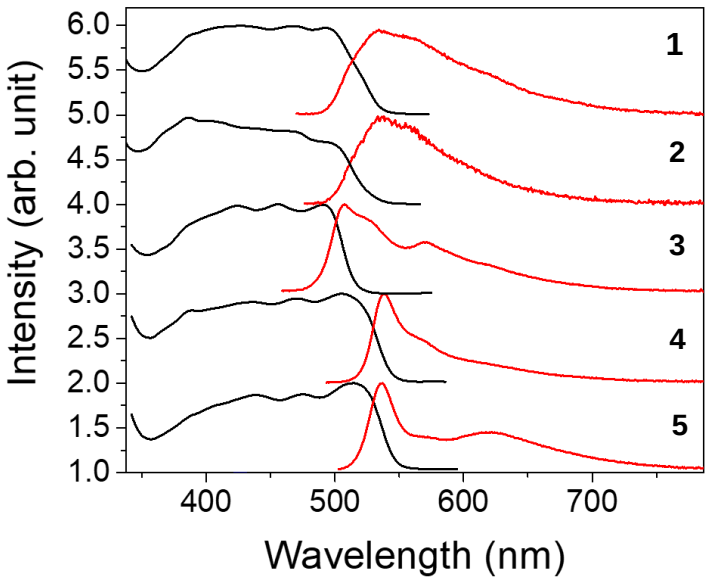

Figure 3.2. Steady-state absorbance and emission of thin films of **1**-**5**.

The triplet energies of the thin films were estimated using triplet energy transfer from palladium octabutoxyphthalocyanine, $PdPc(OBu)_8$ and to singlet oxygen. The estimated triplet energy is 0.98 – 1.24 eV, where the lower limit comes from singlet oxygen and the upper limit from $PdPc(OBu)_8$.[121] Since triplet excitons are more localized than singlet excitons, triplet energies are assumed to be constant amongst the films. Hence, the triplet energy is approximated to be the average between 0.98 eV and 1.24 eV, yielding 1.11 eV. With these assumptions, the thermodynamic driving force for SF is calculated to be the difference between $E(S_1)$ and twice the $E(T_1)$. Film **3** has the greatest thermodynamic driving force of 0.26 eV followed by **1**, **2**, **4** and **5** (**Table 3.2**).

3.3.3 Excited-state dynamics of BPEA derivative thin films

In order to examine the SF dynamics, low-fluence fsTA spectroscopy was used with excitation densities of (1.0×10^{17} excitons·cm^{-3}). It is crucial that the excited state be studied in the low excitation regime to minimize singlet-singlet annihilation. From the fsTA spectra, we observe ground-state bleaching (GSB), stimulated emission (SE) and singlet excited-state absorption (ESA) at early times; at later times, triplet formation is observed around 450-550 nm (**Figure 3.3**). The formation of the triplet is confirmed from singlet oxygen measurements and comparing the fsTA spectra at 7ns of BPEA films to those of the PdPc doped BPEA films. The fsTA spectra for **2**, which is made of purely *Pbcn*, is globally fitted using the kinetic model A $\rightarrow$ B $\rightarrow$ GS where A is purely singlet and B is triplet. Film **1**, which is composed of two different polymorphs, is globally fitted using the two parallel processes of A $\rightarrow$ B $\rightarrow$ GS, where two singlet populations originate from two different polymorphs. From the kinetic fitting, the SF rate of *C*2/*c* polymorph is $(90 \pm 30 \text{ ps})^{-1}$ and that of Pbcn is $(430 \pm 30 \text{ ps})^{-1}$.

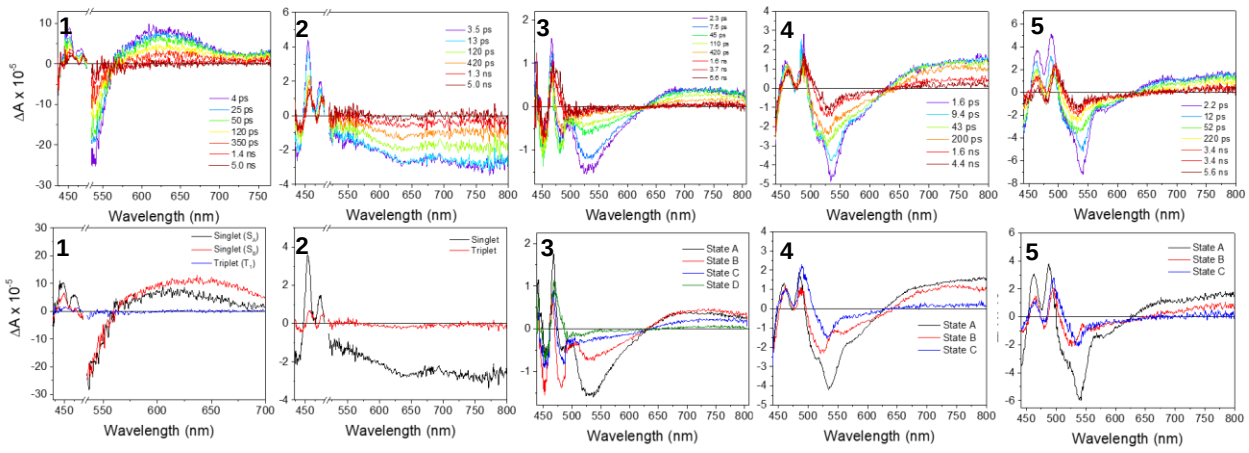

Figure 3.3. Top: Low-fluence fsTA spectra at selected time points. Bottom: evolution-associated spectra from the kinetic fitting using the model discussed in the text.

The BPEA derivatives differ from the parent BPEA films in that the derivatives require more than one singlet excited population, which is attributed to heterogeneity in the film and small degree of excimer formation. Since the excited states are not purely singlet, excimer, or triplet, we use evolution-associated fitting, where each state has mixture of singlet, excimer and/or triplet, similar to that observed in terrylenediimide systems.[3, 139] Film **3** is globally fitted using A $\rightarrow$ B $\rightarrow$ C $\rightarrow$ D $\rightarrow$ GS. Based on the increase in GSB feature in state B and C (**Figure 3.3**), τ_A and τ_B are assigned to SF. Although there is a single polymorph in the thin film of **1**, if some degree of heterogeneity exists in terms of grain size and crystallinity, this could form local hot spots where SF is more favorable, as seen in pentacene[140] and terrylenediimide films[20]. Both films of **4** and **5** are globally fitted using A $\rightarrow$ B $\rightarrow$ C $\rightarrow$ GS. There are distinct spectral changes between state A and B in the film of **5**, where state B resembles the triplet feature. States A and B in the film of **4** have similar spectral features to state B, having increased red-shifted stimulated emission features.

Presumably, state B in the film of **4** has more triplet population than in film **5**. Overall, the BPEA derivatives have more distributed kinetics compared to BPEA films.

Table 3.2. SF time constants from global fits of the fsTA data to the model described in the text, triplet yield, electronic coupling, J_{SE}, and energetic driving force, $\Delta E(S_1\text{-}T_1T_1)$,

Film	τ_{SF1} (ps)	τ_{SF2} (ps)	Φ_T (%)	$\lvert J_{SE}\rvert$ (meV)	$\Delta E(S_1 - T_1T_1)$[a] (eV)
1	90 ± 30	480 ± 40	180 ± 20	7.80	0.21
2	430 ± 30	-	80 ± 20	3.73	0.21
3	16 ± 2	120 ± 10	180 ± 16	2.85	0.26
4	90 ± 20	1100 ± 100	110 ± 4	8.54	0.12
5	120 ± 10	2300 ± 600	168 ± 7	3.80	0.12

[a] $E(T_1T_1)$ is approximated to be 1.11 eV which is a mean value between 0.98 and 1.24 eV.

3.3.4 Triplet yield analysis.

The nsTA spectra of the films were obtained to determine their triplet yields using the singlet depletion method, which is independent of the choice of kinetic model. This method is particularly useful in estimating triplet yields for systems with overlapping GSB and triplet ESA features. The number of excited molecules were calculated from the excitation pulse energy, laser spot size, and film thickness to obtain the expected GSB spectrum; then, the number of triplet states was estimated by adding the scaled ground-state bleach to the excited state triplet nsTA spectrum. Based on this analysis, films of **1** and **3** have the highest triplet yield of 180 % followed by the films of **5** (168 %), **4** (110 %), and **2** (80%).

3.3.5 Electronic coupling, thermodynamic driving force and rate analysis.

Electronic coupling, J_{SE}, is an important factor controlling SF rate and efficiency.[112] We calculated J_{SE} using the dimer model, assuming the mechanism of SF is superexchange. The film of **4** has the highest electronic coupling of 8.54 meV, followed by that of **1** (7.80 meV), **5** (3.80

meV), **2** (3.73 meV) and **3** (2.85 meV). We find strong correlation between electronic coupling and τ_{SF1} in all films except that of **3**. Assuming the reorganization energies are similar, the SF rate is proportional to $|J_{SE}|^2$. For example, films of **1** and **4** have similar $|J_{SE}|^2$ values of 60 and 72 meV^2, respectively, and similar τ_{SF1} of ~90 ps (Table 2). Following this trend, the film of **5** has a greater $|J_{SE}|^2$ value than the film of **2** and thus has faster τ_{SF1} = 120 ps compared to τ_{SF1} = 430 ps for **2**. For films of **1**, **2**, **4,** and **5**, we observed a qualitative trend in electronic coupling and $\tau_{SF1.}$ We also observe a quantitative trend between films **1** and **2**, where the SF rate for *C*2/*c* is estimated to be 4.4 times faster than that of *Pbcn*, matching the experimental rate ratio of 4.5 ± 0.2.

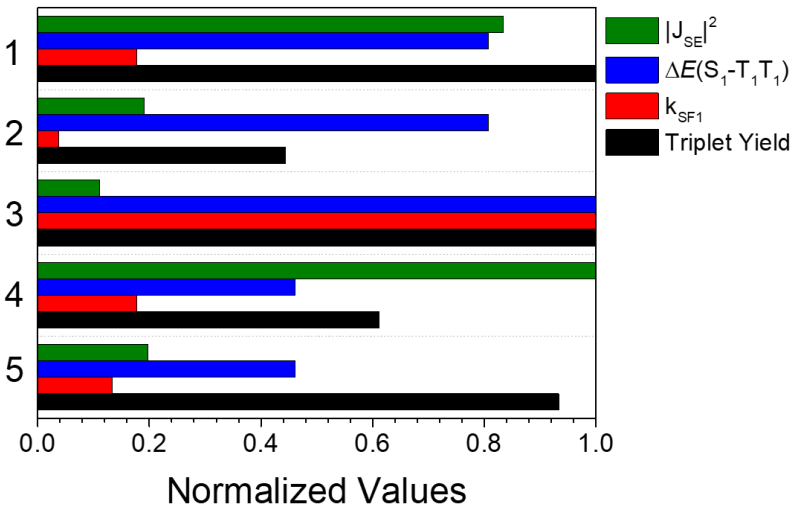

Figure 3.4. Normalized values of electronic coupling, $|J_{SE}|^2$, energetic driving force, $\Delta E(S_1\text{-}T_1T_1)$, experimental singlet fission rate, k_{SF1}, and triplet yield of films of **1**-**5**.

Now, correlating the triplet yield to the SF rate, electronic coupling and thermodynamic driving force, we find that the triplet yield is most strongly correlated to thermodynamic driving force. For instance, although film **3** has the lowest $|J_{SE}|^2$, it undergoes the fastest SF with the highest triplet yield, attributed to the greatest thermodynamic driving force. Following the film of **3**, films of **1**

and **2** have greater thermodynamic driving forces than films of **4** and **5**. The film of **1** has both greater thermodynamic driving force and electronic coupling compared to films of **2**, **4**, and **5** and thus, undergoes faster SF with greater triplet yield; however, film **2** which has greater thermodynamic driving undergoes slower and less efficient SF than films of **4** and **5**. One possible reason is that the crystal structure of the film of **2** enhances fluorescence emission, resulting in the highest fluorescence quantum yield of 30%, meaning that only 70% of the singlet excitons can undergo SF. Between films of **4** and **5**, which have the same thermodynamic driving force, film **4**, which has greater electronic coupling, undergoes less efficient SF. This is because the molecule has push-pull character which results in a low calculated CT energy. Such low CT energy presumably introduces excimer trap states as evidenced in significantly more red-shifted emission

3.4 Conclusions

We studied five different thin film made of BPEA and its derivatives. We can tune the composition of different polymorphs of BPEA in the film by changing the annealing method. Different packing structures in films of **3-5** result from adding functional groups at the *para* positions of the phenyls in BPEA. Among all the structurally different films studied here, triplet yield increases with increasing thermodynamic force. The film of **3**, which has the greatest driving force, undergoes fastest SF with the highest triplet yield, followed by the films of **2** and **5**. The simple dimer model used here to calculate the effective electronic coupling predicts the rate of SF relatively well. The film of **3** has the strongest potential to be used as a solar cell device because of its fast 17 ps SF time and its high 180% triplet yield.

3.5 Supplementary Information

3.5.1 BPEA powder X-ray diffraction (PXRD) analysis. BPEA polycrystalline powder was purchased from Sigma Aldrich and PXRD data were collected at room temperature on a STOE-STADIMP powder diffractometer equipped with an asymmetric curved Germanium monochromator (CuKα1 radiation, λ = 1.54056 Å) and one-dimensional silicon strip detector (MYTHEN2 1K from DECTRIS). The line focused Cu X-ray tube was operated at 40 kV and 40 mA. The pristine powder was packed in a 3 mm metallic mask and sandwiched between two layers of polyimide tape. The instrument was calibrated against a NIST Silicon standard (640d) prior to the measurements. Rietveld analysis[141] was performed using the JANA2006[142] software. From the analysis (Figure S1), there is 40.10(2) % of Pbcn and 59.90(2) % of C2/c polymorphs.

3.5.2 Quantitative analysis of polymorphs in the BPEA solvent annealed film. A small amount of powders was scrapped off the annealed film and measured at room temperature on a Bruker Prospector system equipped with the micro-focused X-ray tube and MX optics. The same analysis

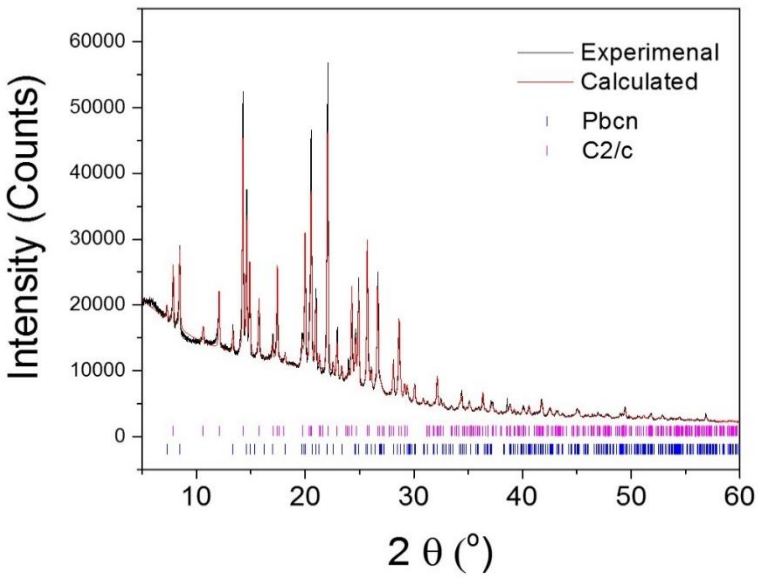

Figure 3.5. The experimental (black) and calculated PXRD pattern of BPEA polycrystalline powder and peak positions of polymorph Pbcn (blue) and C2/c (magenta).

method with the polycrystalline powder (**Figure 3.5**) was used; there is 38.8 ± 0.5 % of Pbcn and 61.2 ± 0.5 % of C2/c polymorphs, which is very similar to the results obtained for the bulk powder.

3.5.3 Triplet sensitization in solid-state films

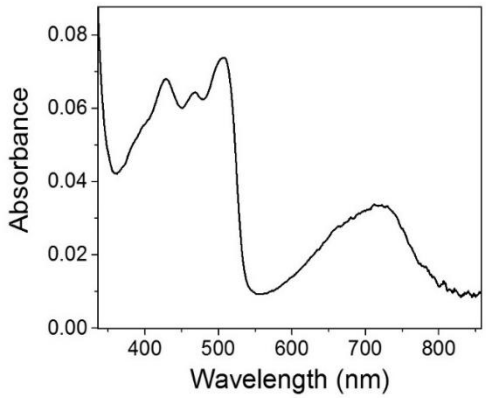

Figure 3.7. Steady-state absorbance of the $PdPc(OBu)_8$ doped BPEA spin-coated film where the bands at 350-550 nm result from BPEA and the band from 550-850 nm results from $PdPc(OBu)_8$.

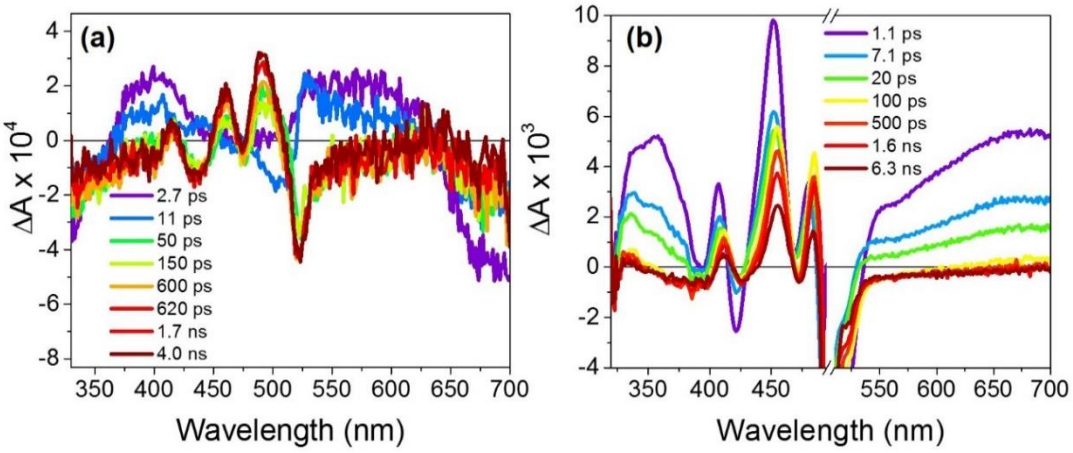

Figure 3.7. The fsTA spectra of (a) the sensitized film excited at 720 nm (b) a BPEA thin film excited at 500 nm.

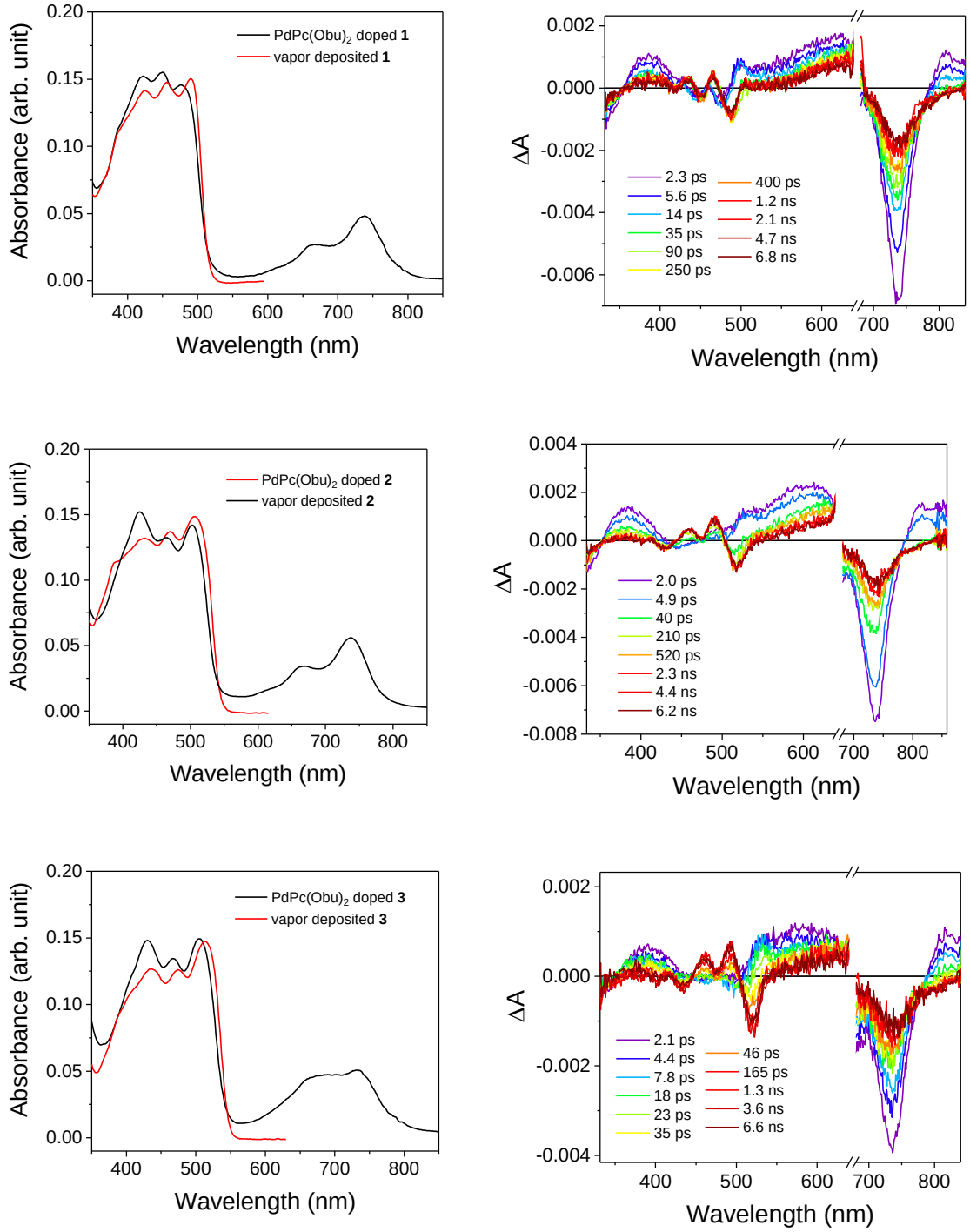

Figure 3.8. Left: Steady-state absorbance and fsTA spectra of the PdPc(OBu)$_8$ doped **F$_2$**, **FOMe**, and **(OMe)$_2$** spin-coated films where the bands at 350-550 nm result from BPEA derivatives and the band from 550-850 nm results from PdPc(OBu)$_8$.

3.5.4 FsTA spectra and the kinetic fitting

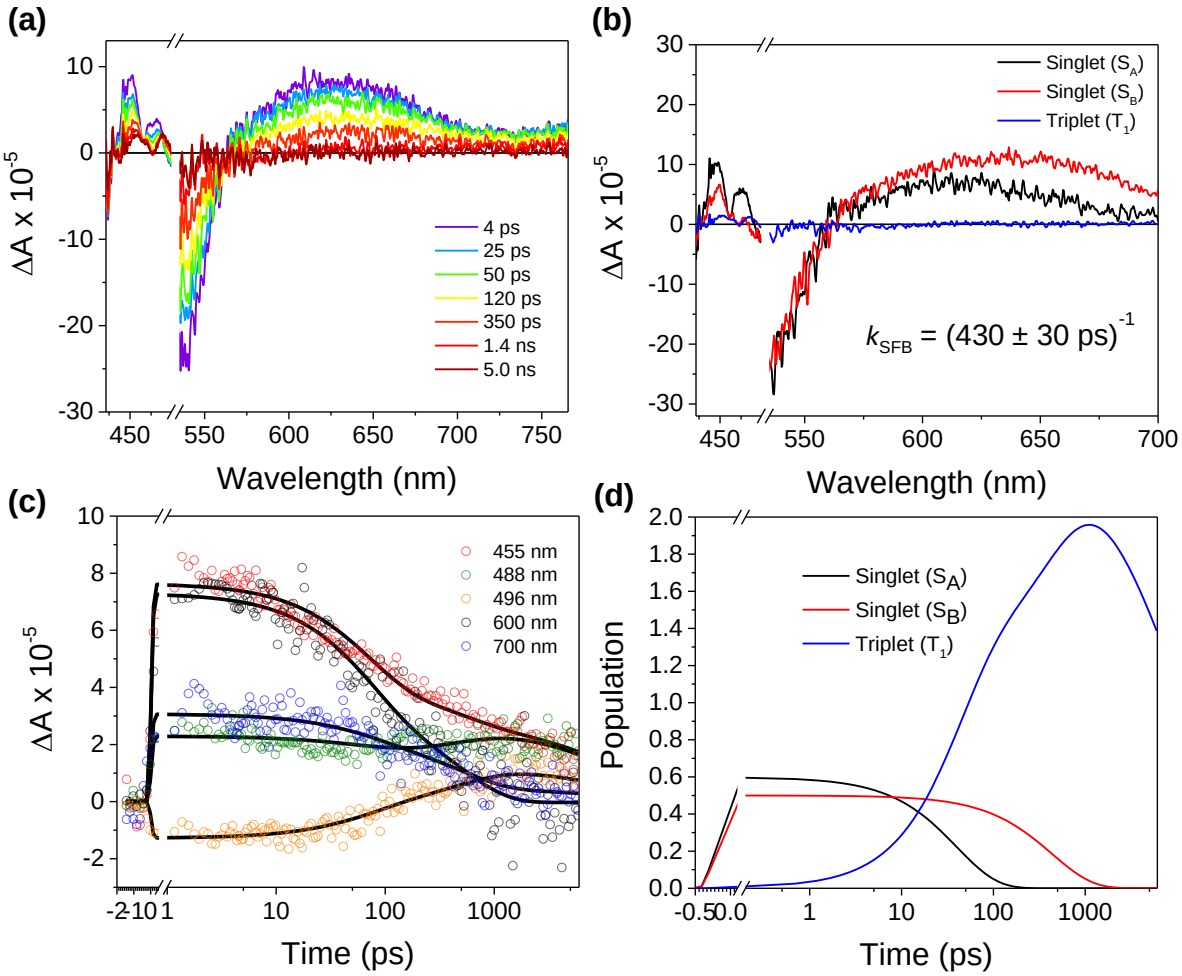

Figure 3.9. FsTA data obtained at 10^{17} cm^{-3} excitation density and a 100 kHz repetition rate. (a) fsTA spectrum of the solvent-annealed BPEA film; (b) the reconstructed species-associated spectra; (c) global fits to selected wavelengths; and (d) a population vs time plot obtained by global fitting to the kinetic model specified in the text.

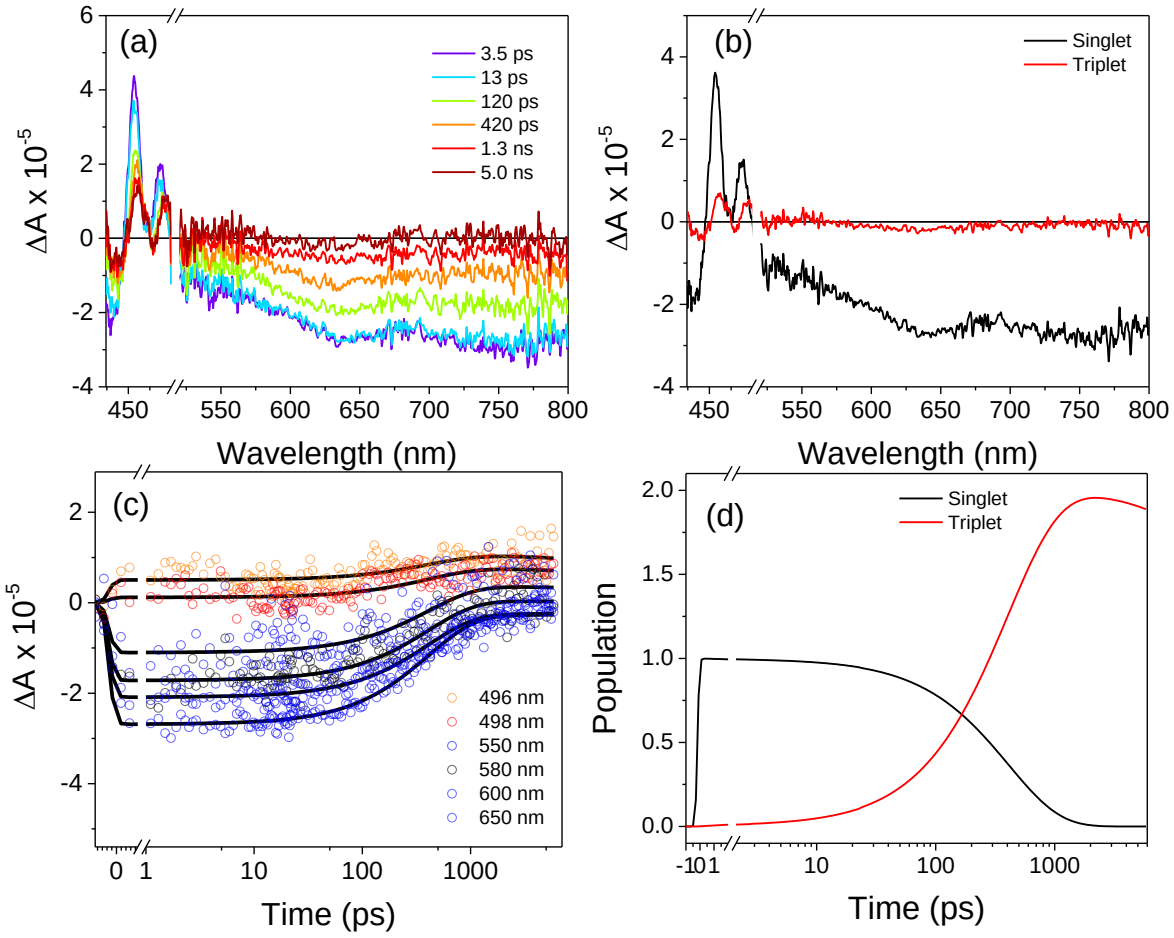

Figure 3.10. FsTA data obtained at 10^{17} cm^{-3} excitation density and a 100 kHz repetition rate. (a) fsTA spectrum of the thermally annealed BPEA film; (b) the reconstructed species-associated spectra; (c) global fits to selected wavelengths; and (d) a population vs time plot obtained by global fitting to the kinetic model specified in the text.

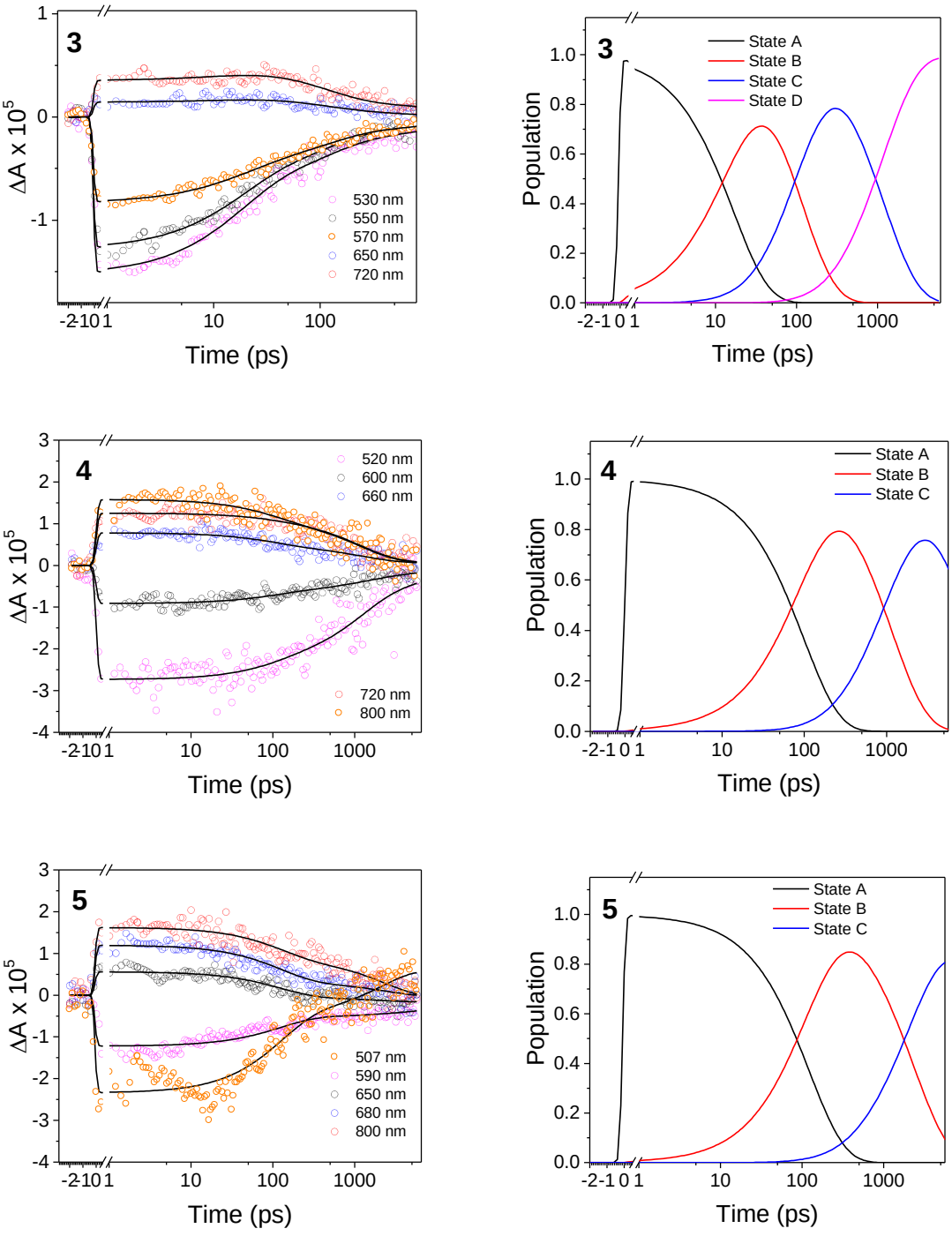

Figure 3.11. Wavelength fitting (left) and population vs time plots (right). A → B → C → D → GS kinetic model is used to fit **3** and A → B → C → GS for **4** and **5**.

3.5.6 Triplet yield calculation using the singlet depletion method.

The singlet depletion method,[143] is based on quantifying the ground-state bleach signal in the nsTA data and relating this to the number of triplets created. The nsTA data, which uses a 7 ns, 416 nm pump pulse at 0.5 mJ is at a low enough excitation density to eliminate singlet-singlet annihilation. The excitation density (ξ) was calculated based on the excitation pulse energy (*E*), wavelength (*λ*), absorption (*A*) at 416 nm, spot size (a), and the film thickness (*l*), using the following equation:

$$\xi = \frac{E \cdot \lambda \cdot K \cdot \left(1 - 10^{-A}\right)}{l \cdot a} \qquad \text{(eq. 3.4)}$$

where *K* is a composite of physical constants, $5.034 \cdot 10^{15}$ J^{-1} nm^{-1}.[3] The spot size for the pump is measured using aperture and probe is matched to that of pump and the film thickness is measured using profilometer (detailed description is written in S-5). The number density is calculated using the following equation:

$$no.density = \frac{Z}{V} \qquad \text{(eq. 3.5)}$$

where unit cell volume (V) of the different derivatives is shown in **Table 3.3** with number of molecules per unit cell (*Z*) equal to 4. All the values of parameters used in the above equations are listed in Table S1. The ratio ξ/ *no. density* gives a scaling factor for the ground-state absorption spectrum that produces expected bleach at 1.5 ns delay. We then subtract this expected ground state bleach from the nsTA spectrum at 50 ns to recover the undistorted triplet spectrum with no negative features. Here, 50 ns was chosen to minimize the signal coming from the fluorescence close to 0 ns. The time-independent triplet yield, φ_T is calculated using the following equation with the corresponding triplet decay constants shown in **Table 3.3**:

$$\varphi_T = \varphi_{T\ at\ t=50\ ns} \cdot \frac{1}{A_1 \cdot e^{-\frac{50\ ns}{\tau_1}} + A_2 \cdot e^{-\frac{50\ ns}{\tau_2}}} \qquad \text{(eq. 3.6)}$$

Table 3.3. All of the values used to calculate the scaling factor for ground state depletion method

Compound	*E* (mJ/pulse)	λ (nm)	Spot size (cm)	*l* (nm)	*Z* (molecules)	*V* (Å^3)
1	0.5	416	0.8	174	4	1983
2	0.5	416	0.8	310	4	1986
3	0.8	420	0.8	125	4	2143
4	0.8	420	0.8	110	4	2061
5	0.8	420	0.8	82	4	2236

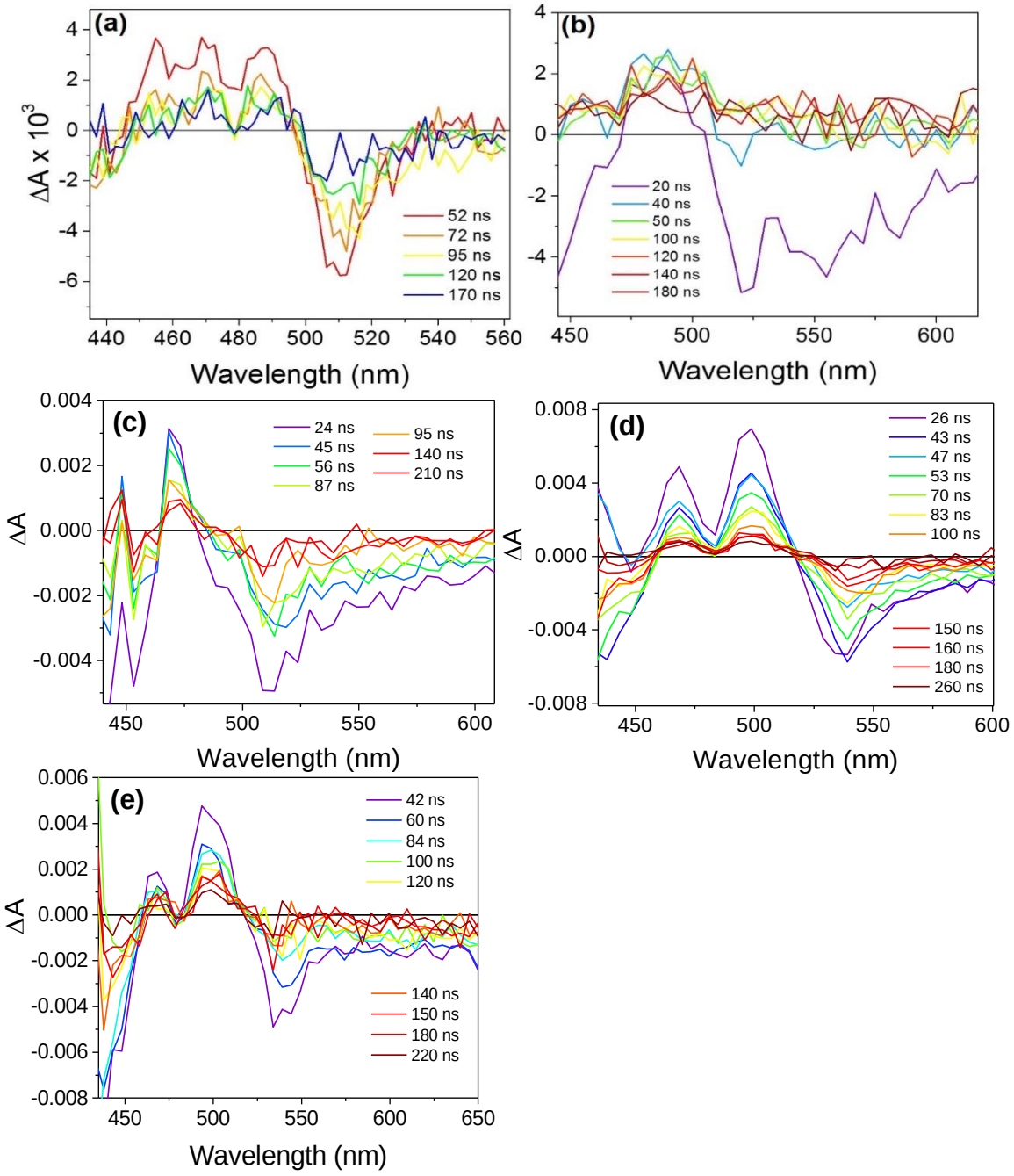

Figure 3.12. The nsTA spectra for the (a) solvent-annealed (b) thermally-annealed BPEA thin films, (c) F_2 (d) FOMe, and (e) $(OMe)_2$- BPEA excited with a 7 ns, 416 nm or 420 nm, 1 mJ pulse. Spectra are sampled at 2 nm increments.

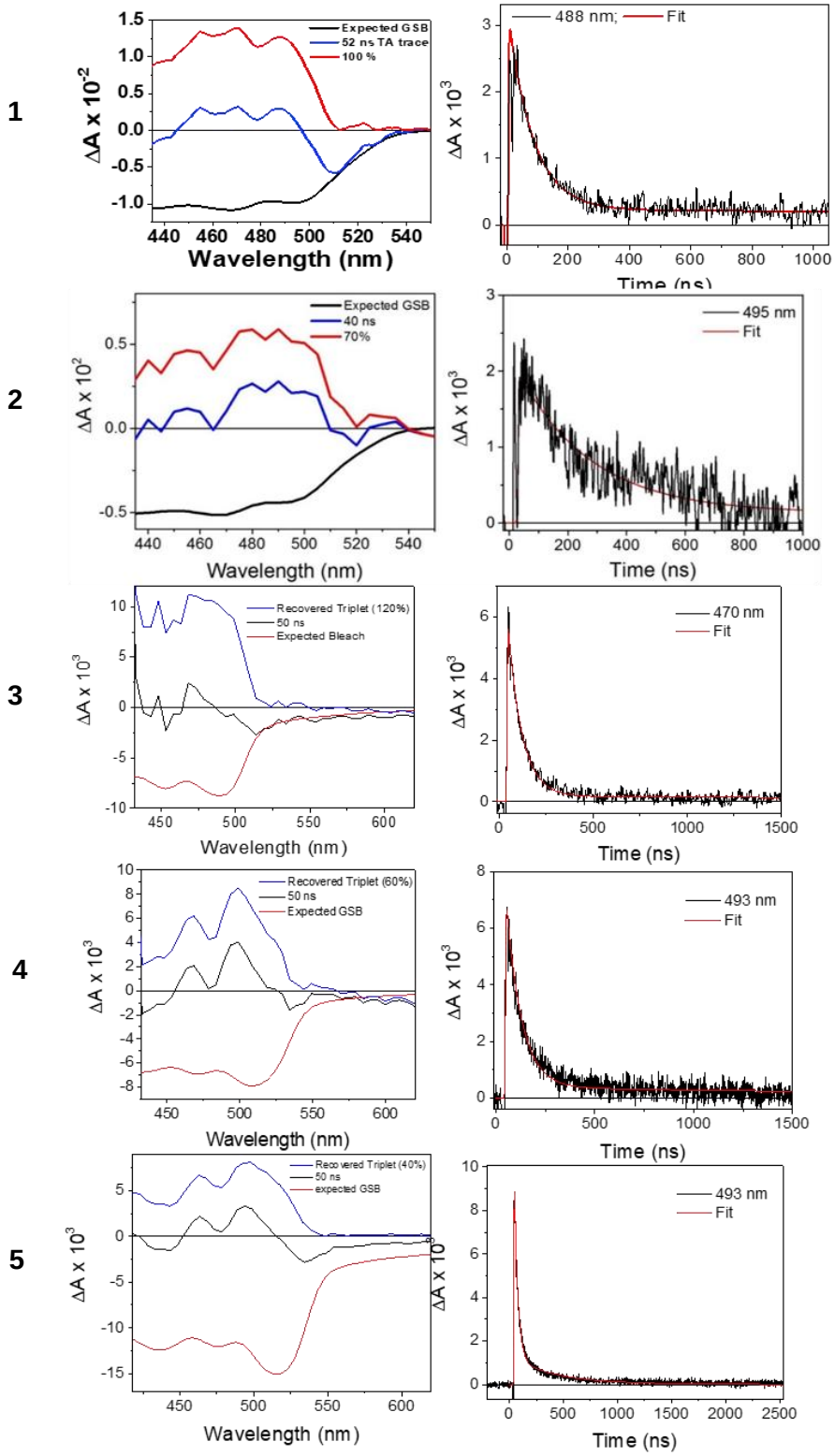

Figure 3.13. The triplet yield at 50 ns obtained using the singlet depletion method and single-wavelength kinetic traces for films **1-5**.

3.5.7 Computational Details

Table 3.4. Calculated overlap integrals (S_{if}), and regular (V_{if}) and effective couplings (J_{if}) between HOMO and LUMO

Dimer Unit	**S_{HH} (meV)**	**S_{HL} (meV)**	**S_{LH} (meV)**	**S_{LL} (meV)**
1	7.05	9.79	-9.79	22.0
2	-8.84	5.69	-5.69	1.58
3	-8.78	-13.3	-13.3	-11.9
4	7.86	7.94	-8.78	-19.3
5	8.84	-7.79	7.79	-18.4
	J_{HH} (meV)	**J_{HL} (meV)**	**J_{LH} (meV)**	**J_{LL} (meV)**
1	-88.1	-111	111	178
2	109	-66.1	66.1	-15.8
3	105	153	153	108
4	-96.4	-89.4	100	157
5	-105	86.3	-86.3	145
	V_{HH} (meV)	**V_{HL} (meV)**	**V_{LH} (meV)**	**V_{LL} (meV)**
1	-50.1	-71.3	71.3	120
2	61.3	-43.3	43.3	-11.7
3	56.4	97.6	97.6	74.3
4	-54.3	-57.8	65.1	10.6
5	-59.5	56.9	-56.9	101

Table 3.5. Calculated E(CT), E(S_1) and E(T_1)

Compound	***E*(CT) (eV)**	***E*(S1) (eV)**	***E*(T1) (eV)**
1	3.51	2.54	1.46
2	3.50	2.59	1.50
3	3.41	2.5	1.41
4	3.24	2.5	1.45
5	3.5	2.52	1.48

3.5.8 TREPR of BPEA films at 85K

In order to probe the triplets formed via SF in BPEA thin film, we performed TREPR measurement of the film at 85K; however, instead of the typical ((*a*,*e*,*e*,*a*,*a*,*e*) spin polarization pattern observed for SF, we observe a broad, entirely absorptive feature. Such feature is too broad to be a radical species. Presumably, triplets are moving too fast in the film. Further study is required to confirm the nature of this triplet polarization pattern.

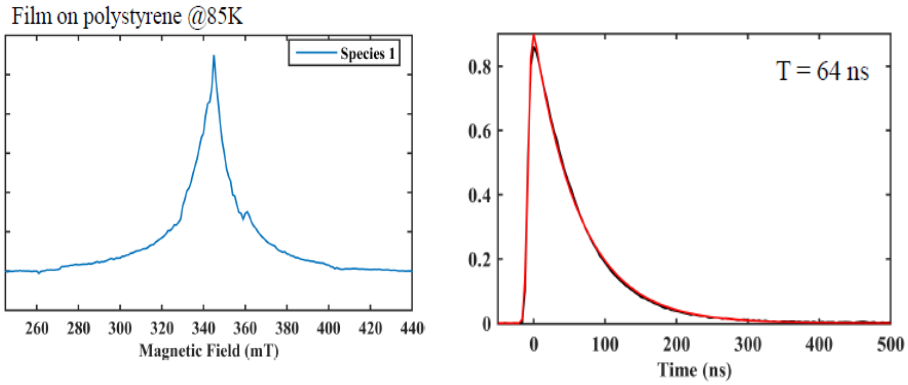

Figure 3.14. Left: TREPR spectra of BPEA film deposited onto polystyrene matrix and right: the kinetic trace at the maximum peak.

Chapter 4. Singlet Fission vs. Spin-Orbit Intersystem Crossing in Anthanthrene Derivatives

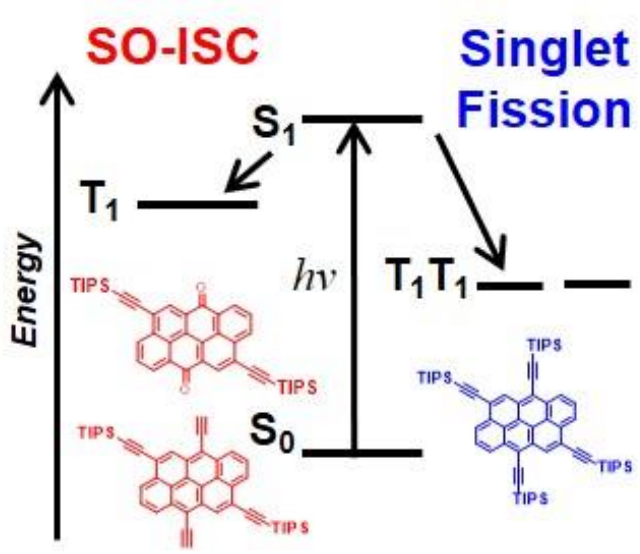

The result of this chapter is published in and adapted with permission from *ChemPlusChem*, **2019**, 84, 1432.

4.1 Introduction

Anthanthrene and anthanthrone chromophores are highly π-conjugated organic molecules with diverse photophysical applications including organic light emitting diodes,[144] dye-sensitized solar cells,[145, 146] and organic field effect transistors.[147, 148] Unlike conjugated polyacenes such as tetracene and pentacene, which are unstable toward light and oxygen due to oxidation,[115] anthanthrene and anthanthrone derivatives are highly stable and chemically tunable.[149] Although the steady-state photophysical properties of anthanthrene-based molecules have been studied extensively,[150] their excited state properties remain underexplored. In order to expand their potential application to singlet fission and triplet fusion, both the singlet and triplet excited decay pathways need to be better understood.

Previous studies of anthanthrene and anthanthrone derivatives have shown that they all undergo spin-orbit-induced intersystem crossing (SO-ISC) with varying triplet yields,[151] where anthanthrone derivatives undergo SO-ISC faster and more efficiently than anthanthrene derivatives. The generation of triplet states in organic molecules has been an interesting topic of research due to the potential leveraging of these excited states to increase photovoltaic device efficiencies.[13] For instance, molecules that can undergo triplet fusion can upconvert near-infrared light to visible wavelengths, whereas molecules that absorb blue light can undergo singlet fission resulting in two triplet states, which can be used to overcome the theoretical Shockley-Queisser efficiency limit for single junction solar cells.[152] Both triplet fusion and fission have been extensively studied in polyacenes.[6, 35, 153, 154] Here, we characterize triplet formation in one anthanthrone and two anthanthrene derivatives (**Scheme 4.1**) in solution using time-resolved optical and EPR spectroscopies.

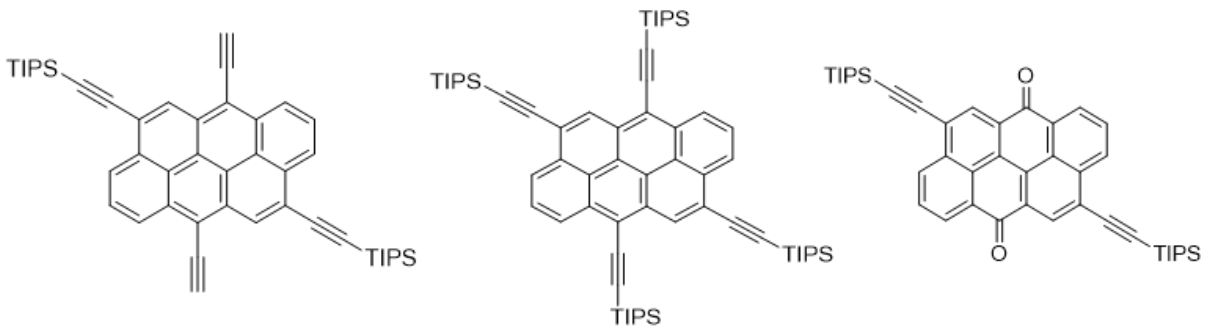

1 **2** **3**

Scheme 4.1. The anthanthrene (**1** and **2**) and anthanthrone (**3**) derivatives studied here.

4.2 Experimental Details

Compounds **1-3** were synthesized using previously reported procedures.[149, 155]

4.2.1 Single crystal structure and x-ray spectroscopy

Crystals of **1** and **2** were grown by slow solvent evaporation of each compound from chloroform solution. The crystals were mounted on a polymer loop with Paratone oil, and the data were collected at 100 K on a Bruker Kappa APEX II CCD diffractometer equipped with a Cu Kα 1 μS microfocus source for crystal **1** and Mo Kα 1 μS for crystal **2** with MX optics. The data were absorption-corrected using SADABS. The structure was solved using SHELXT and refined using SHELXL using Olex 2 software.[132] The structures have been deposited in the Cambridge Crystallographic Data Centre database **1:** CCDC number for **1** is 1937383 and for **2** is 1937384 (**Table 4.5**).

4.2.2 Steady-state spectroscopy

Steady-state absorption spectra of the solution samples were measured using a Shimadzu UV-1800 spectrometer and steady-state fluorescence spectra were measured in the front-face mode with a HORIBA Nanolog spectrofluorimeter equipped with an integrating sphere (Horiba Quanta - φ) for absolute fluorescence quantum yield determination. Steady-state fluorescence spectra were

collected using CCD detector at 295K and phosphorescence spectra are collected using InP/InGaAs detector at 77K.

4.2.3 Singlet oxygen measurement

The singlet oxygen ($^1\Delta_g$) quantum yield (φ_Δ) was measured using zinc *meso*-tetraphenylporphyrin (ZnTPP) in CH_2Cl_2 as the standard (φ_Δ = 0.7).[156] The absorbance of the sample and the standard is matched to within 0.1 at the excitation wavelength (λ_{ex}) of 435 nm. The singlet oxygen emission spectrum was integrated from λ_1 = 1230 nm to λ_2 =1330 nm, and φ_Δ of the sample was determined using the following equation:[157]

$$\varphi_\Delta\ (\text{sample}) = \varphi_\Delta(\text{ZnTPP}) \cdot \frac{\text{ZnTPP OD at } \lambda_{ex}}{\text{sample OD at } \lambda_{ex}} \cdot \frac{\int_{\lambda_1}^{\lambda_2} I_{sample}(\lambda)\, d\lambda}{\int_{\lambda_1}^{\lambda_2} I_{ZnTPP}(\lambda)\, d\lambda} \qquad \text{(eq. 4.1)}$$

4.2.4 Transient absorption spectroscopy and global analysis

Femtosecond transient absorption spectroscopy (fsTA) was performed using a regeneratively amplified Ti:sapphire laser system operating at 1kHz to generate 828 nm. The frequency-doubled 414 nm light is used to pump a lab built optical parametric amplifier to generate tunable pump wavelengths of 495 nm, 500 nm and 580 nm for **1**, **2**, and **3** respectively.[158] Solution samples were prepared in 2 mm path length glass cuvettes and degassed with three freeze-pump-thaw cycles. The TA data were subjected to global kinetic analysis to obtain the evolution- and decay-associated spectra and kinetic parameters as described in detail previously.[159]

4.2.5 Time-resolved electron paramagnetic resonance (TREPR) spectroscopy

X-band (~9.6 GHz) measurements were made using a Bruker Elexsys E680-X/W EPR spectrometer outfitted with a split-ring resonator (ER4118X-MS3). TREPR spectra of **1** - **3** were acquired in iodoethane and toluene at 85 K following photoexcitation with a 7 ns (3 mJ/pulse) laser pulse generated by an optical parametric oscillator (Spectra-Physics Basi-scan), pumped with the output of a frequency-tripled Nd-YAG laser (Spectra-Physics Quanta-Ray LAB-170). The

kinetic traces of the transient magnetization were acquired in quadrature under continuous microwave irradiation (5 mW). The EPR spectra were processed in MATLAB and the spectral simulations were performed using EasySpin.[160]

4.2.6 Computational detail (TDDFT)

The ground-state geometry was optimized using QChem (version 5.0) using DFT and TDDFT at B3LYP/6-31G* level. The excited-state energy was calculated using the ground state geometry in vacuum.

4.3 Results and Discussion

4.3.1 X-ray structural characterization

We report the crystal structures of **2** and **3**, which crystallize into the Pbca and $P2_1/c$ space groups, respectively (**Figure 4.1**). Since the anthanthrene core is planar for both molecules there is significant π-conjugation in **1** and **2**. Comparing the packing structure, there is less π- π stacking in **2** than **1** due to steric hindrance from four TIPS groups rather than two. Thus, the crystal structures of these molecules show that the planar aromatic π-system is maintained throughout the series. Detailed information regarding the single crystal structures are given in the Supplementary Information.

4.3.2 Steady-state optical characterization

In order to obtain the S_1 and T_1 energies ($E[S_1]$, and $E[T_1]$), steady-state absorption spectra, as well as fluorescence and phosphorescence emission spectra were collected. The steady-state absorption and emission spectra of **1-3** have well-resolved vibronic progressions, but the linewidth of **3** is significantly broadened (**Figure 4.2**). The fluorescence quantum yields of **1-3** (φ_{fl}) are 65 ± 5 %, 55 ± 4 %, and 9 ± 2 %, respectively (Table 1). $E[S_1]$ was determined from the onset of absorption and emission spectra. Comparing $E[S_1]$ among the three molecules, **1** has the highest

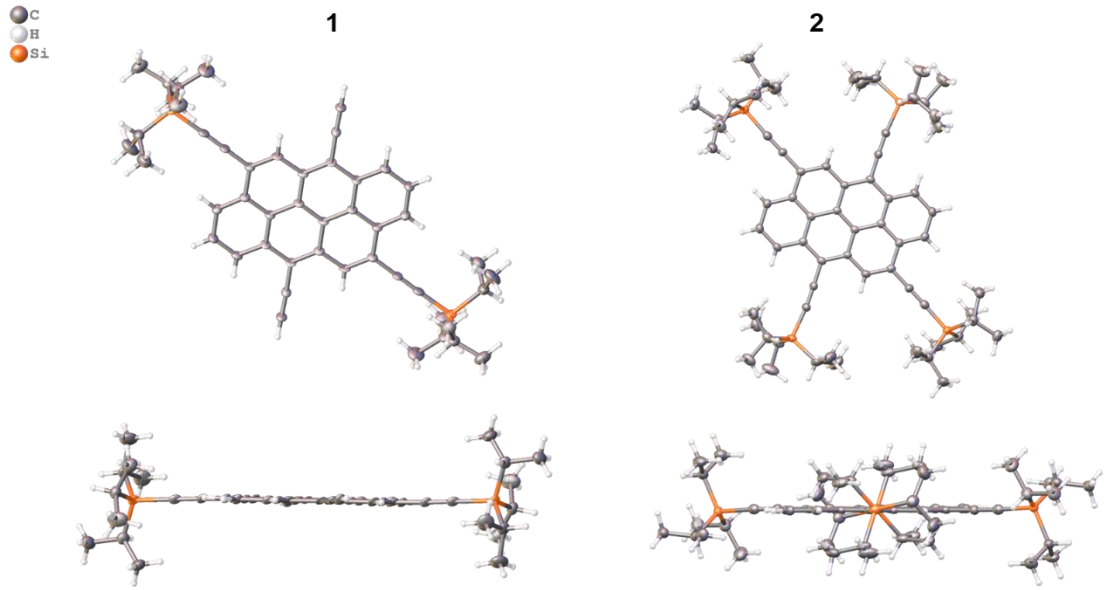

Figure 4.1. Single crystal structure of molecules **1** and **2**. Grey = carbon atoms; white = hydrogen atoms; orange = silicon atoms.

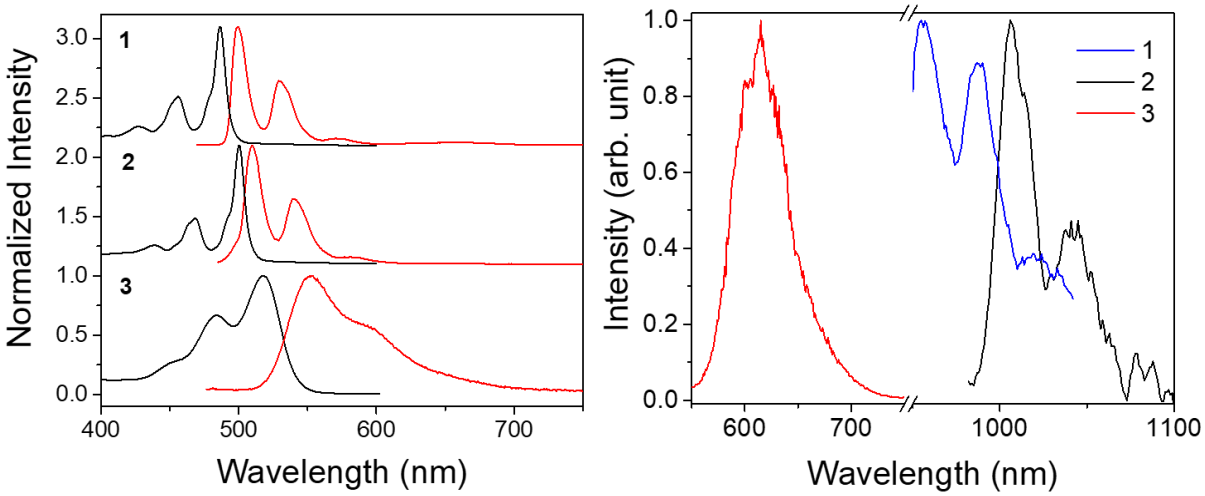

Figure 4.2. Steady-state absorbance and emission in CH_2Cl_2 (left) and phosphorescence emission of **1** and **2** in 100% iodoethane and **3** in CH_2Cl_2 at 77K (right).

E[S_1] (2.51 eV), followed by **2** (2.46 eV) and **3** (2.25 eV). The maximum of the phosphorescence emission spectrum was used to determine *E*[T_1]. Because **1** and **2** have high fluorescence quantum yields, in order to obtain their phosphorescence spectra, pure iodoethane was used as the solvent

to enhance ISC *via* the heavy atom effect. The phosphorescence emission was collected at 77K and the highest $E[T_1]$ was observed for **3** (2.01 eV) followed by **1** (1.30 eV) and **2** (1.23 eV).

Table 4.1. Photophysical properties of **1**-**3** in solution.

	λ_{abs} (nm)	λ_{emis} (nm)	φ_{fl} (%)	$E[S_1]$ (eV)	$E[T_1]$ (eV)	$\Delta E([S_1]-[T_1])$ (eV)	φ_{Δ} (%)
1	486	499	65 ± 5	2.51	1.30[a]	1.21	14 ± 3
2	500	510	55 ± 4	2.46	1.23[a]	1.23	20 ± 4
3	518	553	9 ± 2	2.25	2.01	0.24	50 ± 8

[a] Iodoethane is used as solvent

4.3.3 Triplet quantum yield

Singlet oxygen ($^1\Delta_g$) emission from the samples in CH_2Cl_2 was measured to quantify their triplet yields (Figure 3). In CH_2Cl_2, molecule **3** has the highest singlet oxygen quantum yield of 50 ± 8 % followed by **2** (20 ± 4%) and **1** (14 ± 3 %). This trend follows the fluorescence quantum yield, where highly fluorescent molecule **1** has the lowest singlet oxygen quantum yield. Since the triplet conversion ($^3\Sigma_g^-$) into singlet oxygen ($^1\Delta_g$) is not quantitative, the singlet oxygen quantum yield gives the lower limit of triplet yield and the fluorescence quantum yield gives the upper limit. The triplet yield range for molecule **1** is 15 - 35%, 20 - 45% for **2** and 50 - 90 % for **3**. Since the phosphorescence and TREPR spectra are obtained in iodoethane, the singlet oxygen quantum yield of **1** and **2** in iodoethane was also measured to be 30 ± 2 % and 40 ± 10 % for molecule **1** and **2**, respectively.

4.3.4 Excited-state dynamics of anthanthrone and anthanthrene derivatives

FsTA spectroscopy was used to examine the singlet and triplet excited state deactivation pathways. At early times, we observed ground state bleach (GSB), stimulated emission (SE) and

singlet excited state absorption (ESA) features, while at later times, the SE feature disappears, and spectra indicative of a new species appear (**Figure 4.3**).

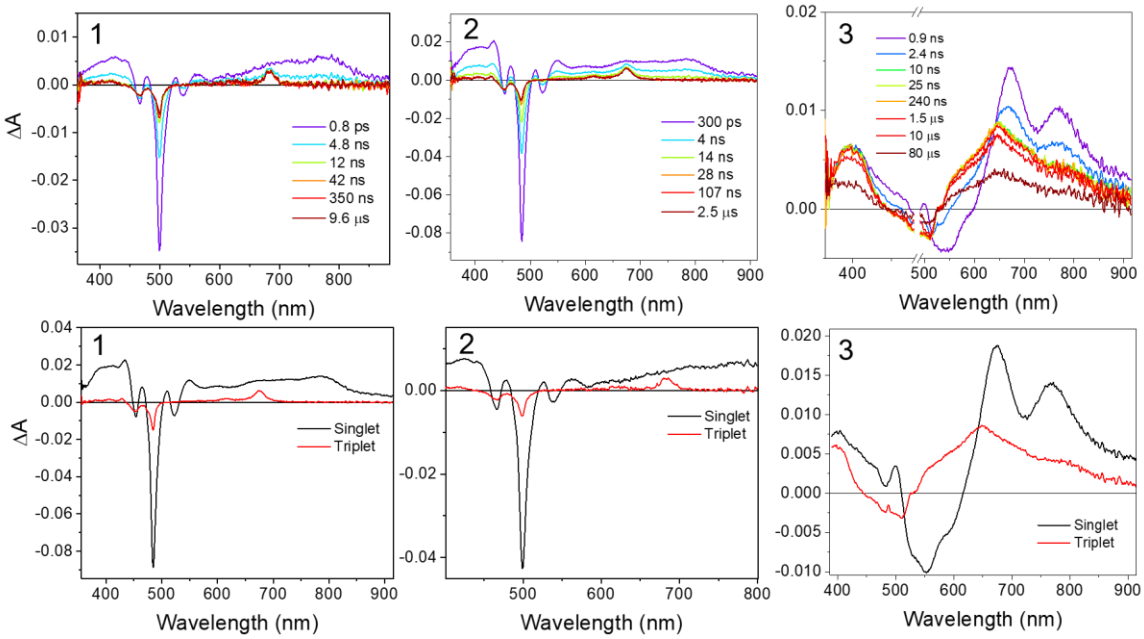

Figure 4.3. FsTA spectra of **1**-**3** in CH_2Cl_2 excited (top) and the species-associated spectra using the kinetic model A → B → GS. The wavelength fitting and population vs. time plots are shown in **Figure 4.7**.

The later time features are assigned to the triplet state because we observe singlet oxygen emission and the lifetime of this long-lived species increases when the sample is degassed. Similar to the steady-state absorption and emission spectra, the ESA in **3** is broadened compared to **1** and **2**. This broadened feature is attributed to a contribution from an n ← π^* transition.[151] Compounds **1** and **2** have spectrally well-resolved singlet and triplet features, where the singlet ESA features have a broad absorption from 350 - 900 nm overlapping with the GSB and SE, while the triplet state spectral features occur at 650 nm and 680 nm for **1** and **2**, respectively. Globally fitting the spectra using an A → B → ground state model yields the species-associated spectra, where state A is

assigned to S_1, state B is assigned to T_1, τ_A is the S_1 lifetime, and τ_B is the T_1 lifetime (**Table 4.2**). The population *versus* time and wavelength fits are shown in Figure S1 in the Supporting Information. Compound **3** has the shortest time constant for τ_A (1.8 ± 0.1 ns) followed by **2** (4.0 ± 0.1 ns) and **1** (5.0 ± 0.1 ns), where the trend agrees well with the fluorescence quantum yields. For τ_B, **3** has the shortest triplet lifetime (105 ± 1 μs), followed by **1** (185 ± 5 μs) and **2** (440 ± 10 μs). The radiative decay (k_r) and intersystem crossing (k_{isc}) rates can be approximated from the effective singlet decay time constant (τ_A) obtained from the fsTA data, as well as the fluorescence (φ_{fl}) and singlet oxygen quantum yields (φ_Δ), using the following equations:

$$k_r = \frac{1}{\tau_A} \cdot \varphi_{fl} \qquad \text{(eq. 4.2)}$$

$$k_{isc} = \frac{1}{\tau_A} \cdot \varphi_\Delta \qquad \text{(eq. 4.3)}$$

Assuming that the triplet yield is equal to singlet oxygen quantum yield, the calculated lower limit for the intersystem crossing rate is given in **Table 4.2**.

Table 4.2. Excited state lifetimes of S_1 and T_1.

	τ_A (ns)	τ_B (μs)	k_r (10^8 s^{-1})	k_{isc} (10^8 s^{-1})
1	5.0 ± 0.1	185 ± 5	1.3 ± 0.1	0.28 ± 0.06
2	4.0 ± 0.1	440 ± 10	1.4 ± 0.1	0.5 ± 0.1
3	1.8 ± 0.1	105 ± 1	0.5 ± 0.1	2.7 ± 0.4

4.3.5 TREPR spectroscopy studies of the intersystem crossing mechanism

TREPR data were collected to identify the mechanism of triplet state formation. Following photoexcitation at 85K in frozen iodoethane and toluene, compound **1** shows a 4-line, spin-polarized TREPR spectrum that is indicative of an axially symmetric electron distribution in T_1 with an (*e*,*a*,*e*,*a*) pattern, where *a* = enhanced absorption and *e* = emission from low to high field (**Figure 4.4**).

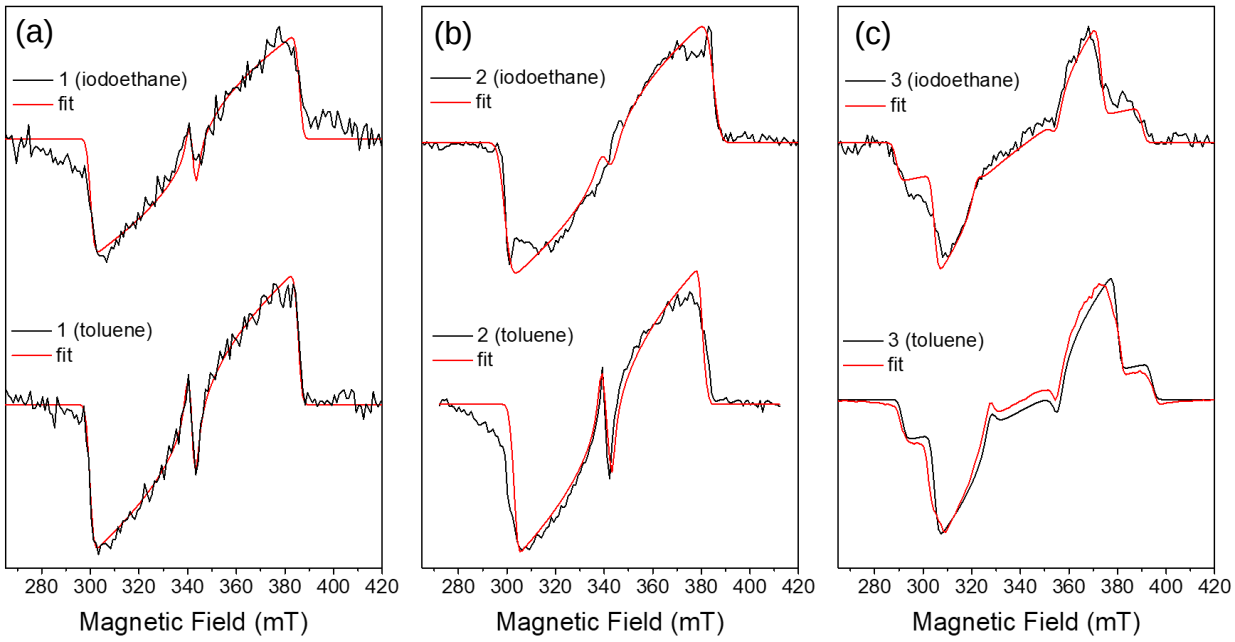

Figure 4.4. TREPR spectra at 9.5 GHz and 85 K of the triplet states of (a) **1** (λ_{ex}= 495 nm), (b) **2** (λ_{ex}= 485 nm) and (c) **3** (λ_{ex} = 520 nm) in iodoethane (top) and in toluene (bottom).

Simulation of the spectrum shows that the triplet zero-field states T_x, T_y and T_z are populated via SO-ISC with relative rates of P_x:P_y:P_z = 0.14:0.48:0.38 in iodoethane and P_x:P_y:P_z = 0.20:0.45:0.38 in toluene (**Table 4.3**). Compound **3** has a 6-line TREPR spectrum spin-polarized TREPR spectrum characteristic of an electron distribution in T_1 having rhombic symmetry with a dominant (*e*,*e*,*e*,*a*,*a*,*a*) polarization pattern, where T_1 populated via SO-ISC with relative rates of P_x:P_y:P_z =0.23:0.77:0 in iodoethane and Px:Py:Pz = 0.14:0.83:0.03 in toluene. In contrast, the TREPR

spectrum of **2** has a different polarization pattern in toluene versus iodoethane. In toluene, the triplet zero-field states T_x, T_y and T_z are populated via SO-ISC with relative rates of P_x:P_y:P_z = 0:0.77:0.23 similar to compound **1** in toluene; in iodoethane, however, there is additional sharp features at the low and high field edges, which cannot be fit using the SO-ISC mechanism alone (**Figure 4.4**). For example, the fit shown in **Figure 4.4b** assumes that only SO-ISC occurs, and yields an axially symmetric spectrum with an (*e*,*a*,*e*,*a*) polarization pattern and relative populations rates of P_x:P_y:P_z = 0.23:0:0.77; however, the deficiencies in the fit are apparent at 310 and 380 mT along with the center feature.

Table 4.3. ZFS parameters (|D| and |E|) and relative population rates P_{xyz}.

	|D| (MHz)	|E| (MHz)	|E|/|D|	P_x	P_y	P_z
1[a]	1215	397	0.32	0.14	0.48	0.38
1[b]	1215	397	0.32	0.20	0.45	0.35
2[a]	1233	380	0.31	0.11	0.89	0
2[b]	1240	360	0.29	0	0.77	0.23
2[c]	1080	249	0.23	-	-	-
3[a]	1416	167	0.12	0.23	0.77	0
3[b]	1440	221	0.15	0.14	0.83	0.03

[a] compound is in [a] iodoethane and [b] toluene. [c] SF-ISC parameters in compound **2**.

It has been shown previously in both polyacenes and terrylenediiimides that singlet exciton fission can result in formation of an initial spin-correlated triplet pair state $^1(T_1T_1)$ that can intersystem cross to first give a quintet spin state $^5(T_1T_1)$, which can then separate to form two T_1

states.[52, 124, 161-163] The quintet state is formed with its $m_s = 0$ sublevel greatly overpopulated, so that this initial non-Boltzmann spin population is carried over to the $m_s = 0$ sublevel of the T_1 states. As a consequence, the resulting TREPR spectrum of T_1 has the same (*a,e,e,a,a,e*) spin polarization as is typically observed for the radical-pair intersystem crossing mechanism.[164] We will label this mechanism singlet fission intersystem crossing (SF-ISC). **Figure 4.5** shows that the T_1 spectrum of **2** is best simulated with a linear combination of SF-ISC (47%) and SO-ISC (53%). Since the concentration of **2** for the TREPR experiments is high, presumably some small aggregates form in the frozen solvent matrix, which undergo singlet fission resulting in the $m_s = 0$ populated triplet states.

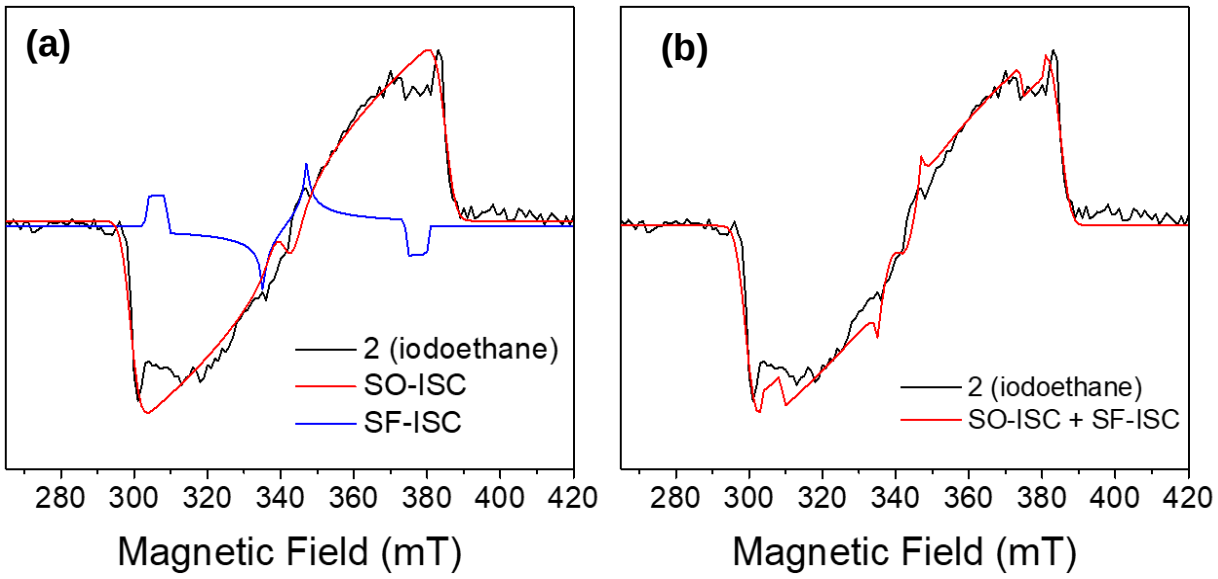

Figure 4.5. TREPR spectral fitting using (a) SO-ISC and SF-ISC and (b) linear combination of 53% SO-ISC and 47% SF-ISC.

Although the concentrations of **2** in toluene and in iodoethane are same, the SF-ISC feature is only observed in iodoethane. Since the heavy atom effect in iodoethane does not change the

triplet polarization pattern in compounds **1** and **3**, we attribute the appearance of the SF-ISC triplet in compound **2** to a change in the electronic coupling among the aggregated molecules of **2**. Aggregation of **2** in solution is indicated by the change in vibronic peak ratio in its steady state absorption spectrum (**Figure 4.9**). In addition, the difference in $|D|$ and $|E|$ values between SO-ISC and SF-ISC triplets (**Table 4.3**) indicates different types of aggregate formation in toluene *versus* iodoethane. It has been shown that $|D|$ and $|E|$ values are different between herringbone and parallel orientations of dilute pentacene films due to a change in the dipolar coupling.[66] The smaller $|D|$ value of compound **2** in iodoethane indicates that the electron distribution in the triplet state is more delocalized in the aggregate formed in iodoethane than it is in toluene. On the other hand, triplet spectrum of **1** in frozen iodoethane can be fit exclusively using the SO-ISC mechanism indicating that aggregates favorable for singlet fission may not form upon cooling solutions of **1** to 85K, or if they do form, either their geometry or energetics are inadequate for singlet fission.

4.3.6 Comparison of experimental and computed excited state energies

In order to understand the S_1 and T_1 energy trends, TDDFT calculations were performed and the results are listed in **Table 4.4**.

Table 4.4. Comparison of Experimental and Computed (TDDFT) values of $E[S_1]$ and $E[T_1]$

	$E[S_1]$ (eV)	$\Delta E([S_1]_{exp}\text{-}[S_1]_{calc})$	$E[T_1]$ (eV)	$\Delta E([T_1]_{exp}\text{-}[T_1]_{calc})$
1	2.45	0.06	1.08	0.22
2	2.37	0.09	1.05	0.18
3	2.62	-0.37	1.56	0.45

Comparing the $E[S_1]$ and $E[T_1]$ values of the derivatives studied here to previously reported anthanthrene and anthanthrone derivatives,[151] which have phenyl and *t*-butylphenyl groups at the 4-, 6-, 10- and 12-positions, $E[S_1]$ and $E[T_1]$ are lower in molecules **1-3**; however, molecules **1** and **2** have a greater S_1-T_1 energy gap relative to previously studied anthanthrene derivatives. Such energetics are desirable for potential applications including singlet fission and/or fusion. For instance, **1** and **2** absorb strongly in the blue region of the visible spectrum and twice the triplet energy is slightly uphill for **1** by only 0.09 eV, S_1 and $2 \times T_1$ are nearly isoenergetic for **2**. Tetracene and perylenediimide systems undergo near quantitative singlet fission despite the fact that this process is endoergic by about 0.2 eV.[19, 153]

Comparing the singlet excited state dynamics in the molecules studied here to the previously reported anthanthrenes, both **1** and **2** are highly fluorescent similar to phenyl and *p*-(*t*-butylphenyl substituted anthanthrene derivatives.[151] Fluorescence is the major deactivation pathway in **1** and **2**; however, **3** has a low fluorescence quantum yield because SO-ISC is competitive with fluorescence decay. Compound **3** has an order of magnitude faster SO-ISC rate compared to **1** and **2**. The smaller S_1-T_1 energy gap (0.24 eV) allows for efficient SO-ISC in **3**. Although the energy gap in **2** is greater than in **1**, SO-ISC is almost twice as efficient in **2** relative to **1**. This could be due to having greater spin-orbit coupling in **2** compared to **1** because there are four TIPS groups; however, as shown in Figure 6, it is more likely that some of the singlet excited state population of **2** may undergo singlet fission, which is a spin-allowed process, to enhance the triplet formation yield.

4.4 Conclusions

We were able to tune the singlet and triplet energies of anthanthrene and anthanthrone derivatives by the addition of TIPS and ethynyl groups at the 4-,6-,10- and 12-positions.

Compound **3** has the largest SO-ISC rate and highest triplet yield, followed by **2** and **1**. Since **3** has the smallest S_1-T_1 energy gap, SO-ISC is significantly enhanced. Although, **1** has a smaller S_1-T_1 energy gap than **2**, the latter undergoes faster ISC attributed to a small population of singlet excitons undergoing singlet fission based on the triplet polarization pattern observed in its TREPR spectrum. Based on the work shown here, derivatives based on **1** and **2** are promising molecules for singlet fission and/or fusion applications.

4.5 Acknowledgements

This work was supported by the U.S. Department of Energy, Office of Science, Office of Basic Energy Sciences under Award DE-FG02-99ER14999 (M.R.W.). This work made use of the IMSERC at Northwestern University, which has received support from the Soft and Hybrid Nanotechnology Experimental (SHyNE) Resource (NSF ECCS-1542205), the State of Illinois, and the International Institute for Nanotechnology (IIN). Y.B. thanks Charlotte Stern for helpful discussions regarding X-ray work. M.B.M. acknowledges support from the Natural Sciences and Engineering Research Council of Canada and Fonds de recherche du Québec – Nature et technologies.

4.6 Supplementary Information

4.6.1 Single crystal structure and x-ray spectroscopy

Table 4.5. Summary of crystal parameters for **1** and **2**

	1	**2**
a	18.870 (5) Å	21.5828 (6) Å
b	7.1479 (2) Å	10.8876 (3) Å
c	14.340 (8) Å	26.3757 (4) Å
α	90 °	90 °
β	97.701 (5) °	90 °
γ	90 °	90 °
Z	2	4
V	1916.8 (8) $Å^3$	6197.9 (3) $Å^3$
CCDC	1937383	1937384

4.6.2 Singlet Oxygen

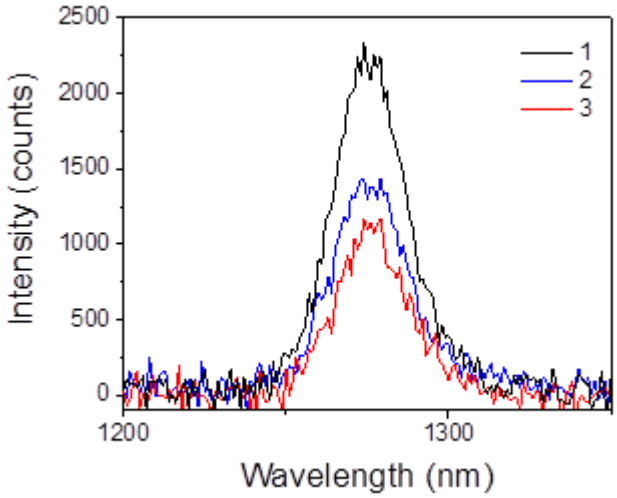

Figure 4.6. Singlet oxygen emission spectrum of **1-3** in CH_2Cl_2

4.6.3 Global Kinetic Analysis

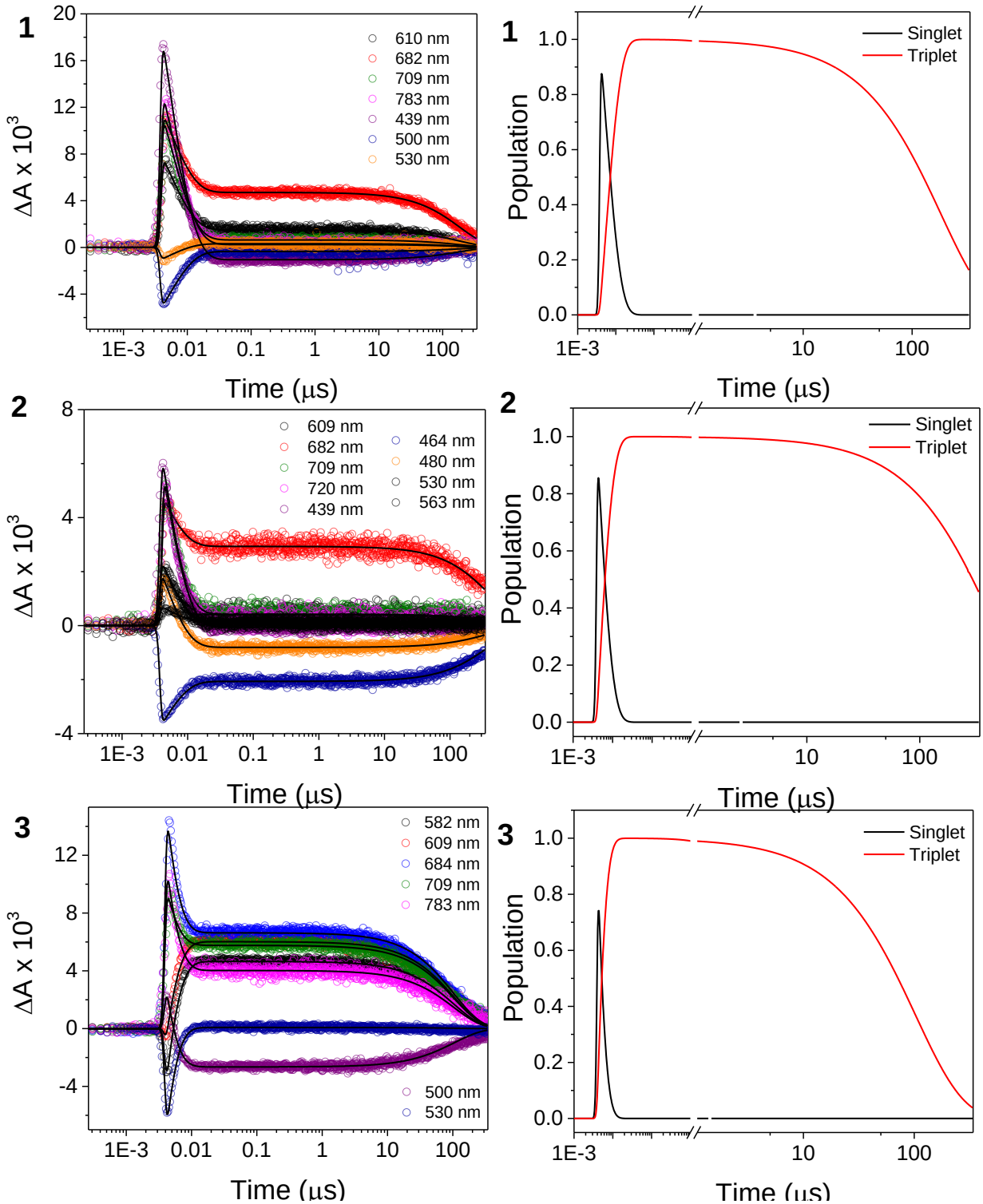

Figure 4.7. Wavelength fitting (left) and population vs time plots (right) using the kinetic model A → B → GS.

4.6.4 TREPR

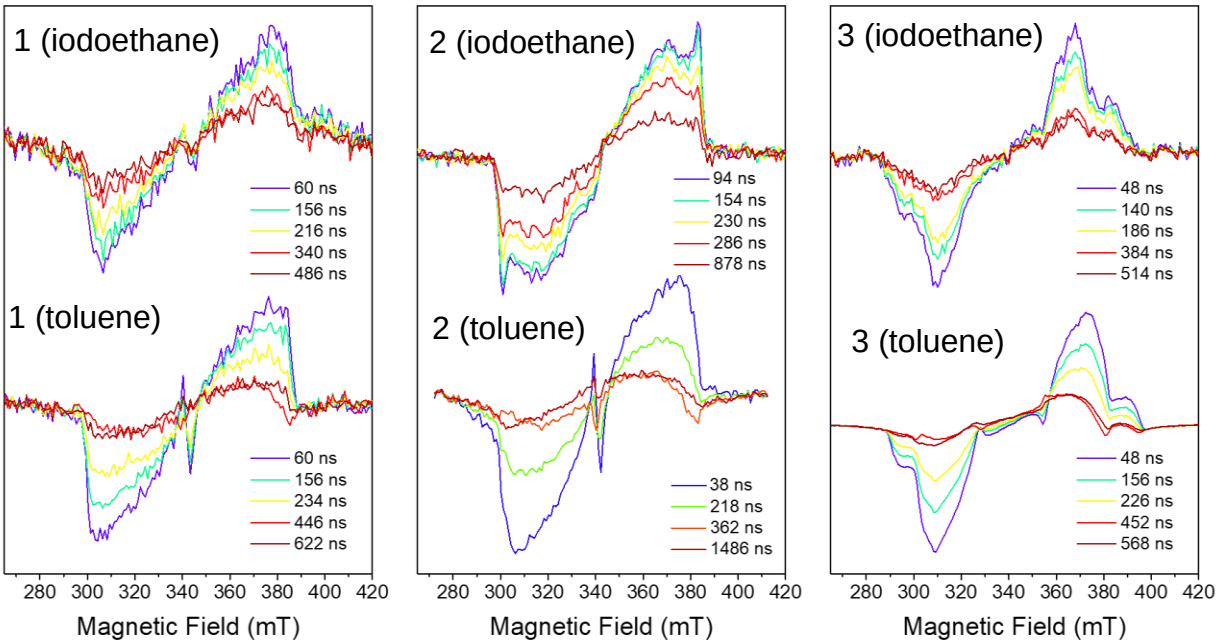

Figure 4.8. TREPR spectra at 9.5 GHz and 85 K of the triplet states of **1** (λ_{ex}= 495 nm), **2** (λ_{ex}= 485 nm) and **3** (λ_{ex} = 520 nm) in iodoethane (top) and in toluene (bottom).

4.6.5 Steady-state absorbance in toluene and iodoethane

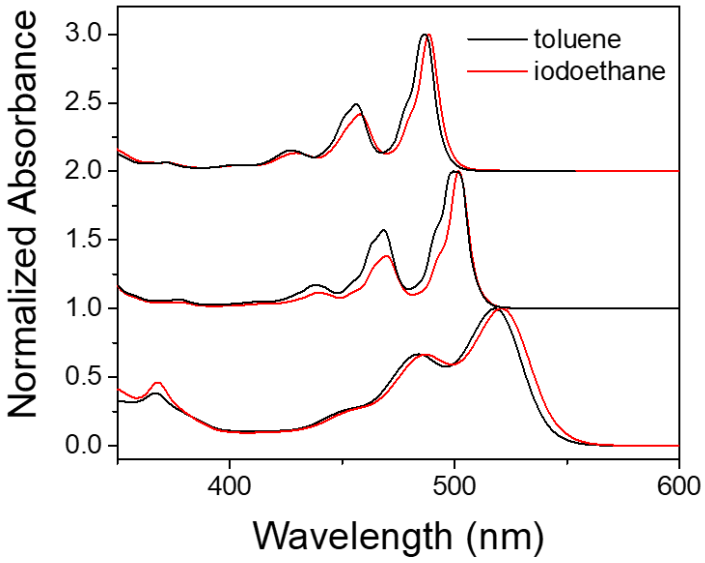

Figure 4.9. Steady-state absorbance of **1**-**3** in toluene (black) and iodoethane

Chapter 5. Spin Dynamics of Quintet and Triplet Resulting from Singlet Fission in Oriented Terrylenediimide and Quaterrylenediimide Films

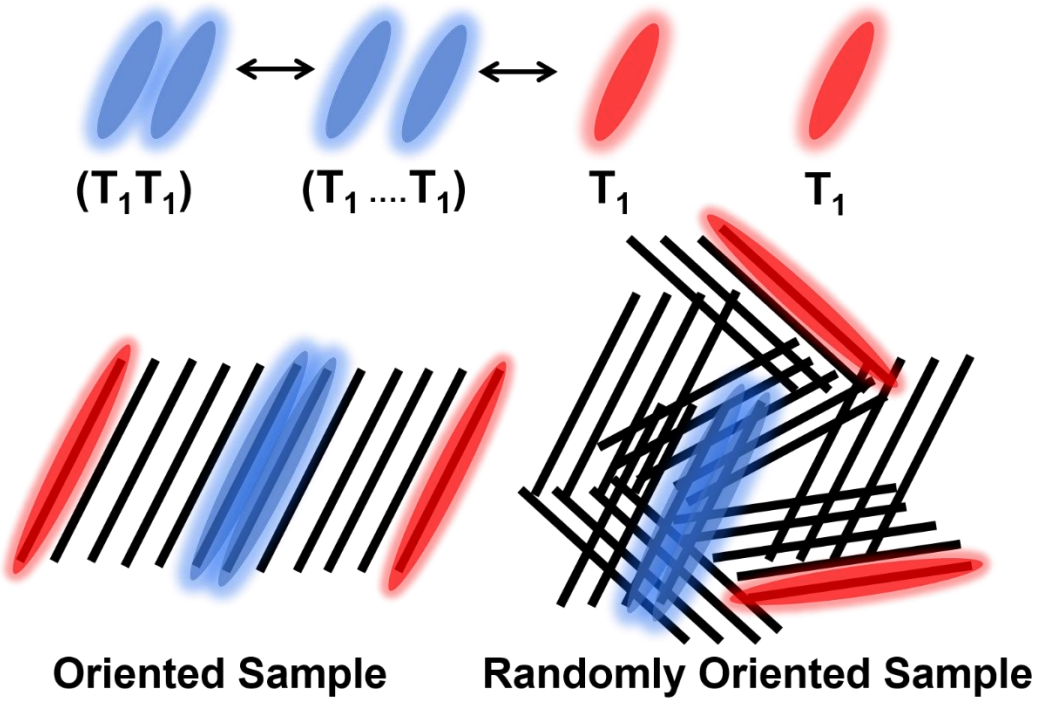

The result of this chapter is published in and adapted with permission from *J. Phys. Chem. C* 2020, 124, 18, 9822–9833.

5.1 Introduction

Understanding spin dynamics in organic semiconductors is essential to the fields of organic photovoltaics,[28, 165] organic-inorganic optoelectronics,[113, 114] and quantum information science.[63] Among the many relevant spin-dependent photophysical processes, singlet fission (SF) is particularly interesting due to its ability to produce quantum entangled quintet and triplet states. SF involves two adjacent chromophores for which absorption of a photon by their ground state $^1(S_0S_0)$ produces a singlet exciton $^1(S_1S_0)$ that is rapidly converted in a spin-allowed process to a correlated triplet pair state, $^1(T_1T_1)$, having an overall singlet spin configuration. This process usually requires $E(S_1) \geq 2E(T_1)$, although SF has also been observed when the process is slightly uphill in energy. Once $^1(T_1T_1)$ is formed, it may rapidly dissociate to form two independent triplet (T_1) states,[3-5] or if dissociation is slow, spin evolution of $^1(T_1T_1)$ can produce the high-spin quintet state $^5(T_1T_1)$ and/or triplet state $^3(T_1T_1)$. The fate of these intermediate states is determined by the degree of mixing with $^1(T_1T_1)$.[166] Since formation of $^1(T_1T_1)$ usually occurs on the fs-ps time scale, transient absorption and emission spectroscopies have been used as primary tools to investigate its excited state dynamics;[33, 35, 51, 54, 112, 167] However, such optical techniques do not provide information about the spin dynamics of these systems due to similarity among electronic energies of the multiple spin states of the correlated triplets $^m(T_1T_1)$.

Recently, there has been an increase in the usage of time-resolved electron paramagnetic resonance (TREPR) spectroscopy to investigate the pin dynamics that occur following generation of $^1(T_1T_1)$ by SF. The majority of TREPR investigations involve covalent dimers,[3, 5, 168, 169] and there exist only few studies of thin solid films.[63, 67, 170] This stems from the fact that covalent dimers provide fine control of interchromophore geometries and electronic interactions; however, understanding the spin evolution of the initial $^1(T_1T_1)$ state, as well as exciton migration and

annihilation in the solid state is critical for device applications. Furthermore, film studies using TREPR have been conducted largely on pentacene and tetracene derivatives.[36] It is equally important to investigate diverse SF chromophores to obtain a deeper understanding of how different molecular structures influence (T_1T_1) state spin dynamics.

In this work, we study spin dynamics of the SF chromophores *N*,*N*-bis(pentadecan-8-yl)terrylene-3,4:11,12-bis(dicarboximide) (**TDI**) and *N*,*N*`-bis(pentadecan-8-yl)quaterrylene-3,4:13,14- bis(dicarboximide) (**QDI**) in thin films. Rylenediimides have received much attention in diverse applications as a result of their chemical and photochemical stability[171] as well as excellent chemical tunability.[59, 119] Various derivatives of perylenediimide[19, 59] and **TDI**[20] have been reported to undergo efficient SF. Also, both theoretical[21, 172] and experimental[21, 172] work on crystalline **QDI** derivatives have shown that they can undergo rapid and efficient SF. Besides the ability to undergo SF efficiently, rylenediimides are also known to crystallize well because of strong intermolecular π-π interactions.[173] In this work, we investigate the structure-function relationship of the spin dynamics of $^5(T_1T_1)$ and the two T_1 states resulting from its dissociation in **TDI** and **QDI** films by correlating crystallographic and TREPR data.

We fabricated two different types of thin film samples where one has crystalline domains that are randomly oriented on the inside surface of a quartz tube, while the other is a highly oriented film on a flat glass substrate. Based on the crystallographic information, we will call the first sample polycrystalline powder sample and the second sample, polycrystalline textured film. At cryogenic temperatures, both exciton and spin diffusion are slow enough that we observe the high-spin quintet, $^5(T_1T_1)$ and triplet, $^3(T_1T_1)$, followed by dissociation into the two separate T_1. Utilizing the zero-field splitting (ZFS) anisotropy of these states, we obtain their molecular orientation relative to the plane of the substrate. The molecular orientations obtained from TREPR

measurements are in good agreement with the crystallographic data, further supporting the high crystallinity of the films as well as the orientation dependent spin dynamics. In the polycrystalline textured samples, the dissociated T_1 states remember their orientation in the $^{m}(T_1T_1)$ state, and spin dynamics changes depending on the orientation of the molecules with respect to the magnetic field. . In addition, we observe different spin dynamics between **TDI** and **QDI**, which arises from difference at molecular level**.** The **TDI** films undergo rapid $^{m}(T_1T_1)$ state formation and dissociation to form triplet excitons, while these processes in the **QDI** films are slower. Moreover, the resulting triplet excitons have longer lifetimes in the **TDI** films relative to the **QDI** films.

5.2 Experimental Details

5.2.1 Synthesis of TDI and QDI.

TDI and **QDI** were synthesized according to the methods described previously.[174, 175]

5.2.2 Film Sample Preparation.

A solution consisting of 10 mg/ml of **TDI** and **QDI** in CH_2Cl_2 was drop-cast onto a glass substrate followed by chlorobenzene solvent vapor annealing for 15 minutes. For TREPR measurements these films were cut into thin slices to fit into a 2.8 mm i.d. quartz tube. The films are fixed with epoxy on one side to avoid movement upon rotation of the tube relative to the applied magnetic field B_0 during TREPR measurement. A solution of the same concentration was also used to coat the wall of a 2.8 mm i.d. quartz tube. The solution was evaporated inside the tube using house vacuum while the tube was rotated to achieve a homogenous coating. The samples coated on the tube walls were also annealed using chlorobenzene solvent vapor.

5.2.3 Steady-state absorption and emission.

The steady-state absorption of the film samples was measured using a Shimadzu UV-3600 UV/Vis/NIR spectrometer equipped with an integrating sphere. Steady-state fluorescence spectra of solution and film samples were measured in the front face mode with a HORIBA Nanolog

spectrofluorimeter equipped with an integrating sphere (Horiba Quanta - φ) for absolute fluorescence quantum yield determination.

5.2.4 Single crystal structures.

Crystals of **TDI** and **QDI** were grown by slow solvent diffusion. Methanol and acetonitrile were used as anti-solvents for growing single crystals of **TDI** and **QDI** in nitrobenzene, respectively. The crystals were mounted on a polymer loop with Paratone oil, and the data were collected at 250 K on a Bruker Kappa APEX II CCD diffractometer equipped with a Cu Kα 1 μS microfocus source. Although the **TDI** crystal diffracts well enough for the entire structure to be solved, we were only able to obtain unit cell parameters for the **QDI** crystal. The reported unit cell parameters for **QDI** (**Table 5.3**) are from multiple measurements of different crystals. In order to predict the **QDI** powder pattern, we modified the unit cell parameters of **TDI** to those of **QDI**, using Olex 2 and Mercury (**Figure 5.10**). The experimental powder pattern of **QDI** crystals is obtained using the same set up for the single crystal measurement with increased detector distance. Since the predicted powder pattern matches well with the experimentally obtained powder pattern of **QDI**, we conclude that both **TDI** and **QDI** have similar packing structures. For the **TDI** crystal, the data were absorption-corrected using SADABS. The structure was solved using SHELXT and refined using SHELXL using Olex 2 software.[132] The **TDI** structure has been deposited in the Cambridge Crystallographic Data Centre database (CCDC #1978605). Additional single crystal structural data is reported in supporting information Table S1.

5.2.5 GIWAXS data on thin films.

Grazing-incidence, wide-angle X-ray scattering (GIWAXS) measurements were performed on thin film samples at the dedicated high-resolution grazing-incidence X-ray scattering beamline 8-ID-E at the Advanced Photon Source at Argonne National Laboratory.[176] A 10.91 keV, 1.136 Å

X-ray beam at an incident angle of 0.14° was directed at the sample, maximizing scattering from the film while minimizing glass substrate scattering. Scattered light was collected with a Pilatus 1 M detector 228 mm from the sample. GIXSGUI applied corrections for pixel efficiency, polarization, flat field and solid angle[177] to the 2D GIWAXS data files and also converted them from pixel space to the scattering vector components $(qx, qy, qz) = (2\pi/\lambda)(\cos(\alpha_f)\cos(2\theta_f) -\cos(\alpha_i), \cos(\alpha_f)\sin(2\theta_f), \sin(\alpha_f)+\sin(\alpha_i))$, where λ is the X-ray wavelength, α_i is the incident angle, α_f is the exit angle in the q_x-q_z plane and $2\theta_f$ is the total scattering angle in the q_x-q_y plane.

Using the 2D GIWAXS data, pole figure analysis was done using the linefit function recently added to the GIXSGUI package[177] in MATLAB, similar to work reported previously.[178] We constructed pole figures from the 2D GIWAXS data considering only one quadrant of the data and integrating over 30 regions spanning 3° in χ, the polar angle in the q_z vs q_r ($q_r=(q_x^2+q_y^2)^{1/2}$)representation of the data. For each region in χ ranging from the out-of-plane ($\chi = 0°$) to the in-plane direction ($\chi = -90°$), the integration yielded the dependence of the intensity on the magnitude of the scattering vector q, $I\chi(q)$. The fits in each region included a sloping background and one pseudo-Voigt function to capture the scattering feature of interest. The integrated areas were used to construct the experimental pole figure for the specific scattering features. Assuming the symmetry of the scattering, the experimental pole figure data from the range of $-90 < \chi < 0$ were reflected to construct the pole figure over the range of $-90° < \chi < 90°$. The pole figures were then fitted using multiple pseudo-Voigt functions and a constant term to obtain an analytical expression for the pole figure that interpolates the region near $\chi=0°$ where the GIWAXS geometry prevents direct observation of the scattering intensity.[179, 180] Working from these analytical expressions, we

integrated the pole figure to calculate the intensity-weighted mean orientation ($\bar{\chi}$) of molecular c-axis using the following equation:

$$\bar{\chi} = \frac{\left(\int_{0^\circ}^{90^\circ} \chi \cdot \sin(\chi) \cdot I(\chi) \cdot d\chi\right)}{\left(\int_{0^\circ}^{90^\circ} \sin(\chi) \cdot I(\chi) \cdot d\chi\right)} \qquad (eq. 5.1)$$

Based on $\bar{\chi}$, we then calculated molecular orientation from the GIWAXS data.

5.2.6 TREPR spectroscopy.

X-band (~9.6 GHz) measurements were made using a Bruker Elexsys E680-X/W EPR spectrometer outfitted with a split-ring resonator (ER4118X-MS3). TREPR spectra of **TDI** and **QDI** were acquired at varying temperatures upon photoexcitation with a 7 ns (3 mJ/pulse) laser pulse generated by an optical parametric oscillator (Spectra-Physics Basi-scan), pumped with the output of a frequency-tripled Nd-YAG laser (Spectra-Physics Quanta-Ray LAB-170). The kinetic traces of the transient magnetization were acquired in quadrature under continuous microwave irradiation (5 mW). The randomly oriented sample was measured at one specific angle and the oriented film sample was measured by rotating the sample. The same spots were measured in duplicate to perform error analysis. Due to heterogeneity of the film samples, different spots showed somewhat different dynamics. The TREPR spectra were processed in MATLAB and the spectral simulations were performed using the function *pepper* present in the EasySpin.[160] The individual transition among m_s sublevls from the *pepper* function in the EasySpin is linearly scaled to fit the correlated and separated triplet spectra. Here, we assumed isotropic population of Q_0 and T_0; however, in theory SQ mixing is magnetic-field dependent and the sublevel transition should be treated anisotopically as shown in the previous work.[181] In addition, time dependent spin-exchange coupling (J) can to be accounted to predict the spectra.[4, 64] The θ value which is an angle between the molecular z-axis and the incident magnetic field, to fit spectra of the polycrystalline

texture film has gaussian distribution with center θ value and full width at half maximum specified in **Table 5.6-5.7**.Further details of the spectral fitting parameters are shown in the supporting information.

5.3 Results

5.3.1 Steady-state optical properties.

Since small differences in molecular structure can modify the packing structure significantly,[23, 33, 182] which ultimately changes the excited state energies of the chromophores, we obtained the steady-state absorbance and emission spectra of both types of **TDI** and **QDI** films (**Figure 5.1**). The solid films of these chromophores have significantly broader spectra than in solution due to long-range exciton interactions in the closely packed solid samples.[88] However, the spectra of the films on the tubes and flat glass substrates are similar. The steady-state emission spectra are shown in **Figure 5.9**. The fluorescence quantum yields of the films are low (< 1%), similar to the reported **TDI** and **QDI** films, where efficient SF was observed.[20,21] The singlet excited state energy $E(S_1)$, is estimated from the onset of steady-state absorbance and emission where $E(S_1)$ of **QDI** is 1.30 eV and that of **TDI** is 1.64 eV. The excited state triplet energy, $E(T_1)$ of **TDI** is reported to be less than 0.77 eV,[131] and that of **QDI** is calculated by using TDDFT to be 0.62 eV.[21] Based on these excited state energies, both **TDI** and **QDI** films studied here satisfy the energetic requirement for SF: ($E(S_1) \geq 2E(T_1)$).

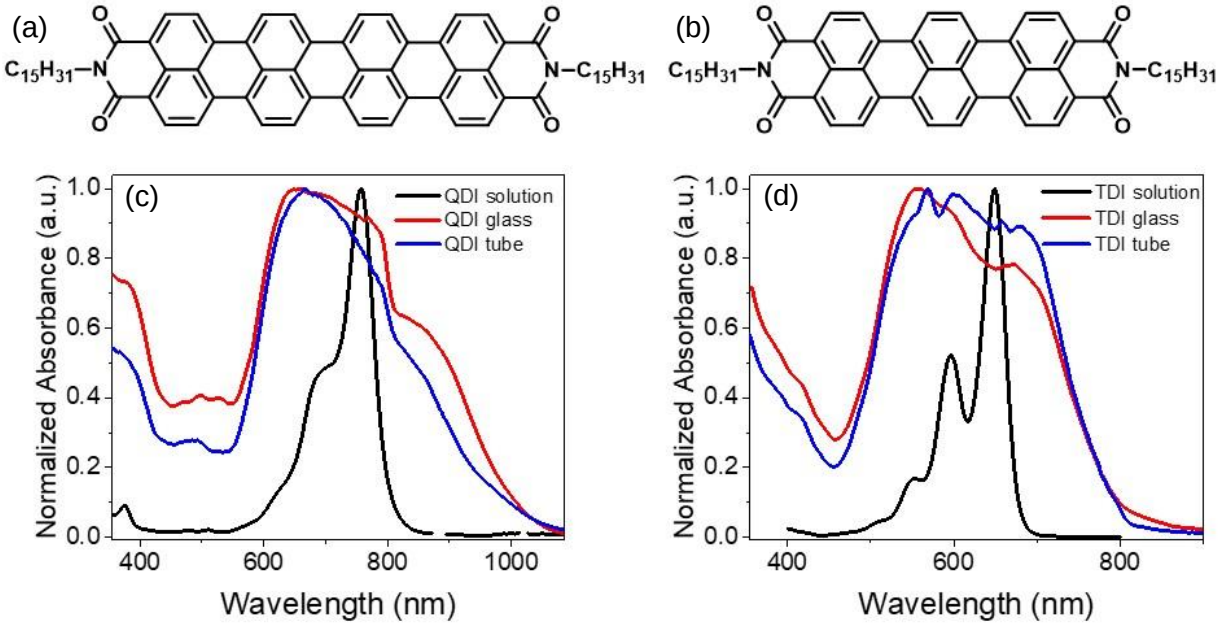

Figure 5.1. Molecular structure of (a) QDI and (b) TDI. The steady state absorbance of (c) the QDI and (d) the TDI film on a flat glass substrate and inside a quartz tube overlaid with its solution spectrum.

5.3.2 X-ray structural analysis.

In order to obtain 3D packing information for the film samples, we grew single crystals of the **TDI** and **QDI** molecules. Although the **TDI** crystal structure was solved, due to the large degree of disorder in **QDI**, we were only able to obtain its unit cell parameters (**Table 5.3**); however, changing the unit cell parameters of **TDI** into those of **QDI** generates a predicted X-ray powder pattern that matches well with the experimental powder pattern of **QDI (Figure 5.10)**. Thus, we conclude that the packing structure of the **QDI** single crystal is similar to that of **TDI**. Since the intensities of the X-ray scattering of the tube films matches closely to that of the simulated powder pattern, we conclude that the tube sample is a polycrystalline powder-like sample (**Figure 5.11**).

We further characterized the crystal structure and molecular orientation of both the tube and the flat glass substrate film samples using X-ray scattering. The line-cuts from the q_z (out-of-plane) and q_r (in-plane) GIWAXS data are in good agreement with the predicted powder pattern from the single crystal structure. Thus, we conclude that the packing structure of the film on both the quartz tube and flat glass substrates resembles that of the single crystal. However, unlike the tube samples

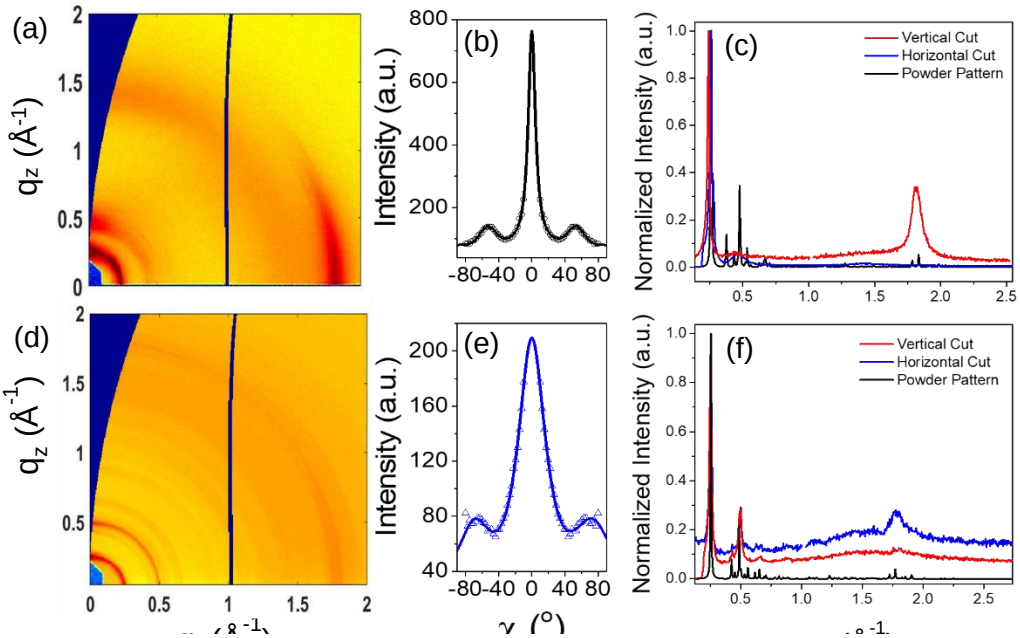

Figure 5.2. GIWAXS plot of (a) the QDI and (d) the TDI film on a glass substrate. The pole figure extracted from the most intense peak at q_r = 0.2542 Å^{-1} for (b) the QDI and q_r = 0.2535 Å^{-1} for (e) the TDI film. A comparison of line-cuts from GIWAXS to the simulated powder pattern of (c) the QDI and (f) the TDI film.

where crystalline domains are randomly oriented, the drop-cast, solvent-vapor-annealed film on the flat glass substrate is highly oriented based on the 2D GIWAXS plots (**Figure 5.2**).

For example, the intense π-π stacking peak at 1.8 Å^{-1} along the q_r direction of the 2D GIWAXS plot indicates edge-on molecular stacking where the pentadec-8-yl chains are in contact with the

substrate. Given that the film packing structure matches well with that of the single crystal structure, we can extract pole figures from the 2D GIWAXS plots and identify the molecular orientation with respect to the substrate. In the **QDI** film, the most intense peak at q_r = 0.2542 $Å^{-1}$ corresponds to a d-spacing of 24.7Å, and it matches well with the length of the c-axis of the **QDI** unit cell (24.6 Å). Similarly, the most intense peak at q_r = 0.2535 $Å^{-1}$ or d = 24.8 Å originates from the c-axis of **TDI** (24.9 Å). To describe the orientational distribution of the molecules in the thin film quantitatively, we extracted the pole figures from the most intense q_r peaks corresponding to the c-axis of the unit cell in **TDI** and **QDI** (**Figure 5.2**). The width of a pole figure gives information about the degree of order or texture in the sample, and since the **QDI** film pole figure has a narrower width, it is more strongly oriented than **TDI**. In addition to the c-axis of the unit-cell, we also extracted the pole figure from the π-π stacking peak of **QDI** (Figure S6). Since the **TDI** sample does not have a high intensity π-π stacking peak, we were not able to extract its pole-figure. By integrating the pole figure extracted from the c-axis of the unit cell, we obtain the intensity weighted mean orientation, $\bar{\chi}$, of **QDI (**52°) and **TDI** (54°). The $\bar{\chi}$ from the π-π stacking peak of **QDI** is 80°. Finally, we obtained the mean contact angle of the molecule to the substrate by calculating how the molecules are oriented with respect to their unit cell axis. There are three different molecular contact angles $\overline{\chi_m}$ (GIWAXS), which are 41°, 70°, and 83° with respect to the b-axis of the unit cell and 47°, 52° and 97° with respect to the a-axis. The molecular orientation of **TDI** in the ordered films on the flat glass substrate along with the crystallographic axes of its unit cell are given in **Figure 5.3**.

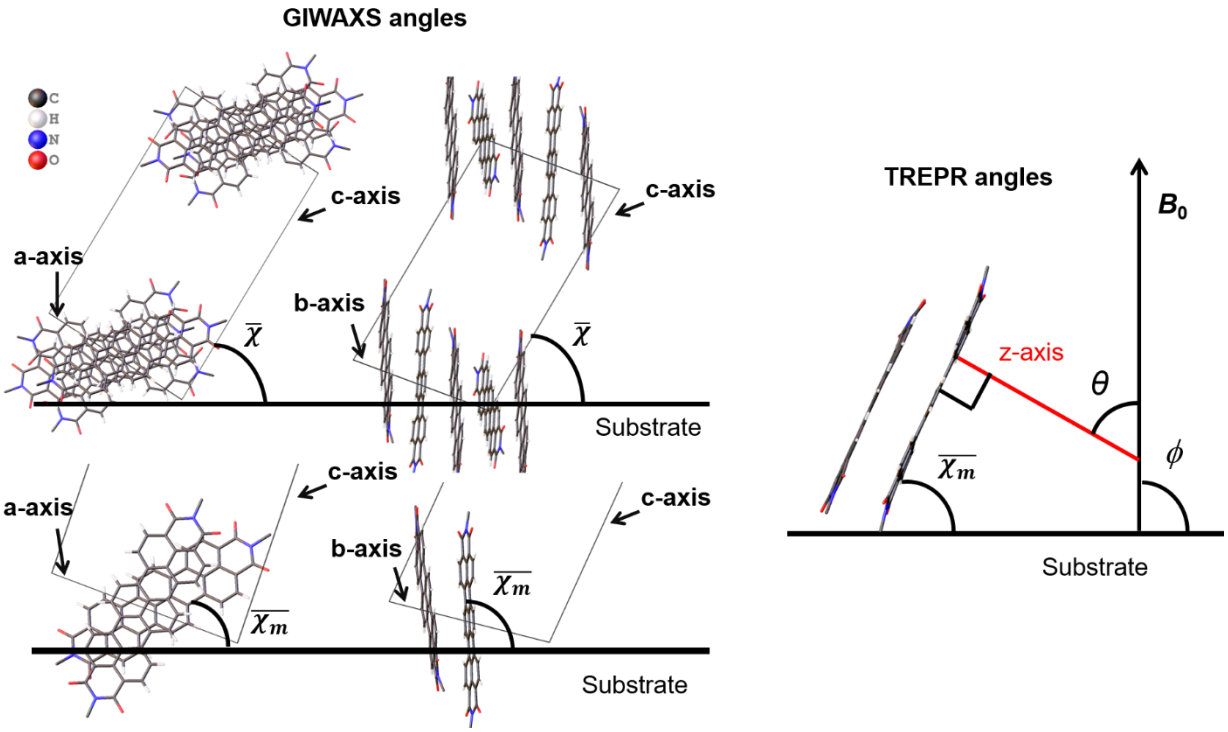

Figure 5.3. A diagram showing the orientation of **TDI** and its crystallographic axes relative to the plane of the flat glass substrate including definitions of angles $\bar{\chi}$ and $\overline{\chi_m}$ from GIWAXS data (left) and $\overline{\chi_m}$, θ, and ϕ from TREPR data (right). The substrate plane is perpendicular to the plane of the page.

5.3.3 Triplet state TREPR spectra.

The TREPR spectra of the triplet excitons in the polycrystalline powder sample confirms that the crystalline domains in the tube sample are indeed randomly oriented because the spectra are powder patterns (**Figure 5.4**); however, there seems to be some degree of preferreed orientation in polycrystalline powder **TDI** sample, since there is mismatch in the Z component between the simulated and the experimetnal triplet spectra (**Figure 5.4**)

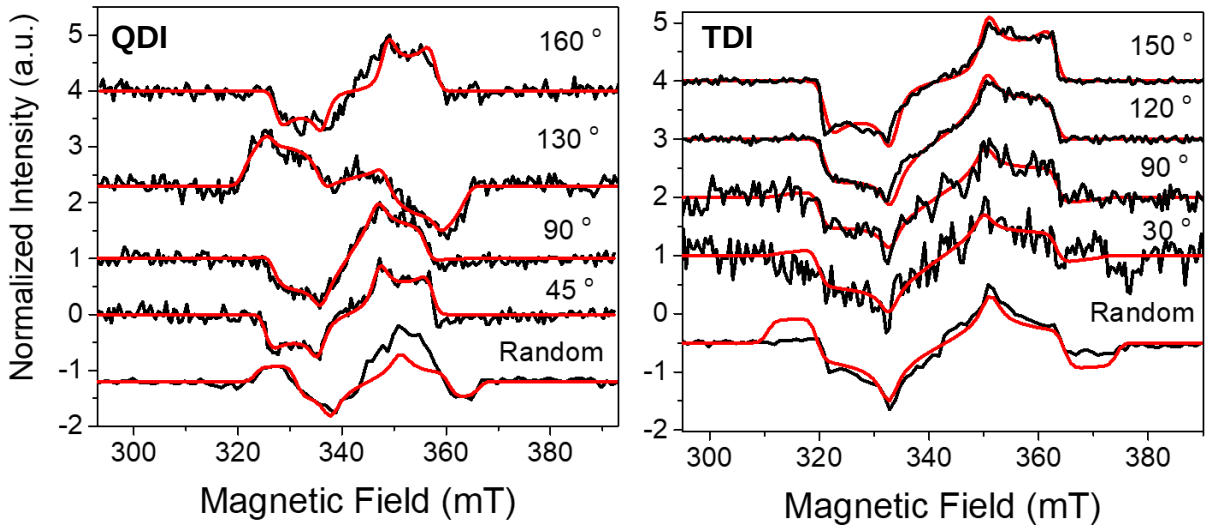

Figure 5.4. The triplet polarization pattern of the randomly oriented and the oriented samples of QDI and TDI. The black curve shows TREPR experimental data at 200 ns at the specified angle ϕ between the substrate and the magnetic field and the red curve shows the fit.

Furthermore, the spin polarization pattern of the six transitions in triplet spectra shows that triplet formation occurs by SF because the observed polarization pattern is (*a*,*e*,*e*,*a*,*a*,*e*), where *a* is enhanced absorption and *e* is emission from low-to-high B_0, which indicates selective population of the $m_s = 0$ Zeeman state.[183] As such, we can rule out triplet formation from spin-orbit intersystem crossing (ISC). The ZFS parameters, $|D|$ and $|E|$ values are 890 MHz and 122 MHz for **TDI**, and 600 MHz and 75 MHz for **QDI**. The ZFS values of **TDI** agree well with those reported for a **TDI** covalent dimer, where $|D| = 848$ MHz and $|E| = 113$ MHz.[3] The smaller $|D|$ value of **QDI** indicates that its triplet state is more delocalized than that of **TDI**, which is reasonable because the size of the π system in **QDI** is larger. The $|D|$ values of **TDI** and **QDI** are larger than those in pentacene and tetracene derivative, whereas the

trend is opposite for the |*E*| values.[170] Such differences in ZFS could change mixing among different spin states, resulting in differences in spin dynamics.[53 184]

In addition to the GIWAXS analysis, TREPR triplet spectra of the polycrystalline textured film samples can provide the molecular orientation relative to the substrate using the zero-field splitting (ZFS) anisotropy of the triplet state.[170, 185, 186] Since the principal axes of the ZFS parameters relative to the

molecular axes are known for rylenediimides,[187] where the ZFS z-axis is perpendicular to the plane of the π system, we can identify the angle (θ) between the z-axis and the applied magnetic field, B_0. Unlike the polycrystalline powder samples, the triplet spectra in the polycrystalline textured films clearly change depending on how the molecules are oriented respect to B_0 (**Figure 5.4**). As a result, the ordering parameter, θ as shown in the **Figure 5.3** is required to fit the triplet spectrum of the textured film samples (**Table 5.1**). Here the θ value is a gaussian distribution with the specified full width at half maximum as shwon in **Table 5.6** and **5.7** along with the additional fitting parameters. The simulated triplet spectra with the fixed sublevel pouplation and varying θ (**Figure 5.17**) shows clear θ dependence of the triplet spectra.

Table 5.1. The angles between the substrate plane and B_0 (ϕ), the molecular z-axis and B_0 (θ) used to fit the triplet spectra in Figure 4, and the molecular contact angle relative to the substrate plane ($\overline{\chi_m}$)from TREPR and GIWAXS measurements.

QDI	ϕ	45°	90°	130°	160°
	θ	115± 15°	70 ± 15°	45±15°	135±15°
	$\overline{\chi_m}$(TREPR)	70°	70°	5°	65°
	$\overline{\chi_m}$(GIWAXS)	70°	70°	-	70°

TDI	ϕ	30°	90°	120°	150°
	θ	70 ± 25°	85±25°	90±25°	110±25°
	$\overline{\chi_m}$(TREPR)	50°	85°	60°	80°
	$\overline{\chi_m}$(GIWAXS)	52°	83°	52°	83°

The triplet signal originates from the **QDI** molecules that have average molecular contact angles of $\langle\overline{\chi_m}\rangle$ = 68 ± 3° with respect to the substrate plane; however, when the substrate is oriented at ϕ = 130°, the triplet signal results from molecules for which $\overline{\chi_m}$ = 5° with respect to the substrate plane. Compared to the **QDI** film, the **TDI** film has a smaller degree of spectral change upon rotating the sample. When the same analysis is performed on the **TDI** film, value of $\overline{\chi_m}$ ranging from 50° to 85° are found (**Table 5.1**); thus, the average molecular orientation of **TDI** contributing to the triplet signal is $\langle\overline{\chi_m}\rangle$ = 65 ± 20°. The broader distribution of molecular orientations in the **TDI** film matches the broader width of pole figure obtained from the 2D GIWAXS data (**Figure 5.2**). If we compare the molecular orientation angles obtained from the GIWAXS data to those from the TREPR spectra, they are generally in good agreement. For instance, $\langle\overline{\chi_m}\rangle$ = 68 ± 3° observed in the **QDI** film from TREPR corresponds to $\overline{\chi_m}$ of 70° in the GIWAXS data. The **TDI** molecular orientations, $\overline{\chi_m}$, contributing to the triplet signal, which are 80° and 85° from TREPR correspond to the molecular orientation that is 83° from the GIWAXS data. Interestingly, for **QDI** film, we observe $\overline{\chi_m}$ = 5° from TREPR but do not observe a corresponding angle from the GIWAXS data. This most likely results from the fact that the crystallographic data is only sensitive to long-range order, while TREPR is sensitive to short range order as well. For instance, the X-ray diffraction peak arises from crystalline domain sizes that are in order of hundreds of nm based on the Scherrer grain size analysis (**Figure 5.12**); however,

TREPR is sensitive to triplet spectra that arise from covalent dimer that are at few Å level. As a result, presumably the different molecular orientation of $\overline{\chi_m}$ = 5° arises from local heterogentiy rather than from macroscopic crystalline domain.

5.3.4 Spin dynamics in polycrystalline powder samples.

Using our understanding of the crystal packing structure and molecular orientations in the tube and flat substrate samples, we studied their excited state spin dynamics using TREPR spectroscopy. For the polycrystalline powder samples at room temperature, we only observe the spectra originating from the dissociated triplets in both **TDI** and **QDI** (**Figure 5.16**). As the temperature is lowered to 20K, the initially observed species has a substantially narrower TREPR spectrum than that of the triplet (**Figure 5.5**), and can be readily simulated by assuming it results from strongly exchange-coupled triplet pairs forming the quintet state, $^5(T_1T_1)$, with total spin of S = 2. The simulations yield zero-field splittings of $D/3$ = 9 mT and 25 mT for the **QDI** quintet and triplet states, respectively, and $D/3$ = 13 mT and 40 mT for the **TDI** quintet and triplet states, respectively. A similar temperature dependent formation of the $^5(T_1T_1)$ state has been observed in TIPS-tetracene films.[63] In addition to the magnitude of the splitting, the similarity of the quintet spectra reported here to those reported by Nagashima *et al.*,[65] further support the assignment of the early species to $^5(T_1T_1)$. Ideally, the spin multiplicity can be identified from transient nutation experiments;[63, 65] however, due to the short $^5(T_1T_1)$ lifetimes, we could not perform nutation experiment, even at very low temperatures. We were able to obtain the relative nutation frequency between the quintet and the triplet species in **TDI** polycrystalline powder sample after subtracting the exponenital population dynamics as shown in **Figure 5.5d**. Because the relative nutation

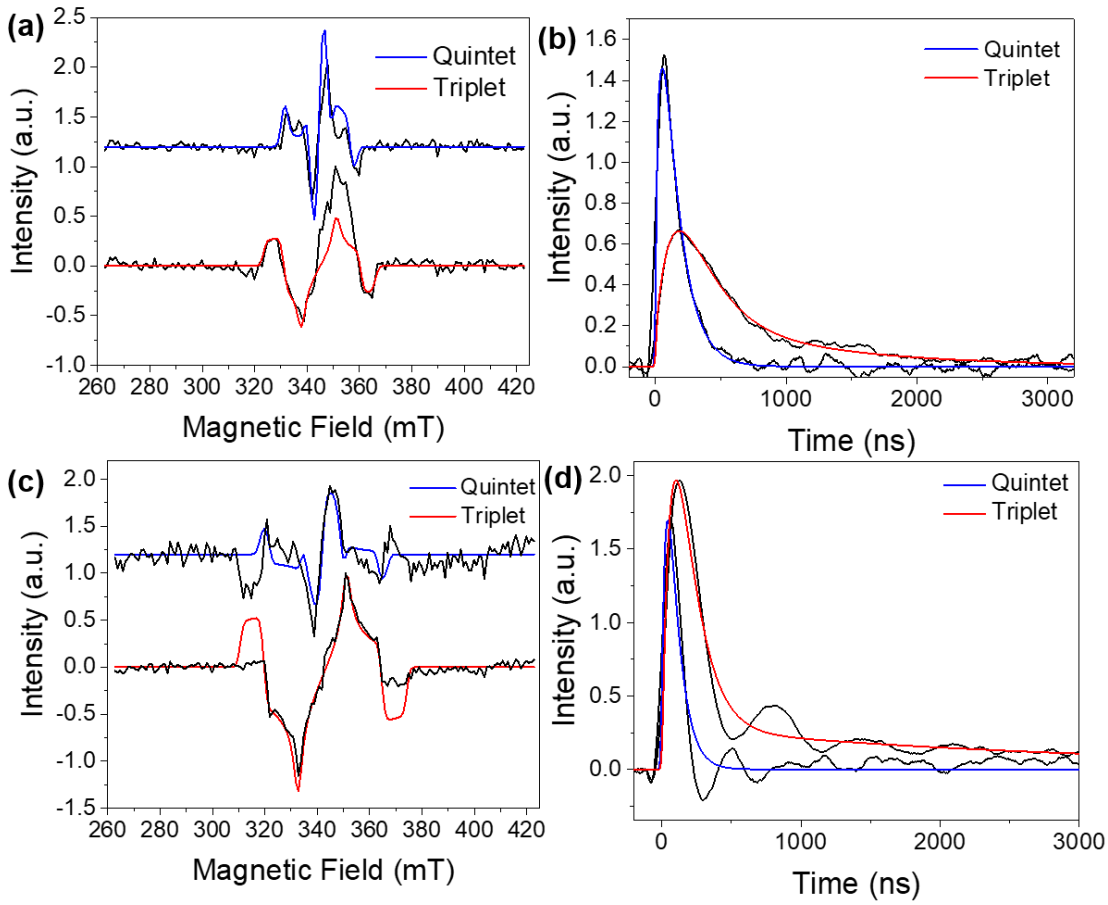

Figure 5.5. The quintet and the triplet spectral fitting of (a) QDI and (b) TDI. The kinetic traces from deconvoluting the 2D TREPR spectra of (b) QDI and (d) TDI using the (a) and (c) as basis spectra, respectively.

frequency between the quintet and the triplet is ~1.73 (**Figure 5.19**), we confirm that both quintet and triplet states come from transitions in $m_s = 0$ state. Here, the formation of the quintet undoubteldy confirms that the triplets formed in both the **TDI** and **QDI** films orginaited from SF.

Assigning the early species to $^5(T_1T_1)$ in both **TDI** and **QDI**, we fit the spectra using the parameters given in the **Table 5.4**. When simulating the quintet spectra we used large *J* value (30 GHz) because we do not observe any magnetic field effect in the relative triplet yield obtained

from femtosecond transient absorption spectrsocopy, between 0-10,000 G magnetic field (Figure S12). In addition, the same order of *J* value has been reported in polyacene solid-state films.[63, 65] It should be noted that because $^5(T_1T_1)$ decays to two T_1 excitons on a time scale that is comparable to the temporal resolution of the TREPR measurement, we cannot fully separate the quintet and triplet signals even at early times. Thus, we subtract the triplet TREPR spectrum from the early time trace (**Figure 5.17**). In addition, due to the overlapping spectral components betwee the $^5(T_1T_1)$ and T_1 even at early time, we exclude formation $^3(T_1T_1)$ in the spectral fitting. Also, we cannot distinguish the spectral feature between $^3(T_1T_1)$ and T_1. Given that the quintet wavefunction spans two different molecules, we can calculate the molecular angles between the two molecules from the crystallographic data (**Figure 5.18**). Euler angles of multiple sets of dimers from the crystal structure were used and the best fit was achieved when α, β and γ values were 1.5°, 30°, and -5°, which corresponds to dimer 2 in Figure S10. This indicates that the quintet and triplet TREPR signals originate from this set of dimers within the crystalline film. The good agreement of the simulated spectra to the experimental data further support the assignment of the early species to $^5(T_1T_1)$ as well as molecular orientation that quintet spectra originate from.

In both **TDI** and **QDI**, the Q_0 sublevel is largely populated with only small populations in the $Q_{\pm1}$ and $Q_{\pm2}$ sublevels. This is further supported from the relative nutation frequnecy between the quintet and the triplet as described above. From the sublevel population of quintet and triplet states of **TDI** and **QDI** (**Table 5.4**) we can elucidate the mechanism of quintet formation and triplet dissociation. Because Q_0 is largely populated in both **TDI** and **QDI**, followed by some population $Q_{\pm1}$ and $Q_{\pm2}$, we conclude that the quintet formation occurs via a diabatic transition, similar to that reported for TIPS-tetracene and pentacene derivatives.[4, 5, 63] The small population in $Q_{\pm1}$ and $Q_{\pm2}$

sublevels can be explained by the mis-alginment between the two molecule which gives non-zero mixing among S, $Q_{\pm1}$ and $Q_{\pm2}$.[184]

Using the simulated quintet and triplet spectra as basis spectra, the 2D TREPR spectra obtained at 20K were deconvoluted to obtain the dynamics of each state (**Figure 5.5**). By fitting the kinetics, we find the quintet formation and decay in the **QDI** film occurs with time constants of 44 ± 15 ns and 125 ± 15 ns, respectively, while in the **TDI** sample, the formation and decay occurs in 30 ± 15 ns and 78 ± 15 ns, respectively. Following the decay of the quintet states, triplet states are formed with time constants of 106 ± 15 ns in **QDI** and 72 ± 15 ns in **TDI**. Although the triplet formation time constant in **TDI** matches that of the quintet decay, the formation of the triplet in **QDI** is slightly faster than that of quintet decay. Presumably, the faster triplet formation in **QDI** indicates that there are multiple pathways for forming dissociated triplet excitons. The triplet excitons in both **TDI** and **QDI** decay biexponentially with time constants reported in **Table 5.2**.

Table 5.2 Kinetic time constants of the quintet (Q) and the triplet (T) states.

QDI	**ϕ = 45°**	**90°**	**130°**	**160°**	**random**
$^{3/5}(T_1T_1)$ rise (ns)	39 ± 15	37 ± 15	-	43 ± 15	44 ± 15
$^{3/5}(T_1T_1)$ decay (ns)	76 ± 15	67 ± 15	-	146 ± 15	125 ± 15
T_1 rise (ns)	82 ± 15	86 ± 15	55 ± 15	150 ± 15	106 ± 15
T_1 decay 1 (ns)	190 ± 20	200 ± 20	130 ± 15	190 ± 20	290 ± 20
T_1 decay2 (ns)	650 ± 90	640 ± 50		1060 ± 30	1030 ± 60
TDI	**ϕ = 45°**	**90°**	**120°**	**150°**	**random**
$^{3/5}(T_1T_1)$ (ns)	25 ± 15	31 ± 15	43 ± 15	29 ± 15	30 ± 15

$^{3/5}(T_1T_1)$ decay (ns)	53 ± 15	53 ± 15	70 ± 15	57 ± 15	78 ± 15
T_1 rise (ns)	64 ± 15	56 ± 15	83 ± 15	60 ± 15	72 ±15
T_1 decay 1 (ns)	110 ± 15	141 ± 15	230 ± 15	130 ± 15	130 ± 15
T_1 decay2 (ns)	3500 ± 100	2870 ± 60	3500 ± 200	2070 ±60	3000 ± 200

5.3.5 Spin dynamics in the polycrystalline textured samples.

Similar spectral fitting and kinetic analysis were performed on the polycrystalline textured films on flat glass substrates. Additional fitting parameters are reported in the Supporting Information (**Tables 5.6** and **5.7**). We fit the early time spectra (50 ns) to the linear combination of $^5(T_1T_1)$ and $^3(T_1T_1)$ correlated triplet states and later time spectrum (200 ns) to the dissociated T_1 triplet states. In order to account for the orientation effect, additional ordering parameter, θ, was used for fitting both the quintet and the triplet spectra. In addition to θ dependence on the T_1 spectra as shown in Figure S9, the $^5(T_1T_1)$ and $^3(T_1T_1)$ spectra are also simulated by varying the θ values at the fixed sublevel population (Figure S16, S17). Upon fitting the correlated triplet spectra of the textured films, Euler angles of (3°,60°,10°) were used for **QDI** and **TDI**. These Euler angles correspond to dimer 3 (see Supporting Information, **Figure 5.18**).

Using the simulated spectra for the correlated and separated triplet in Figure 6 as basis spectra, the 2D TREPR spectra of the **QDI** oriented films were deconvoluted. The most notable difference in the spectra among different angles is that when the substrate is oriented at $\phi = 130°$ to the magnetic field, there is no spectral change over time (**Figure 5.20**). We were able to fit the entire spectrum by only using the dissociated triplet, and by deconvoluting the 2D TREPR spectra, the time constant for triplet formation is 55 ± 15 ns and that of the triplet decay is 130 ± 15 ns. We attribute such differences in spin dynamics to differences in molecular orientation. As mentioned

previously, the molecular orientation contributing to the majority of the signal is $\overline{\chi_m}$ = 5°, whereas the remaining signal comes from an average molecular orientation of $\langle\overline{\chi_m}\rangle$ = 68 ± 3°. In addition, slightly different ZFS values (Table S4) are used to fit the spectrum at ϕ = 130°, which also indicates that the triplet signal at this particular angle differs from those of the remaining population. If the triplet signals were to come from an average molecular orientation of $\langle\overline{\chi_m}\rangle$ = 68 ± 3°, the simulated triplet spectrum at ϕ = 130° should look like that shown in Figure S13; however,

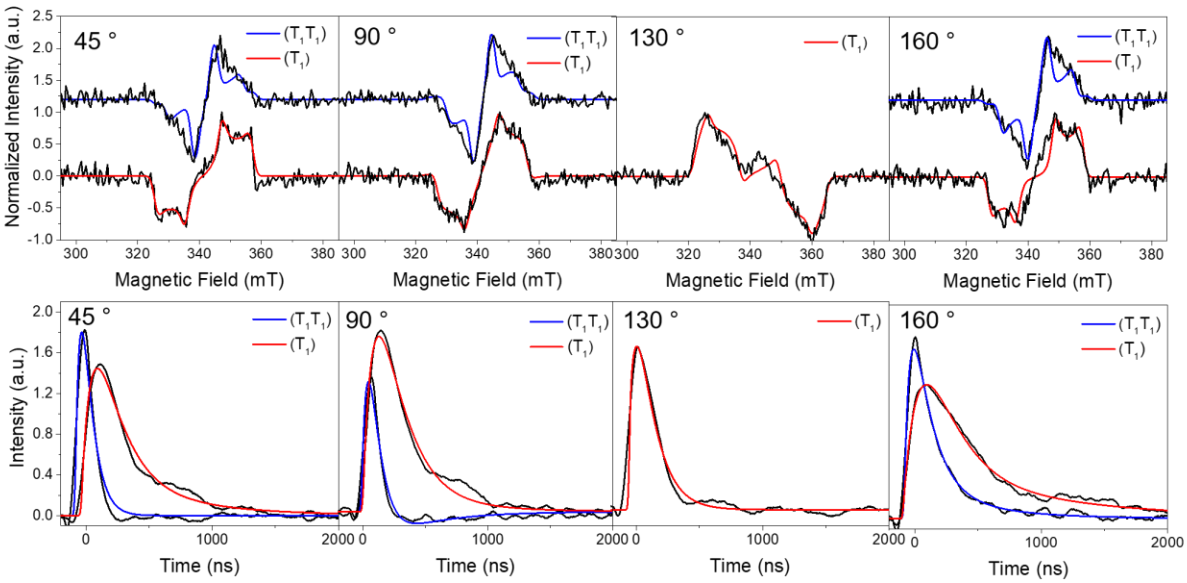

Figure 5.6. (Top) the correlated triplet (50 ns) and the separated triplet (200 ns) spectral fitting of QDI textured film at different ϕ, angles between the substrate and the magnetic field. (Bottom) the respective kinetic traces of the correlated triplet and the separated triplet using the above spectra as basis spectra. The 2D TREPR data are collected at 20K and shown in **Figure 5.24**.

since this simulated spectrum is significantly different from the experimental data, we rule out the signal coming from the same molecular orientation. In addition, we also tried fitting the triplet

spectrum originating from ISC mechanism and setting the molecular oreitnation to be $\langle\overline{\chi_m}\rangle$ = 68 ± 3° (**Figure 5.27**). Although the fitting is reasonable, the *E* value had to be changed significantly, from 85 MHz to 185 MHz, and because such significant difference cannot arise from the same molecule, we rule out the triplet coming ISC. It is reasonable to observe change in spin dynamics from different molecular alignment as shown in the cases of parallel and harringobne molecaulr orientations in dilute pentacene film.[170]

Interestingly, when fitting both the $^{3/5}(T_1T_1)$ and the T_1 triplet spectra in the textured **QDI** film we used the same ordering parameter, θ, at a specific ϕ value. Since both the $^{3/5}(T_1T_1)$ and T_1 spectra are in good agreement with the simulated spectrum, we conclude that formation of the two triplet states from the correlated triplet state preserves the orientation information. Such result is reasonable because of the highly oriented nature of the samples. In the case of the polycrystalline powder sample, even if the orientation information is retained, this orientational memory is lost during the measurement because the excitation probe size of TREPR (1 mm) is much greater than the crystalline domain size (~250nm).

Among the correlated triplet and the independent triplet signals arising from the average molecular orientation of $\langle\overline{\chi_m}\rangle$ = 68 ± 3°, we observe the ϕ dependence of the spin dynamics, or how the molecules are oriented with respect to B_0. For instance, when the substrate is oriented at ϕ = 45° and 90°, the dynamics of the correlated triplet and the independent triplet are similar (Table 2); however, when ϕ = 160°, we observe a two times slower correlated triplet decay and 1.8 times slower dissociated triplet formation (**Table 5.2**). In addition, the overall triplet decay time constants are faster when the substrate is oriented at ϕ = 45° and 90° compared to that when ϕ = 160°. Such differences are expected from the work of Collins et al.,[4] because the molecular

orientation with respect to the magnetic field changes the degree of mixing between $^1(T_1T_1)$ and $^5(T_1T_1)$. The mixing between the two spin states will change the rise of the correlated triplet formation time and the change in rise time will eventually populate the sublevels differently. Thus, as shown in the **Table 5.6**, the sublevel population at different ϕ value is indeed different. The resulting change in sublevel population also changes the decay pathway, and thus we observe the change in decay time constants of the correlated triplet state at different ϕ values.

In the polycrystalline textured film of **TDI** (**Figure 5.7**), we observe spectral changes over time for all values of ϕ, and assign the early time species to the correlated triplet and the later time species to the separated triplet. Although the overall dynamics are similar with the rise and the decay time constants of the correlated triplet ~30 ns and ~60 ns, respectively, when $\phi = 120°$, both the correlated triplet formation and the decay slow down to be 43 ± 15 ns and 70 ± 15 ns, respectively. In addition, the bi-exponential time constants of triplet decay also increase by 1.3 times.

5.4 Discussion

5.4.1 Comparison of spin dynamics in the QDI and the TDI polycrystalline powder samples.

Comparing the two polycrystalline powder samples, **QDI** has ~1.6 times slower quintet formation and decay time constants compared to **TDI**. Such dynamics follows the trend observed in the previous TREPR polyacene studies,[168] namely, that slow dissociation of the two triplet states that comprise $^1(T_1T_1)$ results in more time for spin evolution to take place, resulting in a larger yield of $^5(T_1T_1)$. In fact, the ratio of the quintet and the triplet signals of **QDI** is 2.3, which is greater than the 0.83 ratio of **TDI** (**Figure 5.5**). This indicates triplet dissociation is more efficient in **TDI**, based on the fast decay of the quintet and formation of the triplet. Although the triplet formation is faster in **TDI**, the triplet decay time constant is 2-3 times slower than in **QDI**. Despite the similar

crystal packing structure between **TDI** and **QDI** powder samples, the spin dynamics is significantly different. We contribute this to the difference in ZFS parameters *D* and *E*, which directly influences the mixing between the singlet and the quintet.[53]

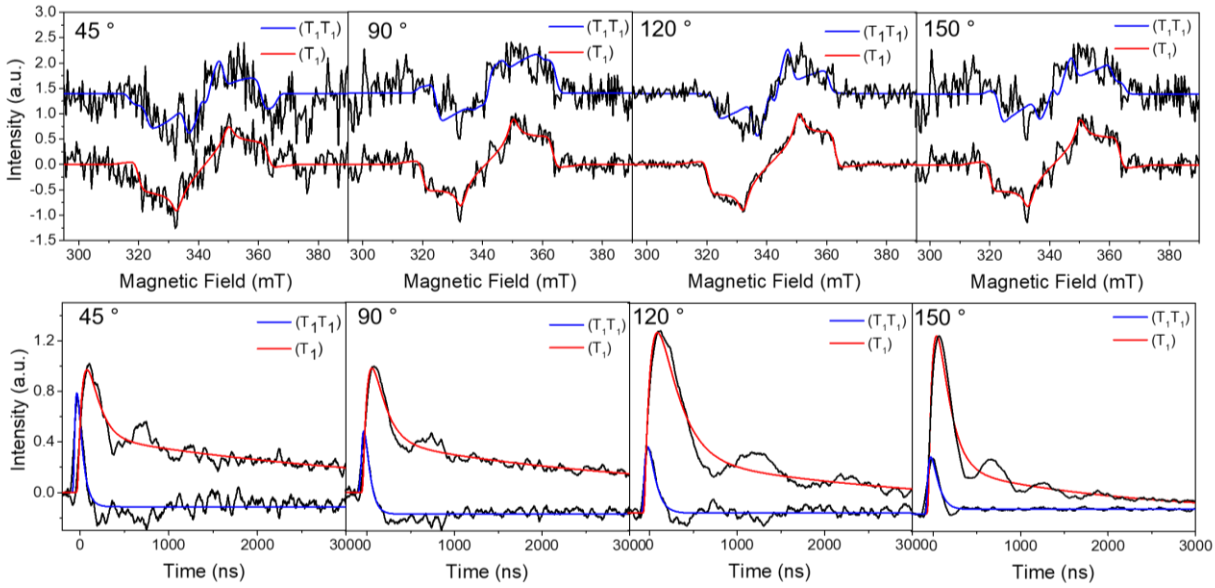

Figure 5.7. (Top) the correlated triplet (50 ns) and the separated triplet (200 ns) spectral fitting of TDI textured film at different ϕ, angles between the substrate and the magnetic field. (Bottom) the respective kinetic traces of the correlated triplet and the separated triplet suing the above spectra as basis spectra. The 2D TREPR data are collected at 20K and shown in **Figure 5.29**.

5.4.2 Comparison of spin dynamics in QDI and TDI oriented samples. The recent theory paper from Tayebjee and co-workers[4] has demonstrated anisotropic generation of spin states due to change in the mixing between $^1(T_1T_1)$ and $^5(T_1T_1)$ at different orientations.[4] For instance, when θ is close to the magic angle (~54.7°), a smaller Q_0 population is observed due to changes in the energy splitting of the m_s spin states. Although such a phenomenon has not been observed in

previous experimental work,[63, 170] we observe significant differences in correlated triplet dynamics depending on how molecules are oriented with respect to the incident magnetic field as shown in Table 2. This orientation effect is especially stronger in the **QDI** textured film, due to a higher degree of order than the **TDI** film (**Figure 5.2**). As mixing between $^1(T_1T_1)$ and $^5(T_1T_1)$ and between $^5(T_1T_1)$ and $^3(T_1T_1)$ are orientation dependent, we observe difference in sublevel populations at different ϕ values in both the **TDI** and **QDI** textured films. For instance, we observe difference in $^3(T_1T_1)$ population when $\phi = 160°$ compared to the rest in the polycrystalline textured **QDI** film, where the slowest correlated triplet formation and decay are observed (**Table 5.6**). In addition, we observe difference in decay time constant of the correlated triplet as well as Q_{-2} sublevel population between $\phi = 45°$ and 120° in textured **TDI** sample, whereas the molecular orientation is the same (**Table 5.7**). Although more rigorous calculations should be used to identify the origin of the ϕ dependence of the spin dynamics such as quantifying the singlet character, anisotropic mixing, and time-dependent J modulation as shown in Kobori and co-workers,[64, 181] based on the differences in time constants of the formation and decay of the correlated triplet and sublevel populations at varying ϕ values, we can qualitatively state that spin dynamics occurring in textured **TDI** and **QDI** films are orientation dependent. It should be noted that in the polycrystalline powder **QDI** film, the quintet decay time constant does not match the rise of the triplet (**Table 5.2**); however, in the oriented film of **QDI**, both time constants match well. Presumably, in the polycrystalline powder sample, the mismatch could arise from the different molecular orientations relative to B_0.

5.4.3 Comparison of QDI and TDI systems to the reported literature. Previous work on a **TDI** covalent dimer in which the two TDI molecules are linked by a single bond between their imide

nitrogen atoms shows that the small exchange coupling, *J*, between the two triplet states within (T_1T_1) leads to mixing of $^5(T_1T_1)$ and $^3(T_1T_1)$, which results in annihilation of the triplets to produce a single uncorrelated T_1 state, instead of two separate triplets. In this work, the **TDI** and **QDI** films both have a much greater *J* value (~30 GHz) Given the small magnitude of $^3(T_1T_1)$ signal in the correlated triplet spectra (**Figure 5.6-5.7**), we assume that the mixing between $^5(T_1T_1)$ and $^3(T_1T_1)$ is less significant compared to that of **TDI** covalent dimer. Although the mechanism of the spin dynamics and the magnitude of *J* are similar between this work and the previous work on polyacene derivatives, the quintet lifetimes are 1-2 orders of magnitude smaller. Presumably this indicates that triplet dissociation is more favorable in the **TDI** and **QDI** films. Considering potential solar cell applications, since dissociation is more efficient in **TDI** than **QDI**, and the overall **TDI** triplet lifetime is longer, harvesting the triplets from **TDI** will be more facile. Long-lived triplet excitons are important for efficient triplet delivery to sites at which the triplet excitons can be split to yield free charge carriers. In addition, the triplet energy of the **TDI** is greater than that of **QDI**, and thus, in terms of energetics as well, **TDI** is a better candidate for SF-enhanced photovoltaics.

5.5 Conclusions

Randomly and highly oriented **TDI** and **QDI** films were fabricated to investigate the dependence of molecular orientation with respect to the direction of an applied magnetic field on the excited state spin dynamics. Based on these results, several conclusions can be made: First, it is important to study an oriented sample as opposed to a randomly oriented sample, because depending on the molecular orientation relative to the applied magnetic field direction, the mixing between multi-spin intermediate states changes, resulting in changes in spin dynamics. In addition,

the dissociated triplets in the oriented sample maintain the same orientation as the correlated triplets. Second, because triplet dissociation in **TDI** is more efficient with a longer-lived triplet lifetime than **QDI**, **TDI** is a more viable candidate for photovoltaic applications. Third, since the **QDI** film readily forms a highly oriented film, and the lifetime of the quintet state is longer than **TDI**, it may be a good candidate for quantum information science applications that require the generation of a quantum-entangled, four-spin state.

5.6 Acknowledgements

This work was supported by the U.S. Department of Energy, Office of Science, Office of Basic Energy Sciences under Award DE-FG02-99ER14999 (M.R.W.). Y.B. gratefully acknowledges support from the Ryan Fellowship and the International Institute for Nanotechnology at Northwestern University. This work made use of the IMSERC at Northwestern University, which has received support from the Soft and Hybrid Nanotechnology Experimental (SHyNE) Resource (NSF ECCS-1542205), the State of Illinois, and the International Institute for Nanotechnology (IIN). GIWAXS and X-ray powder diffraction measurements were performed at Beamlines 8-ID-E and 12-ID-B with the help of Dr. Xiaobing Zuo, respectively, at the Advanced Photon Source, a U.S. Department of Energy (DOE) Office of Science User Facility operated for the DOE Office of Science by Argonne National Laboratory under Contract No. DE-AC02-06CH11357. Y.B. thanks Charlotte Stern, Christos D. Malliakas and Richard S. Hong for helpful discussions regarding single crystal structure solving and the crystallographic related data analysis and Samantha Harvey for performing magnetic field dependent transient absorption spectroscopy. This work was also supported by KAKENHI JP17J01125, JP18KK0161 and JP19K15506 (H.N.).

5.7 Supplementary Information

5.7.1 Steady State Emission Spectra

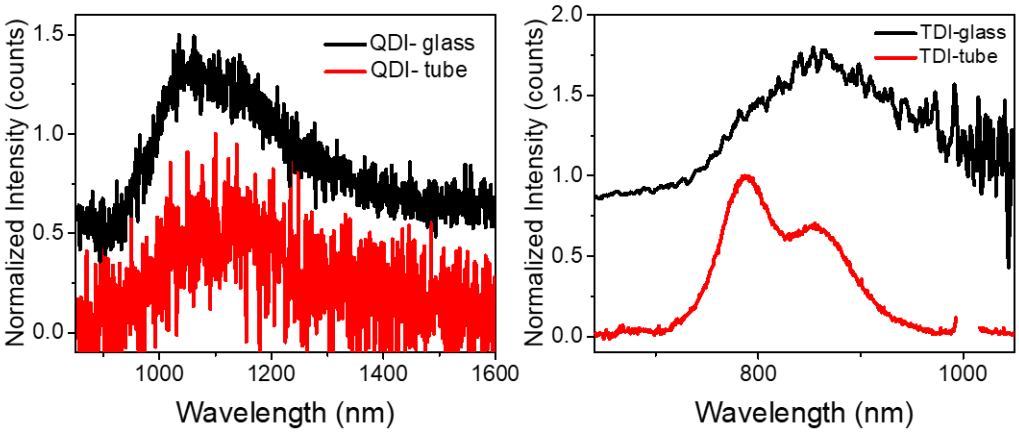

Figure 5.8. Steady state emission spectra of (a) **QDI** and (b) **TDI** films on the glass substrate (black) and inside the quartz tube (red).

5.7.2 Single Crystal Structure and X-ray Spectroscopy

Table 5.3. Summary of crystal parameters for **TDI** and **QDI**

	TDI	**QDI**
a	14.6569 (14) Å	14.2 Å
b	15.3071 (12) Å	17.4 Å
c	24.9808 (12) Å	24.6 Å
α	89.021 (5) °	82 °
β	79.724 (7) °	80 °
γ	74.797 (80 °	75 °
Z	1	1
V	5319.1 (8) $Å^3$	5753.43 $Å^3$
CCDC	1978605	-

5.7.3 X-Ray Powder Pattern of QDI

The experimental powder pattern is obtained using the same diffractometer used to collect single crystals of **TDI** and **QDI**. Paratone oil was used to hold **QDI** powder and the data was collected for 45 minutes. Since the predicted powder-pattern matches well with the experimental powder-pattern, we conclude that the **QDI** crystals have similar packing structure to the **TDI**.

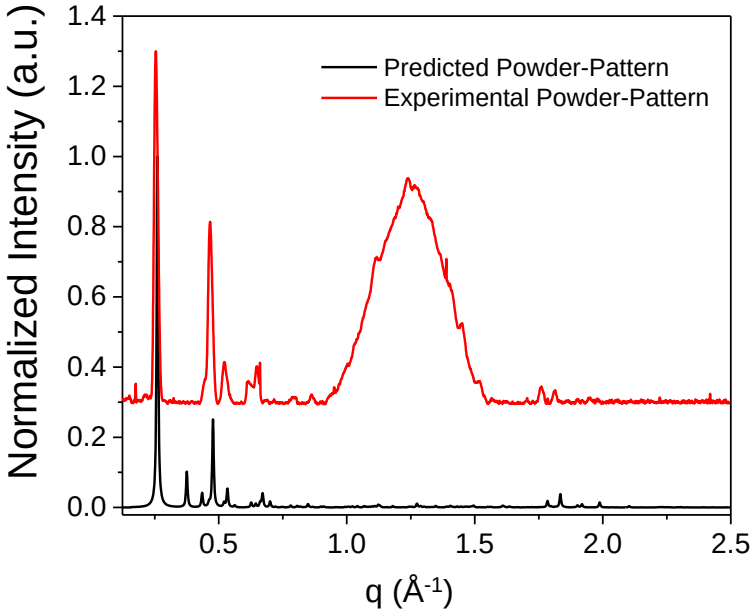

Figure 5.9. Comparison of X-ray powder pattern of **QDI** polycrystalline sample (red) and the predicted powder pattern by changing unit-cell parameters of the **TDI** single crystal.

5.7.4 X-Ray Powder Pattern of QDI and TDI Tube Samples

The following X-ray powder pattern was collected at beamline 12ID-B at the Advanced Photon Source (APS), Argonne National Laboratory using a Pilatus 2 M detector with 14 keV incident radiation. A high-power X-ray light source was necessary to obtain the powder-pattern from the weakly scattering sample. The capillary sample holder was used to load 2.5 mm quartz tube and transmission mode was used to collect the data. Figure S3 shows the X-ray powder pattern form the tube sample overlaid with the predicted powder pattern as discussed in the main text.

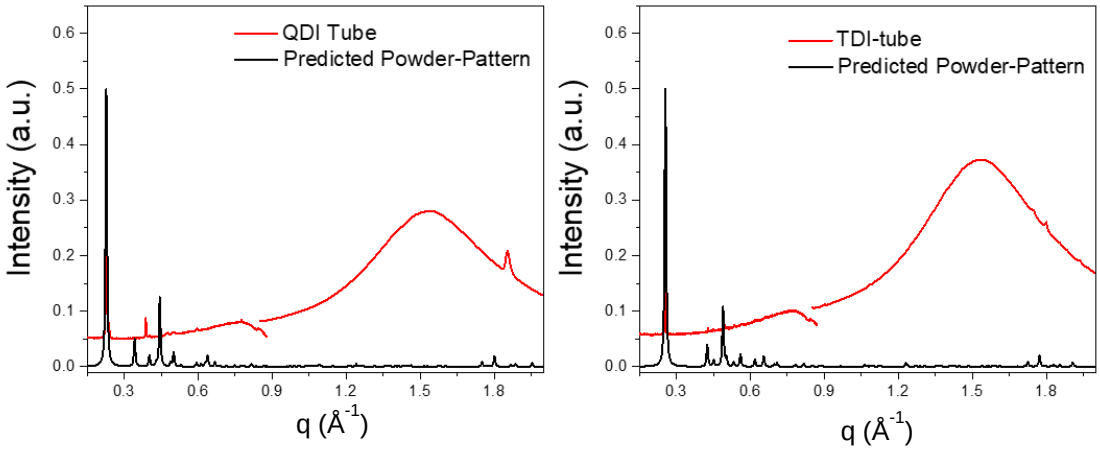

Figure 5.10. X-ray scattering spectrum of (a) **QDI** and (b) **TDI** of the tube samples

5.7.5 Grain Size Analysis Using Scherrer equation

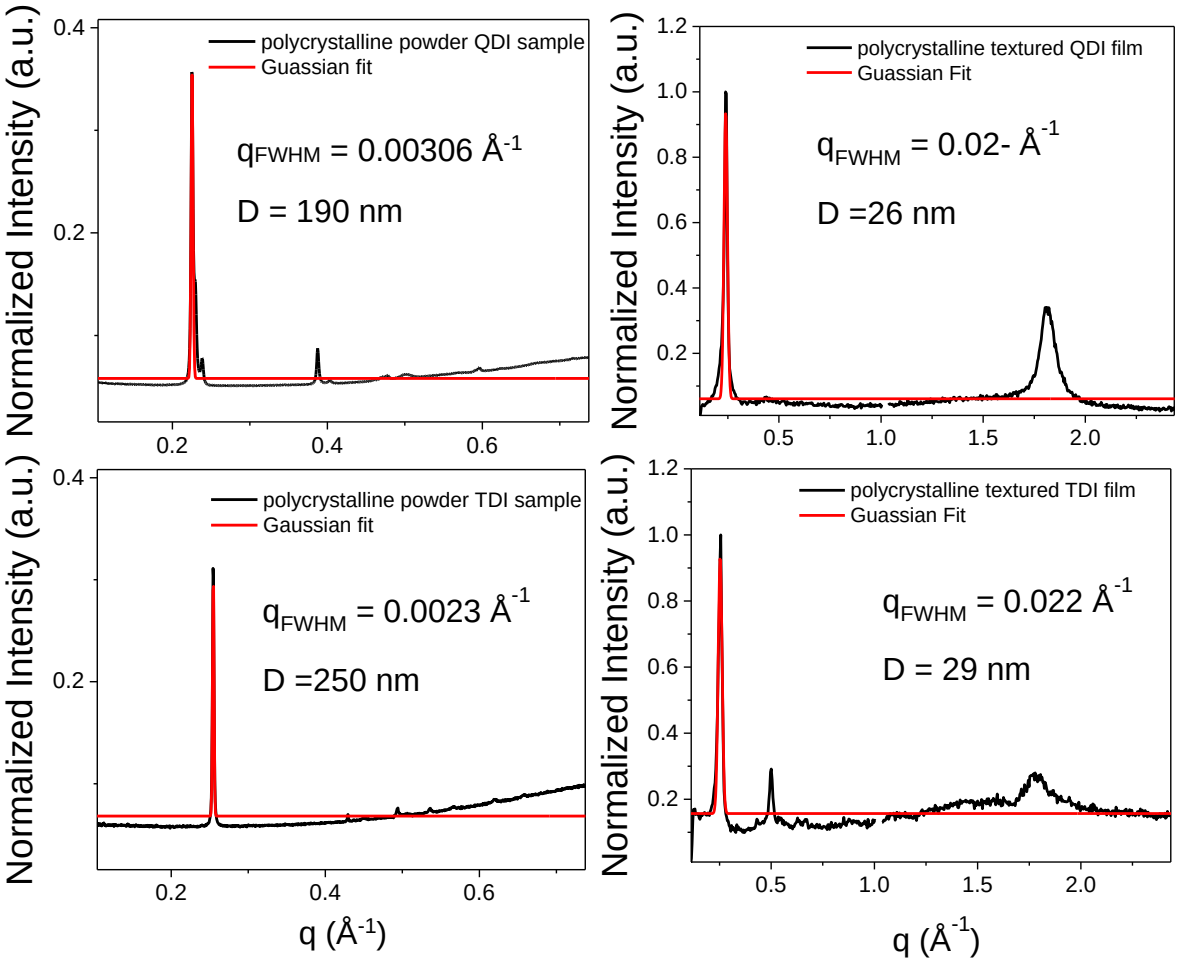

Figure 5.11. The full width at half-maximum (FWHM) of the q peak used to calculate average grain size(D) analysis of the **TDI** and **QDI** polycrystalline powder and textured. The q_{FWHM} peak is fitted using Gaussian fit and D values are calculated using eq. 5.1.

The average grain size (D_{hkl}) of the TDI and QDI polycrystalline powder and textured samples are measured using the Scherrer equation:

$$D_{hkl} = \frac{2 \cdot \pi \cdot K}{q_{FWHM\ at\ hkl}} \qquad (eq.5.1)$$

Here, K is the Scherrer constant (0.93) (ref) and q_{FWHM} is the full-width-half-maximum of the first q for both **TDI** and **QDI**.

5.7.6 GIWAXS Pole Figure Analysis

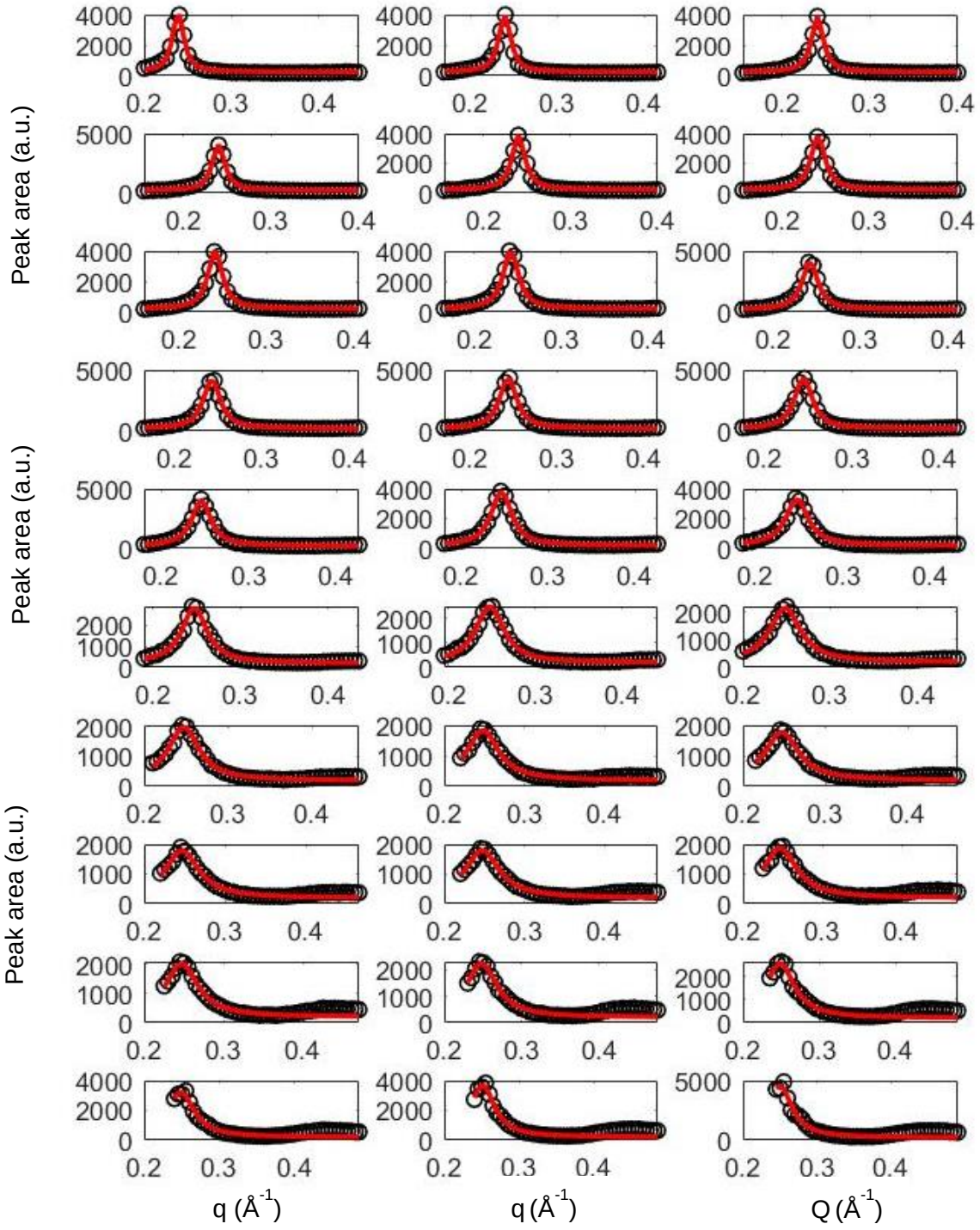

Figure 5.12. Constructing the pole figure extracted from q_r = 0.2542 Å^{-1} peak in the **QDI** film. Integration over successive regions panning from -80° to -10° by step size of 3° of the polar angle χ yielded a family of 1D curves I(q_r) vs. q_r.

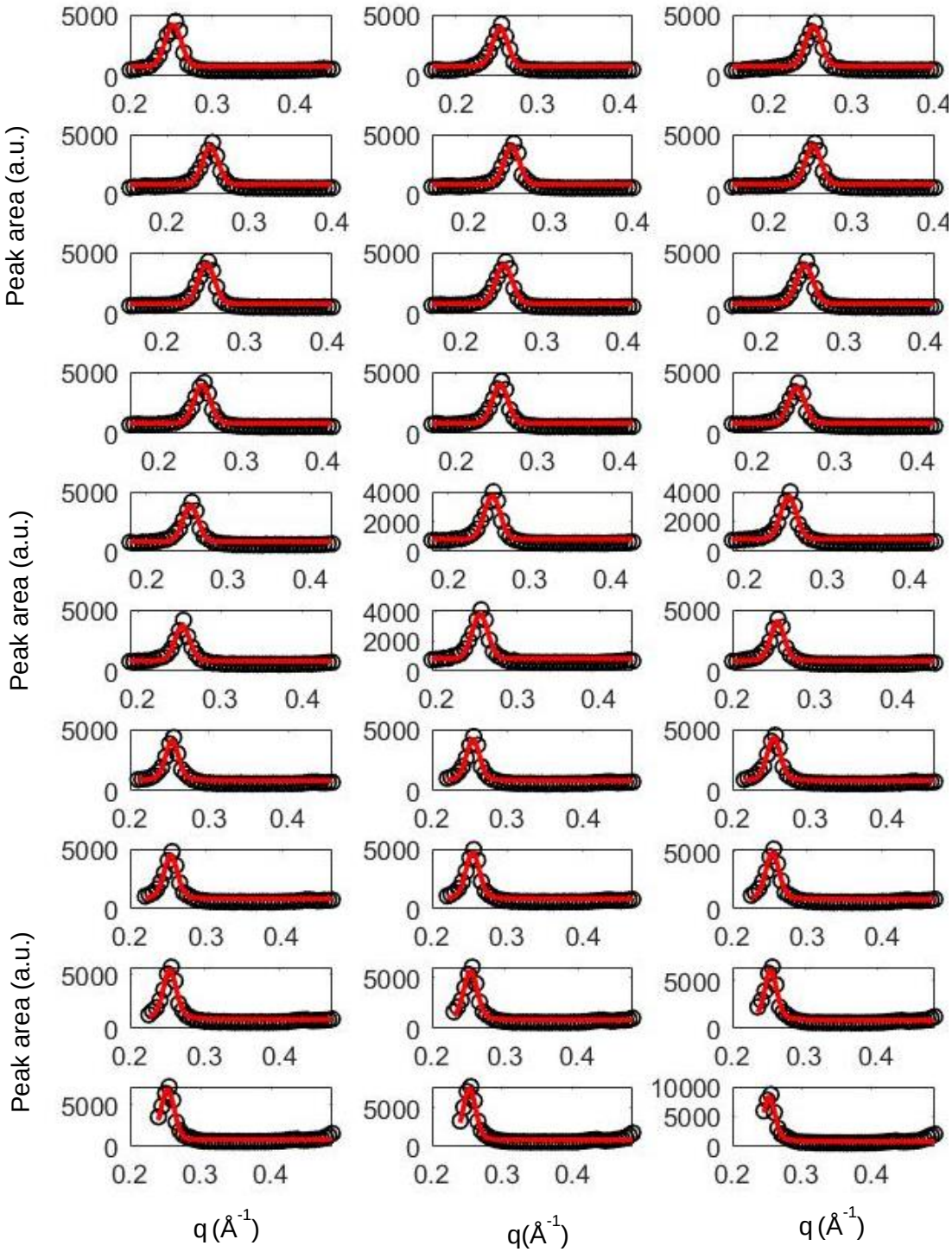

Figure 5.13. Constructing the pole figure extracted from q_r = 0.2535 $Å^{-1}$ peak in the **TDI** film. Integration over successive regions panning from -80° to -10° by step size of 3° of the polar angle χ yielded a family of 1D curves $I(q_r)$ vs. q_r.

Pole Figure Extracted from the QDI π- π Peak

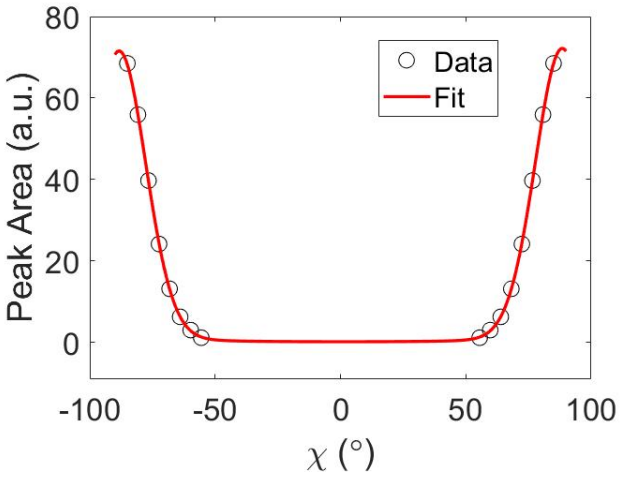

Figure 5.14. Pole figure extracted from q_r = 1.8 $Å^{-1}$ in the **QDI** film.

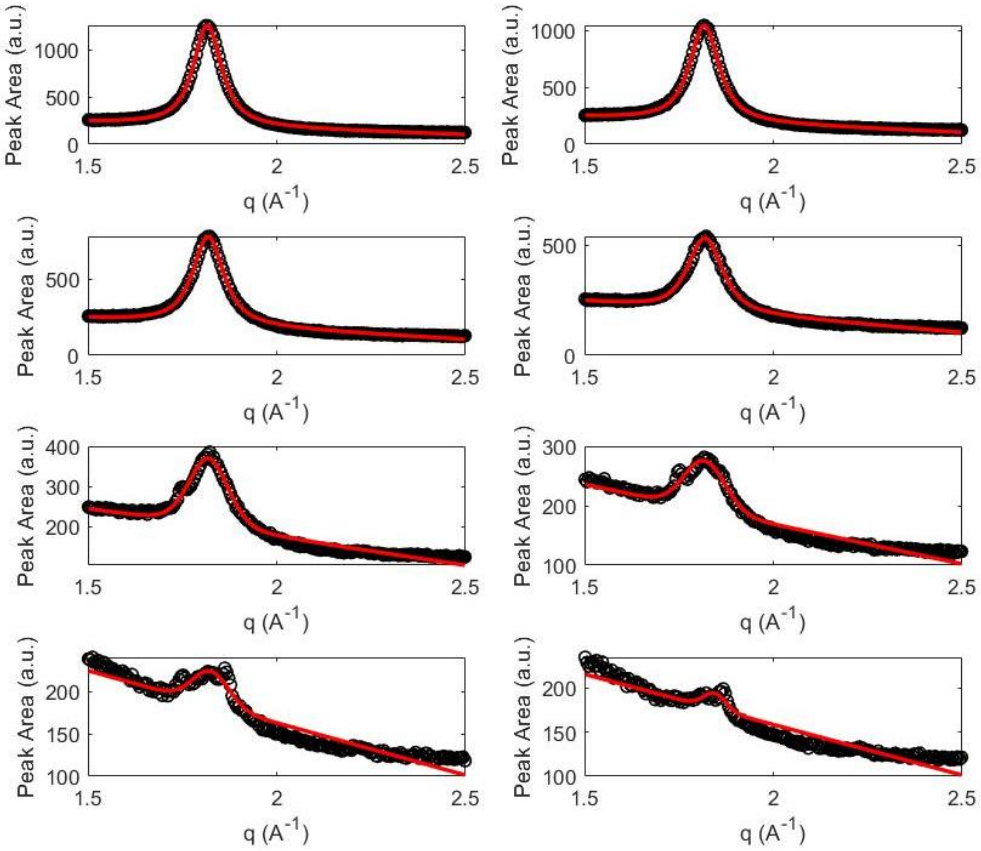

Figure 5.15. Constructing the pole figure extracted from q_r = 1.8 $Å^{-1}$ peak in the **QDI** film. Integration over successive regions panning from -85° to -55° by step size of 4° of the polar angle χ yielded a family of 1D curves $I(q_r)$ vs. q_r. Beyond -55°, there is no peak and thus the fits are not shown.

5.7.7. TREPR Data

The Simulated Triplet Spectra by Varying θ Values

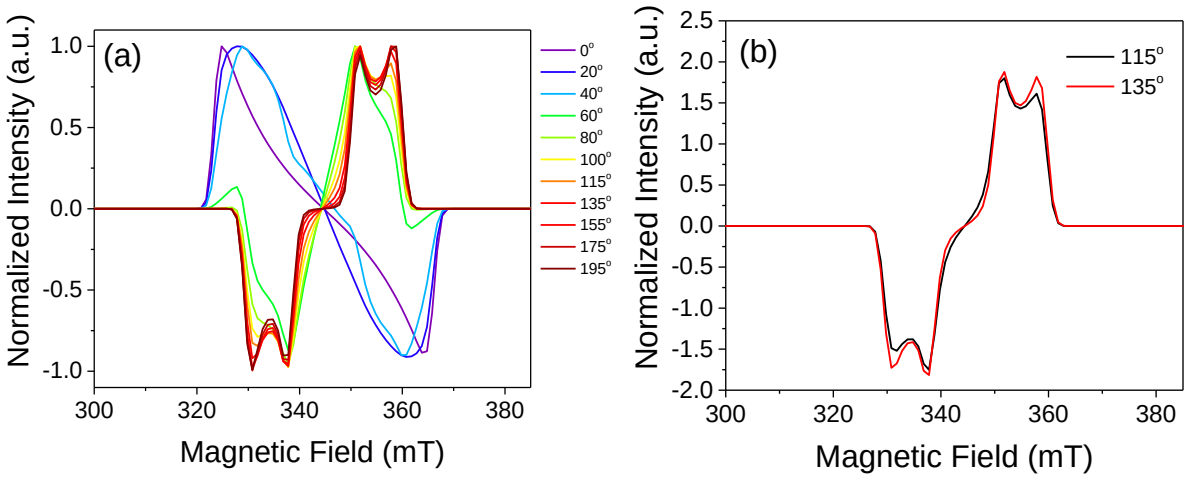

Figure 5.16. (a) The simulated triplet spectra using populations (T_{+1} T_0 T_{-1}) population as (0, 86, 14) at different θ values. (b) The triplet spectra showing the similarity between θ = 115° and 135° which correspond to the triplet spectra at ϕ = 45° and 160°, respectively.

Temperature Dependence of Tube Samples

Although at room temperature only dissociated triplets are observed in TREPR, as the temperature is lowered to 20K, the quintet spin state is observed, similar to what observed in tetracene film.[63]

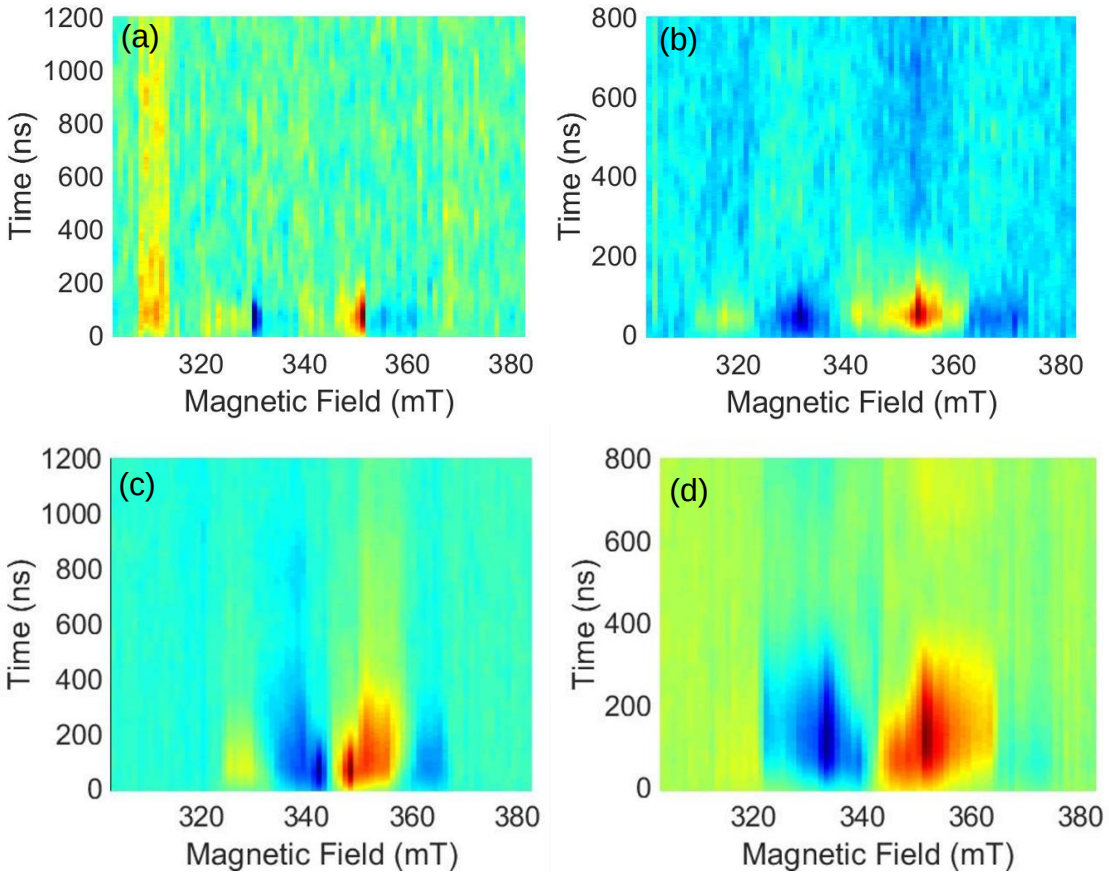

Figure 5.17. The room temperate TREPR spectra of (a) the **QDI** and (b) the **TDI** tube films. As the temperature is lowered to 20K, the new species is observed in (c) **QDI** and (d) **TDI** tube films.

Nutation Frequency

The kinetic trace of the **TDI** polycrystalline powder sample (Figure 5d) shows oscillation coming from spin nutation signals. This kinetic trace is obtained by deconvoluting the 2D TREPR spectra at 20K using the basis spectra of the quintet and the triplet spectra as shown in **Figure 5.5c**. The nutation signal is separated (**Figure 5.18**) by subtracting the population dynamics from the kinetic trace using the multi-exponential fits. The frequency of the quintet and the triplet are obtained by fitting the spectra (**Figure 5.18**) using a damped sine wave. The ratio between the frequency of the quiet and the triplet gives information about the m_s sublevel as shown in the following equation:

$$w_{Q/T} = \sqrt{\frac{S_Q(S_Q+1) - m_{S_Q}\left(m_{s_Q} \pm 1\right)}{S_T(S_T+1) - m_{S_T}\left(m_{s_T} \pm 1\right)}} \qquad (eq.5.2)$$

where S is the total spin number and for the triplet S= 1 and the quintet S= 2. If the transitions come from $m_s = 0$ state, the ratio of nutation frequency for pure quintet and triplet state is $\sqrt{3}$ or ~1.73. The frequency ratio between the quintet (199^{-1} ns^{-1}) and the triplet (345^{-1} ns^{-1}) is 1.73, which indicates that the quintet and triplet signals come from the transitions in $m_s = 0$ state.

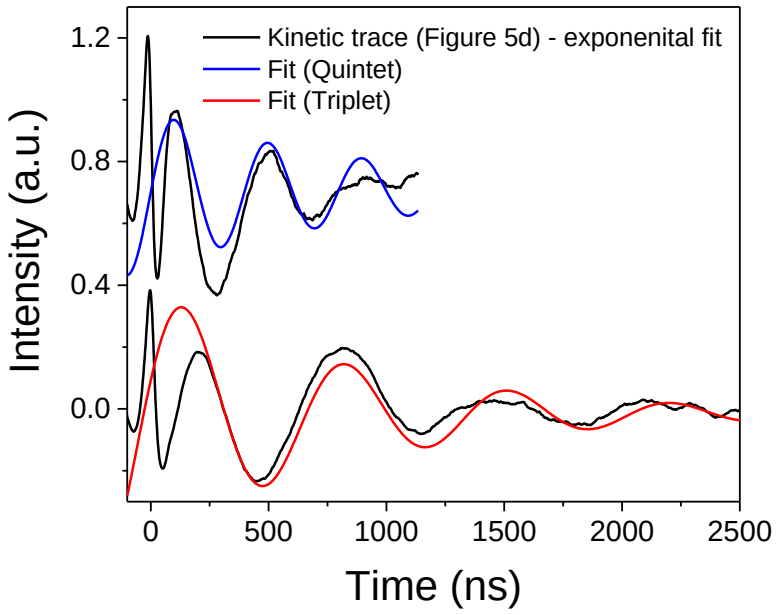

Figure 5.18. The nutation signal of the polycrystalline powder **TDI** film and the spectral fitting using a damped sine wave function.

Magnetic Field Effect

The magnetic field dependent transient absorption spectra were collected using the previously described method.[166] The femtosecond transient absorption (fsTA) spectra for QDI film at 0 magnetic field are shown in **Figure 5.19**. The amplitude vs. external magnetic field strength plot is generated by averaging the signal in the triplet excited stated absorption signal between 606 and 670 nm and by integrating the signal from 0-20 ns. Here, the amplitude is analogous to relative triplet yield formed. Since the signal amplitude does not change in the magnetic field range of 0G – 10000 G, we conclude that the spin-exchange coupling *J* in both the **TDI** and **QDI** films are in order of tens of GHz.

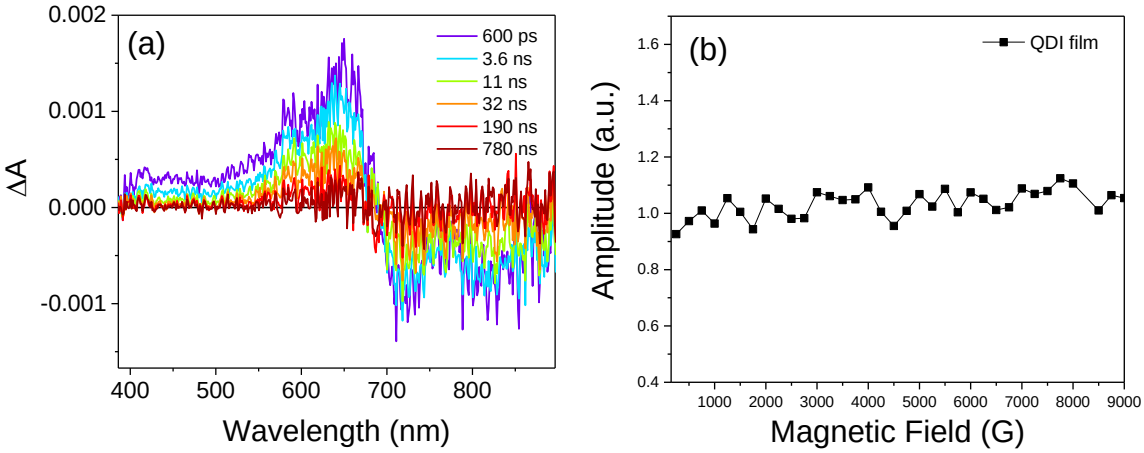

Figure 5.19. (a) The fsTA spectra of **TDI** film obtained in the absence of the external magnetic field, at room temperature with the laser excitation wavelength at 690 nm. (b) The amplitude vs. magnetic field plot is generated by averaging the signal in the

Triplet Subtraction in QDI and TDI Tube Film

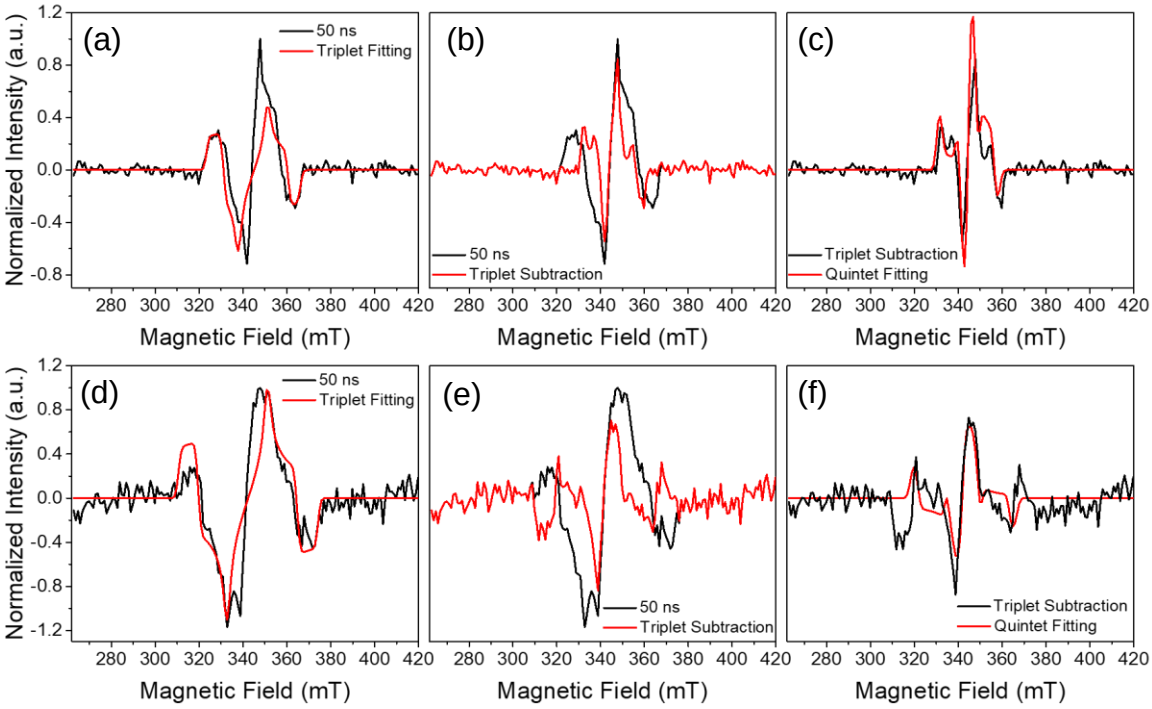

Figure 5.20. The triplet spectral fitting of the (a) **QDI** and the (b) **TDI** tube films at early time, followed by the subtraction (b) and (e), respectively. The quintet spectral

Magnetic Parameters for the Spectral Simulation of QDI and TDI Tube Film

Table 5.4. TRPER fitting parameters used to fit the quintet and the triplet of the **QDI** and the **TDI** tube films.

	QDI at 50 ns	**QDI** at 200 ns	**TDI** at 50 ns	**TDI** at 200 ns
G	2.002	2.002	2.002	2.002
$\|D\|$ (MHz)	600	600	891	891
$\|E\|$	75	75	124	124
Euler angle (α,β,γ) of zero-field splitting (1st triplet)	(0,30,0)	-	(0,30,0)	-
Euler angle (α,β,γ) of zero-field splitting (2nd triplet)	(0,0,0)	-	(0,0,0)	-
J (GHz)	~30		~30	
Dipolar coupling (MHz)	55		55	
$\rho(\|Q_{+2}\rangle)$	0	-	0	-
$\rho(\|Q_{+1}\rangle)$	26	-	29	-
$\rho(\|Q_{0}\rangle)$	39	-	40	-
$\rho(\|Q_{-1}\rangle)$	25	-	31	-
$\rho(\|Q_{-2}\rangle)$	10	-	0	-
$\rho(\|T_{+1}\rangle)$	0	0	0	0
$\rho(\|T_{0}\rangle)$	84	81	97	83
$\rho(\|T_{-1}\rangle)$	16	18	3	17

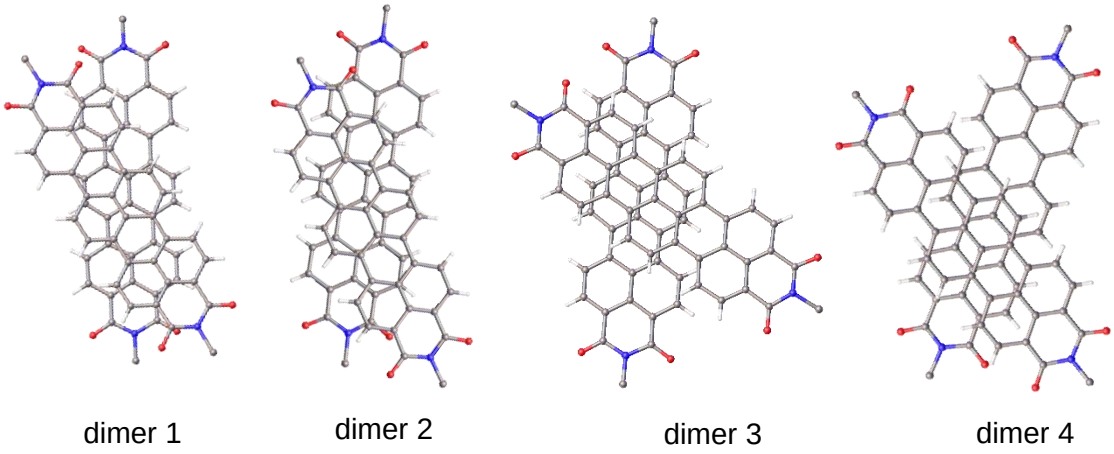

Figure 5.21. Different pair of dimers within the crystal packing of **TDI** and **QDI.** The alkyl chains are removed for a cleaner view.

Table 5.5. The distances and angles in x, y, and z direction of dimer sets in **Figure 5.22**.

	Long-axis slip distance (Å)	Short-axis slip distance (Å)	π- π distance (Å)	Yaw angle (°)	Pitch angle (°)	Roll angle (°)
Dimer 1	0.854	1.25	3.45	30.1	2.41	71.5
Dimer 2	2.03	0.755	3.51	30.2	1.47	-5.43
Dimer 3	0.298	2.35	6.93	60.4	3	10
Dimer 4	1.84	0.481	7.08	-60.5	2.3	2.54

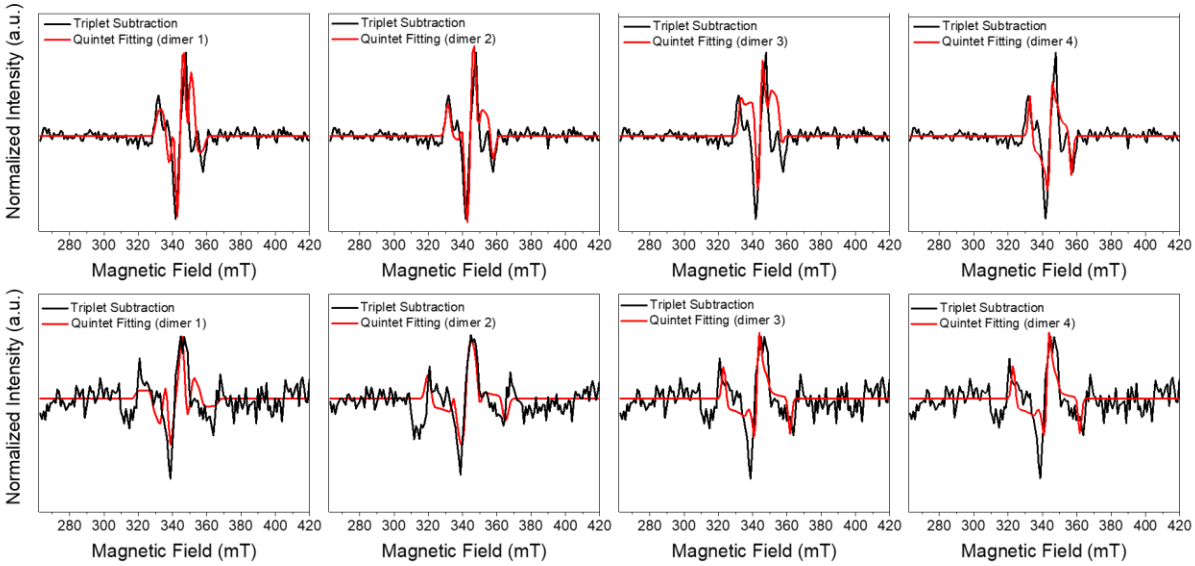

Figure 5.22. The quintet spectral fitting of (top) **QDI** and (bottom) **TDI** using the four different dimers shown in **Figure 5.21**.

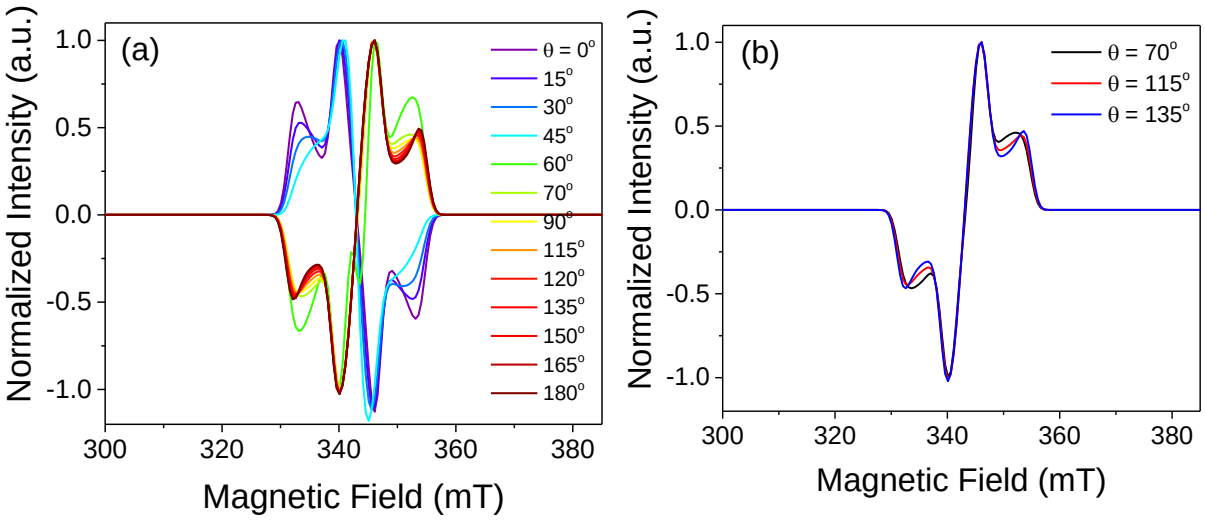

Figure 5.23. (a) The simulated quintet spectra using (Q_{+2} Q_{+1} Q_0 Q_{-1} Q_{-2}) population as (0, 25, 50, 25, 0) at different θ values. (b) The quintet spectra showing the similarity between θ = 70° 115° and 135° which correspond to the triplet spectra at ϕ = 45°, 90° and 160°, respectively.

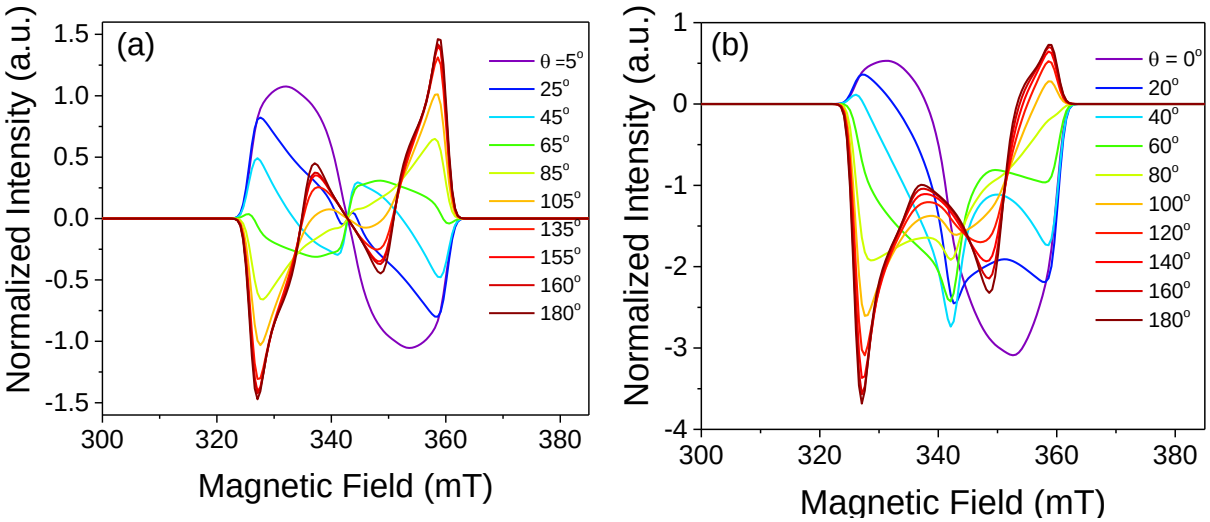

Figure 5.24. (a) The simulated $^{3}(T_1T_1)$ spectra using (T_{+1} T_0 T_{-1}) population as (0, 100, 0)

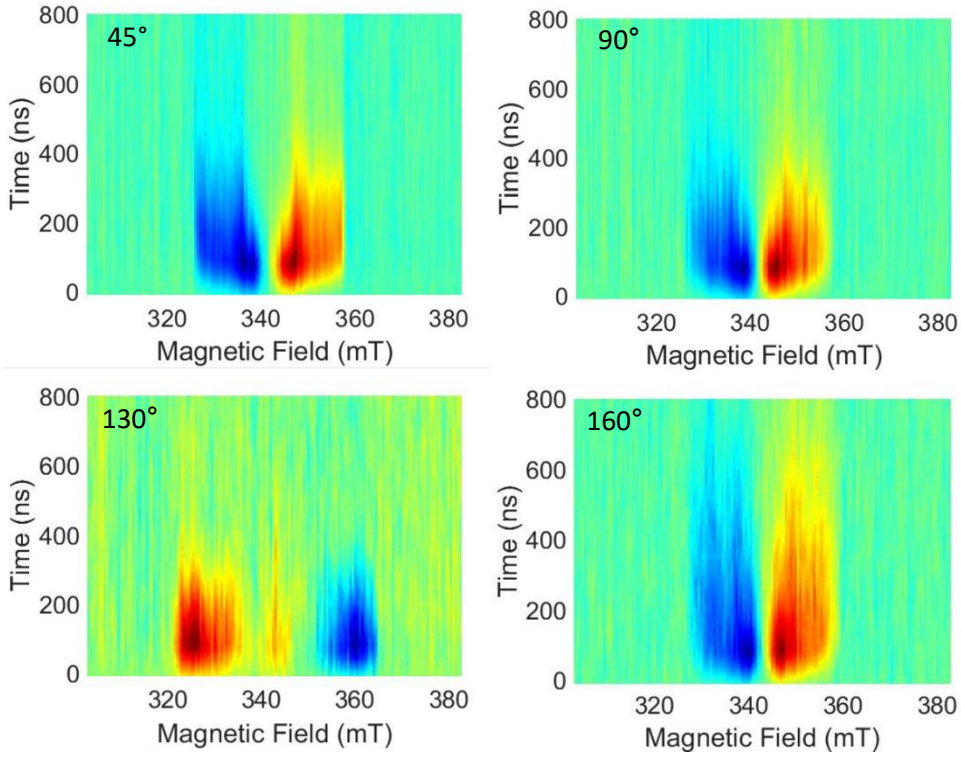

Figure 5.25. TREPR spectra of the **QDI** oriented film at the specific angle between the substrate and the magnetic field.

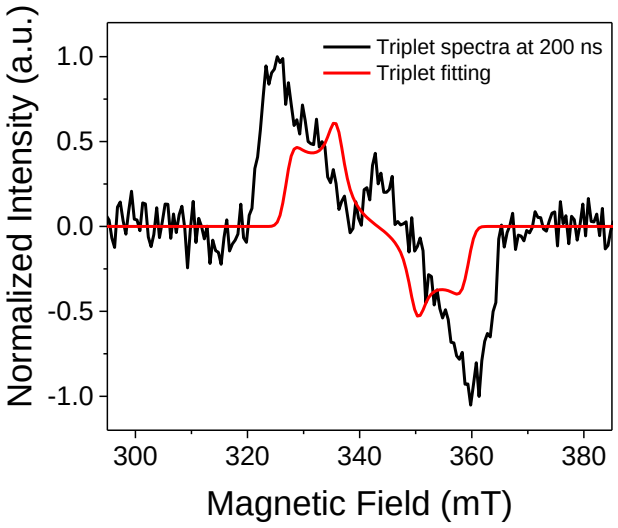

Figure 5.26. The triplet spectrum at 200 ns of the **QDI** oriented film at ϕ = 130° between the substrate and the magnetic field (black) overlaid with the simulated triplet spectrum originating from molecular orientation $\langle\overline{\chi_m}\rangle$ = 68°, where θ = 110°.

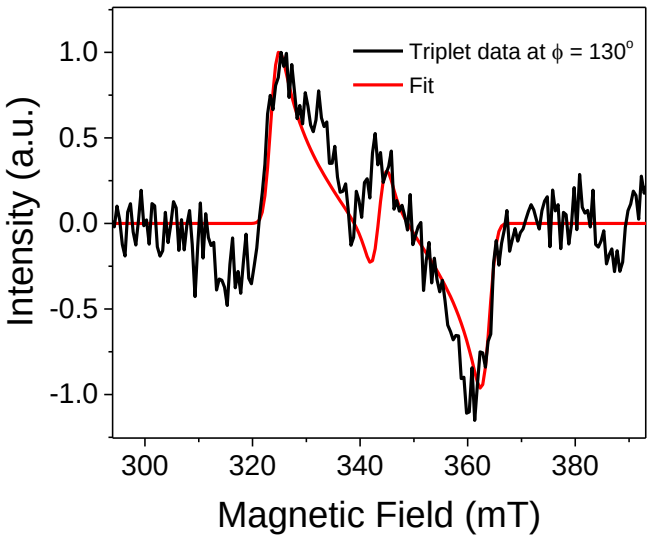

Figure 5.27. The triplet spectrum at 200 ns of the **QDI** oriented film at ϕ = 130° between the substrate and the magnetic field (black) overlaid with the simulated triplet spectrum originating from intersystem crossing at molecular orientation $\langle\overline{\chi_m}\rangle$ = 68°, where θ = 110°. The ZFS parameters used to fit this spectrum is |*D*| = 588 MHz and |*E*| = 185 MHz.

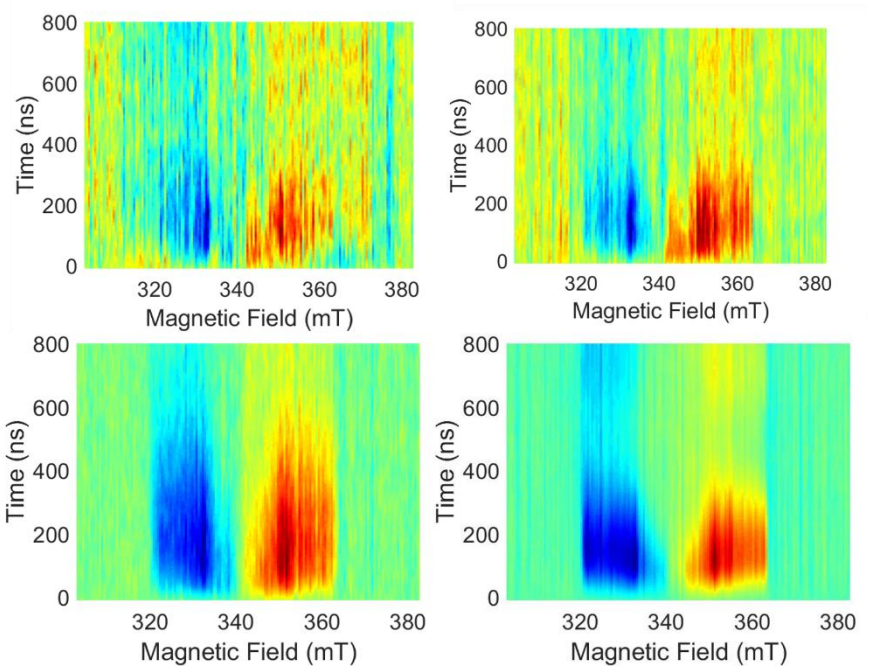

Figure 5.28. TREPR spectra of the **TDI** oriented film at the specific angle between the substrate and the magnetic field.

Table 5.6. TRPER fitting parameters used to fit the quintet and the triplet of the **QDI** oriented film.

QDI (ϕ)	**45°**	**90°**	**130°**	**160°**
g	2.002	2.002	2.002	2.002
$\|D\|$ (MHz)	565	565	650	565
$\|E\|$	85	85	85	85
Euler angle (α,β,γ) of zero-field splitting (1st triplet)	(3°,60°,10°)	(3°,60°,10°)	-	(3°,60°,10°)
Euler angle (α,β,γ) of zero-field splitting (2nd triplet)	(0°,0°,0°)	(0°,0°,0°)	-	(0°,0°,0°)
J (GHz)	30	30	-	30
Dipolar coupling (MHz)	50	50	-	50
θ	115°	70°	45°	135°
FWHM θ	30°	30°	30°	30°
Molecular orientation	70°	70°	5°	65°
$\rho(\|^5(TT)_{+2}\rangle)$	0	0	-	0
$\rho(\|^5(TT)_{+1}\rangle)$	23	26	-	30
$\rho(\|^5(TT)_{0}\rangle)$	47	43	-	43
$\rho(\|^5(TT)_{-1}\rangle)$	29	26	-	28
$\rho(\|^5(TT)_{-2}\rangle)$	0	5	-	0
$\rho(\|^3(TT)_{+1}\rangle)$	0	0	-	0
$\rho(\|^3(TT)_{0}\rangle)$	72	58	-	100
$\rho(\|^3(TT)_{-1}\rangle)$	27	41	-	0
$\rho(\|T_{+1}\rangle)$	0	0	0	0
$\rho(\|T_{0}\rangle)$	86	90	96	80
$\rho(\|T_{-1}\rangle)$	14	10	4	20

Table 5.7. TREPR fitting parameters used to fit the quintet and the triplet of the **TDI** oriented film.

TDI (ϕ)	**45°**	**90°**	**120°**	**160°**
g	2.002	2.002	2.002	2.002
$\|D\|$ (MHz)	851	851	851	851
$\|E\|$	112	112	112	112
Euler angle (α,β,γ) of zero-field splitting (1st triplet)	(3°,60°,10°)	(3°,60°,10°)	(3°,60°,10°)	(3°,60°,10°)
Euler angle (α,β,γ) of zero-field splitting (2nd triplet)	(0°,0°,0°)	(0°,0°,0°)	(0°,0°,0°)	(0°,0°,0°)
J (GHz)	30	30	30	30
Dipolar coupling (MHz)	50	50	50	50
θ	70°	85°	90°	110°
FWHM	50°	50°	50°	50°
Molecular orientation	50°	85°	60°	80°
$\rho(\|^5(TT)_{+2}\rangle)$	0	0	0	0
$\rho(\|^5(TT)_{+1}\rangle)$	28	27	29	28
$\rho(\|^5(TT)_{0}\rangle)$	35	28	42	34
$\rho(\|^5(TT)_{-1}\rangle)$	28	26	30	28
$\rho(\|^5(TT)_{-2}\rangle)$	9	18	0	9
$\rho(\|^3(TT)_{+1}\rangle)$	0	0	0	0
$\rho(\|^3(TT)_{0}\rangle)$	44	52	80	50
$\rho(\|^3(TT)_{-1}\rangle)$	56	48	20	45
$\rho(\|T_{+1}\rangle)$	10	0	0	0
$\rho(\|T_{0}\rangle)$	90	94	93	92
$\rho(\|T_{-1}\rangle)$	0	6	7	8

References

1. Singh, S.; Jones, W. J.; Siebrand, W.; Stoicheff, B. P.; Schneider, W. G., Laser Generation of Excitons and Fluorescence in Anthracene Crystals. *J. Chem. Phys.* **1965,** *42* (1), 330-342.
2. Smith, M. B.; Michl, J., Singlet Fission. *Chem. Rev.* **2010,** *110* (11), 6891-6936.
3. Chen, M.; Bae, Y. J.; Mauck, C. M.; Mandal, A.; Young, R. M.; Wasielewski, M. R., Singlet Fission in Covalent Terrylenediimide Dimers: Probing the Nature of the Multiexciton State Using Femtosecond Mid-Infrared Spectroscopy. *J. Am. Chem. Soc.* **2018,** *140* (29), 9184-9192.
4. Collins, M. I.; McCamey, D. R.; Tayebjee, M. J. Y., Fluctuating exchange interactions enable quintet multiexciton formation in singlet fission. *J. Chem. Phys* **2019,** *151* (16), 164104.
5. Tayebjee, M. J. Y.; Sanders, S. N.; Kumarasamy, E.; Campos, L. M.; Sfeir, M. Y.; McCamey, D. R., Quintet multiexciton dynamics in singlet fission. *Nat. Phys.* **2017,** *13* (2), 182-188.
6. Singh, S.; Jones, W. J.; Siebrand, W.; Stoicheff, B. P.; Schneider, W. G., Laser Generation of Excitons and Fluorescence in Anthracene Crystals. *The Journal of Chemical Physics* **1965,** *42* (1), 330-342.
7. Swenberg, C. E.; Stacy, W. T., Bimolecular radiationless transitions in crystalline tetracene. *Chem. Phys. Lett.* **1968,** *2* (5), 327-328.
8. Geacintov, N.; Pope, M.; Vogel, F., Effect of Magnetic Field on the Fluorescence of Tetracene Crystals: Exciton Fission. *Phys. Rev. Lett.* **1969,** *22* (12), 593-596.
9. Merrifield, R. E.; Avakian, P.; Groff, R. P., Fission of singlet excitons into pairs of triplet excitons in tetracene crystals. *Chem. Phys. Lett.* **1969,** *3* (6), 386-388.
10. Merrifield, R. E., Theory of Magnetic Field Effects on the Mutual Annihilation of Triplet Excitons. *J. Chem. Phys.* **1968,** *48* (9), 4318-4319.
11. Johnson, R. C.; Merrifield, R. E., Effects of Magnetic Fields on the Mutual Annihilation of Triplet Excitons in Anthracene Crystals. *Phys. Rev. B* **1970,** *1* (2), 896-902.
12. Suna, A., Kinematics of Exciton-Exciton Annihilation in Molecular Crystals. *Phys. Rev. B* **1970,** *1* (4), 1716-1739.
13. Hanna, M. C.; Nozik, A. J., Solar conversion efficiency of photovoltaic and photoelectrolysis cells with carrier multiplication absorbers. *J. Appl. Phys.* **2006,** *100* (7), 074510.

14. Lee, J.; Jadhav, P.; Reusswig, P. D.; Yost, S. R.; Thompson, N. J.; Congreve, D. N.; Hontz, E.; Van Voorhis, T.; Baldo, M. A., Singlet Exciton Fission Photovoltaics. *Acc. Chem. Res.* **2013,** *46* (6), 1300-1311.
15. Rao, A.; Friend, R. H., Harnessing singlet exciton fission to break the Shockley-Queisser limit. *Nature Reviews Materials* **2017,** *2* (10), 17063.
16. Piland, G. B.; Burdett, J. J.; Dillon, R. J.; Bardeen, C. J., Singlet fission: From coherences to kinetics. *J. Phys. Chem. Lett.* **2014,** *5*, 2312-2319.
17. Geacintov, N. E.; Burgos, J.; Pope, M.; Strom, C., Heterofission of pentacene excited singlets in pentacene-doped tetracene crystals. *Chem. Phys. Lett.* **1971,** *11* (4), 504-508.
18. Maliakal, A.; Raghavachari, K.; Katz, H.; Chandross, E.; Siegrist, T., Photochemical Stability of Pentacene and a Substituted Pentacene in Solution and in Thin Films. *Chem. Mat.* **2004,** *16* (24), 4980-4986.
19. Eaton, S. W.; Shoer, L. E.; Karlen, S. D.; Dyar, S. M.; Margulies, E. A.; Veldkamp, B. S.; Ramanan, C.; Hartzler, D. A.; Savikhin, S.; Marks, T. J.; Wasielewski, M. R., Singlet Exciton Fission in Polycrystalline Thin Films of a Slip-Stacked Perylenediimide. *Journal of the American Chemical Society* **2013,** *135* (39), 14701-14712.
20. Margulies, E. A.; Logsdon, J. L.; Miller, C. E.; Ma, L.; Simonoff, E.; Young, R. M.; Schatz, G. C.; Wasielewski, M. R., Direct Observation of a Charge-Transfer State Preceding High-Yield Singlet Fission in Terrylenediimide Thin Films. *J. Am. Chem. Soc.* **2017,** *139* (2), 663-671.
21. Chen, M.; Powers-Riggs, N. E.; Coleman, A. F.; Young, R. M.; Wasielewski, M. R., Singlet Fission in Quaterrylenediimide Thin Films. *J. Phys. Chem. C* **2020**.
22. Mauck, C. M.; Hartnett, P. E.; Margulies, E. A.; Ma, L.; Miller, C. E.; Schatz, G. C.; Marks, T. J.; Wasielewski, M. R., Singlet Fission via an Excimer-Like Intermediate in 3,6-Bis(thiophen-2-yl)diketopyrrolopyrrole Derivatives. *J Am Chem Soc* **2016,** *138* (36), 11749-61.
23. Hartnett, P. E.; Margulies, E. A.; Mauck, C. M.; Miller, S. A.; Wu, Y.; Wu, Y.-L.; Marks, T. J.; Wasielewski, M. R., Effects of Crystal Morphology on Singlet Exciton Fission in Diketopyrrolopyrrole Thin Films. *J. Phys. Chem. B* **2016,** *120* (7), 1357-1366.
24. Lee, J.; Jadhav, P.; Baldo, M. A., High efficiency organic multilayer photodetectors based on singlet exciton fission. *Appl. Phys. Lett.* **2009,** *95* (3), 033301.
25. Congreve, D. N.; Lee, J.; Thompson, N. J.; Hontz, E.; Yost, S. R.; Reusswig, P. D.; Bahlke, M. E.; Reineke, S.; Van Voorhis, T.; Baldo, M. A., External Quantum Efficiency Above 100% in a Singlet-Exciton-Fission–Based Organic Photovoltaic Cell. *Science* **2013,** *340* (6130), 334.
26. Ehrler, B.; Wilson, M. W. B.; Rao, A.; Friend, R. H.; Greenham, N. C., Singlet Exciton Fission-Sensitized Infrared Quantum Dot Solar Cells. *Nano Lett.* **2012,** *12* (2), 1053-1057.
27. Futscher, M. H.; Rao, A.; Ehrler, B., The Potential of Singlet Fission Photon Multipliers as an Alternative to Silicon-Based Tandem Solar Cells. *ACS Energy Lett.* **2018,** *3* (10), 2587-2592.
28. Einzinger, M.; Wu, T.; Kompalla, J. F.; Smith, H. L.; Perkinson, C. F.; Nienhaus, L.; Wieghold, S.; Congreve, D. N.; Kahn, A.; Bawendi, M. G.; Baldo, M. A., Sensitization of silicon by singlet exciton fission in tetracene. *Nature* **2019,** *571* (7763), 90-94.
29. Zhu, T.; Wan, Y.; Guo, Z.; Johnson, J.; Huang, L., Two Birds with One Stone: Tailoring Singlet Fission for Both Triplet Yield and Exciton Diffusion Length. *Adv. Mater.* **2016,** *28* (34), 7539-7547.

30. Wan, Y.; Wiederrecht, G. P.; Schaller, R. D.; Johnson, J. C.; Huang, L., Transport of Spin-Entangled Triplet Excitons Generated by Singlet Fission. *J. Phys. Chem. Lett.* **2018,** *9* (23), 6731-6738.
31. Chan, W.-L.; Ligges, M.; Jailaubekov, A.; Kaake, L.; Miaja-Avila, L.; Zhu, X. Y., Observing the Multiexciton State in Singlet Fission and Ensuing Ultrafast Multielectron Transfer. *Science* **2011,** *334* (6062), 1541.
32. Pazos-Outón, L. M.; Lee, J. M.; Futscher, M. H.; Kirch, A.; Tabachnyk, M.; Friend, R. H.; Ehrler, B., A Silicon–Singlet Fission Tandem Solar Cell Exceeding 100% External Quantum Efficiency with High Spectral Stability. *ACS Energy Lett.* **2017,** *2* (2), 476-480.
33. Bae, Y. J.; Christensen, J. A.; Kang, G.; Zhou, J.; Young, R. M.; Wu, Y.-L.; Van Duyne, R. P.; Schatz, G. C.; Wasielewski, M. R., Substituent effects on energetics and crystal morphology modulate singlet fission in 9,10-bis(phenylethynyl)anthracenes. *J. Chem. Phys* **2019,** *151* (4), 044501.
34. Bae, Y. J.; Christensen, J. A.; Kang, G.; Malliakas, C. D.; Zhou, J.; Nelson, J. N.; Young, R. M.; Wu, Y. L.; van Duyne, R. P.; Schatz, G. C.; Wasielewski, M. R., Design principles for efficient singlet fission in anthracene-based organic semiconductors. *Proc. SPIE 11084, Physical Chemistry of Semiconductor Materials and Interfaces XVIII* **2019,** *110840Q*
35. Mauck, C. M.; Bae, Y. J.; Chen, M.; Powers-Riggs, N.; Wu, Y.-L.; Wasielewski, M. R., Charge-Transfer Character in a Covalent Diketopyrrolopyrrole Dimer: Implications for Singlet Fission. *ChemPhotoChem* **2018,** *2* (3), 223-233.
36. Fallon, K. J.; Budden, P.; Salvadori, E.; Ganose, A. M.; Savory, C. N.; Eyre, L.; Dowland, S.; Ai, Q.; Goodlett, S.; Risko, C.; Scanlon, D. O.; Kay, C. W. M.; Rao, A.; Friend, R. H.; Musser, A. J.; Bronstein, H., Exploiting Excited-State Aromaticity To Design Highly Stable Singlet Fission Materials. *Journal of the American Chemical Society* **2019,** *141* (35), 13867-13876.
37. Conrad-Burton, F. S.; Liu, T.; Geyer, F.; Costantini, R.; Schlaus, A. P.; Spencer, M. S.; Wang, J.; Sánchez, R. H.; Zhang, B.; Xu, Q.; Steigerwald, M. L.; Xiao, S.; Li, H.; Nuckolls, C. P.; Zhu, X., Controlling Singlet Fission by Molecular Contortion. *Journal of the American Chemical Society* **2019,** *141* (33), 13143-13147.
38. Perkinson, C. F.; Tabor, D. P.; Einzinger, M.; Sheberla, D.; Utzat, H.; Lin, T.-A.; Congreve, D. N.; Bawendi, M. G.; Aspuru-Guzik, A.; Baldo, M. A., Discovery of blue singlet exciton fission molecules via a high-throughput virtual screening and experimental approach. *J. Chem. Phys.* **2019,** *151* (12), 121102.
39. Rao, A.; Friend, R. H., Harnessing singlet exciton fission to break the Shockley–Queisser limit. *Nature Reviews Materials* **2017,** *2*, 17063.
40. Wilson, M. W. B.; Rao, A.; Clark, J.; Kumar, R. S. S.; Brida, D.; Cerullo, G.; Friend, R. H., Ultrafast Dynamics of Exciton Fission in Polycrystalline Pentacene. *Journal of the American Chemical Society* **2011,** *133* (31), 11830-11833.
41. Musser, A. J.; Liebel, M.; Schnedermann, C.; Wende, T.; Kehoe, T. B.; Rao, A.; Kukura, P., Evidence for conical intersection dynamics mediating ultrafast singlet exciton fission. *Nat. Phys.* **2015,** *11* (4), 352-357.
42. Halpin, A.; Johnson, P. J. M.; Tempelaar, R.; Murphy, R. S.; Knoester, J.; Jansen, T. L. C.; Miller, R. J. D., Two-dimensional spectroscopy of a molecular dimer unveils the effects of vibronic coupling on exciton coherences. *Nat. Chem.* **2014,** *6* (3), 196-201.

43. Tempelaar, R.; Reichman, D. R., Vibronic exciton theory of singlet fission. III. How vibronic coupling and thermodynamics promote rapid triplet generation in pentacene crystals. *J. Chem. Phys.* **2018,** *148* (24), 244701.
44. Monahan, N. R.; Sun, D.; Tamura, H.; Williams, K. W.; Xu, B.; Zhong, Y.; Kumar, B.; Nuckolls, C.; Harutyunyan, A. R.; Chen, G.; Dai, H.-L.; Beljonne, D.; Rao, Y.; Zhu, X. Y., Dynamics of the triplet-pair state reveals the likely coexistence of coherent and incoherent singlet fission in crystalline hexacene. *Nat. Chem.* **2017,** *9* (4), 341-346.
45. Miyata, K.; Kurashige, Y.; Watanabe, K.; Sugimoto, T.; Takahashi, S.; Tanaka, S.; Takeya, J.; Yanai, T.; Matsumoto, Y., Coherent singlet fission activated by symmetry breaking. *Nat. Chem.* **2017,** *9* (10), 983-989.
46. Hart, Stephanie M.; Silva, W. R.; Frontiera, R. R., Femtosecond stimulated Raman evidence for charge-transfer character in pentacene singlet fission. *Chem. Sci.* **2018,** *9* (5), 1242-1250.
47. Bera, K.; Douglas, C. J.; Frontiera, R. R., Femtosecond Raman Microscopy Reveals Structural Dynamics Leading to Triplet Separation in Rubrene Singlet Fission. *J. Phys. Chem. Lett.* **2017,** *8* (23), 5929-5934.
48. Grieco, C.; Kennehan, E. R.; Kim, H.; Pensack, R. D.; Brigeman, A. N.; Rimshaw, A.; Payne, M. M.; Anthony, J. E.; Giebink, N. C.; Scholes, G. D.; Asbury, J. B., Direct Observation of Correlated Triplet Pair Dynamics during Singlet Fission Using Ultrafast Mid-IR Spectroscopy. *J. Phys. Chem. C* **2018,** *122* (4), 2012-2022.
49. Wan, Y.; Guo, Z.; Zhu, T.; Yan, S.; Johnson, J.; Huang, L., Cooperative singlet and triplet exciton transport in tetracene crystals visualized by ultrafast microscopy. *Nat. Chem.* **2015,** *7* (10), 785-792.
50. Folie, B. D.; Haber, J. B.; Refaely-Abramson, S.; Neaton, J. B.; Ginsberg, N. S., Long-Lived Correlated Triplet Pairs in a π-Stacked Crystalline Pentacene Derivative. *J. Am. Chem. Soc.* **2018,** *140* (6), 2326-2335.
51. Burdett, J. J.; Bardeen, C. J., Quantum beats in crystalline tetracene delayed fluorescence due to triplet pair coherences produced by direct singlet fission. *J Am Chem Soc* **2012,** *134* (20), 8597-607.
52. Chen, M.; Krzyaniak, M. D.; Nelson, J. N.; Bae, Y. J.; Harvey, S. M.; Schaller, R. D.; Young, R. M.; Wasielewski, M. R., Quintet-triplet mixing determines the fate of the multiexciton state produced by singlet fission in a terrylenediimide dimer at room temperature. *Proceedings of the National Academy of Sciences of the United States of America* **2019,** *116* (17), 8178-8183.
53. Wakasa, M.; Kaise, M.; Yago, T.; Katoh, R.; Wakikawa, Y.; Ikoma, T., What Can Be Learned from Magnetic Field Effects on Singlet Fission: Role of Exchange Interaction in Excited Triplet Pairs. *J. Phys. Chem. C* **2015,** *119* (46), 25840-25844.
54. Bayliss, S. L.; Weiss, L. R.; Mitioglu, A.; Galkowski, K.; Yang, Z.; Yunusova, K.; Surrente, A.; Thorley, K. J.; Behrends, J.; Bittl, R.; Anthony, J. E.; Rao, A.; Friend, R. H.; Plochocka, P.; Christianen, P. C. M.; Greenham, N. C.; Chepelianskii, A. D., Site-selective measurement of coupled spin pairs in an organic semiconductor. *Proceedings of the National Academy of Sciences of the United States of America* **2018,** *115* (20), 5077-5082.
55. Burdett, J. J.; Piland, G. B.; Bardeen, C. J., Magnetic field effects and the role of spin states in singlet fission. *Chem. Phys. Lett.* **2013,** *585*, 1-10.

56. Bayliss, S. L.; Chepelianskii, A. D.; Sepe, A.; Walker, B. J.; Ehrler, B.; Bruzek, M. J.; Anthony, J. E.; Greenham, N. C., Geminate and Nongeminate Recombination of Triplet Excitons Formed by Singlet Fission. *Phys. Rev. Lett.* **2014,** *112* (23), 238701.
57. Agostini, G.; Corvaja, C.; Giacometti, G.; Pasimeni, L., Optical, zero-field ODMR and EPR studies of the triplet states from singlet fission in biphenyl-TCNQ and biphenyl-tetrafluoro-TCNQ charge-transfer crystals. *Chem. Phys.* **1993,** *173* (2), 177-186.
58. Rao, A.; Wilson, M. W. B.; Albert-Seifried, S.; Di Pietro, R.; Friend, R. H., Photophysics of pentacene thin films: The role of exciton fission and heating effects. *Phys. Rev. B* **2011,** *84* (19), 195411.
59. Le, A. K.; Bender, J. A.; Arias, D. H.; Cotton, D. E.; Johnson, J. C.; Roberts, S. T., Singlet Fission Involves an Interplay between Energetic Driving Force and Electronic Coupling in Perylenediimide Films. *Journal of the American Chemical Society* **2018,** *140* (2), 814-826.
60. Nichols, V. M.; Broch, K.; Schreiber, F.; Bardeen, C. J., Excited-State Dynamics of Diindenoperylene in Liquid Solution and in Solid Films. *J. Phys. Chem. C* **2015,** *119* (23), 12856-12864.
61. Yarmus, L.; Rosenthal, J.; Chopp, M., EPR of triplet excitions in tetracene crystals: spin polarization and the role of singlet exciton fission. *Chem. Phys. Lett.* **1972,** *16* (3), 477-481.
62. Swenberg, C. E.; van Metter, R.; Ratner, M., Comments on exciton fission and electron spin resonance in tetracene single crystals. *Chem. Phys. Lett.* **1972,** *16* (3), 482-485.
63. Weiss, L. R.; Bayliss, S. L.; Kraffert, F.; Thorley, K. J.; Anthony, J. E.; Bittl, R.; Friend, R. H.; Rao, A.; Greenham, N. C.; Behrends, J., Strongly exchange-coupled triplet pairs in an organic semiconductor. *Nat. Phys.* **2016,** *13*, 176.
64. Matsuda, S.; Oyama, S.; Kobori, Y., Electron spin polarization generated by transport of singlet and quintet multiexcitons to spin-correlated triplet pairs during singlet fissions. *Chem. Sci.* **2020,** *11* (11), 2934-2942.
65. Nagashima, H.; Kawaoka, S.; Akimoto, S.; Tachikawa, T.; Matsui, Y.; Ikeda, H.; Kobori, Y., Singlet-Fission-Born Quintet State: Sublevel Selections and Trapping by Multiexciton Thermodynamics. *J. Phys. Chem. Lett.* **2018,** *9* (19), 5855-5861.
66. Lubert-Perquel, D.; Salvadori, E.; Dyson, M.; Stavrinou, P. N.; Montis, R.; Nagashima, H.; Kobori, Y.; Heutz, S.; Kay, C. W. M., Identifying triplet pathways in dilute pentacene films. *Nat. Comm.* **2018,** *9* (1), 4222.
67. Bayliss, S. L.; Kraffert, F.; Wang, R.; Zhang, C.; Bittl, R.; Behrends, J., Tuning Spin Dynamics in Crystalline Tetracene. *J. Phys. Chem. Lett.* **2019,** *10* (8), 1908-1913.
68. Margulies, E. A.; Shoer, L. E.; Eaton, S. W.; Wasielewski, M. R., Excimer formation in cofacial and slip-stacked perylene-3,4:9,10-bis(dicarboximide) dimers on a redox-inactive triptycene scaffold. *Phys. Chem. Chem. Phys.* **2014,** *16* (43), 23735-23742.
69. Cook, R. E.; Phelan, B. T.; Kamire, R. J.; Majewski, M. B.; Young, R. M.; Wasielewski, M. R., Excimer Formation and Symmetry-Breaking Charge Transfer in Cofacial Perylene Dimers. *J. Phys. Chem. A* **2017,** *121* (8), 1607-1615.
70. Sung, J.; Kim, P.; Fimmel, B.; Würthner, F.; Kim, D., Direct observation of ultrafast coherent exciton dynamics in helical π-stacks of self-assembled perylene bisimides. *Nat. Comm.* **2015,** *6* (1), 8646.
71. Hong, Y.; Kim, J.; Kim, W.; Kaufmann, C.; Kim, H.; Würthner, F.; Kim, D., Efficient Multiexciton State Generation in Charge-Transfer-Coupled Perylene Bisimide Dimers via Structural Control. *J. Am. Chem. Soc.* **2020,** *142* (17), 7845-7857.

72. Myong, M. S.; Zhou, J.; Young, R. M.; Wasielewski, M. R., Charge-Transfer Character in Excimers of Perylenediimides Self-Assembled on Anodic Aluminum Oxide Membrane Walls. *J. Phys. Chem. C* **2020,** *124* (8), 4369-4377.
73. Walker, B. J.; Musser, A. J.; Beljonne, D.; Friend, R. H., Singlet exciton fission in solution. *Nat. Chem.* **2013,** *5* (12), 1019-1024.
74. Pensack, R. D.; Ashmore, R. J.; Paoletta, A. L.; Scholes, G. D., The Nature of Excimer Formation in Crystalline Pyrene Nanoparticles. *J. Phys. Chem. C* **2018,** *122* (36), 21004-21017.
75. Vollbrecht, J., Excimers in organic electronics. *New J. Chem.* **2018,** *42* (14), 11249-11254.
76. Chen, Z.; Stepanenko, V.; Dehm, V.; Prins, P.; Siebbeles, L. D. A.; Seibt, J.; Marquetand, P.; Engel, V.; Würthner, F., Photoluminescence and Conductivity of Self-Assembled π–π Stacks of Perylene Bisimide Dyes. *Chem. Eur. J.* **2007,** *13* (2), 436-449.
77. Singh, R.; Kim, M.; Lee, J.-J.; Ye, T.; Keivanidis, P. E.; Cho, K., Excimer formation effects and trap-assisted charge recombination loss channels in organic solar cells of perylene diimide dimer acceptors. *J. Mater. Chem. C* **2020,** *8* (5), 1686-1696.
78. Wasielewski, M. R., Self-Assembly Strategies for Integrating Light Harvesting and Charge Separation in Artificial Photosynthetic Systems. *Acc. Chem. Res.* **2009,** *42* (12), 1910-1921.
79. Matsui, A. H., Excitonic processes in aromatic molecular crystals of strong exciton-phonon coupling. *Pure Appl. Chem.* **1995,** *67* (3), 429-436.
80. Fink, R. F.; Seibt, J.; Engel, V.; Renz, M.; Kaupp, M.; Lochbrunner, S.; Zhao, H.-M.; Pfister, J.; Würthner, F.; Engels, B., Exciton Trapping in π-Conjugated Materials: A Quantum-Chemistry-Based Protocol Applied to Perylene Bisimide Dye Aggregates. *J. Am. Chem. Soc.* **2008,** *130* (39), 12858-12859.
81. Dover, C. B.; Gallaher, J. K.; Frazer, L.; Tapping, P. C.; Petty Ii, A. J.; Crossley, M. J.; Anthony, J. E.; Kee, T. W.; Schmidt, T. W., Endothermic singlet fission is hindered by excimer formation. *Nat. Chem.* **2018,** *10*, 305.
82. Brown, K. E.; Salamant, W. A.; Shoer, L. E.; Young, R. M.; Wasielewski, M. R., Direct Observation of Ultrafast Excimer Formation in Covalent Perylenediimide Dimers Using Near-Infrared Transient Absorption Spectroscopy. *J. Phys. Chem. Lett.* **2014,** *5* (15), 2588-2593.
83. Sung, J.; Nowak-Król, A.; Schlosser, F.; Fimmel, B.; Kim, W.; Kim, D.; Würthner, F., Direct Observation of Excimer-Mediated Intramolecular Electron Transfer in a Cofacially-Stacked Perylene Bisimide Pair. *J. Am. Chem. Soc.* **2016,** *138* (29), 9029-9032.
84. Azumi, T.; Armstrong, A. T.; McGlynn, S. P., Energy of Excimer Luminescence. II. Configuration Interaction between Molecular Exciton States and Charge Resonance States. *J. Chem. Phys.* **1964,** *41* (12), 3839-3852.
85. Kim, W.; Nowak-Król, A.; Hong, Y.; Schlosser, F.; Würthner, F.; Kim, D., Solvent-Modulated Charge-Transfer Resonance Enhancement in the Excimer State of a Bay-Substituted Perylene Bisimide Cyclophane. *J. Phys. Chem. Lett.* **2019,** *10* (8), 1919-1927.
86. Wu, Y.; Zhou, J.; Phelan, B. T.; Mauck, C. M.; Stoddart, J. F.; Young, R. M.; Wasielewski, M. R., Probing Distance Dependent Charge-Transfer Character in Excimers of Extended Viologen Cyclophanes Using Femtosecond Vibrational Spectroscopy. *Journal of the American Chemical Society* **2017,** *139* (40), 14265-14276.
87. Kasha, M.; Rawls, H. R.; El-Bayoumi, M. A., The exciton model in molecular spectroscopy. *Pure Appl. Chem.* **1965,** *11* (3-4), 371-392.

88. Hestand, N. J.; Spano, F. C., Molecular Aggregate Photophysics beyond the Kasha Model: Novel Design Principles for Organic Materials. *Acc. Chem. Res.* **2017,** *50* (2), 341-350.
89. Kaufmann, C.; Bialas, D.; Stolte, M.; Würthner, F., Discrete π-Stacks of Perylene Bisimide Dyes within Folda-Dimers: Insight into Long- and Short-Range Exciton Coupling. *Journal of the American Chemical Society* **2018,** *140* (31), 9986-9995.
90. Bae, Y. J.; Kang, G.; Malliakas, C. D.; Nelson, J. N.; Zhou, J.; Young, R. M.; Wu, Y. L.; Van Duyne, R. P.; Schatz, G. C.; Wasielewski, M. R., Singlet Fission in 9,10-Bis(phenylethynyl)anthracene Thin Films. *J Am Chem Soc* **2018,** *140* (45), 15140-15144.
91. Young, R. M.; Dyar, S. M.; Barnes, J. C.; Juricek, M.; Stoddart, J. F.; Co, D. T.; Wasielewski, M. R., Ultrafast Conformational Dynamics of Electron Transfer in ExBox4+⊂Perylene. *J. Phys. Chem. A* **2013,** *117* (47), 12438-12448.
92. Greenfield, S. R.; Wasielewski, M. R., Near-transform-limited visible and near-IR femtosecond pulses from optical parametric amplification using type II b-barium borate. *Opt. Lett.* **1995,** *20* (12), 1394-6.
93. te Velde, G.; Bickelhaupt, F. M.; Baerends, E. J.; Fonseca Guerra, C.; van Gisbergen, S. J. A.; Snijders, J. G.; Ziegler, T., Chemistry with ADF. *J. Comput. Chem* **2001,** *22* (9), 931-967.
94. Senthilkumar, K.; Grozema, F. C.; Bickelhaupt, F. M.; Siebbeles, L. D. A., Charge transport in columnar stacked triphenylenes: Effects of conformational fluctuations on charge transfer integrals and site energies. *J. Chem. Phys.* **2003,** *119* (18), 9809-9817.
95. Renaud, N.; Sherratt, P. A.; Ratner, M. A., Mapping the relation between stacking geometries and singlet fission yield in a class of organic crystals. *J. Phys. Chem. Lett.* **2013,** *4* (7), 1065-1069.
96. McCarthy, B. D.; Hontz, E. R.; Yost, S. R.; Van Voorhis, T.; Dincă, M., Charge Transfer or J-Coupling? Assignment of an Unexpected Red-Shifted Absorption Band in a Naphthalenediimide-Based Metal–Organic Framework. *J. Phys. Chem. Lett.* **2013,** *4* (3), 453-458.
97. Hestand, N. J.; Spano, F. C., Expanded Theory of H- and J-Molecular Aggregates: The Effects of Vibronic Coupling and Intermolecular Charge Transfer. *Chem. Rev.* **2018,** *118* (15), 7069-7163.
98. Levitus, M.; Garcia-Garibay, M. A., Polarized Electronic Spectroscopy and Photophysical Properties of 9,10-Bis(phenylethynyl)anthracene. *J. Phys. Chem. A* **2000,** *104* (38), 8632-8637.
99. Yamane, S.; Sagara, Y.; Kato, T., Steric effects on excimer formation for photoluminescent smectic liquid-crystalline materials. *Chem. Comm.* **2013,** *49* (37), 3839-3841.
100. Sagara, Y.; Simon, Y. C.; Tamaoki, N.; Weder, C., A mechano- and thermoresponsive luminescent cyclophane. *Chem. Comm.* **2016,** *52* (33), 5694-5697.
101. Winters, M. U.; Pettersson, K.; Mårtensson, J.; Albinsson, B., Competition between Superexchange-Mediated and Sequential Electron Transfer in a Bridged Donor–Acceptor System. *Chem. Eur. J.* **2005,** *11* (2), 562-573.
102. Miller, C. E.; Wasielewski, M. R.; Schatz, G. C., Modeling Singlet Fission in Rylene and Diketopyrrolopyrrole Derivatives: The Role of the Charge Transfer State in Superexchange and Excimer Formation. *J. Phys. Chem. C* **2017,** *121* (19), 10345-10350.

103. Mauck, C. M.; Hartnett, P. E.; Margulies, E. A.; Ma, L.; Miller, C. E.; Schatz, G. C.; Marks, T. J.; Wasielewski, M. R., Singlet Fission via an Excimer-Like Intermediate in 3,6-Bis(thiophen-2-yl)diketopyrrolopyrrole Derivatives. *J. Am. Chem. Soc.* **2016,** *138* (36), 11749-11761.
104. Galstyan, A.; Maurya, Y. K.; Zhylitskaya, H.; Bae, Y. J.; Wu, Y.-L.; Wasielewski, M. R.; Lis, T.; Dobrindt, U.; Stępień, M., π-Extended Donor–Acceptor Porphyrins and Metalloporphyrins for Antimicrobial Photodynamic Inactivation. *Chem. Eur. J.* **2020,** *26* (37), 8262-8266.
105. Monahan, N.; Zhu, X. Y., Charge Transfer–Mediated Singlet Fission. *Annu. Rev. Phys. Chem* **2015,** *66* (1), 601-618.
106. Nesterov, E. E.; Zhu, Z.; Swager, T. M., Conjugation Enhancement of Intramolecular Exciton Migration in Poly(p-phenylene ethynylene)s. *Journal of the American Chemical Society* **2005,** *127* (28), 10083-10088.
107. Shao, Y.; Gan, Z.; Epifanovsky, E.; Gilbert, A. T. B.; Wormit, M.; Kussmann, J.; Lange, A. W.; Behn, A.; Deng, J.; Feng, X.; Ghosh, D.; Goldey, M.; Horn, P. R.; Jacobson, L. D.; Kaliman, I.; Khaliullin, R. Z.; Kuś, T.; Landau, A.; Liu, J.; Proynov, E. I.; Rhee, Y. M.; Richard, R. M.; Rohrdanz, M. A.; Steele, R. P.; Sundstrom, E. J.; Woodcock, H. L.; Zimmerman, P. M.; Zuev, D.; Albrecht, B.; Alguire, E.; Austin, B.; Beran, G. J. O.; Bernard, Y. A.; Berquist, E.; Brandhorst, K.; Bravaya, K. B.; Brown, S. T.; Casanova, D.; Chang, C.-M.; Chen, Y.; Chien, S. H.; Closser, K. D.; Crittenden, D. L.; Diedenhofen, M.; DiStasio, R. A.; Do, H.; Dutoi, A. D.; Edgar, R. G.; Fatehi, S.; Fusti-Molnar, L.; Ghysels, A.; Golubeva-Zadorozhnaya, A.; Gomes, J.; Hanson-Heine, M. W. D.; Harbach, P. H. P.; Hauser, A. W.; Hohenstein, E. G.; Holden, Z. C.; Jagau, T.-C.; Ji, H.; Kaduk, B.; Khistyaev, K.; Kim, J.; Kim, J.; King, R. A.; Klunzinger, P.; Kosenkov, D.; Kowalczyk, T.; Krauter, C. M.; Lao, K. U.; Laurent, A. D.; Lawler, K. V.; Levchenko, S. V.; Lin, C. Y.; Liu, F.; Livshits, E.; Lochan, R. C.; Luenser, A.; Manohar, P.; Manzer, S. F.; Mao, S.-P.; Mardirossian, N.; Marenich, A. V.; Maurer, S. A.; Mayhall, N. J.; Neuscamman, E.; Oana, C. M.; Olivares-Amaya, R.; O'Neill, D. P.; Parkhill, J. A.; Perrine, T. M.; Peverati, R.; Prociuk, A.; Rehn, D. R.; Rosta, E.; Russ, N. J.; Sharada, S. M.; Sharma, S.; Small, D. W.; Sodt, A.; Stein, T.; Stück, D.; Su, Y.-C.; Thom, A. J. W.; Tsuchimochi, T.; Vanovschi, V.; Vogt, L.; Vydrov, O.; Wang, T.; Watson, M. A.; Wenzel, J.; White, A.; Williams, C. F.; Yang, J.; Yeganeh, S.; Yost, S. R.; You, Z.-Q.; Zhang, I. Y.; Zhang, X.; Zhao, Y.; Brooks, B. R.; Chan, G. K. L.; Chipman, D. M.; Cramer, C. J.; Goddard, W. A.; Gordon, M. S.; Hehre, W. J.; Klamt, A.; Schaefer, H. F.; Schmidt, M. W.; Sherrill, C. D.; Truhlar, D. G.; Warshel, A.; Xu, X.; Aspuru-Guzik, A.; Baer, R.; Bell, A. T.; Besley, N. A.; Chai, J.-D.; Dreuw, A.; Dunietz, B. D.; Furlani, T. R.; Gwaltney, S. R.; Hsu, C.-P.; Jung, Y.; Kong, J.; Lambrecht, D. S.; Liang, W.; Ochsenfeld, C.; Rassolov, V. A.; Slipchenko, L. V.; Subotnik, J. E.; Van Voorhis, T.; Herbert, J. M.; Krylov, A. I.; Gill, P. M. W.; Head-Gordon, M., Advances in molecular quantum chemistry contained in the Q-Chem 4 program package. *Mol. Phys.* **2015,** *113* (2), 184-215.
108. López-Tarifa, P.; Liguori, N.; van den Heuvel, N.; Croce, R.; Visscher, L., Coulomb couplings in solubilised light harvesting complex II (LHCII): challenging the ideal dipole approximation from TDDFT calculations. *Phys. Chem. Chem. Phys.* **2017,** *19* (28), 18311-18320.

109. Quarti, C.; Fazzi, D.; Del Zoppo, M., A computational investigation on singlet and triplet exciton couplings in acene molecular crystals. *Phys. Chem. Chem. Phys.* **2011,** *13* (41), 18615-18625.
110. Kirkus, M.; Wang, L.; Mothy, S.; Beljonne, D.; Cornil, J.; Janssen, R. A. J.; Meskers, S. C. J., Optical Properties of Oligothiophene Substituted Diketopyrrolopyrrole Derivatives in the Solid Phase: Joint J- and H-Type Aggregation. *J. Phys. Chem. A* **2012,** *116* (30), 7927-7936.
111. Rihter, B. D.; Kenney, M. E.; Ford, W. E.; Rodgers, M. A. J., Synthesis and photoproperties of diamagnetic octabutoxyphthalocyanines with deep red optical absorbance. *J. Am. Chem. Soc.* **1990,** *112* (22), 8064-8070.
112. Smith, M. B.; Michl, J., Recent Advances in Singlet Fission. *Annu. Rev. Phys. Chem* **2013,** *64* (1), 361-386.
113. Thompson, N. J.; Wilson, M. W. B.; Congreve, D. N.; Brown, P. R.; Scherer, J. M.; Bischof, Thomas S.; Wu, M.; Geva, N.; Welborn, M.; Voorhis, T. V.; Bulović, V.; Bawendi, M. G.; Baldo, Marc A., Energy harvesting of non-emissive triplet excitons in tetracene by emissive PbS nanocrystals. *Nat. Mater.* **2014,** *13*, 1039.
114. Tabachnyk, M.; Ehrler, B.; Gélinas, S.; Böhm, M. L.; Walker, B. J.; Musselman, K. P.; Greenham, N. C.; Friend, R. H.; Rao, A., Resonant energy transfer of triplet excitons from pentacene to PbSe nanocrystals. *Nat. Mater.* **2014,** *13*, 1033.
115. Fudickar, W.; Linker, T., Why Triple Bonds Protect Acenes from Oxidation and Decomposition. *J. Am. Chem. Soc.* **2012,** *134* (36), 15071-15082.
116. Ribierre, J. C.; Ruseckas, A.; Cavaye, H.; Barcena, H. S.; Burn, P. L.; Samuel, I. D. W., Photophysical Properties of 9,10-Disubstituted Anthracene Derivatives in Solution and Films. *J. Phys. Chem. A* **2011,** *115* (26), 7401-7405.
117. Giménez, R.; Piñol, M.; Serrano, J. L., Luminescent Liquid Crystals Derived from 9,10-Bis(Phenylethynyl)anthracene. *Chem. Mat.* **2004,** *16* (7), 1377-1383.
118. Suneesh, C. V.; Vinayak, M. V.; Gopidas, K. R., Photoinduced Charge Separation in Two Bis(phenylethynyl)anthracene-Based Triads: Inverted Region Effect vs Distance Effect on Back Electron Transfer. *J. Phys. Chem. C* **2010,** *114* (43), 18735-18744.
119. Vura-Weis, J.; Ratner, M. A.; Wasielewski, M. R., Geometry and Electronic Coupling in Perylenediimide Stacks: Mapping Structure−Charge Transport Relationships. *J. Am. Chem. Soc.* **2010,** *132* (6), 1738-1739.
120. Margulies, E. A.; Kerisit, N.; Gawel, P.; Mauck, C. M.; Ma, L.; Miller, C. E.; Young, R. M.; Trapp, N.; Wu, Y.-L.; Diederich, F.; Wasielewski, M. R., Substituent Effects on Singlet Exciton Fission in Polycrystalline Thin Films of Cyano-Substituted Diaryltetracenes. *J. Phys. Chem. C* **2017,** *121* (39), 21262-21271.
121. Hartnett, P. E.; Margulies, E. A.; Mauck, C. M.; Miller, S. A.; Wu, Y.; Wu, Y.-L.; Marks, T. J.; Wasielewski, M. R., Effects of Crystal Morphology on Singlet Exciton Fission in Diketopyrrolopyrrole Thin Films. *The Journal of Physical Chemistry B* **2016,** *120* (7), 1357-1366.
122. Basel, B. S.; Zirzlmeier, J.; Hetzer, C.; Reddy, S. R.; Phelan, B. T.; Krzyaniak, M. D.; Volland, M. K.; Coto, P. B.; Young, R. M.; Clark, T.; Thoss, M.; Tykwinski, R. R.; Wasielewski, M. R.; Guldi, D. M., Evidence for Charge-Transfer Mediation in the Primary Events of Singlet Fission in a Weakly Coupled Pentacene Dimer. *Chem* **2018,** *4* (5), 1092-1111.
123. Kumarasamy, E.; Sanders, S. N.; Tayebjee, M. J. Y.; Asadpoordarvish, A.; Hele, T. J. H.; Fuemmeler, E. G.; Pun, A. B.; Yablon, L. M.; Low, J. Z.; Paley, D. W.; Dean, J. C.;

Choi, B.; Scholes, G. D.; Steigerwald, M. L.; Ananth, N.; McCamey, D. R.; Sfeir, M. Y.; Campos, L. M., Tuning Singlet Fission in π-Bridge-π Chromophores. *J. Am. Chem. Soc.* **2017,** *139* (36), 12488-12494.
124. Basel, B. S.; Zirzlmeier, J.; Hetzer, C.; Phelan, B. T.; Krzyaniak, M. D.; Reddy, S. R.; Coto, P. B.; Horwitz, N. E.; Young, R. M.; White, F. J.; Hampel, F.; Clark, T.; Thoss, M.; Tykwinski, R. R.; Wasielewski, M. R.; Guldi, D. M., Unified model for singlet fission within a non-conjugated covalent pentacene dimer. *Nat. Commun.* **2017,** *8*, 15171.
125. Lukman, S.; Chen, K.; Hodgkiss, J. M.; Turban, D. H. P.; Hine, N. D. M.; Dong, S.; Wu, J.; Greenham, N. C.; Musser, A. J., Tuning the role of charge-transfer states in intramolecular singlet exciton fission through side-group engineering. *Nat. Commun.* **2016,** *7*, 13622.
126. Zirzlmeier, J.; Lehnherr, D.; Coto, P. B.; Chernick, E. T.; Casillas, R.; Basel, B. S.; Thoss, M.; Tykwinski, R. R.; Guldi, D. M., Singlet fission in pentacene dimers. *Proc. Natl. Acad. Sci. U.S.A.* **2015,** *112* (17), 5325-5330.
127. Tayebjee, M. J. Y.; Schwarz, K. N.; MacQueen, R. W.; Dvorak, M.; Lam, A. W. C.; Ghiggino, K. P.; McCamey, D. R.; Schmidt, T. W.; Conibeer, G. J., Morphological Evolution and Singlet Fission in Aqueous Suspensions of TIPS-Pentacene Nanoparticles. *J. Phys. Chem. C* **2016,** *120*, 157–165.
128. Wu, Y.; Liu, K.; Liu, H.; Zhang, Y.; Zhang, H.; Yao, J.; Fu, H., Impact of Intermolecular Distance on Singlet Fission in a Series of TIPS Pentacene Compounds. *J. Phys. Chem. Lett.* **2014,** *5* (20), 3451-3455.
129. Mandal, A.; Chen, M.; Foszcz, E. D.; Schultz, J. D.; Kearns, N. M.; Young, R. M.; Zanni, M. T.; Wasielewski, M. R., Two-Dimensional Electronic Spectroscopy Reveals Excitation Energy-Dependent State Mixing during Singlet Fission in a Terrylenediimide Dimer. *J. Am. Chem. Soc.* **2018,** *140* (51), 17907-17914.
130. Chen, M.; Bae, Y. J.; Mauck, C. M.; Mandal, A.; Young, R. M.; Wasielewski, M. R., Singlet Fission in Covalent Terrylenediimide Dimers: Probing the Nature of the Multiexciton State Using Femtosecond Mid-Infrared Spectroscopy. *J. Am. Chem. Soc.* **2018,** *140* (29), 9184-9192.
131. Margulies, E. A.; Miller, C. E.; Wu, Y.; Ma, L.; Schatz, G. C.; Young, R. M.; Wasielewski, M. R., Enabling singlet fission by controlling intramolecular charge transfer in π-stacked covalent terrylenediimide dimers. *Nat. Chem.* **2016,** *8*, 1120-1125.
132. Dolomanov, O. V.; Bourhis, L. J.; Gildea, R. J.; Howard, J. A. K.; Puschmann, H., OLEX2: a complete structure solution, refinement and analysis program. *J. Appl. Crystallogr* **2009,** *42* (2), 339-341.
133. Zhylitskaya, H.; Cybińska, J.; Chmielewski, P.; Lis, T.; Stępień, M., Bandgap Engineering in π-Extended Pyrroles. A Modular Approach to Electron-Deficient Chromophores with Multi-Redox Activity. *J. Am. Chem. Soc.* **2016,** *138* (35), 11390-11398.
134. Young, R. M.; Singh, A. P. N.; Thazhathveetil, A.; Cho, V. Y.; Zhang, Y.; Renaud, N.; Grozema, F. C.; Beratan, D. N.; Ratner, M. A.; Schatz, G. C.; Berlin, Y. A.; Lewis, F. D.; Wasielewski, M. R., Charge Transport across DNA-Based Three-Way Junctions. *J. Am. Chem. Soc.* **2015,** *137* (15), 5113-5122.
135. Swart, M.; van Duijnen, P. T., DRF90: a polarizable force field. *Mol. Simulat.* **2006,** *32* (6), 471-484.

136. Mirjani, F.; Renaud, N.; Gorczak, N.; Grozema, F. C., Theoretical investigation of singlet fission in molecular dimers: The role of charge transfer states and quantum interference. *J. Phys. Chem. C* **2014,** *118* (26), 14192-14199.
137. Berkelbach, T. C.; Hybertsen, M. S.; Reichman, D. R., Microscopic theory of singlet exciton fission. II. Application to pentacene dimers and the role of superexchange. *J Chem Phys* **2013,** *138* (11), 114103.
138. Grieco, C.; Doucette, G. S.; Munro, J. M.; Kennehan, E. R.; Lee, Y.; Rimshaw, A.; Payne, M. M.; Wonderling, N.; Anthony, J. E.; Dabo, I.; Gomez, E. D.; Asbury, J. B., Triplet Transfer Mediates Triplet Pair Separation during Singlet Fission in 6,13-Bis(triisopropylsilylethynyl)-Pentacene. *Adv. Funct. Mater* **2017,** *27* (46), 1703929.
139. Mandal, A.; Chen, M.; Foszcz, E. D.; Schultz, J. D.; Kearns, N. M.; Young, R. M.; Zanni, M. T.; Wasielewski, M. R., Two-Dimensional Electronic Spectroscopy Reveals Excitation Energy-Dependent State Mixing during Singlet Fission in a Terrylenediimide Dimer. *Journal of the American Chemical Society* **2018,** *140* (51), 17907-17914.
140. Broch, K.; Dieterle, J.; Branchi, F.; Hestand, N. J.; Olivier, Y.; Tamura, H.; Cruz, C.; Nichols, V. M.; Hinderhofer, A.; Beljonne, D.; Spano, F. C.; Cerullo, G.; Bardeen, C. J.; Schreiber, F., Robust singlet fission in pentacene thin films with tuned charge transfer interactions. *Nat. Commun.* **2018,** *9* (1), 954.
141. Rietveld, H., A profile refinement method for nuclear and magnetic structures. *J. Appl. Crystallogr* **1969,** *2* (2), 65-71.
142. Petříček, V.; Dušek, M.; Palatinus, L., Crystallographic Computing System JANA2006: General features. In *Zeitschrift für Kristallographie - Crystalline Materials*, 2014; Vol. 229, p 345.
143. Carmichael, I.; Hug, G. L., Triplet–Triplet Absorption Spectra of Organic Molecules in Condensed Phases. *J. Phys. Chem. Ref. Data* **1986,** *15* (1), 1-250.
144. Shah, B. K.; Neckers, D. C.; Shi, J.; Forsythe, E. W.; Morton, D., Photophysical Properties of Anthanthrene-Based Tunable Blue Emitters. *J. Phys. Chem. A* **2005,** *109* (34), 7677-7681.
145. Geng, Y.; Yi, C.; Bircher, M. P.; Decurtins, S.; Cascella, M.; Grätzel, M.; Liu, S.-X., Anthanthrene dye-sensitized solar cells: influence of the number of anchoring groups and substitution motif. *RSC Advances* **2015,** *5* (119), 98643-98652.
146. Zhang, L.; Walker, B.; Liu, F.; Colella, N. S.; Mannsfeld, S. C. B.; Watkins, J. J.; Nguyen, T.-Q.; Briseno, A. L., Triisopropylsilylethynyl-functionalized dibenzo[def,mno]chrysene: a solution-processed small molecule for bulk heterojunction solar cells. *J. Mater. Chem* **2012,** *22* (10), 4266-4268.
147. Giguère, J.-B.; Sariciftci, N. S.; Morin, J.-F., Polycyclic anthanthrene small molecules: semiconductors for organic field-effect transistors and solar cells applications. *J. Mater. Chem. C* **2015,** *3* (3), 601-606.
148. Zhang, L.; Fonari, A.; Zhang, Y.; Zhao, G.; Coropceanu, V.; Hu, W.; Parkin, S.; Brédas, J.-L.; Briseno, A. L., Triisopropylsilylethynyl-Functionalized Graphene-Like Fragment Semiconductors: Synthesis, Crystal Packing, and Density Functional Theory Calculations. *Chem. Eur. J.* **2013,** *19* (52), 17907-17916.
149. Giguère, J.-B.; Boismenu-Lavoie, J.; Morin, J.-F., Cruciform Alkynylated Anthanthrene Derivatives: A Structure–Properties Relationship Case Study. *J. Org. Chem.* **2014,** *79* (6), 2404-2418.

150. Shah, B. K.; Neckers, D. C.; Shi, J.; Forsythe, E. W.; Morton, D., Anthanthrene Derivatives as Blue Emitting Materials for Organic Light-Emitting Diode Applications. *Chem. Mat.* **2006,** *18* (3), 603-608.
151. Stewart, D. J.; Shi, J.; Naranjo, T. R.; Grusenmeyer, T. A.; Artz, J. M.; McCleese, C. L.; O'Donnell, R. M.; Cooper, T. M.; Shensky, W. M.; Haley, J. E., Manipulating triplet states: tuning energies, absorption, lifetimes, and annihilation rates in anthanthrene derivatives. *Phys. Chem. Chem. Phys.* **2018,** *20* (45), 28412-28418.
152. Shockley, W.; Queisser, H. J., Detailed Balance Limit of Efficiency of p-n Junction Solar Cells. *J. Appl. Phys.* **1961,** *32* (3), 510-519.
153. Burdett, J. J.; Müller, A. M.; Gosztola, D.; Bardeen, C. J., Excited state dynamics in solid and monomeric tetracene: The roles of superradiance and exciton fission. *J. Chem. Phys.* **2010,** *133* (14), 144506.
154. Marciniak, H.; Fiebig, M.; Huth, M.; Schiefer, S.; Nickel, B.; Selmaier, F.; Lochbrunner, S., Ultrafast Exciton Relaxation in Microcrystalline Pentacene Films. *Phys. Rev. Lett.* **2007,** *99* (17), 176402.
155. Giguère, J.-B.; Verolet, Q.; Morin, J.-F., 4,10-Dibromoanthanthrone as a New Building Block for p-Type, n-Type, and Ambipolar π-Conjugated Materials. *Chem. Eur. J.* **2013,** *19* (1), 372-381.
156. Redmond, R. W.; Gamlin, J. N., A Compilation of Singlet Oxygen Yields from Biologically Relevant Molecules. *Photochem. Photobiol.* **1999,** *70* (4), 391-475.
157. Epelde-Elezcano, N.; Palao, E.; Manzano, H.; Prieto-Castañeda, A.; Agarrabeitia, A. R.; Tabero, A.; Villanueva, A.; de la Moya, S.; López-Arbeloa, Í.; Martínez-Martínez, V.; Ortiz, M. J., Rational Design of Advanced Photosensitizers Based on Orthogonal BODIPY Dimers to Finely Modulate Singlet Oxygen Generation. *Chem. Eur. J.* **2017,** *23* (20), 4837-4848.
158. Greenfield, S. R.; Wasielewski, M. R., Near-transform-limited visible and near-IR femtosecond pulses from optical parametric amplification using Type II β-barium borate. *Optics Letters* **1995,** *20* (12), 1394-1396.
159. Young, R. M.; Jensen, S. C.; Edme, K.; Wu, Y.; Krzyaniak, M. D.; Vermeulen, N. A.; Dale, E. J.; Stoddart, J. F.; Weiss, E. A.; Wasielewski, M. R.; Co, D. T., Ultrafast Two-Electron Transfer in a CdS Quantum Dot–Extended-Viologen Cyclophane Complex. *Journal of the American Chemical Society* **2016,** *138* (19), 6163-6170.
160. Stoll, S.; Schweiger, A., EasySpin, a comprehensive software package for spectral simulation and analysis in EPR. *J Magn Reson* **2006,** *178* (1), 42-55.
161. Bayliss, S. L.; Weiss, L. R.; Rao, A.; Friend, R. H.; Chepelianskii, A. D.; Greenham, N. C., Spin signatures of exchange-coupled triplet pairs formed by singlet fission. *Phys. Rev. B* **2016,** *94* (4), 045204/1-045204/7.
162. Weiss, L. R.; Bayliss, S. L.; Kraffert, F.; Thorley, K. J.; Anthony, J. E.; Bittl, R.; Friend, R. H.; Rao, A.; Greenham, N. C.; Behrends, J., Strongly exchange-coupled triplet pairs in an organic semiconductor. *Nat. Phys.* **2017,** *13*, 176-181.
163. Tayebjee, M. J. Y.; Sanders, S. N.; Kumarasamy, E.; Campos, L. M.; Sfeir, M. Y.; McCamey, D. R., Quintet multiexciton dynamics in singlet fission. *Nat. Phys.* **2017,** *13*, 182-188.
164. Dance, Z. E. X.; Ahrens, M. J.; Vega, A. M.; Ricks, A. B.; McCamant, D. W.; Ratner, M. A.; Wasielewski, M. R., Direct observation of the preference of hole transfer over electron

transfer for radical ion pair recombination in donor-bridge-acceptor molecules. *J. Am. Chem. Soc.* **2008,** *130* (3), 830-832.
165. Rao, A.; Chow, P. C. Y.; Gélinas, S.; Schlenker, C. W.; Li, C.-Z.; Yip, H.-L.; Jen, A. K. Y.; Ginger, D. S.; Friend, R. H., The role of spin in the kinetic control of recombination in organic photovoltaics. *Nature* **2013,** *500* (7463), 435-439.
166. Chen, M.; Krzyaniak, M. D.; Nelson, J. N.; Bae, Y. J.; Harvey, S. M.; Schaller, R. D.; Young, R. M.; Wasielewski, M. R., Quintet-triplet mixing determines the fate of the multiexciton state produced by singlet fission in a terrylenediimide dimer at room temperature. *Proc. Natl. Acad. Sci. U. S. A.* **2019,** *116* (17), 8178-8183.
167. Yong, C. K.; Musser, A. J.; Bayliss, S. L.; Lukman, S.; Tamura, H.; Bubnova, O.; Hallani, R. K.; Meneau, A.; Resel, R.; Maruyama, M.; Hotta, S.; Herz, L. M.; Beljonne, D.; Anthony, J. E.; Clark, J.; Sirringhaus, H., The entangled triplet pair state in acene and heteroacene materials. *Nat. Comm.* **2017,** *8* (1), 15953.
168. Basel, B. S.; Zirzlmeier, J.; Hetzer, C.; Phelan, B. T.; Krzyaniak, M. D.; Reddy, S. R.; Coto, P. B.; Horwitz, N. E.; Young, R. M.; White, F. J.; Hampel, F.; Clark, T.; Thoss, M.; Tykwinski, R. R.; Wasielewski, M. R.; Guldi, D. M., Unified model for singlet fission within a non-conjugated covalent pentacene dimer. *Nat. Comm.* **2017,** *8* (1), 15171.
169. Papadopoulos, I.; Zirzlmeier, J.; Hetzer, C.; Bae, Y. J.; Krzyaniak, M. D.; Wasielewski, M. R.; Clark, T.; Tykwinski, R. R.; Guldi, D. M., Varying the Interpentacene Electronic Coupling to Tune Singlet Fission. *J. Am. Chem. Soc.* **2019,** *141* (15), 6191-6203.
170. Lubert-Perquel, D.; Salvadori, E.; Dyson, M.; Stavrinou, P. N.; Montis, R.; Nagashima, H.; Kobori, Y.; Heutz, S.; Kay, C. W. M., Identifying triplet pathways in dilute pentacene films. *Nat. Comm.* **2018,** *9* (1), 4222.
171. Zhan, X.; Facchetti, A.; Barlow, S.; Marks, T. J.; Ratner, M. A.; Wasielewski, M. R.; Marder, S. R., Rylene and Related Diimides for Organic Electronics. *Adv. Mater.* **2011,** *23* (2), 268-284.
172. Wang, X.; Liu, X.; Cook, C.; Schatschneider, B.; Marom, N., On the possibility of singlet fission in crystalline quaterrylene. *J. Chem. Phys.* **2018,** *148* (18), 184101.
173. Zhan, X.; Facchetti, A.; Barlow, S.; Marks, T. J.; Ratner, M. A.; Wasielewski, M. R.; Marder, S. R., Rylene and Related Diimides for Organic Electronics. *Adv. Mater.* **2011,** *23* (2), 268-284.
174. Pisula, W.; Kastler, M.; Wasserfallen, D.; Robertson, J. W. F.; Nolde, F.; Kohl, C.; Müllen, K., Pronounced Supramolecular Order in Discotic Donor–Acceptor Mixtures. *Angew. Chem. Int. Ed.* **2006,** *45* (5), 819-823.
175. Nolde, F.; Pisula, W.; Müller, S.; Kohl, C.; Müllen, K., Synthesis and Self-Organization of Core-Extended Perylene Tetracarboxdiimides with Branched Alkyl Substituents. *Chem. Mat.* **2006,** *18* (16), 3715-3725.
176. Jiang, Z.; Li, X. F.; Strzalka, J.; Sprung, M.; Sun, T.; Sandy, A. R.; Narayanan, S.; Lee, D. R.; Wang, J., The dedicated high-resolution grazing-incidence X-ray scattering beamline 8-ID-E at the Advanced Photon Source. *J Synchrotron Radiat* **2012,** *19*, 627-636.
177. Jiang, Z., GIXSGUI: a MATLAB toolbox for grazing-incidence X-ray scattering data visualization and reduction, and indexing of buried three-dimensional periodic nanostructured films. *J. Appl. Crystallogr* **2015,** *48* (3), 917-926.
178. Wang, G.; Swick, S. M.; Matta, M.; Mukherjee, S.; Strzalka, J. W.; Logsdon, J. L.; Fabiano, S.; Huang, W.; Aldrich, T. J.; Yang, T.; Timalsina, A.; Powers-Riggs, N.; Alzola, J.

M.; Young, R. M.; DeLongchamp, D. M.; Wasielewski, M. R.; Kohlstedt, K. L.; Schatz, G. C.; Melkonyan, F. S.; Facchetti, A.; Marks, T. J., Photovoltaic Blend Microstructure for High Efficiency Post-Fullerene Solar Cells. To Tilt or Not To Tilt? *J. Am. Chem. Soc.* **2019,** *141* (34), 13410-13420.
179. Savikhin, V.; Babics, M.; Neophytou, M.; Liu, S.; Oosterhout, S. D.; Yan, H.; Gu, X.; Beaujuge, P. M.; Toney, M. F., Impact of Polymer Side Chain Modification on OPV Morphology and Performance. *Chem. Mat.* **2018,** *30* (21), 7872-7884.
180. Rivnay, J.; Mannsfeld, S. C. B.; Miller, C. E.; Salleo, A.; Toney, M. F., Quantitative Determination of Organic Semiconductor Microstructure from the Molecular to Device Scale. *Chem. Rev.* **2012,** *112* (10), 5488-5519.
181. Matsui, Y.; Kawaoka, S.; Nagashima, H.; Nakagawa, T.; Okamura, N.; Ogaki, T.; Ohta, E.; Akimoto, S.; Sato-Tomita, A.; Yagi, S.; Kobori, Y.; Ikeda, H., Exergonic Intramolecular Singlet Fission of an Adamantane-Linked Tetracene Dyad via Twin Quintet Multiexcitons. *J. Phys. Chem. C* **2019,** *123* (31), 18813-18823.
182. Buchanan, E. A.; Kaleta, J.; Wen, J.; Lapidus, S. H.; Císařová, I.; Havlas, Z.; Johnson, J. C.; Michl, J., Molecular Packing and Singlet Fission: The Parent and Three Fluorinated 1,3-Diphenylisobenzofurans. *J. Phys. Chem. Lett.* **2019,** *10* (8), 1947-1953.
183. Bae, Y. J.; Krzyaniak, M. D.; Majewski, M. B.; Desroches, M.; Morin, J.-F.; Wu, Y.-L.; Wasielewski, M. R., Competition between Singlet Fission and Spin-Orbit-Induced Intersystem Crossing in Anthanthrene and Anthanthrone Derivatives. *ChemPlusChem* **2019,** *84* (9), 1432-1438.
184. Yago, T.; Ishikawa, K.; Katoh, R.; Wakasa, M., Magnetic Field Effects on Triplet Pair Generated by Singlet Fission in an Organic Crystal: Application of Radical Pair Model to Triplet Pair. *J. Phys. Chem. C* **2016,** *120* (49), 27858-27870.
185. Roessler, M. M.; Salvadori, E., Principles and applications of EPR spectroscopy in the chemical sciences. *Chem. Soc. Rev.* **2018,** *47* (8), 2534-2553.
186. Dance, Z. E. X.; Mickley, S. M.; Wilson, T. M.; Ricks, A. B.; Scott, A. M.; Ratner, M. A.; Wasielewski, M. R., Intersystem Crossing Mediated by Photoinduced Intramolecular Charge Transfer: Julolidine−Anthracene Molecules with Perpendicular π Systems. *J. Phys. Chem. A* **2008,** *112* (18), 4194-4201.
187. Miura, T.; Carmieli, R.; Wasielewski, M. R., Time-Resolved EPR Studies of Charge Recombination and Triplet-State Formation within Donor−Bridge−Acceptor Molecules Having Wire-Like Oligofluorene Bridges. *J. Phys. Chem. A* **2010,** *114* (18), 5769-5778.